Fluid-structure interaction analysis of the aortic valve in young healthy, ageing and post treatment conditions

Anna Maria Tango

A thesis submitted
for the degree of
Doctor of Philosophy

Department of Mechanical Engineering
University College London

Disclaimer

I, Anna Maria Tango, confirm that the work presented in this thesis is my own.

Where information has been derived from other sources, I confirm that this has been indicated in the work.

Part of the research presented in this thesis has been published in one article and one book chapter:

J. Salmonsmith, A. M. Tango, A. Ducci, and G. Burriesci, "Haemodynamics issues with transcatheter aortic valve implantation," in *Transcatheter Aortic Valve Implantation: Clinical, Interventional, and Surgical Perspectives.*, A. Giordano, G. Biondi-Zoccai, and G. Frati, Eds. Springer International (2019).

Tango, A.M., Salmonsmith, J., Ducci, A., & Burriesci, G. (2018). Validation and Extension of a Fluid–Structure Interaction Model of the Young healthy Aortic Valve. *Cardiovascular Engineering and Technology*, *9*(4), 739–751.

And has been presented at:

9th International Congress on Industrial and Applied Mathematics, Valencia, Spain.

Frontiers of Simulation and Experimentation for Personalised Cardiovascular Management and Treatment, London, UK.

8th World Congress of Biomechanics, Dublin, Ireland.

7th International Conference on Computational Bioengineering, Compiègne, France.

Funding

This work was supported by the Rosetrees Trust (Grant Ref. A730) and supporting benefactors.

Abstract

Optimal aortic valve function, limitation of blood damage, and frequency of thromboembolic events are all dependent upon the haemodynamics within the aortic root. Improved understanding of the young healthy physiological state via investigation of the fluid dynamics around and through the aortic valve is essential to identify detrimental changes leading to pathologies and develop novel therapeutic procedures. The aim of this study is to develop a numerical model that can support a better comprehension of the valve function and serve as a reference to identify the changes produced by specific pathologies and treatments.

A Fluid-structure interaction (FSI) numerical model was developed and adapted to accurately replicate the conditions of a previous in vitro investigation into aortic valve dynamics, performed by means of particle image velocimetry (PIV).

The model was validated on equivalent physical settings, in a pulse duplicator replicating the physiological healthy flow and pressure experienced in the left heart chambers. The resulting velocity fields and hydrodynamic valve performance indicators of the two analyses were qualitatively and quantitatively compared to validate the numerical model.

The validated FSI model was then used to describe realistic young healthy, ageing and post treatment conditions, by eliminating the experimental and methodological limitations and approximations. In detail, in terms of treatments, both surgical and transcatheter valve replacement procedures were investigated. In terms of pathologies, typical alterations frequently due to ageing, namely thickening of the valve leaflets and progressive dilation of the aortic chamber, were studied.

The analysis was performed by comparing the data obtained for the ageing and post treatment configurations with those of the young healthy root environment. The results were analysed in terms of leaflets kinematics, flow dynamics, pressure and valve performance parameters.

The study suggests a new operating mechanism for the young healthy aortic valve leaflets considerably different from what reported in the literature to date and largely more efficient in terms of hydrodynamic performance.

Impact Statement

The study presented in this thesis builds upon the need to overcome the limitations related to experimental studies in order to expand findings hence enhancing the understanding of the haemodynamics within the aortic root.

This work provides a validated numerical method that can support a better comprehension of the phenomena that participate in the correct valve functioning and may serve as a benchmark to identify the changes produced by specific pathologies and treatments, supplying a powerful tool in the design of novel and/or improved devices and therapies. In fact, a new operating mechanism behind the young healthy aortic valve functioning was observed, revealing the intended function of the Valsalva sinuses. On the other hand, the implantation of prosthetic devices was shown to produce major haemodynamics alterations which alters the valve dynamics and leads to inefficient functioning and diminished performance.

This demonstrates how, currently, the design of prosthetic devices is not optimised to mimic realistic native conditions, since the full leaflets opening profile is based on a cylindrical shape. Although, among treatments, transcatheter devices provide systolic features more similar to those observed in the young healthy aortic chamber, neither surgical nor treatments via catheter are able to fully restore physiological healthy conditions.

As for pathological conditions, most of the flow features observed for the young healthy aortic valve model, were also detected in the ageing configurations.

However, the combination of stiffened leaflets and dilated aortic root, which is often the case in ageing patients, was shown to lead to the overall worst performance. On the other hand, a larger aortic chamber seems to be able to globally improve the haemodynamics when pathologies are concomitant.

These results have been disseminated in both written form, via an article in the Cardiovascular Engineering and Technology Journal and a book chapter in ‘Transcatheter Aortic Valve Implantation: Clinical, Interventional, and Surgical Perspectives’, and aurally, via presentations at the 9th International Congress on Industrial and Applied Mathematics, Frontiers of Simulation and Experimentation for Personalised Cardiovascular Management and Treatment Conference, 8th World Congress of Biomechanics and 7th International Conference on Computational Bioengineering.

This study also confirms the crucial role that numerical approaches, complemented with experimental findings, can play in overcoming some of the limitations inherent in experimental techniques, supporting the full understanding of complex physiological phenomena.

Acknowledgements

I first would like to gratefully acknowledge both my supervisors Gaetano Burriesci and Andrea Ducci for their worth support and encouragement which has led to the success of this work.

I am extremely grateful to my family and friends for being so supportive throughout my life, without their support I would have been able not achieved such goals. I also would like to thank my colleagues at UCL who have shared joys and sorrows of this journey with me and made this PhD a wonderful experience.

I am very thankful to my boyfriend Paolo who always inspires me and prompts me to do my best.

I also gratefully acknowledge the funding received towards my PhD from the Rosetrees Trust (Grant number A730 UCL) and benefactor's family.

Contents

List of figures

List of tables

Nomenclature

Abbreviations

2D Two-dimensional

3D Three-dimensional

AVA Aortic Valve Area

CO Cardiac Output

EOA Effective Orifice Area

ET Ejection Time

HR Heart Rate

LCA Left Coronary Artery

LVOT Left Ventricular Outflow Tract

NCA Non-Coronary Artery

RCA Right Coronary Artery

SEP Systolic Ejection Period

SV Stroke Volume

TAVI Transcatheter Aortic Valve Implantation

VTI Velocity Time Integral

WSS Wall Shear Stress

Symbols

A	Area
ΔP	Systolic transvalvular pressure drop
σ	Stress
ε	Strain
e	Mechanical energy
ρ	Density
v	Material velocity
u	Mesh velocity
L_c	Characteristic length of the element
c	Speed of sound
f	Time step scale factor
μ	Dynamic viscosity
$q_{v_{RMS}}$	Root mean square forward flow
Q	Flow rate
R	Radius
t	Time
τ	Shear stress
τ_W	Wall shear stress

Thesis outline

This thesis is divided into eight chapters including the background, development and validation and applications of the computational models used for the analysis of the aortic valve functioning in young healthy, ageing and post treatment conditions. In detail, the objectives of this are presented in the different chapters as follows:

In Chapter 1 the clinical background of this work is presented. In order to explain the clinical need, a description of the cardiovascular system, the main diseases affecting the aortic valve and the most common solutions adopted in the treatment of aortic valve pathologies, is provided.

In Chapter 2 a review of the literature for healthy, diseased and treated aortic valves is presented along with the main findings from the literature, aims and objectives of this work.

In Chapter 3 a description of the computational methodology employed and numerical framework used to model the aortic valve environment along with the features characterising each model, is provided.

In Chapter 4 validation of the numerical framework employed in this study is achieved through a qualitative and quantitative comparison with experimental findings from a previous *in vitro* study.

In Chapter 5, the results obtained for the young healthy aortic valve configuration, which describes the benchmark against which the effect of ageing and treatments is measured, are presented.

In Chapters 6 the results obtained for the young healthy and ageing aortic valve conditions are analysed and compared in order to evaluate the haemodynamics alterations produced by the ageing process. The related discussion is provided at the end of the chapter.

In Chapters 7 a comparison between the findings from the young healthy and post treatment aortic valve configurations is described and discussion is provided at the end of the chapter.

In Chapter 8 the potential and limitations of this work are analysed.

Chapter 1 Background

Introduction

Heart valves are thin flaps of tissue that open and close under the effect of hydrodynamic forces, enforcing unidirectionality in the blood flow. When, due to valvular diseases, they become severely dysfunctional, they need to be replaced with prosthetic devices designed to replicate their operating function. The main artificial substitutes are surgical (mechanical and biological heart valves) and transcatheter devices.

This chapter provides an insight into the cardiovascular physiology, the main pathologies affecting the aortic valve and the most common treatments and related complications.

1.1 The heart

The heart is a muscular organ that, acting as a pump, supplies blood to all parts of the body through a one-way circuit system. The transportation of blood to the tissues and organs in the human body is essential to provide oxygen and nutrients and remove waste. Actually, as the heart is divided into two halves, the right and left heart, it can be considered to consist of two synchronous pumps (J.R. Levick, 2009). Each half comprises two chambers: a thin-walled atrium and a thick-walled ventricle (Tu, Inthavong, & Wong, 2015). The two pumps are connected through a network of vessels constituted by arteries on the right side of the heart, and by veins on the left side of the heart. The arteries carry blood away from the heart while the veins return blood to the heart (Silverthorn, 2013). Blood flow through the heart is regulated by two pairs of valves: the mitral and tricuspid valves, which separate the atria and the ventricles, and the aortic and pulmonary valves which are situated between the ventricles and the major arteries (Figure 1.1) (Farley, McLafferty, & Hendry, 2012).

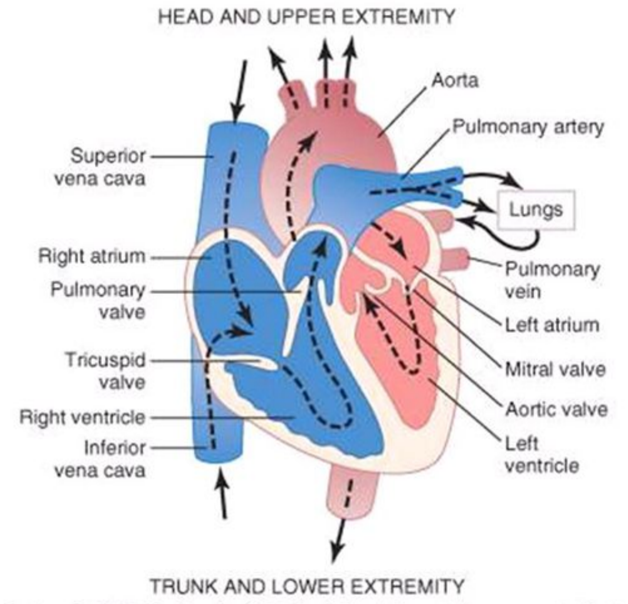

Figure 1.1. The pathway of blood flow through the heart (Hall, J. E., & Guyton, 2011).

The flow of blood through the cardiovascular system is driven by the pressure gradient (Silverthorn, 2013). The heart receives low pressure blood from the veins, generates high pressure through its contractions, and then ejects the blood into the arteries (Klabunde, 2011). After circulating through the body and delivering oxygen and nutrients, low pressure blood, at about 0 mmHg, flows to the right atrium through veins (the superior and inferior vena cava).

Blood flows from the right atrium into the right ventricle across the tricuspid valve. Towards the end of filling, when the ventricle is nearly full, blood begins to collect in the atrium and the atrium contracts.

Next, when the ventricle contracts, the blood is pumped to the lungs through the pulmonary valve. This generates a pressure in the pulmonary artery ranging from 20 to 30 mmHg. From the lungs, oxygen-rich blood enters the left atrium by pulmonary veins dropping the pressure to 10 mmHg. The left atrium fills with blood and it contracts pumping blood to the left ventricle through the mitral valve. Finally, the pressure rises to values ranging from 100 to 140 mmHg, and oxygenated blood, passing through the aortic valve, reaches the aorta (Klabunde, 2011).

Since the left heart typically achieves pressures much higher than those experienced by the right heart over the cardiac cycle, (Michael S. Sacks, Merrryman, & Schmidt, 2010), the left ventricle can be considered as an high pressure pump, while the right ventricle as a low pressure pump (Klabunde, 2011).

1.2 Heart valves

The presence of valves within this closed loop pumping system supports unidirectional flow (Klabunde, 2011). The mitral and tricuspid valves are called atrioventricular valves, while the aortic and pulmonary valves are called arterioventricular due to their locations between the exit to the ventricles and the great arteries or semilunar valves because of their leaflets half moon shape. Since the atrioventricular valves are anchored to the heart muscle through the papillary muscles and the fibrous bands called chordae tendinae, they are considered to respond actively to cardiac contractions (Thubrikar M., 1990). On the other hand, semilunar valves, that are not tethered to the cardiac muscle, are believed to act passively following the blood flow (Thubrikar M., 1990).

1.2.1 The aortic valve

The aortic valve guarantees the unidirectionality of the blood flow between the left ventricle and the ascending aorta. Anatomically, it can be considered being a part of different structures that all together contribute to the proper valve functioning (Schnabel, Lichtenberg, Herpel, Warth, & Gassler, 2010).

This semilunar valve consists of three leaflets whose profile forms a three-pointed coronet (Thubrikar M., 1990). The base of this coronet that represent the leaflets anchoring zone to the vessel wall, has been erroneously called ‘annulus’ implying the presence of a fibrous ring made of collagene describing a circumference (Sutton, 1995). In fact, it is well known that the annulus resembles a crown shape and not a circular structure (Charitos & Sievers, 2013). However, as shown in Figure 1.2, two virtual rings can be obtained by projecting the three attachment points at the nadir of each cusps, and the coronet tips into circles, known as the Annulus and Sino-tubular junction, respectively (G. S. Bloomfield et al., 2012).

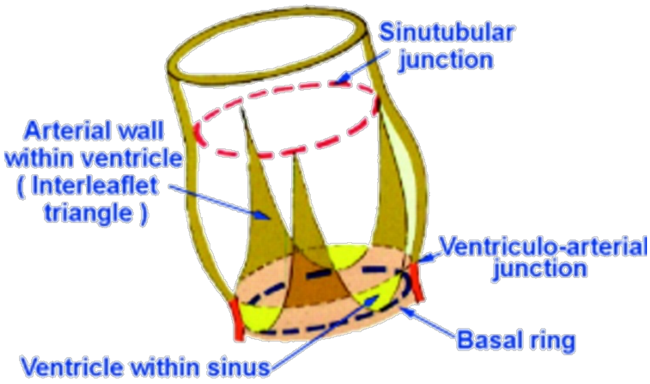

Figure 1.2. Schematic drawing of the aortic root structure (Anderson, 2000).

Each leaflet presents different parts: a belly, a free edge, and a basal attachment (Charitos & Sievers, 2013). The belly is the leaflet part that divides the left ventricle and the aorta into two chambers and is subject to the aortic pressure load, while the free edge provides the contact area of neighbouring leaflets in closed position (Thubrikar M., 1990). Each leaflet free margin presents a thickened circular node in the centre, called node of Arantius (Otto, C.M., Bonow, 2014). The thin borders of the leaflets surfaces overlapping during the valve closure delimited by the Arantius node creating a semilunar shape, are called lunulae (Gassler & Schnabel, 2010; Tamburino,C.,Ussia, 2012).The portion of the lunulae attached to the aortic wall at the sino-tubular junction is called commissure (Tamburino,C.,Ussia, 2012).

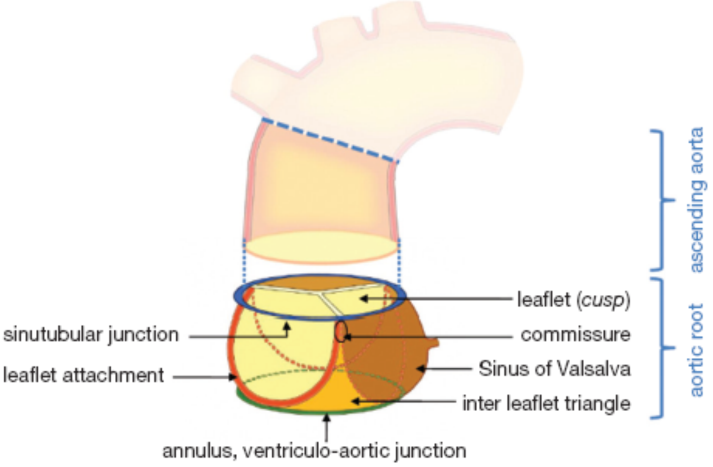

Figure 1.3. The aortic valve structure view (Charitos & Sievers, 2013).

As shown in Figure 1.3, the part of the aorta where the aortic valve is anchored is called aortic root. The latter comprises the aortic valve leaflets, the interleaflet triangles and the Valsalva sinuses (Sutton, 1995). The Valsalva sinuses are bulges surrounding the valve leaflets which extend from the left ventricular outflow tract to the sino-tubular junction (Otto, C.M., Bonow, 2014). As result of the coronet shape leaflet profile, three fibrous regions separating each sinus are formed. These are called interleaflet triangles (Anderson, 2000). Two of the three sinuses give rise to the coronary arteries, usually below or at the level of the sino-tubular junction, and therefore are named accordingly as the left, the right and non-coronary sinus (Charitos & Sievers, 2013).

The aortic valve opens and closes approximately 103,000 times per day and 3.7 billion times in its lifespan (Thubrikar M., 1990).

In summary, the aortic root represents a complex system comprising a number of different anatomical parts which together provide for a well-functioning aortic valve (Muraru, Badano, Vannan, & Iliceto, 2012). The basal parts experience ventricular pressure and consequently expand during ventricular filling and contract during systole. The upper parts instead, undergo aortic pressure loads and therefore expand during systole supporting the valve opening (Sutton, 1995). The role played by the Valsalva sinuses in terms of haemodynamics is discussed in Chapter 2.

1.2.1.1 Leaflets histology and mechanical properties

The aortic valve is characterised by a complex layered structure which is primarily composed of fibrous connective tissue outwardly covered by a layer of endothelial cells (Croft, L. R., Mofrad, M.R.K., 2010). The leaflet tissue is composed of three main layers: the ventricularis, the spongiosa, and the fibrosa, in order of inflow surface to outflow surface (Schoen & Levy, 1999)(Figure 1.4).

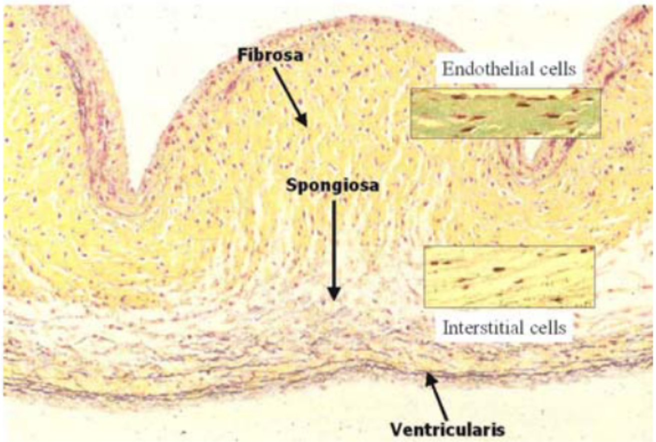

Figure 1.4. Cusps layered structure (Mendelson & Schoen, 2006).

The ventricularis, which faces the ventricular chamber, is the thinnest layer and consist of collagen and elastin fibers, where the latter are mainly radially aligned (Rozeik, Wheatley, & Gourlay, 2014). This arrangement contributes to reduce the large radial strains occurring at the systolic peak when the valve is fully open (Michael S. Sacks et al., 2010). Due to its high elastin content and its attachment to the fibrosa via the spongiosa, the ventricularis has been reported to exert compressive forces that keep the fibrosa in the undulated conformation(Stella & Sacks, 2007; Ivan Vesely & Noseworthy, 1992). It is also responsible for the elastic recoil present in the unloaded leaflets (Ivan Vesely, 1997).

The spongiosa layer, is gel-like, contains mainly proteoglycans and is believed to act as lubrication between the fibrous layers (Billiar & Sacks, 2000). It presents multiple corrugations oriented along the circumferential direction (Stella & Sacks, 2007) (see Figure 1.4). The fibrosa, which is the layer closest to the outflow, is predominantly made up of collagen fibers oriented in the circumferential direction and therefore provides the necessary endurance to the heavy loads experienced by the closed valve (Mendelson & Schoen, 2006). When the leaflet is unloaded, the network of collagen fibers exhibit a highly undulated arrangement(Stella & Sacks, 2007).

The resulting architecture allows the leaflets to adapt to different loading conditions according to the physiological needs due to its changes in shape and dimension, transferring the stress to the annulus and the aortic wall, and contributing to ongoing repair and remodelling (Schoen & Levy, 1999). The different constituents are arranged in a non-random orientation within this layered structure leading to highly anisotropic properties (Schoen & Levy, 1999).

The valve cusps present complex anisotropic and viscoelastic mechanical properties as result of the circumferential and radial alignments of the collagen and elastin fibres (Michael S. Sacks, 2000).

In fact, cusp displacement consists of flexion during the valve opening movement and tension when the valve shuts at diastole bearing the diastolic pressure (M. S Sacks & Yoganathan, 2007). At systole, the crimped collagen fibres extend along the force direction and corrugate (Figure 1.5(A) Systole). This translates into in an initial toe region as the collagen straightens out and a linear stress-strain relationship (Figure 1.5(B)). At closure instead, the collagen fibres unfold and the stress due to loading transfers from elastin to collagen increasing steadily during leaflets coaptation (Figure 1.5(A) Diastole). During opening, the corrugated configuration of the cusp is restored by the elastin (Schoen & Levy, 1999).

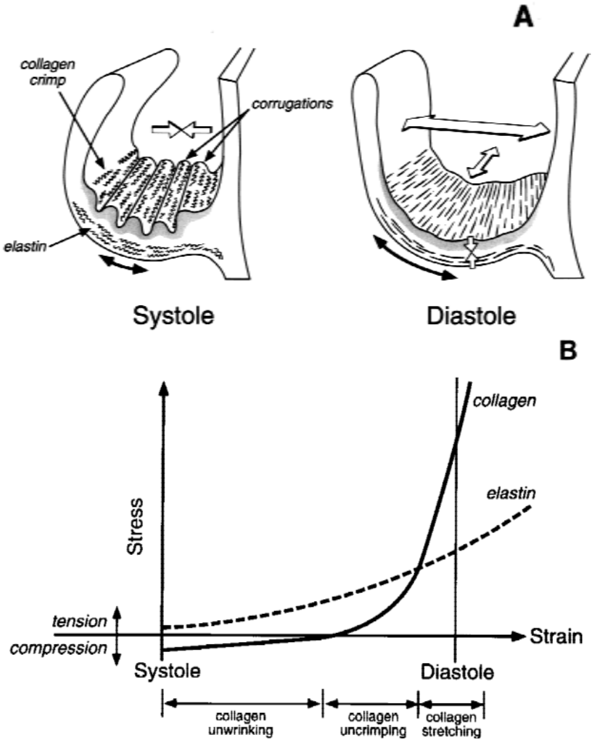

Figure 1.5. Schematic representation of cuspal configuration and architecture of collagen and elastin in systole and diastole(A), schematic representation of biomechanical cooperativity between elastin and collagen during valve motion(B) (Schoen & Levy, 1999).

The cusps behaviour is viscoelastic as their mechanical properties show both elastic and viscous features (Rozeik et al., 2014). Therefore, the material properties of aortic valve leaflets are commonly described as highly non-linear, incompressible and anisotropic (Croft, L. R., Mofrad, M.R.K., 2010).

From ex vivo measurements, the average leaflet thickness for the healthy aortic valve has been reported to be 423.7 ± 163.0 µm (Hutson et al., 2016).

1.3 The cardiac cycle

The quantity of blood pumped by the heart in one minute is known as the cardiac output and it is determined by the stroke volume, that is the volume ejected per contraction, and by the number of contractions occurring in one minute i.e., the heart rate (J.R. Levick, 2009). The typical value for the cardiac output at rest is five litres per minute but it can increase according to the body's demands (J.R. Levick, 2009). The heart rate triggers the cardiac contractions that, in turn, dictate the cardiac cycle phases. These contractions are driven by the electrical impulses originating from the nervous tissue in the wall of the right atrium known as the pacemaker or sino-atrial node (Caro, C., Pedley, T., Schroter, R., Seed, W., & Parker, 2012).

The cardiac cycle includes the series of events happening in the heart every heartbeat. These events occur nearly simultaneously for both sides of the heart. The typical frequency of the cardiac cycle at rest for an adult is 60-90 beats/min (bpm) (Tu et al., 2015).The cardiac cycle consists of four phases: ventricular filling, isovolumetric contraction, ejection or systole and isovolumetric relaxation.

The cycle starts with the ventricular filling through atrioventricular valvular orifices. Then, the pressure in the ventricles increases and when it exceeds that in the atria, the atrioventricular valves close preventing the backflow. Thus, the valves closure leads to the formation of two closed chambers causing a rise in the ventricular pressure. The ventricles begin to contract giving what is known as the phase of isovolumetric contraction.

As soon as the pressure in the ventricles overcomes that in the aorta for the left side of the heart, and of the pulmonary artery for the right side of the heart, the aortic and pulmonary valves, respectively, open. Lastly, during the isovolumetric relaxation phase, the heart muscle starts relaxing, the arterioventricular valves close generating again closed ventricular chambers causing a drop in ventricular blood pressures that when exceeded by the atrial pressure leads to opening of the AV valves and the start of a new cardiac cycle (J.R. Levick, 2009) (Figure 1.6). Hence, the pulsatile nature of the arterial pressure can be seen as a result of ejection and relaxation phases characterising the cardiac cycle (Pappano, Achilles J., Withrow Gil Wier, 2012).

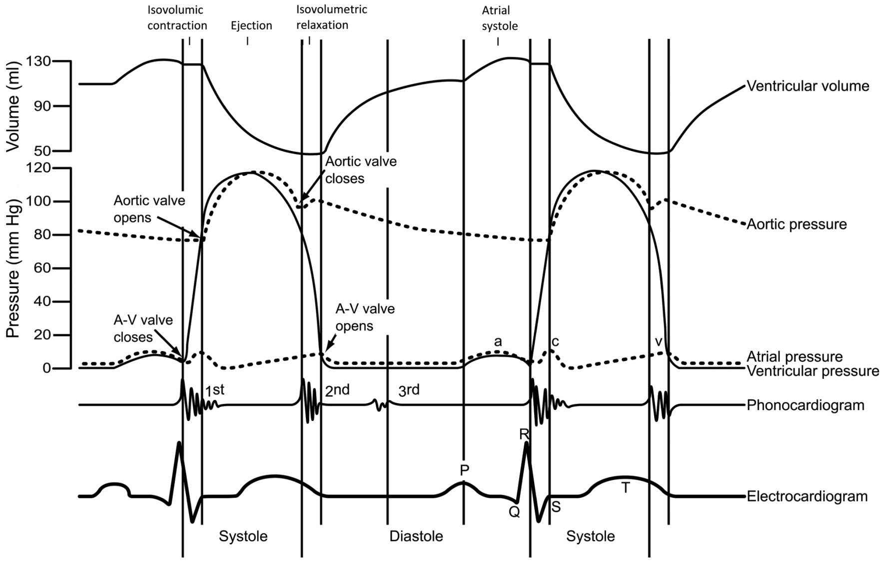

Figure 1.6. The cardiac cycle and its main phases (Berntson, G., Quigley, K., Norman, G., & Lozano, 2016).

1.4 Valvular diseases

A young healthy valve presents little resistance to forward flow and therefore a low transvalvular pressure gradient during the valve opening, and then a prompt closure which prevents reverse flow (Klabunde, 2011). A valve becomes dysfunctional if it obstructs the forward flow or it fails to shut correctly, allowing the passage of backflow. In the former case, the pathology is called stenosis, while the latter is called regurgitation or insufficiency (B.Hilton, Robert E.Yutzey, 2011).

Both diseases have an impact on the pressure distribution and physiological flow rate during the normal valve function (Klabunde, 2011).

Valve pathologies can be congenital, acquired or both. Acquired diseases can have rheumatic or nonrheumatic origin however, nowadays, rheumatic fever has become rare among the developed countries (Otto, C.M., Bonow, 2014). There are relatively few new cases of rheumatic fever seen the effects rheumatic valvular disease may take several decades to emerge so the consequences may still be seen in the elderly.

As already discussed in section 1.1, the left heart can be considered as a high-pressure pump while the right heart as a low-pressure pump. Consequently, the two valves on the left side of the heart are subject to much higher loads than those on the right heart. For this reason, most of valvular diseases involve left heart valves i.e., the mitral and aortic valves (Ragavendra R. Baliga, Kim A. Eagle, William F Armstrong, David S Bach, 2008). In particular, aortic valve pathologies represent a common clinical concern whose prevalence is likely increasing with population ageing (Saibal, Kar, Prediman, 2006).

1.4.1 Aortic valve pathologies: stenosis and regurgitation

Aortic valve stenosis is the most common pathology among valvular diseases (Iung et al., 2003). Stenosis is associated with a narrowing of the valve orifice, resulting in an increase in terms of resistance to the forward flow, thereby leading to a pressure gradient rise across the open valve (Klabunde, 2011). This disease can originate from congenital valve malformations, such as in the event of bicuspid aortic valve where the valve presents only two leaflets instead of three; alternatively its cause can be degenerative, for example, due to calcium deposits on the aortic side of the cusps (Nishimura, 2002). Stenosis can be distinguished as subvalvular, valvular or supravalvular stenosis depending on the obstruction location, depending on whether occurs just below the valve, i.e., at the level of the left ventricular outflow tract, or at the level of valve cusps, or just above the aortic sinuses, respectively (Gassler & Schnabel, 2010). The most frequent form of stenosis is the valvular stenosis. When the opening of the aortic valve becomes narrowed, the work load in the left ventricle is significantly increased to maintain an adequate flow rate. Thus, the muscle walls in the left ventricle become thicker and dilate to support the extra load. This compensatory mechanism actuated by the left ventricle is named hypertrophy (Carabello, 2007).

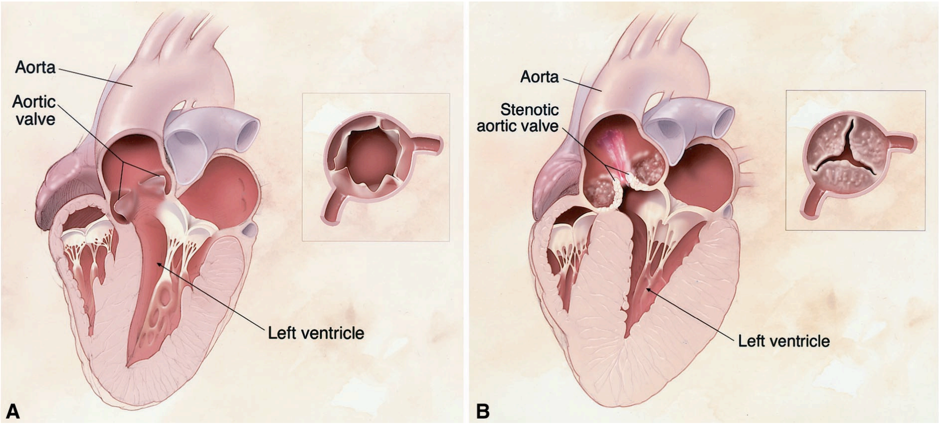

Figure 1.7. Young healthy (A) and stiffened aortic valve (B) during systole (Nishimura, 2002).

Congenital abnormalities represent the most frequent form of aortic stenosis in young adults and may be characterised by the presence of a unicuspid, bicuspid or tricuspid aortic valve (Ward, 2006). Bicuspid aortic valve (BAV) is the most recurrent type of congenital heart valve defect. In such circumstance, the two cusps are unequal in size, as one results from the fusion of two cusps (Rozeik et al., 2014).

The incidence of bicuspid aortic valve disease is higher in males than females and concerns the 1-2 % of the population (Robert O. Bonow, Douglas L. Mann, Douglas P. Zipes, 2011).

However, calcific degeneration of the leaflets represents the most common cause of stenosis globally, affecting mostly the elderly with an occurrence of 2-7% (Iung et al., 2003; Ward, 2006).

Calcification is a process evolving during the years as a results of the gradual calcium deposition on the fibrous part of the leaflets which thicken the valve restricting the cusps motion (Tamburino,C.,Ussia, 2012). Its etiology is still a subject of debate (B.Hilton, Robert E.Yutzey, 2011).

However, several studies suggest that unphysiological hemodynamic forces (such as high shear and bending stresses) experienced by the valve leaflets can cause tissue remodelling and inflammation, leading to calcification, stenosis, and ultimately tissue degradation and valve failure (Balachandran, Sucosky, & Yoganathan, 2011; Boon, Cheriex, Lodder, & Kessels, 1997; Mohler et al., 2001; Rajamannan et al., 2011, 2003; Stewart et al., 1997; Sun, Chandra, & Sucosky, 2012; Wheatley, Fisher, Reece, Spyt, & Breeze, 1987).

The valvular lesions tend to predominantly affect the aortic side tissue of the leaflets. This may be due to the differences in terms of both biomechanical and haemodynamic forces between the ventricular and the aortic side of the valve leaflets, but also to the different morphology of the two sides of the valve (Bäck, Gasser, Michel, & Caligiuri, 2013)

At the same time, a malformed valve over time may be more prone to develop degenerative disease due to the mechanical stress of wear and tear (Gassler & Schnabel, 2010; Tamburino,C.,Ussia, 2012).

Different parameters allow to clinically assess the severity of stenosis, they are: effective orifice area (EOA), jet velocity, ejection fraction and transvalvular pressure gradients. The EOA is the minimal cross-sectional area of the forward flow jet downstream the valve. Cardiac catheterisation and Doppler echocardiography represent two standard methods to calculate it (Rozeik et al., 2014). The first method is based on the revised Gorlin formula (Cohen, Michael V., Gorlin, 1972):

$$\mathrm{A} = \frac{\mathrm{CO}}{\mathrm{HR} \cdot \mathrm{SEP} \cdot 44.3 \cdot \mathrm{C} \cdot \sqrt{\Delta \mathrm{P}}} \tag{1}$$

where A is the orifice area of the valve (cm^2), CO is the cardiac output ($\frac{\mathrm{cm}^3}{\mathrm{min}}$), HR is the heart rate in beats per minute, SEP is the systolic ejection period in seconds per heartbeat, 44.3C is an empirical constant (C is assumed to be 1.0 for the aortic valve), and ΔP is the transvalvular pressure gradient in mmHg. Cardiac catheterisation is employed in order to evaluate the pressure gradient across the valve (Dumesnil & Yoganathan, 1991).

The second method, instead, uses the continuity equation to measure the EOA:

$$\mathrm{EOA} = \frac{\mathrm{A}_{\mathrm{LVOT}} . \mathrm{VTI}_{\mathrm{LVOT}}}{\mathrm{VTI}_{\mathrm{VC}}} = \frac{\mathrm{SV}}{\mathrm{VTI}_{\mathrm{VC}}} \tag{2}$$

where A is the geometric area, VTI is the velocity time integral and SV is the stroke volume.

The formula assumes that the flow in the left ventricular outflow tract (LVOT) is equal to the flow in the vena contracta, which is the area where the flow jet is minimum (Garcia & Kadem, 2006).

The VTI on a prescribed cross section is obtained from an integration in time of Doppler velocity measurements over the systolic phase of the cardiac cycle (Shadden, Astorino, & Gerbeau, 2010).

As Doppler echocardiography bases its EOA estimation on the VTI at the vena contracta and the use of the continuity equation is subject to measurements errors, this approach tends to overestimate the severity of the aortic stenosis, leading to unnecessary clinical measures (Rozeik et al., 2014).

However, it is still debated if the area calculated using the Gorlin formula can be equivalent to that calculated using the continuity equation as the transvalvular pressure gradient measurement is strictly dependent on the catheter tip position. They can be considered equivalent only if the pressure acquisitions are within the vena contracta (Garcia & Kadem, 2006).

Aortic stenosis is classified into mild, moderate or severe according to the parameters based on echocardiographic measurements described in Table 1.1 (Baumgartner et al., 2009):

Table 1.1. Parameters to classify aortic stenosis severity.

Parameters	**Mild**	**Moderate**	**Severe**
Aortic jet velocity ($\frac{m}{s}$)	2.6-2.9	3.0-4.0	<4.0
Mean gradient (mmHg)	<20 (<30^a)	20-40^b (30-50^a)	>40^b (>50^a)
Aortic valve area (AVA) (cm^2)	>1.5	1.0-1.5	<1
Indexed AVA ($\frac{cm^2}{m^2}$)	>0.85	0.60-0.85	<0.6
Velocity ratio $\frac{VTI_{LVOT}}{VTI_{AV}}$	>0.50	0.25-0.50	<0.25

[a] ESC Guidelines.

[b] AHA/ACC Guidelines.

Over the years, aortic stenosis develops by increasing the aortic flow velocity by 0.3 $\frac{\mathrm{m}}{\mathrm{s}}$ each year and decreasing the aortic-valve area of 0.1 cm^2 per year; however, this average rate changes within each individual (Otto et al., 1997).

The other pathology that affects the aortic valve is aortic regurgitation or insufficiency. Aortic regurgitation is a disease where the aortic valve leaks. It occurs when the aortic valve fails to seal properly allowing the blood to flow from the aorta to the left ventricle during the diastolic phase (Figure 1.8(B)) (J.R. Levick, 2009).

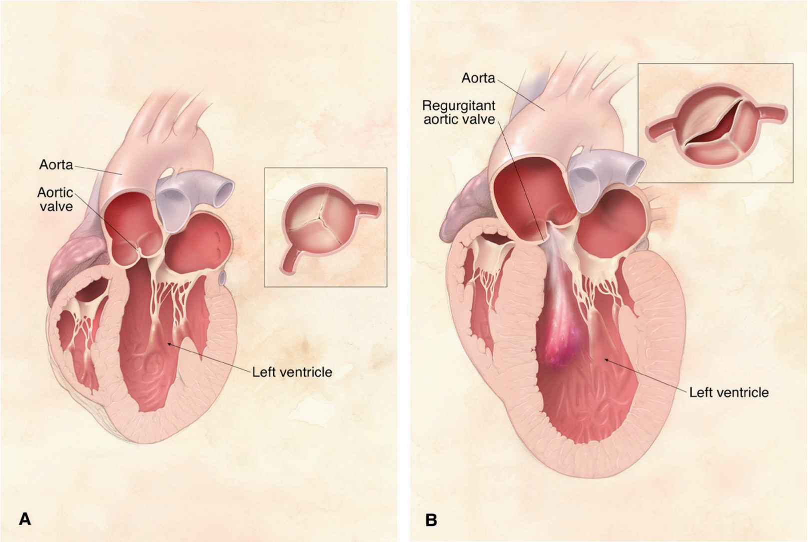

Figure 1.8. Young healthy (A) and incompetent aortic valve (B) during diastole (Nishimura, 2002).

Aortic insufficiency can be due to leaflets and/or aortic root malformations (Underwood, Khoury, Deronck, Glineur, & Dion, 2000). Different studies have shown that the most common causes are: aortic dilatation, congenital abnormalities such as bicuspid aortic valves, post-inflammatory diseases, and endocarditis infection (Dare, Veinot, Edwards, Tazelaar, & Schaff, 1993; Olson, Subramanian, & Edwards, 1984).

Because of the presence of reverse flow, the left ventricle needs to pump more blood to compensate the physiological blood flow rate. In this case, the ventricle adapts to this abnormality by gradually enlarging to support the greater workload. Unlike pressure hypertrophy, which occurs in aortic stenosis, volume hypertrophy causes a much faster ventricular dilatation, leading to cardiac failure sooner than in case of aortic stenosis.

Another consequence of aortic valve incompetence is the decrease in terms of flow reaching the coronary arteries (Schnabel et al., 2010).

However, the incidence of aortic regurgitation is less frequent than stenosis (Iung & Vahanian, 2011). In the Euro Heart survey it accounted for only 13.3 % of native valve diseases, while stenosis accounted for 43.1 % (Iung et al., 2003).

On the other hand, it is worth mentioning that aortic insufficiency is a disease often concomitant with aortic stenosis. This happens since valve abnormalities such as bicuspid valves, present stenosis which in turn, causes aortic root dilatation and hence, leaflets separation and incompetence (Carabello, 2007).

1.4.2 Progressive aortic dilation

As reported in the literature, aortic stenosis is one of the most common degenerative valvular diseases and, in presence of severe stenosis, thickening of the valve cusps may often lead to concomitant aortic regurgitation and other comorbidities which significantly affect valve function (Honda et al., 2012; Otto, 2006).

For instance, the presence of anatomical anomalies in the aortic chamber anatomy is one of these and therefore in some cases, although the pathology impairing the valve is not severe, the rate of progressive dilation of the aortic root represents the leading factor in deciding the surgery timing (Otto, 2006). Therefore, many studies state that replacement of a dysfunctional valve may delay the level of dilation (Lu, Thadani, & Hope, 2013; Nataf, 2006; Wilton & Jahangiri, 2006).

In case of stenosis, dilation of the ascending aorta can develop due to the force exerted by a faster jet which weakens the aortic arch walls eventually leading to an increase in the vessel diameter of more than 50% (Kirali & Günay, 2017) known as aneurism (Abbas, Franey, Goldstein, & Lester, 2013; Yoganathan, 1988).

Dilation may also evolve in presence of congenital defects such as bicuspid heart valve and other valvular diseases such as aortic regurgitation (Nataf, 2006; Reul et al., 1990; Wilton & Jahangiri, 2006).

Hence, as reported by Reul *et al.*, specific valvular pathologies can be associated with anatomical variations for the aortic root (Reul et al., 1990).

Root dilation causes are mostly related to diseases affecting the aortic walls such as pathologies of the connective tissue like Marfan's disease or Ehlers-Danlos syndrome, more than due to alterations within the haemodynamics (Cozijnsen et al., 2011; Wilton & Jahangiri, 2006).

However, such changes in the aortic chamber geometry can be often related to aging, since from the age of 40, the root naturally expands, stiffens and remodels in the STJ and sinuses region (Guala, Camporeale, & Ridolfi, 2015).

Ascending aorta dilation can be classified into "supravalvular aortic aneurysms" downstream from the STJ, and "aortic root aneurysms" where valve sparing or replacement is necessarily needed (Nataf, 2006).

An enlarged aortic root can eventually evolve into dissection or rupture, which given the increase in tension on the walls, could be fatal (Hope, Sedlic, & Dyverfeldt, 2013; Nataf, 2006; Wilton & Jahangiri, 2006).

Surgery is recommended when dilation of the ascending aorta exceeds 55 mm with no other linked pathologies, or if it exceeds 50 mm with a diagnosed connective tissue pathology, if it exceeds 45 mm and the patient has already undergone aortic valve replacement (Cozijnsen et al., 2011). To treat root dilation two procedures can be performed: "remodeling" of the aortic root using a scalloped Dacron tube graft sutured in the supravalvular position and "reimplantation" of the aortic valve within a cylindrical tube (straight conduit) implanted in the sub-valvular position (Escobar Kvitting et al., 2004; Underwood et al., 2000). The first aims at preserving the native shape of the sinuses (Nataf, 2006), resulting in more physiological valve dynamics and flow patterns (Yankah, Weng, & Hetzer, 2010).

In some valve sparing procedures in addition to root remodeling, correction of the cusps free-edge length is strongly advised since, due to the expansion of the root and increase of the STJ diameter, the leaflets present separation at the commissures' level and therefore the valve cannot achieve a competent closure (Thubrikar et al., 2005).

1.5 Treatments: aortic valve replacement

Heart valve replacement is a common procedure in case of patients suffering from aortic valvular diseases. It involves the replacement of the native damaged aortic valve with a prosthetic device (Iung et al., 2003). In the event of severe aortic stenosis and insufficiency, valve replacement needs to be fulfilled before the extra load supported by the heart muscle leads to ventricular failure (Nishimura, 2002).

Heart valve replacement requires an open-heart surgery operation, where the patient native cusps are removed and replaced with artificial substitutes.

Dr Dwight Harken, a pioneer in heart valve surgery, summarised the requirements for an ideal valve prosthesis, into what he defined the "Ten Commandments of Satisfactory Prosthetic Aortic Valves". The latter include: good haemodynamics, being chemically inert, easy to implant, durable, biocompatible, not inducing haemolysis and thrombogenesis, lasting composing materials and design, effective anchorage, anatomic suitability of the valve to its implanted location, and having a prompt and full closure (Harken et al., 1962).

Heart valve prostheses consist of two main categories: mechanical and biological devices. Mechanical valves are made of pyrolytic carbon or combination of pyrolytic carbon and metallic components while biological substitutes are manufactured from a heart valve or cardiac tissue from animals (Nishimura, 2002).

1.5.1 Mechanical valves

The main drawback of mechanical valves is the requirement of an anticoagulant therapy because the patients are exposed to an high risk of thrombosis and thromboembolism (Kidane et al., 2009). They are very durable, lasting 20 to 30 years, though (W.Vongpatanasin, L. D. Hillis, 1996).

The most widely implanted mechanical devices worldwide include three types: the Starr-Edwards ball in cage heart valve, approved by the US Food and Drug Administration in 1965, the Medtronic-Hall single tilting disc prosthesis, realised by Karl-Victor Hall, Arne Woien, and Robert Kaster subsequently purchased by Medtronic, Inc., and the St. Jude bileaflet prosthesis, both approved in 1977 (Figure 1.9) (Vlahakes, 2007).

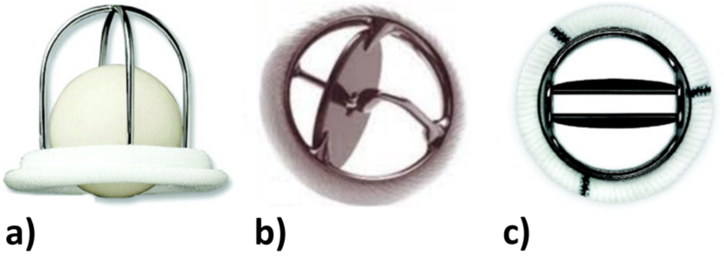

Figure 1.9. Starr-Edwards ball in cage (a), Medtronic-Hall single tilting disc (b) and St. Jude bileaflet mechanical valves (Pibarot & Dumesnil, 2009).

The development progress went primarily from ball and cage to single leaflet to bileaflet design.

The ball and cage prosthesis consists of an occluder ball of silastic or silicon rubber which can move up and down in a cage made of stainless steel, or solid Teflon, or Lucite. The sewing ring for the Starr-Edwards design, is made from Teflon cloth.

However, different versions of this valve have been developed to improve its haemodynamics performance. In fact, it has been found to induce thrombosis due to the material and design adopted, and hemolysis due to the rubbing of the occluder against the suture ring (Rozeik et al., 2014). Moreover, it presents a large vertical profile which impinges on the coronary arteries flow and makes the implantation more difficult (Miller, 2006). The presence of the occluder introduces excessive turbulence in the flow which reduces the valve effective orifice area (Lakshmi P. Dasi, Simon, Sucosky, & Yoganathan, 2009).

The tilting disk valve design, instead of a ball, comprises a graphite disk coated with pyrolite carbon, which tilts between two struts of the housing made of stainless steel or titanium (P. Bloomfield, 2002).

The disk during the opening phase, as a result of the constraints applied through the struts assembly, opens to an angle of between 60° and 75° (depending on the specific model), while during the closing phase shuts the valve orifice in order to prevent backflow (Miller, 2006).

Design improvements were developed for instance, changing the disc to a convexo-concave shape, as done for the Björk–Shiley design. However, the most implanted tilting disk device is the Medtronic-Hall valve, whose disk is flat (Lakshmi P. Dasi et al., 2009).

The latter presents an improved opening of the disk, which is able to open to an angle of 75°, a thin strut and a hole in the middle of the disk used as a guide (Zilla, Brink, Human, & Bezuidenhout, 2008). As the disk rotates freely between the struts, the blood can flow around the tilted disk and around the outer sides without impinging on the central forward flow and hence, it requires a smaller transvalvular pressure to open the valve, compared to the ball and cage valve (Miller, 2006).

Friction and wear of the disk on the struts and fracture of the struts caused by high mechanical loading during closure represent the most common complications (Rozeik et al., 2014).

The bileaflet disk valve designed by St. Jude has two semicircular cusps, made of carbon pyrolite, which are attached through hinges to the valve housing. As the hinges are located towards the centre of the valve orifice, three orifices are formed during the valve opening one central and two lateral (P. Bloomfield, 2002).

The carbon pyrolite has been shown to own the best features in terms of biocompatibility, thromboresistance and wear resistance compared with other materials (Lakshmi P. Dasi et al., 2009).

The EOA in bileaflet devices was found to range from 2.4 to 3.2 cm^2 while in the case of tilting disk valve it ranged from 1.5 to 2.1 cm^2 (Laas, Kleine, Hasenkam, & Nygaard, 1999). Thus, bileaflet valves show enhanced haemodynamic performance compared with previous generations of mechanical valves. However, stagnation zones were observed at the hinge region eventually leading to thrombosis and blood damage (Ellis, T. J., Yoganathan, 1996).

As a result of its design, the bileaflet valve presents mild leakage (Miller, 2006) which has the benefit of preventing thrombus accumulation at the hinge points.

The bileaflet device is the most common implanted mechanical valve worldwide with more than 600000 implants (P. Bloomfield, 2002).

These valves exhibit a greater EOA, show a good biocompatibility, are the least thrombogenic among mechanical valves, and as a result, they need only mild anticoagulants treatment (Filová, Straka, Ejovský, Mašín, & Œková, 2009).

1.5.2 Biological valves

Biological valves were introduced in the early 1960s. In 1962, native aortic valves obtained from human cadavers were transplanted to other individuals (Ross, 1961). In such case, when the new valve is transplanted from a human donor, is called homograft.

In 1967, an operation called the Ross procedure was introduced. This involved the replacement of the patient's dysfunctional aortic valve with their own pulmonary valve, which in turn was replaced with a homograft. In this circumstance, the valve is known as an autograft as it is just relocated from one position to another within the body (P. Bloomfield, 2002).

Less than a decade later, following the development of a tissue-fixation procedure using glutaraldehyde, chemically treated stent-mounted tissue valves were commercially produced and implanted (Schoen & Levy, 2005). This type of valve was named a 'bioprosthesis' by Carpentier (Carpentier, 2007).

Nowadays, bioprosthetic valves are mainly made from porcine aortic valves or bovine pericardial tissue. They are referred to xenografts as the valve is transplanted from animals such as a pig, or manufactured from biological tissue such as bovine pericardium (P. Bloomfield, 2002). For example, porcine valves are treated with glutaraldehyde which sterilises the valve tissue and helps to prevent immunologic reaction (Miller, 2006). They can be stented or stentless. The support used for the stented bioprostheses is usually a metallic or plastic stent with three struts surrounded by a sewing cuff usually made of Dacron fabric, which helps the suturing procedure. Stentless valves are obtained extracting the valve from animals together with the portion of vessel where they are attached to. Thus, they are ready to be sewn. They show better haemodynamics properties compared with stented valves for instance, a greater

EOA and less shear stress, however they are more difficult to implant (P. Bloomfield, 2002; Rozeik et al., 2014).

Two popular porcine stented bioprostheses commercially distributed are the Hancock II Porcine (Medtronic) (Figure 1.10(a)) and the Carpentier-Edwards Bioprosthesis (Edwards Lifesciences) (Figure 1.10(b)). Stents may differ in design, flexibility, and materials among models (Schoen & Levy, 1999).

In fact, the Hancock II valve cusps are sewn on a rigid ring with flexible struts, while those of Carpentier-Edwards are sewn on a totally flexible frame (Lakshmi P. Dasi et al., 2009).

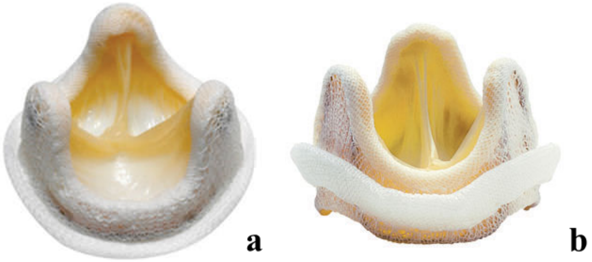

Figure 1.10. Medtronic Hancock II (a) and Carpentier-Edwards (b) porcine valves.

Bovine pericardial bioprosthetic valves are made from cow pericardium leaflets mounted on a stent. The first pericardial valve was the Ionescu-Shiley valve which was developed in 1971 and commercially distributed in 1976. This valve used bovine pericardium stitched on a Dacron covered titanium stent. In 1987, it was withdrawn from the market as a result of several structural failure occurrences (Rozeik et al., 2014).

The Carpentier-Edwards bovine pericardial valve was introduced in 1981. In order to overcome drawbacks reported for earlier models of pericardial valves, the valve pericardium is stitched to the stent with sutures on the inner part of the Dacron cuff, rather than on the Dacron cloth (P. Bloomfield, 2002).

In terms of durability, it shows better performance than previous generation pericardial valves (Gao, Wu, Grunkemeier, Furnary, & Starr, 2004).

1.5.2.1 Mechanical versus Biological valves

By the mid-1970s the major drawbacks related to the use of mechanical and biological prostheses were well known. The first induce thrombosis (and therefore require long-term anticoagulant therapy) but are very durable, the second present a more physiologic haemodynamics than the mechanical ones but have limited durability due to progressive valve tissue deterioration (Hammermeister et al., 2000; Schoen & Levy, 2005).

Causes of bioprostheses failures are considered to be accelerated calcification in the young in particular occurring at high stresses regions, and mechanical damage (I. Vesely, 2003).

Consequently, based on the above-mentioned pros and cons, mechanical valves are usually selected for young patients or those with a life expectancy of more than 10 to 15 years, or patients already following an anticoagulant therapy due to other pathologies. On the other hand, bioprostheses are selected for elderly patients or those with a life expectancy of less than 10 to 15 years or those who cannot be treated with anticoagulants (P. Bloomfield, 2002; W.Vongpatanasin, L. D. Hillis, 1996).

1.5.3 TAVI

Aortic valve replacement represents the standard treatment in case of severe aortic valvular disease. However, there is a category of patients, in particular young children and elderly patients, that cannot go through surgery because is considered too risky for them (Kidane et al., 2009). For instance, many elderly patients whose health is worsened by significant comorbidities, are considered inoperable. An emerging alternative to the surgical technique which addresses the need of a less invasive approach, is Transcatheter aortic valve implantation (TAVI). In such approach, the prosthetic device is a collapsible valve mounted on an expandable stent which is delivered over the native valve using a catheter (Lutter, Ardehali, & Cremer, 2004).

In 1992, Andersen et al. showed that TAVI was feasible by using a porcine aortic valve, sutured and folded into a balloon-expandable stent and implanting it into a pig heart (Andersen, Knudsen, & Hasenkam, 1992). Ten years later, Cribier et al. performed the first successful TAVI in humans by delivering a percutaneous valve in a patient suffering from aortic stenosis (Cribier, 2002).

Three types of transcatheter valves lead the market nowadays: the Edwards-Sapien transcatheter valve (Edwards Lifesciences)(Figure 1.11(A)), the Edwards-Sapien XT transcather valve (Edwards Lifesciences)(Figure 1.11(B)), and the CoreValve ReValving system (Medtronic)(Figure 1.11(C)). The first two valves have a balloon expandable tubular stent with bovine pericardium cusps, but the first is mounted on a stainless-steel frame while the second on a cobalt chromium alloy frame. In both models, the inlet portion of the stent is covered with fabric to provide an annular seal (Webb & Wood, 2012) (Vahanian et al., 2008).

On the other hand, the CoreValve, whose leaflets were initially bovine and are currently porcine, is fixed in a self-expanding nitinol frame which uses the malleability properties of a nickel-titanium alloy to self-deploy. The stent presents an high profile frame which serves as anchoring point to the sino-tubular junction and aortic annulus and a design supporting the radial fixation (Padala et al., 2010).

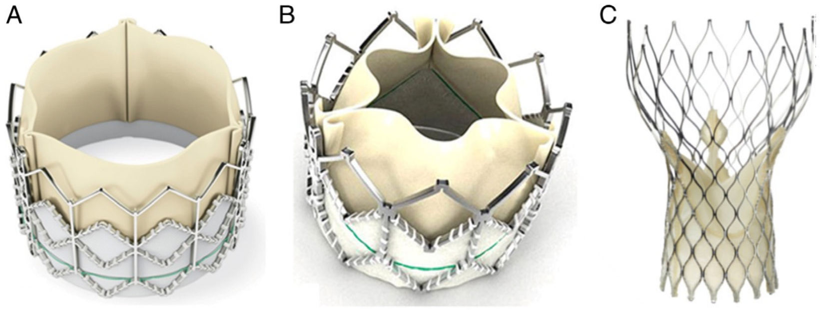

Figure 1.11. Edwards-Sapien (A), Edwards-Sapien XT (B) and CoreValve (C) transcatheter devices (Webb & Wood, 2012).

Percutaneous valve implantation can be performed though two access routes: the retrograde transfemoral approach, that means creating an access through the femoral artery; or using a minimally invasive approach which requires a small incision in the chest and entering through a large artery in the chest or through the tip of the left ventricle (the apex), which is known as the anterograde transapical approach (Vahanian et al., 2008).

For example, in the second approach the catheter is inserted into the body through the left ventricle apex and guided into the left heart, as shown in Figure 1.12.

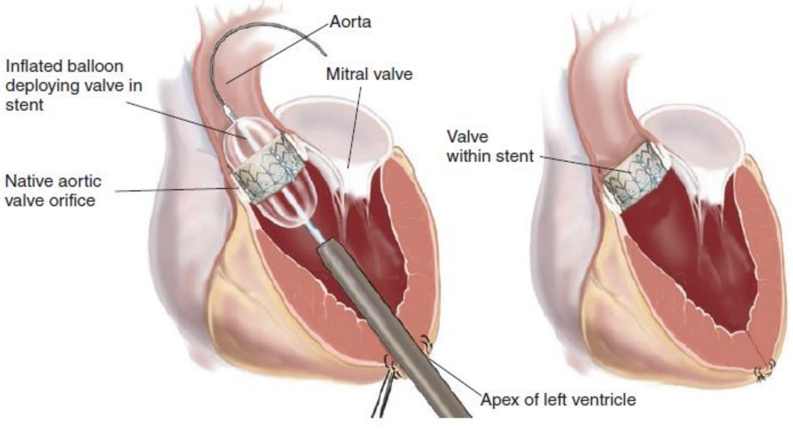

Figure 1.12. Percutaneous valve implantation procedure (Carpentier, 2007).

When the catheter system reaches the aortic root, in case of a balloon expandable stent, the balloon is inflated, causing the expansion of the crimped transcatheter valve which in turn displaces the diseased native leaflets against the aortic wall and places the prosthesis in its final position (Padala et al., 2010).

TAVI has been proven to be a very promising technique however, typical complications associated with transcatheter devices are paravalvular leakage, stent migration, major vascular complications, conduction disturbances and stroke (Kodali et al., 2012; Toggweiler et al., 2012) In order to overcome such drawbacks, some engineering challenges need to be addressed. The latter includes a better understanding of the haemodynamics of TAVI devices within the native calcified leaflets, of the structural mechanics of the implanted valve and the degenerated aortic valve and root, and of the safety of radial valve anchoring in a high pressure and high flow environment (Padala et al., 2010).

The investigation of the haemodynamics within the aortic valve will be the object of this thesis and its pertinent aspects will be discussed in detail in the second chapter.

1.6 Blood damage

As mentioned previously, the implantation of current valve prostheses can alter the flow pattern in the aortic root leading to potential blood damage and therefore inducing thrombosis.

Blood is a two-phased suspension of formed elements, which include red blood cells (RBCs, deformable and non-spherical formed elements which transport and deliver oxygen and carbon dioxide) white blood cells (immune system cells which defend the body against diseases) and platelets (anuclear fragments of megakaryocytes which trigger blood clotting and help minimise blood loss), within plasma, an aqueous solution of organic proteins, molecules and salts (Baskurt & Meiselman, 2003). The apparent viscosity of blood depends on the existing shear forces (i.e., blood behaves as a non-Newtonian fluid) and is determined by number of RBCs, plasma viscosity, RBC aggregation, and the mechanical properties of RBCs (Baskurt & Meiselman, 2003).

Blood exerts its force on the aortic walls with two contributions: blood pressure and wall shear stress. The blood pressure acts in the normal direction to the wall, while the wall shear stress acts tangentially. Despite the fact that wall shear stress is usually much lower than blood pressure, the endothelium is much more affected by shear than to pressure, making the walls very sensitive to local flow conditions (Peter F Davies, 2008).

Blood damage can be triggered by the contact between blood and foreign materials resulting in: thrombosis, (i.e. the formation of a blood clot (thrombus) inside a blood vessel, which obstructs the flow of blood through the circulatory system (Ku, Casa, & Hastings, 2017)), haemolysis, (which the rupture of red blood cells and the release of their contents (haemoglobin) into the surrounding fluid), and/or platelet activation (Vogel & Thein, 2018).

In particular, thrombotic events may occur due to the simultaneous presence of three factors known as Virchow's triad. They are: stasis (fluid stasis and/or elevated fluid shear stresses), vascular injury (surface phenomena related to foreign materials) and hypercoagulability (altered blood biochemistry)(Bagot & Arya, 2008; Wei, Sonntag, Toma, Singh-Gryzbon, & Sun, 2018)(Figure 1.13).

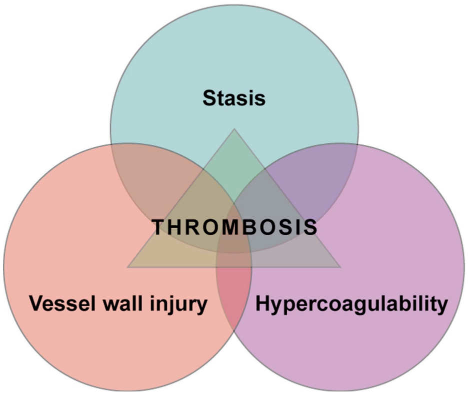

Figure 1.13. Virchow's triad (Kyrle & Eichinger, 2013).

A fluid environment presenting high velocity with elevated shear stresses through the valve and accompanied by flow separation areas, may lead to hemolysis or blood activation (Lowe, 2004), whereas recirculation zones characterised by slow flow velocities are prone to platelet aggregation and thrombus deposition (Reul et al., 1990; Yoganathan, Chandran, & Sotiropoulos, 2005; Yoganathan, He, & Casey Jones, 2004).

High fluid shear stresses, impacting red cells and platelets, can also damage the endothelial cells lining the vascular walls (Yoganathan et al., 2005). In response to vascular injury, the damaged vessel tissue becomes exposed to the blood stream leading to the activation of platelets, whose function is to stop the bleeding. Similarly, in case of medical devices such as heart valve substitutes, such activation of blood components can be induced by the presence of artificial surfaces, whose biocompatibility and interaction with the surrounding biological structures has an impact on the tissue, possibly resulting in damage to the endothelial cells lining the vascular wall (Roudaut, Serri, & Lafitte, 2007). Thus, valve material and design can strongly affect the formation of thrombi since the blood stream encounters its foreign surfaces (Cannegieter, Rosendaal, & Briet, 1994).

As soon as the blood is exposed to the tissue factor, which is a protein that can be released by the damaged tissue or is present in the blood, the coagulation cascade starts triggering platelets activation and circulation (Furie & Furie, 2008). The formation of blood clots degenerates in a thrombus when the fibrin, which is the end product of coagulation, is deposited. Then, the thrombus may rapidly propagate thanks to the recruitment of other neighbour platelets. This process is called platelets aggregation (Mackman, 2008) and is regulated by the physiological system responsible for inhibiting platelet activation with the endothelium being one of the major contributors (Fuster, V., Topol, E.J. , Nabel, 2005). In this stage of the coagulation process flow changes may assume a significant role in expanding or inhibiting the thrombogenesis (Breddin, 1989).

In fact, in terms of haemodynamics, as postulated by Virchow, alterations in the blood flow also influence the thrombus formation process. Specifically, stasis is considered the dominating factor within the triad (D. R. Kumar, Hanlin, Glurich, Mazza, & Yale, 2010). In heart valves, factors such as low or reduced cardiac output, turbulence and stagnation contribute to stasis (Cannegieter et al., 1994). Therefore, the prosthesis haemodynamics performance and its site of implantation may have an impact on these features (Roudaut et al., 2007).

As well as the amount of flow stasis, thrombogenicity is affected by abnormalities in platelets and factors regulating the coagulation process (hypercoagulability), which support platelets aggregation and play a significant role in the blood clots formation process (D. R. Kumar et al., 2010). Washout of a region will decrease the risk of thrombosis, with a RBC residence time less than 10 s significantly reducing the chance of cell aggregation, with blood flow speeds higher than as 0.05 m/s drastically reducing any persistent stagnation (Corbett, Ajdari, Coskun, & Nayeb-Hashemi, 2010; Wootton & Ku, 1999). The washout effect associated with the vortex shedding of the aortic leaflets reduces the prolonged presence of activated platelets in the sinuses of Valsalva (Corbett, Ajdari, Coskun, & Nayeb-Hashemi, 2010). Once thrombi form and grow, portions may break away from the primary site and block distal vessels, causing downstream areas of the body to become starved of oxygen and other nutrients, with potentially fatal consequences, such as a stroke or myocardial infarction (K. B. Chandran, Rittgers, & Yoganathan, 2012).

In summary, "thrombus formation is a dynamic process in which some platelets adhere to and others separate from the developing thrombus, and in which shear, flow, turbulence, and the number of platelets in the circulation greatly influence the architecture of the clot" (Furie & Furie, 2008).

On the other hand, haemolysis is caused by RBCs rupture and consequent release of haemoglobin into the plasma. Also, a significant degree of haemolysis may lead to anaemia and, the exposure of the kidney to large quantities of free haemoglobin in the plasma may result in kidney damage (Pietrabissa, 1996). RBCs haemolytic trauma and platelet activation are not only affected by cell contact with foreign surfaces, but are also influenced by flow shear stress magnitude (Vahidkhah et al., 2016).

Therefore, such events need to be prevented by guaranteeing fluid dynamics conditions which minimise fluid shear stresses and impacts (Pietrabissa, 1996).

Chapter 2 Literature review

Introduction

“ The term haemodynamics describes the physical factors governing blood flow within the circulatory system”(Klabunde, 2011).

The comprehensive understanding of the optimum haemodynamics environment that regulates the operating mechanisms of the young healthy aortic valve is essential in enabling a correct interpretation of diseased conditions and their implications, and to devise effective therapies that restore or mimic the crucial physiological functions. It is therefore understandable that a substantial amount of literature has been produced on the topic.

The need for a better insight into the establishment of optimum fluid dynamics in the aortic valve region has now become a timely and critical issue, due to the significant correlation with clinical complications recently reported with surgical and transcatheter bioprosthetic replacements, namely ischemic lesions and dementia (Kahlert et al., 2010; Makkar et al., 2015; Rodés-Cabau et al., 2010), which can be associated with the non-physiological flow environment that they produce (Lakshmi P. Dasi et al., 2009; Ducci, Pirisi, Tzamtzis, & Burriesci, 2016; Falahatpisheh & Kheradvar, 2012).

These concerns prompted to investigate the native and modified fluid dynamics of the aortic root.

2.1 Haemodynamics of young healthy valves

The native aortic valve opens and closes under the effect of hydrodynamic forces, driven by the pressure gradient. During systole, when the pressure in the left ventricle exceeds that in the aorta, the pressure gradient guides the blood flow into the aortic arch forcing the aortic valve leaflets to open (see Figure 2.1). As valve opening is initiated, it is important that the valve provides minimal resistance, promptly reconfiguring to offer the largest possible orifice area of the valve and, hence, conserve as much of the energy and pressure of the flow as possible (Burriesci, Marincola, & Zervides, 2010). In this stage, the valve resistance is related to the energy needed to reverse the leaflet curvature between the shut and open configurations. A ready opening, requiring smaller pressure, results in minimum loss of flow energy, and lower levels of strain and stress in the leaflets (Burriesci et al., 2010). During the ejection phase, the widest valve opening is desirable, as it would utilise as much of the aortic lumen as possible, reducing the energetic losses. In physiological conditions, the blood flows through the aortic orifice reaching a peak value of 1.35 ± 0.35 m/s during the jet acceleration at systole (Rossvoll et al., 1991).

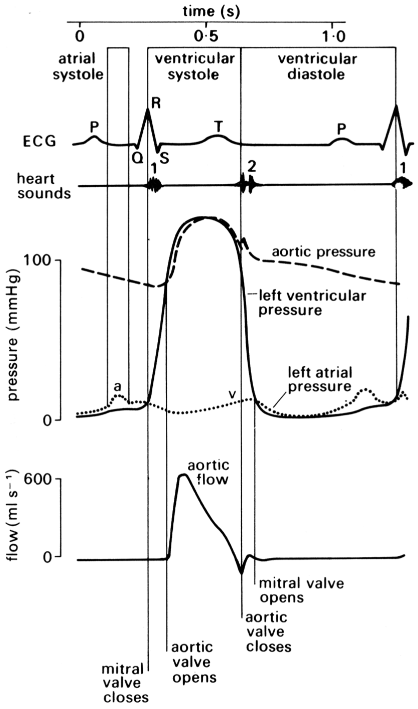

Figure 2.1. Aortic valve physiological flow rate and pressure (Caro, C., Pedley, T., Schroter, R., Seed, W., & Parker, 2012).

At diastole, when the pressure in the aorta is higher than that in the left ventricle, the leaflets close with very little reverse flow through the valve orifice (Michael S. Sacks et al., 2010). Therefore, valve closure is determined by a combination of reverse transvalvular pressure, due to the drop in pressure in the left ventricle as effect of its diastolic relaxation, and vortical behaviour in the sinuses, which guide the leaflets profile before and during closure (Bellhouse & Bellhouse, 1968). The synergy between these two effects reduces the closing regurgitant volume, and the loss of flow energy. Similar to valve opening, a reduced resistance to the change in leaflets' curvature also contributes to decrease the stresses in the leaflets and the energy consumed during closing.

The aortic valve function is also supported by the surrounding anatomical structures, which are known as aortic sinuses (Yacoub, Kilner, Birks, & Misfeld, 1999).

The role of Valsalva sinuses has been the subject of several studies, which recognise the interplay between the pulsatile flow and the root shape. As hypothesised by Da Vinci in the first place, Valsalva sinuses play a key role in optimising the haemodynamics in the aortic arch and reducing energy losses (Salica et al., 2016). In detail, their function has shown to consist in the transmission of the blood flow from the left ventricle to the ascending aorta by offering minimal resistance, optimising coronary flow (Ranga, Bouchot, Mongrain, Ugolini, & Cartier, 2006), minimising tissue damage, maintaining laminar flow (Yacoub et al., 1999) and reducing the effects of flexural stresses at the leaflet/sinus interface (M. S Sacks & Yoganathan, 2007).

Whilst there is consensus that the haemodynamics established within the aortic root plays a key role in the proper valve function (Bellhouse & Talbot, 1969; Michael S. Sacks, David Merryman, & Schmidt, 2009; Salica et al., 2016; Van Steenhoven & Van Dongen, 1979), there is no agreement on the specific mechanisms involved (Bellhouse, Bellhouse, & Reid, 1968; Ranga et al., 2006; Wald, Liberzon, & Avrahami, 2017). Although the Valsalva sinuses are commonly indicated to promote fluid recirculations, which in turn act upon the leaflets, some investigations report that these vortices form within the sinuses in early systole (K. Dumont, Stijnen, Vierendeels, van de Vosse, & Verdonck, 2004; Moore & Dasi, 2015; Yap, Saikrishnan, & Yoganathan, 2012), while others claim that these structures only occur during late systole (De Hart, Peters, Schreurs, & Baaijens, 2003; Escobar Kvitting et al., 2004; Nobari, Mongrain, Leask, & Cartier, 2013; Sturla, Votta, Stevanella, Conti, & Redaelli, 2013). The number and locations of these vortices are also disputed, with contrasting research indicating multiple vortices within each sinus (K. Dumont et al., 2004), a single vortex fully contained within each sinus (Sturla et al., 2013) or a vortex only partially within the sinus (Escobar Kvitting et al., 2004; Nobari et al., 2013)(Figure 2.2).

Furthermore, some postulate that the presence of strong vortical structures may promote platelet activation (Bäck et al., 2013) whereas others state that recirculation areas are actively involved in the valve opening and closure mechanisms (Bellhouse & Bellhouse, 1968; Escobar Kvitting et al., 2004; Salica et al., 2016).

Consequently, the basic understanding of the native aortic valve's operating process is still fragmentary.

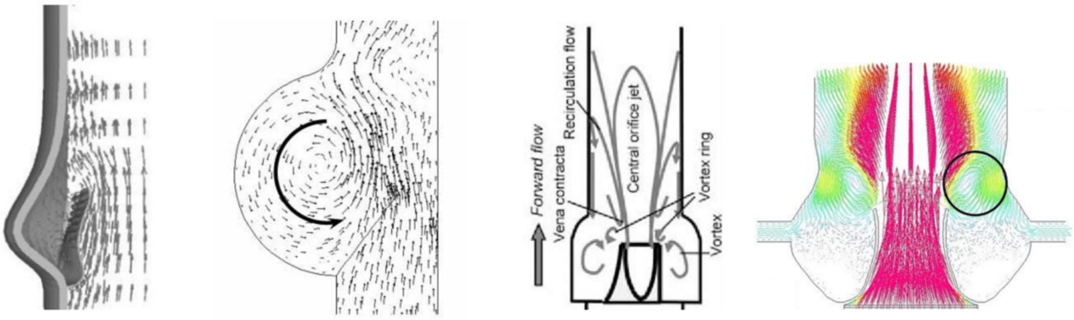

a) b) c) d)

Figure 2.2 Flow patterns within Valsalva sinuses a) (De Hart et al., 2003) b) (K. Dumont et al., 2004) c) (Lakshmi P. Dasi et al., 2009) d) (Wald et al., 2017).

The presence of vortices has been shown to have direct correlation with the aortic coronaries pressure gradient. Whether they are weak or far from the leaflets, they lead to high pressure in the sinuses and therefore high coronary flow (Wald et al., 2017).

2.2 Haemodynamics in diseased valves

2.2.1 Haemodynamics in stenotic valves

The flow features described for a young healthy valve are altered when the valve presents diseases such as stenosis. In this case, as already mentioned in the previous chapter, the incomplete opening of the valve causes a reduction of the EOA which results in an increase of the transvalvular gradient pressure (Sadeghpour, Fatouraee, & Navidbakhsh, 2017).

The vortical pattern regulating the valve dynamics and guaranteeing an efficient valve opening and closure movement (Michael S. Sacks et al., 2010), in a stiffened valve is characterised by bigger and distorted vortices which, at diastole, instead of promoting blood circulation in the sinuses, vanish completely (Amindari, Saltik, Kirkkopru, Yacoub, & Yalcin, 2017).

Yoganathan et al. conducted an *in vitro* study to investigate the flow in bioprosthetic valves replicating different levels of aortic stenosis (Yoganathan, 1988).

The results showed that the flow pattern in a stiffened valve presents an asymmetric and angulated jet. In addition, comparing the flow measurements in a normal and stiffened aortic valve at the systolic peak, a central jet with a maximum axial velocity of 1.20 m/s was observed in the young healthy case, whereas an angulated forward flow with maximum axial velocities ranging between 2 m/s and 7 m/s according to the severity of stenosis, and presenting flow separation regions and highly turbulent shear layers, was reported for the stiffened cases (Figure 2.3).

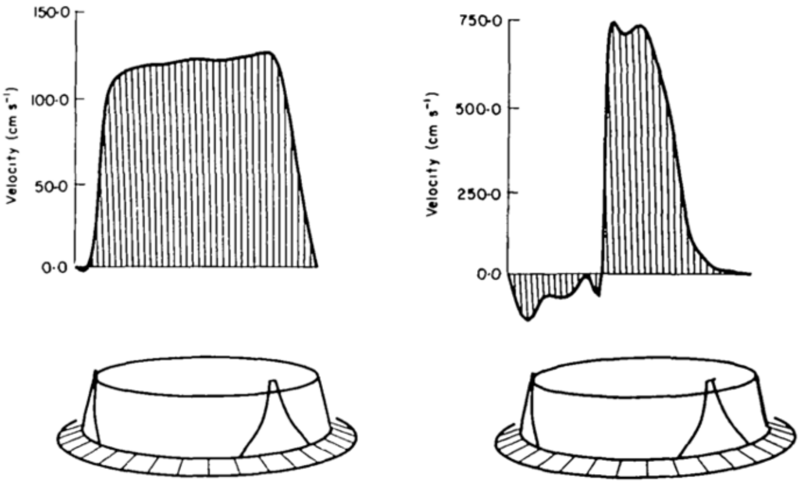

Figure 2.3. Velocity profile at peak systole distal to the normal aortic valve (a) and severely stiffened aortic valve (b) (Yoganathan, 1988).

Furthermore, the jet size reduction, peak velocities together with the jet instability were found to increase consistently with the severity of stenosis.

The elevated levels of turbulence measured downstream of the stiffened valves are considered high enough to cause damage to the blood elements (red blood cells and platelets) and the walls of the ascending aorta, eventually leading also to root dilation (Balachandran et al., 2011; Yoganathan, 1988).

Variations in wall shear stresses and in coronary arteries velocity profiles, were reported in a study by Nobari et al. which showed how changes due to the stiffening of the leaflets, impinge also on the coronary arteries function (Nobari et al., 2013).

2.2.2 Haemodynamics in valves within a dilated root

A dilated aortic root can cause numerous changes to the flow dynamics environment, such as the presence of enlarged vortical areas alongside the forward flow which result in the development of an angulated systolic jet (Toninato, Salmon, Susin, Ducci, & Burriesci, 2016) and high shear stress regions (Barannyk & Oshkai, 2015).

Dilation leads to a delay in achieving valve closure (Querzoli, Fortini, Espa, Costantini, & Sorgini, 2014), an increase in the cusps stress of 150% and a decrease in coaptation of 8% (Grande, Cochran, Reinhall, & Kunzelman, 2000).

For instance, Marfan's syndrome has been correlated with an increased stiffness of the aortic chamber walls therefore, in order to measure the arterial stiffness and the progression of aortic dilation related to it, a technique called pulse wave velocity is usually implemented (Lu et al., 2013). In fact, a reduction in the pulse wave velocity caused by an oversized root can also affect the left ventricle causing an increase in its workload (Guala et al., 2015).

An expansion of the STJ diameter also corresponds with an increase in the shear stress distribution on the leaflets and a reduction of the valve opening area (Marom et al., 2013).

2.3 Haemodynamics in treated valves

2.3.1 Haemodynamics in surgical valves

Surgical valves include biological and mechanical artificial valve substitutes. The first implanted mechanical prostheses were the ball and cage and caged disk valves that, due to their inferior haemodynamics characteristics, were replaced by ‘tilting disk’ and ‘bileaflet’ devices (Lakshmi P. Dasi et al., 2009). The bileaflet mechanical heart valve is, at present, the most popular mechanical design and accounts for approximately 80% of implanted mechanical valves (Lakshmi P. Dasi et al., 2009).

Many studies have been conducted to investigate the haemodynamics in bileaflet mechanical valves, mostly based on the St. Jude bileaflet mechanical valve design. The flow through a bileaflet mechanical valve orifice generates a typical three forward flow jets configuration, a central narrow jet accompanied by two lateral jets forming at the leaflet tips. The presence of the lateral jets makes the flow migrate from the high pressure central region to the lateral low pressure regions, creating a small recirculation zone at the leaflet tips (Jahandardoost, Fradet, & Mohammadi, 2015).

Yoganathan et al., in an in experimental *in vitro* study using a St. Jude bileaflet mechanical valve, reported a value of 2 m/s for the velocity peak in the central forward flow and a value of 2.2 m/s occurring in the lateral orifices (Yoganathan et al., 2004). Therefore, during the peak of the acceleration phase the side jets present an higher velocity than the central flow (Jahandardoost et al., 2015; Nobili et al., 2008).

As observed by King and Ge et al. (Ge, Jones, Sotiropoulos, Healy, & Yoganathan, 2003; King, Corden, David, & Fisher, 1996), during systole, vortical structures originate from the leading and trailing edges of the leaflets and the downstream end of the aortic sinus evolving into chaotic flow during the deceleration phase. Thus, strong shear layers form from the valve housing and the tips of the leaflets, shedding a wake of vortices during the deceleration phase (Morbiducci et al., 2009). These vortices roll on top of each other, and extend as far as twice the leaflet length downstream (Danny Bluestein, Rambod, & Gharib, 1999)(Figure 2.4).

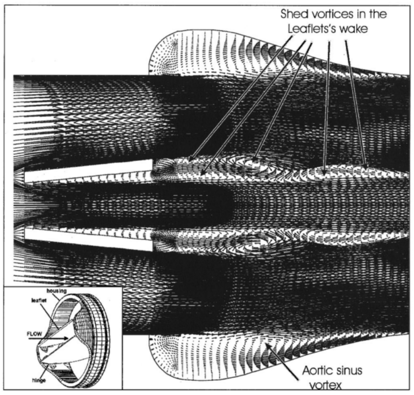

Figure 2.4. Flow across a bileaflet valve(Danny Bluestein et al., 1999).

As the highest levels of shear stresses are detected in the area around the leaflets and the wake, the platelets flowing above or below the leaflets remain trapped in the shed vortices formed at the leaflets wake, experiencing strong deformation stresses (Danny Bluestein et al., 1999; Morbiducci et al., 2009).

As reported by De Tullio et al. and Bluestein et al. (Danny Bluestein et al., 1999; De Tullio, Cristallo, Balaras, & Verzicco, 2009), high levels of shear stress generated in the valve wake and resulting from the flow separation at the leaflets, are responsible for haemolysis and platelet activation.

Investigating the impact of rotational and axial flows in the wake of the valve on platelets, Morbiducci et al. (Nobili et al., 2008) confirmed that the magnitude and alignment of velocity and vorticity flow field has an influence on the activation of platelets. The hypothesis is that these alterations in terms of flow field lead to aggregation of blood cells, therefore, formation of blood clots.

In conclusion, comparing the role of vortices in a native and a mechanical valve, Bluestein et al. (Danny Bluestein et al., 1999) noted that, while in the native valve the vortices play an active role in promoting the valve closure, the wake of the vortices in a mechanical valve only play a marginal role within the sinuses.

In contrast to mechanical devices, bioprosthetic valves are believed to present more physiological haemodynamics as their leaflets are made from biological tissue (Lakshmi P. Dasi et al., 2009). However, they are still not able to replicate the behaviour of native valves (Burriesci et al., 2010; Toninato et al., 2016). In fact, the presence of the supporting stent and the implantation approach result in a mismatch between the aortic root and the shape and position of the prosthetic leaflets. The presence of the sewing ring and pledget-armed sutures used to fix the valve into place at the basal annulus, together with the restriction due to the stent thickness, result in a reduction of the EOA (Capelli et al., 2017). Similarly, the man-made commissures construction and the increased stiffness of the crosslinked tissue, result in the formation of a non-physiological vortex above the commissures, expanding as the flow rate decreases in late systole and impinging upon the central jet flow (Toninato et al., 2016), whilst affecting the sinus flow (Hatoum et al., 2017). Depending on the proportion between the valve and the root portions, the start-up vortex generated in early systole may remain in the sinus, as the physiological case, or migrates into the aortic root, narrowing the flow and decreasing the potential performance of the valve (Toninato et al., 2016). In its stead, a second vortex forms in the sinus, with the opposite direction of the initial vortex, still providing washout of the sinuses and supporting the closing mechanism of the valve (the configuration produces similar levels of regurgitation to a larger surgical valve with vortical behaviour more closely aligned to that observed physiologically) (Toninato et al., 2016).

All these factors contribute towards producing a slightly more stenotic valve, characterised by an increase of peak jet velocity by 70%, the pressure drop rising by 60%, and the EOA reducing by 30%, when compared with a native valve in the same size aortic root (Toninato et al., 2016; Yoganathan et al., 2004). The smaller leaflet lengths appear to reduce the closing regurgitant volume, mitigating some of the energy loss due to smaller EOA (Toninato et al., 2016). Bioprosthetic valve performance can be improved by using stentless configurations, which give less forward low obstruction and improved haemodynamics performance than their stented equivalents (Yoganathan et al., 2004). However, their production and implantation procedure is more complex, and their performance can be affected by the irregularity of the host anatomy, and by procedural inaccuracies. In fact, the leaflets are normally designed to operate optimally in a regular circular configuration, which is difficult to attain in the absence of a supporting stent. Generally, stentless valves are reported to restore flow velocities closed to the physiological ones, and better coronary flow than their stented equivalents, due to the resultant lower transvalvular pressure drop, and the decreased turbulence downstream of the valve (Ben-Dor et al., 2014).

2.3.2 Haemodynamics in Transcatheter valves

Patient aortic root anatomy, valve design, orientation of the implanted heart valve, and deployment method are all factors that contribute to establish the haemodynamics within the aortic arch and which can lead to alterations in the flow pattern. In case of TAVI, the aortic root anatomy plays an important role as represents the landing zone and provides the radial force needed to securely house the valve (Padala et al., 2010). In fact, transcatheter device deployment can lead to an elliptical valve orifice which in turn, can result in coaptation mismatch (Gunning, Vaughan, & McNamara, 2014).

Though the clinical benefit of the treatment has been demonstrated, some post procedural complications have emerged. In particular, the occurrence of silent ischaemic lesions and dementia is considerably higher than with surgical valve replacement (Kahlert et al., 2010; Rodés-Cabau et al., 2010). The source of these pathologies is still unclear, but a potential cause has been recently identified as haemodynamics perturbations downstream the valve (Ducci, Tzamtzis, Mullen, & Burriesci, 2013).

TAVI devices introduce disturbances in the flow pattern since the native valve is not removed from its anatomical site resulting in a valve-in-valve configuration where the physiological diseased valve, or failed bioprosthesis is pushed against the aortic root wall acting as a physical barrier within the Valsalva sinuses region (Figure 2.5). This change in terms of anatomical configuration seems to affect the flow, and may establish haemostatic conditions typically associated with thrombus formation since it obstructs the circulation of blood within the sinuses which would otherwise prevent stagnation and blood damage (Ducci et al., 2016).

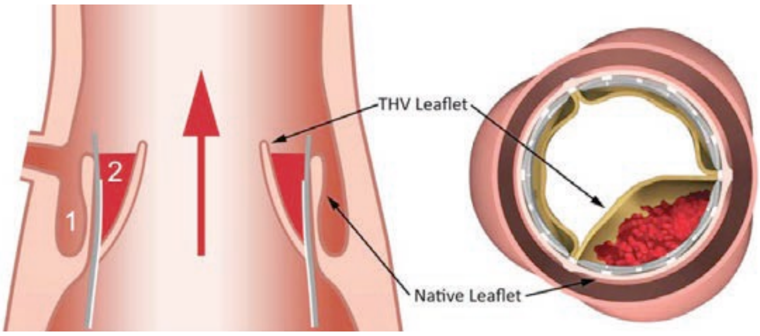

Figure 2.5. TAVI configuration (Midha et al., 2017).

A computational study from Laadhari et al. (Laadhari & Székely, 2017) confirms this hypothesis, stating that TAVI approach used has a major impact on the blood flow, leading to the formation of zones characterised by slow flow velocities (velocity ≤ 0.1 cm/s) in the lower region of sinuses which may promote pathological conditions. In addition, the presence of calcified leaflets, makes the recirculation process even more difficult.

Increased blood residence times have also been observed close to the leaflets and around the sinuses in general, resulting in thrombotic conditions (Vahidkhah, Barakat, et al., 2017).

Folding or geometric confinement of the leaflets may increase the blood residence time, linked as a permissive factor in TAV leaflet thrombosis, with no preference with occurrence on the leaflet associated with the non-coronary sinus (Vahidkhah, Javani, et al., 2017).

Blood residence time is reported to increase also in the sinuses, in proximity to the TAV leaflets, with a longer residence time during systole (about 40% longer), and higher mean value of residence time from the end of systole until mid-diastole (about 150% longer), elevating the thromboembolic risk for the valve (Vahidkhah, Barakat, et al., 2017).

TAVI also determines major variations in both the fluid mechanics and operating mechanisms of the valve (Ducci et al., 2016). In the case of TAVI devices, the start-up vortices generated during opening do not hold in position at the tip of the dynamic leaflets inside the upper part of the sinus, but form further downstream at the edge of the native leaflets, which form a continuous wall (Ducci et al., 2016). This is associated with slower washout of the sinuses (Ducci et al., 2016; Gunning, Saikrishnan, McNamara, & Yoganathan, 2014) and a delay of around 10 ms in the opening of the valve (Ducci et al., 2013; G. Kumar, Raghav, Lerakis, & Yoganathan, 2015).

During systole, for most designs the valve stent prevents the operating leaflets from opening beyond 90°, resulting in a narrower, centrally located systolic jet (Ducci et al., 2013; G. Kumar et al., 2015), characterised by higher peak velocities than in young healthy native valves (at a cardiac output (CO) of 5 lpm in the range of 2.1 - 2.3 m/s)(Saikrishnan, Gupta, & Yoganathan, 2013; Saikrishnan & Yoganathan, 2013) vs. the 1.1-1.7 m/s for the young healthy physiological valve (Michael S. Sacks et al., 2009). The raised central jet velocities result in higher viscous shear stresses, up to 6 N/m^2 (Gunning, Saikrishnan, et al., 2014), Though the shear stress of blood flow in the root has been experimentally determined to be beneath the haemolytic threshold of 400 N/m^2 (Ducci, Tzamtzis, Mullen, & Burriesci, 2012).

During valve closing, the return of fluid in the axial direction is not accompanied by the vortical structures observed in the physiological representation, which aid wash-out of the sinuses (Ducci et al., 2016). The presence of the static native leaflets also alters the effect of the fluid suction generated by the closing leaflets upon the fluid within the sinuses (Ducci et al., 2012). Consequently, closure is delayed by approximately 10 ms (Ducci et al., 2013; G. Kumar et al., 2015), and an extended and prolonged stagnation zone develops between the sinus and the native leaflets. This is present throughout the entire cardiac cycle with a shear rate below 100 s^{-1} (Ducci et al., 2016; Groves, Falahatpisheh, Su, & Kheradvar, 2014).

As for the coronary blood flow, an higher coronary blood flow with respect to physiological valves was reported in both low and high profile stent frame TAVI design (Wald et al., 2017).

2.4 Main findings

The main findings from the literature review can be summarised as follows:

- Cardiovascular efficiency depends on a well-functioning aortic valve, which in turn depends on its surrounding anatomical parts and fluid environment. A prosthetic device able to minimise flow separation, vortices and stagnation with an haemodynamics characterised by low pressure drop and disturbance-free velocity field is highly desirable (Reul et al., 1990).

- Computational studies, focused on the aortic valve, contributed to improve the understanding of the mechanics of the native young healthy aortic valve, and gain insights into the evolution of valvular diseases (Croft, L. R., Mofrad, M.R.K., 2010). However, aortic valve root function and its impact on haemodynamic performance is not yet fully understood.

- Many studies have been conducted to shed light on the haemodynamics regulating the functioning mechanism of the aortic valve; however contradictory opinions are still present in literature making difficult to achieve a comprehensive understanding of the aortic valve operating process. In particular, vortices are generated in the sinuses of Valsalva during each cardiac cycle: these vortices are affected by the surrounding geometry, but the mechanics of vortex generation and propagation in the aortic root has not been agreed upon. Vortices may also be involved in the proper function of the aortic valve but there is no consensus within the literature regarding the vortical properties of a physiological, young healthy heart, and accordingly there is not complete agreement on how these vortices affect the valve function, either in case of native valves, valvular prostheses, or in case of diseases.

- Few studies were found in literature which addressed the importance of including compliant aortic walls in models mimicking the aortic valve and root behaviour. Since the compliance of the aortic walls is difficult to replicate *in vitro*, most studies use rigid material. Therefore, the influence of the aortic root compliance upon the flow pattern still needs to be addressed (Barannyk & Oshkai, 2015).

- The valve-in-valve configuration produced by TAVI leads to an alteration in the haemodynamics of the aortic root region: these alterations have been linked to the formation of downstream silent ischemic lesions and dementia (Ducci et al., 2016).

• The valve-in-valve configuration may affect coronary artery flow, in which case, this may in turn impinge on the well-functioning of the cardiovascular system as well.

• Valvular stenosis leads to an increase in the velocity of the jet through the valve orifice and a reduction in the EOA. Such pathology progresses over the years promoting the occurrence of comorbidities.

• Dilation of the ascending aorta can be often related to, and develop due to, the presence of severe stenosis. It may lead to variations in blood flow dynamics.

2.5 Aims

Aortic valve replacement is intended to guarantee patients the ordinary functioning of the aortic valve for the rest of their life. Such goal dictates for the implanted prosthetic devices to be able to closely match physiological standards without leading to any complication (Bakhtiary et al., 2007).

Thus, the understanding of the optimum function of the young healthy aortic valve is essential in interpreting the effect of pathologies in the region, and in devising effective treatments to restore the physiological functions. Still, there is no consensus on the operating mechanism that regulate the valve opening and closing dynamics. Nowadays, although different therapies are being employed in the treatment of aortic valve diseases, the optimal conditions are not known yet.

The aim of this study is to develop a numerical model which, validated against accurate *in vitro* studies (Toninato et al., 2016), will be able to gain in depth insights into the full 3D flow dynamics of the aortic root in young healthy, ageing and treated conditions.

Several studies focused on the aortic valve dynamics were carried out, hence contributing to improve the understanding of the native aortic valve mechanics and gaining insights into the evolution of valvular disease. However, no agreement has been achieved yet about the main flow features characterising the optimal aortic valve functioning mechanism. This inevitably led to inaccurate results and discrepancies between study findings.

Experiments using an optical technique called Particle image velocimetry (PIV), were performed in our research group to augment the knowledge on this subject, however such techniques introduce approximations and limitations.

With regard to the 2D PIV optical method, this experimental technique presents some restrictions such as the possibility to perform flow investigations only across selected cross sections, and on a limited range of fluids and materials. For instance, the use of rigid material as substitute for biological tissue anatomical parts, which results in neglecting the effect of the root compliance, and the use of 'blood alike' fluids whose properties cannot exactly match the same properties of blood.

Also, being the optical system 2D and phase averaged, it could not identify out-of-plane structures and could not track all the cycles. Hence, a computational model able to obtain information on the 3D flow field in the aortic valve allows these experimental limitations to be overcome and a more comprehensive understanding to be achieved. In this scenario, a computational analysis such as FSI, can be used as a reference to identify what should be expected in terms of young healthy conditions.

Therefore, once the numerical framework used to construct the initial numerical model was validated by the results from the previous *in vitro* study, the simulation was altered to better represent an idealised young healthy aortic valve first and then ageing and treated conditions. Some of the major limitations affecting the benchtop investigation, such as the presence of the oversized bioprosthetic valve stent, the rigid material used for the mock aortic root and the use of a test fluid denser than blood, could be corrected in the other computational models, although based on the same framework as the validated model.

Obtaining an accurate model of the native young healthy aortic valve allowed to investigate the impact that existing treatments, and pathologies have upon the valve functioning mechanism.

2.6 Objectives

This study builds upon the work by Ducci et al. (Ducci et al., 2013) utilising *in vitro* methods based on PIV measurements to investigate the haemodynamics after TAVI in a left heart simulator.

The objectives of this thesis develop from the need to overcome the limitations related to experimental studies hence expanding the findings and improving the understanding of current results and are:

To obtain a reliable FSI model since, due to the complexity of valve dynamics, the correct tuning of the involved parameters is crucial to attain trustworthy representations of the studied phenomena. As recommended by the International Organization for Standardization (ISO) working group (Wei et al., 2018), complementing experimental and computational studies is crucial to obtain reliable results from complex numerical simulations (Yoganathan et al., 2005).

To achieve a more comprehensive understanding of valve function by means of FSI methods. This means that an investigation of the full 3D flow field is needed. Computational techniques allow to obtain pressure and velocity maps for the entire 3D geometry and in addition, present a better temporal resolution than experimental optical techniques offering a variety of material models available to replicate both the fluid and the vessel properties.

To identify the optimal haemodynamics conditions which characterise efficient opening closing dynamics of the native aortic valve. The young healthy native model reproduces an accurate physiological condition where the stent is removed, the fluid properties are closely replicating the blood and the compliance of the aortic vessel is taken into account.

To investigate the flow alterations induced by the presence of the most common prosthetic devices and ageing related pathologies by comparing the results with respect to the physiological configuration system.

Chapter 3 Materials and Methods

Introduction

Several *in vivo*, *in vitro* and computational studies are focused on the valve dynamics to enlighten the native and prosthetic valves functioning, the correlation between mechanical stresses and valve diseases and the interdependence between haemodynamics performance and post implantation complications (K. Chandran, 2010; Yoganathan et al., 2005). Unfortunately, *in vivo* studies based on techniques such as MRI and ultrasound present practical limitations in measuring the velocity field, due to their reduced spatial and temporal resolution (M. S Sacks & Yoganathan, 2007); and *in vitro* studies, although capable of capturing the main flow features downstream of the valve, only allow the measurements in limited regions, normally outside of the valve structure (Barannyk & Oshkai, 2015; Ducci et al., 2016, 2013; Mao, Li, & Sun, 2016; Yoganathan et al., 2004).

These experimental drawbacks translate into restrictions in terms of measurements and data obtained, but nonetheless experiments yield very valuable information, since they are capable of mimicking realistic conditions (K. Chandran, 2010).

For instance, experimental studies focused on the flow through prosthetic devices have shown the ability of capturing the main flow features downstream the valve. However, in order to find a correlation between the flow field and clinical parameters such as platelet activation or haemolysis, a more in-depth investigation is needed (Yoganathan et al., 2005).

In this scenario, the opportunity to adopt numerical models in order to comprehend complex dynamics of the valve is apparent. In fact, *in silico* simulations can offer a comprehensive representation of the valvular structures and flow dynamics across the valve at different spatial and temporal scales (K. Chandran, 2010). This requires the development of high resolution fluid-structure interaction (FSI) models, which allow the description of both the mechanical behaviour of the tissue components and the fluid dynamics throughout the cardiac cycle, which play a significant role towards the achievement of a more extensive understanding of the valve function (Yoganathan et al., 2005). Nevertheless, due to the complexity of the valve dynamics, the correct tuning of the involved parameters is crucial to attain trustworthy representations of the studied phenomena. This has been clearly acknowledged by the International Organization for Standardization (ISO) working group (Wei et al., 2018), which strongly endorses the combination of advanced experimental and computational studies to obtain reliable results from complex numerical simulations (Yoganathan et al., 2005).

This synergistic approach was adopted in the present study, with the aim to understand the optimum flow dynamics that should be expected within a young healthy and ideal aortic root, in physiologically normal operating conditions. The same model was then used to replicate also ageing and treated conditions, whose results were compared with respect to the physiological findings.

3.1 Finite element method

FSI is a computational technique based on the finite element method (FEM). In order to obtain the numerical solution of the governing equations, this method requires the geometry to be divided into a grid of cells/elements, where the variables of interest are calculated. The discretization (in space and time) of the governing differential equations results in a system of algebraic equations, whose numerical solution yields the problem variables at the mesh points (Katritsis et al., 2007).

In dynamic models, the basic equation of motion is:

$$[M]\{\ddot{u}\} + [C]\{\dot{u}\} + [K]\{u\} = \{F\} \tag{3}$$

where {F} is the applied force, [M], [C] and [K] are the mass, damping and stiffness matrices and $\{\ddot{u}\}$,$\{\dot{u}\}$ and {u} are the acceleration, velocity and displacement vectors, respectively (Rao, 2005).

To solve this equation, the time needs to be discretized using either an implicit or explicit method by dividing the event into a number of time steps.

In an implicit scheme, the displacement vector {u} at time t+Δt is a function of the properties known at time t, but it also depends on the properties at time t+Δt. Therefore, as reported in Eq. 4 implicit approaches find the solution by solving an equation which involves the current state of the system and the later one (Bui, 2010).

$$\{u\}_{n+1} = f\,(\{\ddot{u}\}_{n+1}, \{\dot{u}\}_{n+1}, \{u\}_{n+1}, \{\ddot{u}\}_{n}, \{\dot{u}\}_{n}, \{u\}_{n}, \dots) \tag{4}$$

In this case, the acceleration varies linearly within a timestep, which results in a more accurate representation so that the timestep can be longer. However, the inversion of the stiffness matrix significantly complicates the solution since the size of the matrix is proportional to the number of elements and inversion can require 75–90% of the solution time. (Carmody, Burriesci, Howard, & Patterson, 2006). In this case, the search for convergence is iterative as it is performed each time-step. Therefore, successful convergence can be very difficult to achieve (Einstein, Reinhall, Nicosia, Cochran, & Kunzelman, 2003).

In the explicit approach, the solution is based on a central difference scheme for time. The displacement vector {u} at time t+Δt is a function of quantities known at previous time steps (t and t-Δt), and it does not require any complex matrix inversion. As shown in Eq.5, Explicit methods calculate the state of the system at a later time from the state of the system at the current time without the need to solve algebraic equations.

$$\{\mathrm{u}\}_{n+1} = \mathrm{f}\left(\{\ddot{u}\}_{n}, \{\dot{u}\}_{n}, \{\mathrm{u}\}_{n}, \{\ddot{u}\}_{n-1}, \{\dot{u}\}_{n-1}, \{\mathrm{u}\}_{n-1}, \ldots\right) \tag{5}$$

The solution by explicit integration is simplified since the acceleration is assumed constant over each timestep and therefore, no inversion of the stiffness matrix is needed (Souli & Benson, 2013). Nodal displacements and velocities are updated without forming the stiffness matrix and without solving any algebraic equations, given a diagonal mass matrix. In other words, there are no solution iterations on the time step (Ted Belytschko, Wing Kam Liu, Brian Moran, 2013). Convergence is achieved using a maximum time-step criterion (Einstein et al., 2003).

Thus, the explicit method is usually employed for models presenting a large number of degrees of freedom since allows to significantly save the computational cost (Einstein et al., 2003) and furthermore, it simplifies the implementation of complex non-linear constitutive equations (Ted Belytschko, Wing Kam Liu, Brian Moran, 2013).

Hence, a code based on explicit integration was chosen to perform the analysis because of the large size of the models in both temporal and spatial domains.

3.2 FSI numerical approaches

A sufficiently accurate model of the physiological mechanisms that characterise the heart valve function, involves the synergistic interaction of highly non-linear deformable structures (the valve and the artery) with pulsatile fluid flows (the blood). In fact, in order to simulate the valve behaviour, both the leaflets mechanical response and their motion due to the load exerted by the surrounding fluid, need to be included in the numerical model (Michael S. Sacks et al., 2010).

Therefore, complex numerical analyses able to support Fluid-Structure interactions (FSI) appear the most suitable and comprehensive computational approach to adopt; they can expose phenomena which could not be investigated performing an independent structural or fluid dynamics simulation (Marom, 2015), allowing to detect the typical features of the valve dynamics (Carmody et al., 2006; Sturla et al., 2013).

There is no standard approach to perform FSI analyses, but different methodologies were developed in response to the need of tackling a variety of clinical scenarios (Croft, L. R., Mofrad, M.R.K., 2010). Two major methods are usually adopted for FSI problems: the Arbitrary-Lagrangian-Eulerian (ALE), which is a boundary conforming mesh approach, and the Immersed Boundary formulation (IB), which is a non-boundary conforming mesh approach (Guccione, J.M., Kassab, G., Ratcliffe, 2010).

As already stated, FSI includes both structure and fluid domains. The first is usually modelled using a Lagrangian formulation, where the mesh grid moves together with the deformation of the material. The fluid domain instead, is modelled using a Eulerian formulation, where the mesh grid is fixed and the material passes through it (Croft, L. R., Mofrad, M.R.K., 2010).

In the ALE method the fluid is discretised using a reference frame whose motion follows the solid mesh grid at the fluid-structure interface (Mohammadi, Cartier, & Mongrain, 2016). The interaction between the solid and the fluid domain is obtained constraining the velocity interface to be equal to that of the boundary (Guccione, J.M., Kassab, G., Ratcliffe, 2010). Thus, this approach needs the solid mesh to conform the fluid grid at the boundary since the interface is part of the solution process and therefore remeshing is required as the structure deforms (De Hart et al., 2003).

On the other hand, in the IB method, the fluid part has a stationary mesh frame and the solid structure is modelled with a Lagrangian formulation which is allowed to move within the fluid grid (Bavo et al., 2016). As a consequence, this approach requires the fluid grid to overlap the solid structures without the need of a conforming mesh at the boundary (Griffith, 2012). Accordingly, the equations for the solid and fluid domain are solved separately, so remeshing is not require (Mohammadi et al., 2016). The coupling between the solid and the fluid at the boundary is provided by adding forcing terms to the fluid motion governing equations (Peskin, 1972).

These features make IB method a suitable technique to model problems including structures undergoing large deformations. As the fluid frame is fixed, the Lagrangian deformation of the leaflets cannot lead to the distortion of the fluid mesh grid and consequent computational instability (Bavo et al., 2016; Borazjani, 2013; De Hart et al., 2003). However, this technique cannot accurately capture the interface interactions parameters (Kheradvar et al., 2015; Sturla et al., 2013; van Loon, Anderson, & van de Vosse, 2006).

Contrary to IB method, ALE technique, as a result of the limitations introduced by its body-fitted grids requirement and consequent remeshing process, is not recommended for problems with large structural displacements. Therefore, this method did not succeed in modelling native and prosthetic heart valves (Croft, L. R., Mofrad, M.R.K., 2010; Joda, Jin, Haverich, Summers, & Korossis, 2016; Weinberg & Kaazempur Mofrad, 2007).

Overall, due to the complexity of the cardiovascular physiology, optimal FSI is usually achieved implementing a hybrid formulation obtained from the combination of the two approaches (Yoganathan et al., 2005). Since the flow in heart valves is pulsatile and the valve undergoes very large deformations, performing a FSI analysis of heart valves has proven to be a challenging task (Croft, L. R., Mofrad, M.R.K., 2010).

3.3 LS-DYNA FSI algorithm

The analyses were performed on an Intel Core i7 3.4 GHz workstation using the explicit finite element software LS-DYNA Release 9.2 (LSTC, Livermore, CA, USA), which is a general purpose solver specialised in nonlinear transient dynamic problems suitable to investigate complex phenomena involving large deformations, sophisticated material models and fluid structure coupling (Hallquist, 2006). This package is widely used in industry for modelling dynamic events, it has been used previously for the analysis of heart valves (Black, Howard, Huang, & Patterson, 1991; Carmody et al., 2006; Howard, Patterson, & Yoxall, 2003; Nobari, Mongrain, Gaillard, Leask, & Cartier, 2012; Ranga et al., 2006; Sturla et al., 2013), and, lastly, it is included in the ISO working group list of recommended commercial software to be used to perform FSI (Wei et al., 2018).

Such simulation tools numerically solve the more fundamental time-dependant equations of continuum mechanics, and therefore are able to model multi-material and transient continuum (i.e. fluid and/or solid) mechanics problems overcoming the limitations of traditional computational fluid mechanics or computational solid dynamics codes (Smith & Stojko, 2004).

As already stated, FSI computations adopt a Lagrangian approach to model the solid structure and a Eulerian/ALE approach to model the fluid.

In LS-DYNA, Lagrangian and Eulerian/ALE solution methods can be combined in the same model and the FSI may be handled by a coupling algorithm (*LS-DYNA Aerospace Working Group Modeling Guidelines Document*, 2011).

Therefore, the simulations were performed coupling a Lagrangian model of an ideal aortic root with a Eulerian fluid domain through the hybrid ALE algorithm available in LS-DYNA. Following this approach, the solid structures are immersed in the fluid control volume where each domain is modelled independently and without the need of a conforming mesh at fluid-structure boundary (Croft, L. R., Mofrad, M.R.K., 2010).

In fact, in FSI analyses, the solid deformations can lead to excessive distortion of the fluid mesh, especially along the boundary, therefore causing a very small time step value for explicit calculations. LS-DYNA ALE approach instead, allows to limit computational instability since a new undistorted mesh for the fluid domain is created (M. Souli, A. Ouahsine, 2017). This means that, given the boundary conditions, the solution is remapped from the distorted to the undistorted mesh so that the mesh topology is fixed (Hallquist, 2006; M. Souli, A. Ouahsine, 2017).

LS-DYNA uses an "operator split" technique to solve the fluid domain, and the ALE algorithm to couple the two domains (Borazjani, 2013; Croft, L. R., Mofrad, M.R.K., 2010; Weinberg & Kaazempur Mofrad, 2007). Remeshing is being allowed only for the elements based on the Lagrangian formulation since their mesh topology changes as the material deforms whilst the fluid domain is based on a Eulerian fixed mesh grid (Croft, L. R., Mofrad, M.R.K., 2010). In order to solve the fluid motion equations, the time integration cycle is split into two steps: a Lagrangian time step and a "remap" or "advection" step where an advection term is applied to remap the fluid domain to its original configuration (N. Aquelet, Seddon, Souli, & Moatamedi, 2005) (Figure 3.1). During the Lagrangian phase the fluid grid can distort, but then during the advection phase the solution must be referred back to the undistorted initial frame (Carmody et al., 2006). This process describes the so-called "operator split" technique (Hallquist, 2006).

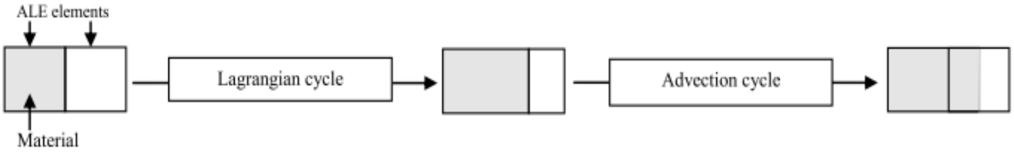

Figure 3.1. Lagrangian and advection cycles in a computational time step (Nicolas Aquelet, 2012).

3.3.1 Governing equations

The conservation of mass, momentum and energy are the governing equations for the motion of a fluid. When these equations are solved to compute displacements and velocities using a computational grid, they can be written as (N. Aquelet et al., 2005; M. Souli, A. Ouahsine, 2017; Sturla et al., 2013):

mass conservation
$$\frac{\partial \rho}{\partial t} = (-\rho)\mathrm{div}(v) - (v - u)\nabla\rho$$

momentum conservation
$$\rho\frac{\partial v}{\partial t} = \sigma - \rho(v - u)\nabla v \tag{6}$$

energy conservation
$$\rho\frac{\partial e}{\partial t} = \sigma\varepsilon - \rho(v - u)\nabla e$$

where ρ is the fluid density, t is time, v and u are the material and mesh velocity, e is the total mechanical energy, σ is the stress and ε is the strain.

Two reference frames can be used to obtain the numerical solution of these equations: Lagrangian and Eulerian. In the Lagrangian approach, used primarily to solve structural problems, mesh nodes move with the deformation of the material, so that $u = v$.

In the Eulerian approach, most commonly used for the advection of fluids through a mesh, the mesh is fixed though, so that $u = 0$. Therefore, the relative velocity between the material and the reference configuration $(v - u)$ is equal to the material velocity (v). The term in the relative velocity is usually referred to as the advective term, and accounts for the transport of material past the mesh (M. Souli, A. Ouahsine, 2017).

As already mentioned, in LS-DYNA the computation of field variables for the fluid domain within a FSI simulation is performed through two steps at each time increment, which combine the two described approaches:

Lagrangian step. Mesh nodal velocity (u) is equal to the fluid velocity (v); this ensure that mass is conserved. Mesh node characteristics, displacements and velocities are calculated and the resulting deformed mesh is obtained.

Eulerian step (advection). The deformed mesh is superimposed to the initial, fixed one. The flux of mass, energy and momentum associated to the deformation of the mesh are then used to map the field variables computed in the Lagrangian step back on the Eulerian mesh.

3.3.2 Time step calculation

The timestep selection plays a major role since it has to be small enough to avoid any numerical instability but large enough to allow the solution to proceed at an acceptable speed (Carmody et al., 2006).

The time step size is set automatically in LS-DYNA and its calculation is based on the time needed for a sound wave to pass through the smallest solid element in the model (Souli & Benson, 2013).

The maximum time step size is limited by the Courant-Friedrichs-Lewy condition, producing an algorithm which typically requires many relatively inexpensive time steps. Using this criterion, the solution is unconditionally stable. Since the solution is solving for displacements at nodal points, the time step must allow the calculation to progress across the element without "skipping" nodes. This means that the time step must ensure that the stress wave stays within the element. Hence, the explicit solution is limited in time step by the element size and the speed sound in that element under study.

It follows that the time step is calculated as the minimum stable time step in any deformable finite element of the mesh, controlled by the element velocity u, the speed of sound in the material c and the characteristic length of the element L_c (Hallquist, 2006; Sturla et al., 2013):

$$\Delta t_{CFL} = f \frac{L_c}{c + u} \tag{7}$$

where f is the time step scale factor, set by default to 0.9.

The time step size was ranging between $1.8 \cdot 10^{-7}$ and $2.4 \cdot 10^{-7}$ throughout all numerical analyses requiring on average 266 hours to run three cardiac cycles.

3.4 Laminar flow in a pipe

As recommended by the ISO Working group (Wei et al., 2018), prior to conducting the analysis of heart valves, the software solver and the coupling method were verified against the solution of a benchmark analytical test case: a laminar flow in a pipe. Therefore, an FSI model including a rigid pipe subjected to steady laminar blood flow, was realised.

As discussed previously in section 2.1, the blood flow is driven by the pressure gradient and its motion encounters the resistance exerted by the blood vessel network.

As stated by equation 8, the resistance is influenced by three factors: the tube length (L), the tube radius (r), and the viscosity of the fluid (η).

$$R = \frac{\mu \cdot L}{r^4} \tag{8}$$

Therefore, the flow (Q) in a vessel can be described using the following expression known as Poiseuille's law (Silverthorn, 2013) :

$$Q = \frac{\Delta P}{R} \tag{9}$$

where ΔP is the gradient pressure and R is the resistance.

The Poiseuille's full equation considers a resistance factor given by:

$$R = \frac{8 \cdot \mu \cdot L}{\pi \cdot r^4} \tag{10}$$

where $\frac{8}{\pi}$ is a constant.

This means that the flow is directly dependent on the vessel length and the fluid viscosity while is inversely proportional to the radius. However, this relation meets the assumptions that the blood is a Newtonian fluid, its motion is laminar and the vessels are straight and rigid tubes.

This introduction was essential in order to give an insight about the law governing the blood motion in the aorta and understand how a change in these parameters can have an impact on the flow (Klabunde, 2011).

3.4.1 Numerical model details

The blood was modelled as Newtonian and laminar with a density (ρ) of 1060 $\frac{kg}{m^3}$ and a dynamic viscosity (μ), of 0.004 Pa·s, more details will be given in section 3.5.3.

The solver used in LS-DYNA is a compressible flow solver so the incompressibility of the flow was achieved setting the fluid bulk modulus to a magnitude order of 10^4, which resulted adequate since the fluid density variation was found to be below 0.01 % of the initial density value, therefore the effects of the fluid compressibility were negligible. The analysis was performed on a straight, rigid pipe with a diameter of 25 mm, which is the same diameter of the young healthy idealized aortic root model for an adult. The length of the pipe is chosen due to the requirement that the flow has to be fully developed for a certain pipe length. This requirement has to be achieved in order to compare the simulations with the analytical solution for a laminar fully developed pipe flow. According to (Sherman, 1992), the pipe length needed for the flow to reach a fully developed profile, known as entry length (L), is related to the pipe diameter, d, and the Reynolds number, Re, as:

$$\mathrm{L} = 0.05 \cdot \mathrm{Re} \cdot \mathrm{d} \sim 625\ \mathrm{mm} \tag{11}$$

Therefore, the pipe length was chosen to be 700 mm.

Assuming a laminar flow with a Reynolds number equal to 430, and given a vessel diameter of 25 mm, the velocity can be calculated using the definition of Reynolds number for the flow in a pipe as follows (White, 2002):

$$\mathrm{v} = \frac{\mathrm{Re} \cdot \mu}{\rho \cdot \mathrm{d}} \tag{12}$$

where v is the velocity, Re is the Reynolds number, d is the vessel diameter and μ and ρ are the blood dynamic viscosity and density, respectively.

Therefore, a steady uniformly distributed velocity of 65 $\frac{\mathrm{mm}}{\mathrm{s}}$ was set as boundary condition at the inlet, a pressure boundary condition of 0 Pa was applied at the outlet and a no slip boundary condition was applied on the pipe walls. Since the pipe was assumed to be axisymmetric, only one fourth of the pipe was modelled and symmetry constraints were set on the symmetry planes. This allowed to reduce the computational time.

From the analytical solution of the Navier-Stokes equations written in cylindrical coordinates for a Newtonian, laminar, steady, incompressible and fully developed flow through a straight rigid pipe, which is commonly referred to as Poiseuille flow, the velocity profile along the stream wise coordinate can be derived. Therefore, the analytical solution for the velocity profile obtained by applying the above-mentioned assumptions and the no-slip condition at the wall to the Navier-Stokes equations is (Katritsis et al., 2007):

$$u(r) = \frac{dp}{dx} \cdot \frac{1}{4\mu} (R^2 - r^2) \tag{13}$$

where r is the local radius, R the pipe radius, x is the stream wise coordinate and $\frac{dp}{dx}$ the pressure gradient in the stream wise direction. The velocity profile is parabolic with a maximum at the centerline and a minimum at the pipe wall (White, 2002) (Figure 3.2).

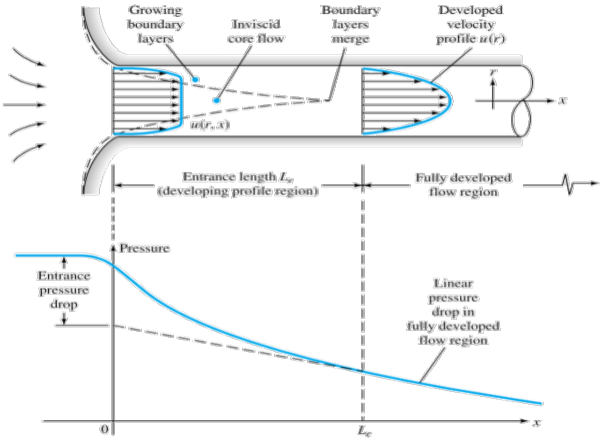

Figure 3.2. Developing velocity profiles and pressure changes in the entrance of a duct flow (White, 2002).

After a simulated time of 10 seconds, the data from the numerical simulation of the straight rigid pipe are sampled at the outlet cross-section. At this point, the flow is considered to be fully developed (Figure 3.3).

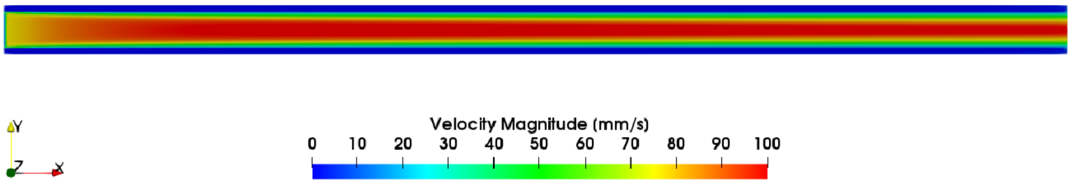

Figure 3.3. Velocity map of a pipe section at 10 s.

Figure 3.4 displays the velocity profiles along a line of the outlet cross-section at different time instants. The results show the presence of the boundary layer, and therefore the development of a parabolic profile for the velocity (Figure 3.4), as expected.

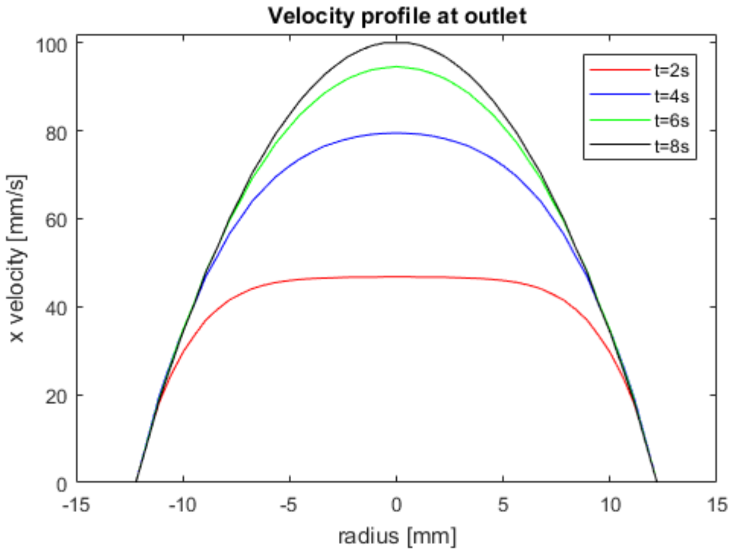

Figure 3.4. Velocity profile at different time instants.

Furthermore, the calculated velocity profile was found to be consistent with the analytical solution (Figure 3.5).

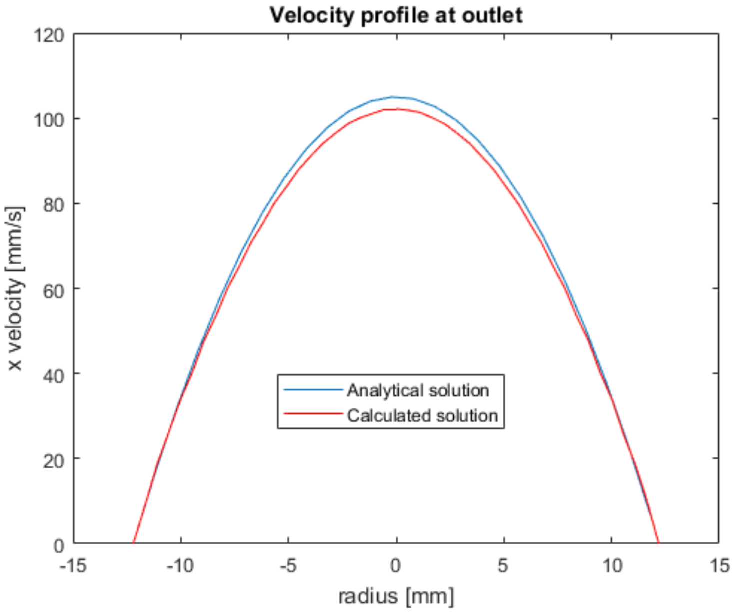

Figure 3.5. Comparison with the analytical solution.

3.5 Aortic valve FSI model

In order to obtain a FSI model of the aortic valve region, first an idealised geometry of the aortic root and valve was designed following the dimensional guidelines given by Swanson and Clark (Swanson & Clark, 1974) and Thubrikar (Thubrikar M., 1990). Then, the geometry was discretised into mesh grids using the software ICEM 17.0 (ANSYS, Inc., Canonsburg, PA, USA) and exported to LS-DYNA. Physiological boundary conditions were applied on the fluid domain as well as a no slip boundary condition on the vessel walls, and a coupling implementation between the fluid and structural parts.

3.5.1 Geometry

All models included aortic root and aortic valve anatomical parts immersed within a fluid control volume.

The aortic root geometry was based on the description of the young healthy human anatomy provided by Swanson and Clark (Swanson & Clark, 1974) (Figure 3.6.a), in reference to an annulus equal to 25 mm, corresponding to an average young healthy adult (Thubrikar et al., 2005). The aortic root cross section was approximated by an epitrochoid function assuming identical dimensions for the three Valsalva sinuses, as suggested by Reul at al.(Reul et al., 1990). The epitrochoid is a curve generated by a point which lies inside a circle, which again rolls on the perimeter of a second circle (Reul et al., 1990).

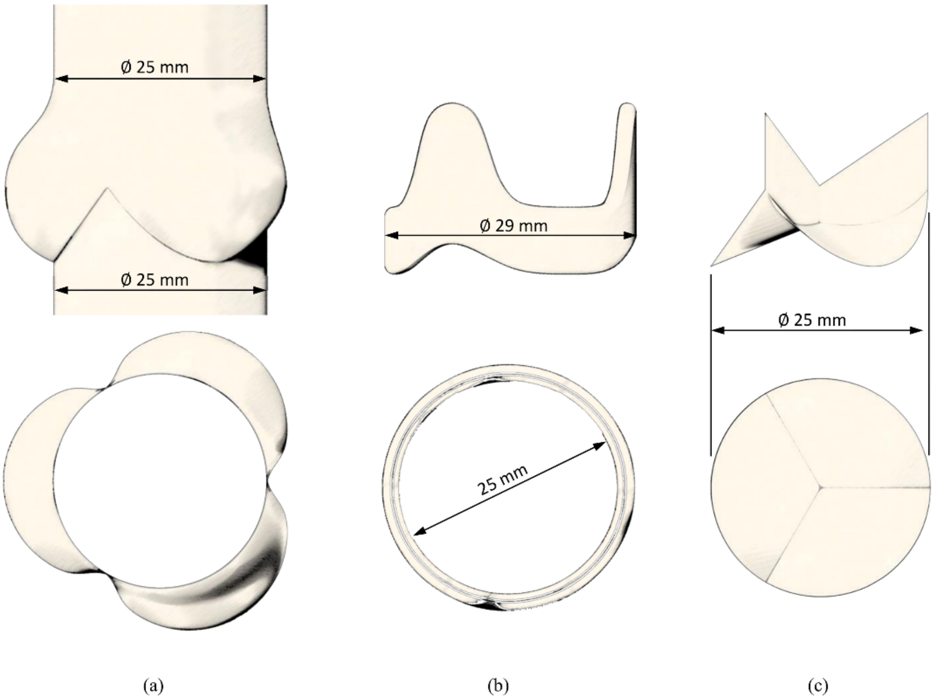

Figure 3.6. Sketch of the aortic root (a), the valve stent (b) and the leaflets (c) geometries used in the numerical model (Tango, Salmonsmith, Ducci, & Burriesci, 2018).

Therefore, the epitrochoid equations were implemented in the CAD software Catia V5 (Dassault Systems, France)(Figure 3.7) using the dimensional parameters given by Swanson and Clark (Swanson & Clark, 1974), assuming a 120-degree geometrical symmetry for the three leaflets and Valsalva sinuses.

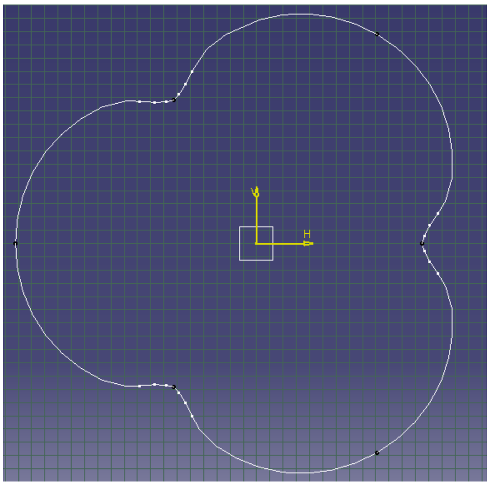

Figure 3.7. Epitrochoid function used to model the aortic root cross section

As the shape of the leaflets is very complex to replicate (Yoganathan et al., 2005), and the intent of the study was to analyse a generalised configuration representative of ideal native conditions, the leaflet geometry adopted for the numerical model was based on the description of the idealised young healthy human aortic valve provided by Thubrikar (Thubrikar M., 1990) for an annulus diameter equal to 25 mm (Figure 3.6.c and Figure 3.8).

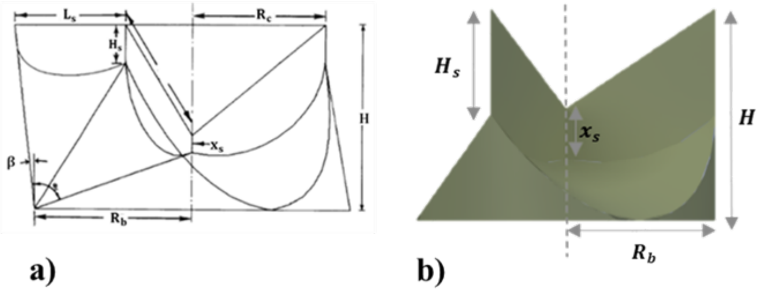

Parameters	Value
R_b	12.5 mm
H	17.75 mm
H_s	8.875 mm
x_s	4.25 mm

Figure 3.8. Thubrikar's schematic drawing of the aortic valve on the left (a) and valve CAD model with related design parameters: R_b is the annulus radius, H is the valve height, H_s is the commissure height and x_s is the coaptation height (b).

Since Thubrikar's description of the aortic leaflets provides information to generate a fully closed valve configuration, whilst the bioprosthetic porcine valve used for the in vitro validation was characterised by a semi-open shape when at rest in saline solution, a pre-expansion procedure was undertaken. To achieve this, the leaflets were initially modelled as linear elastic, with a Young's modulus of 1 MPa and a Poisson's ratio of 0.45, and then expanded by applying a uniformly distributed opening pressure of 5 mmHg. The resulting configuration, which resulted similar to that observed for the prosthetic porcine leaflets used in the in vitro experiment, was then adopted as the initial unloaded shape, by rezeroing the stresses and strains in the model. The obtained model of the valve structure is represented in Figure 3.9.

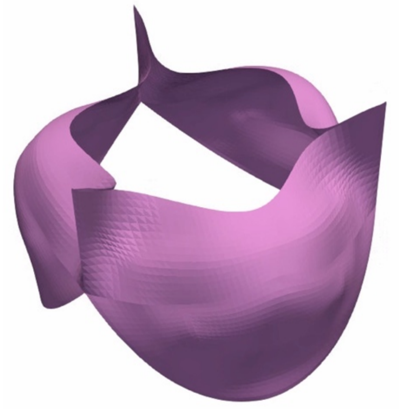

Figure 3.9. Semi-open valve configuration geometry.

The fluid control volume geometry used to model the blood flow is a solid obtained by scaling the epitrochoid function profile so that it could overlap the aortic root and valve models.

3.5.1 Mesh grid independence

Element dimensions were chosen after performing a mesh grid independence analysis on three different fluid and structure meshes: coarse (approximately 15.000 elements for the fluid and 10.000 for the shell), medium (approximately 110.000 elements for the fluid and 25.000 for the shell), and fine (approximately 900.000 elements for the fluid and 100.000 for the shell).

The results of the related FSI analyses were compared in terms of velocity profiles extracted along the vertical axis from the annulus height to the STJ height, as indicated by the dashed line in Figure 3.10, Figure 3.11, Figure 3.12 and Figure 3.13 which represented the area that most influenced the valvular dynamics.

The analysed instants of the cardiac cycle correspond to the same instants used for the model validation but, in this case, taken during the first cycle. This was due to the exceedingly expensive computational time required to run the numerical analysis with the fine mesh grid.

The velocity maps and profiles obtained at a cross section of the aortic root at the specific instants for the three different mesh models are reported in in Figure 3.10, Figure 3.11, Figure 3.12 and Figure 3.13. The region where the maximum velocity magnitude was observed is contoured by a red square.

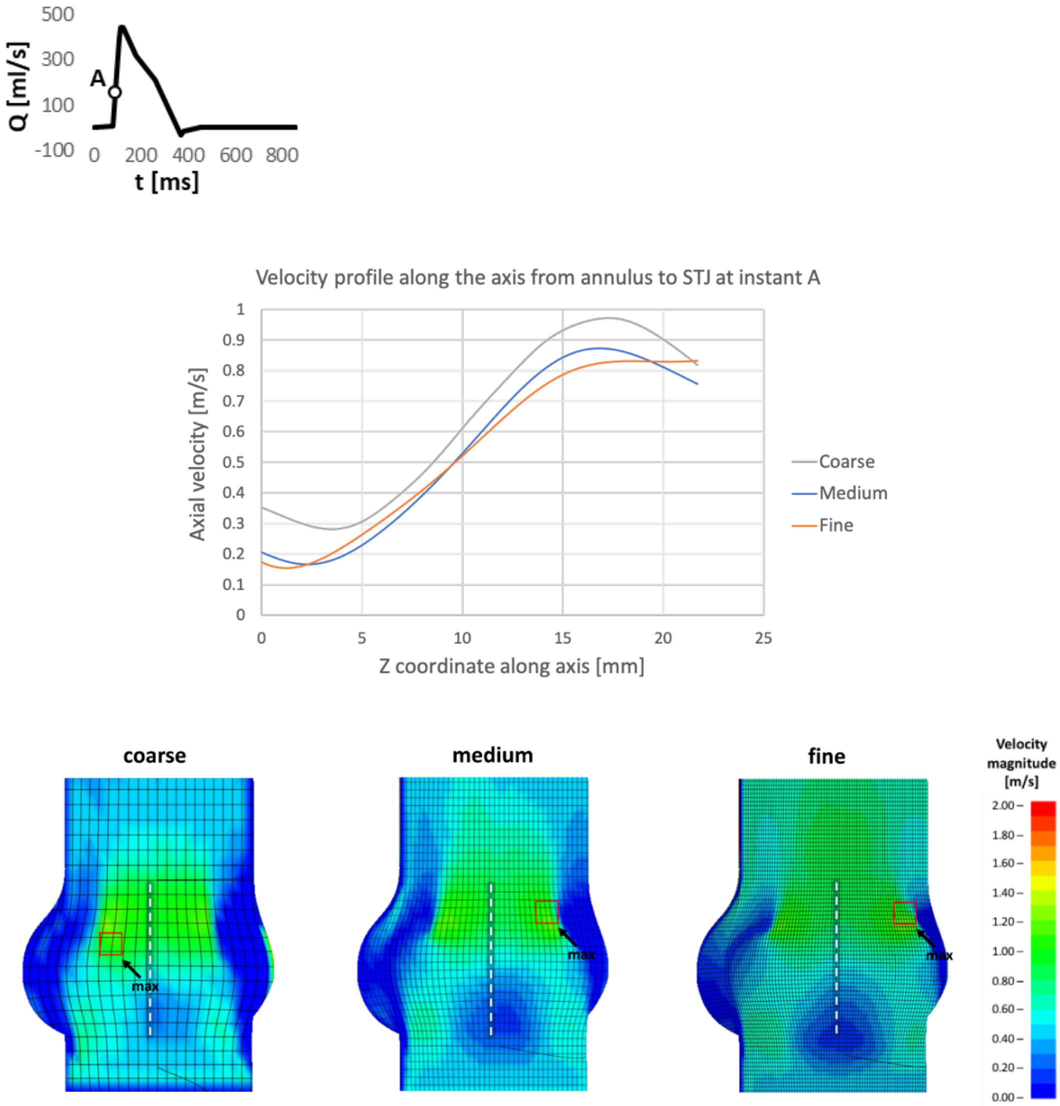

Figure 3.10. Velocity maps at instant A.

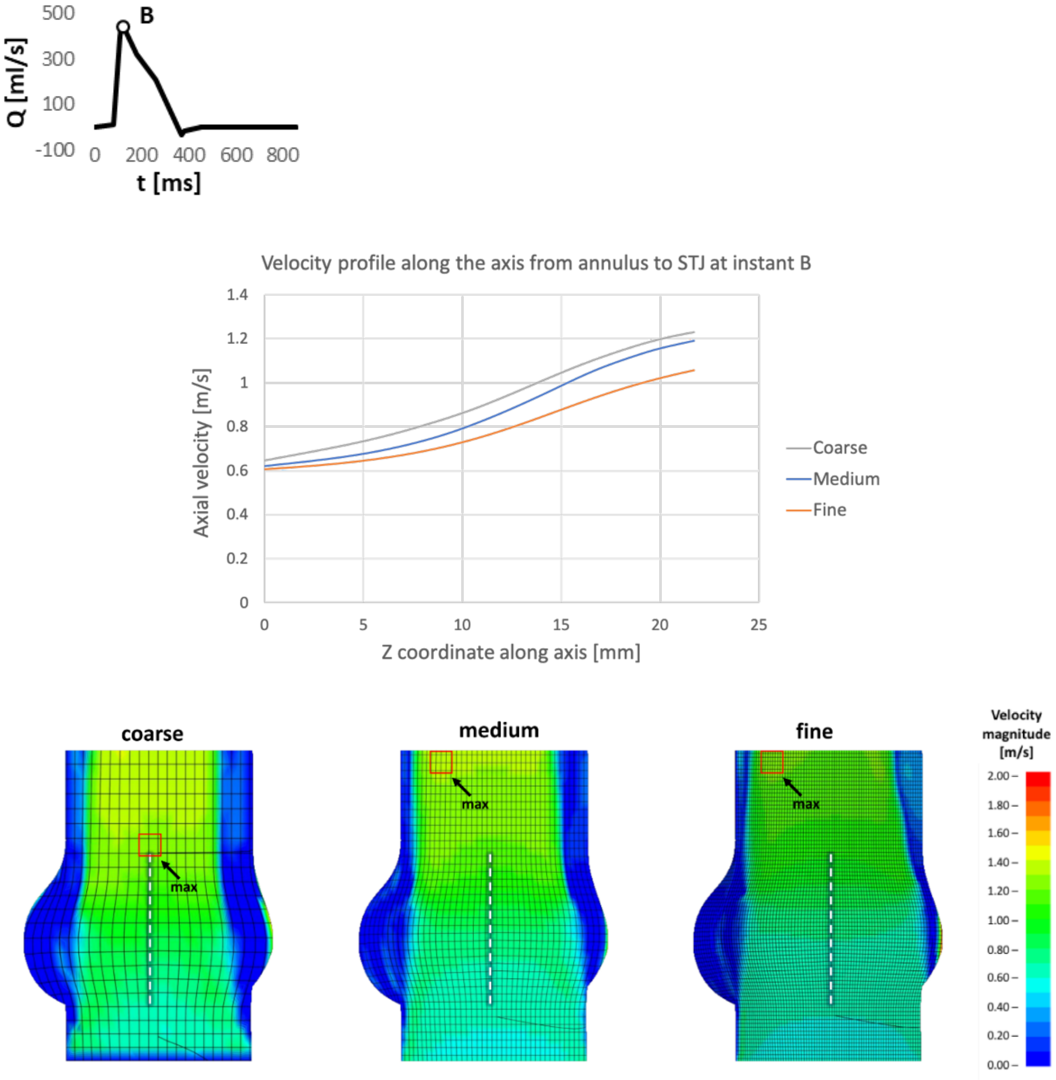

Figure 3.11. Velocity maps comparison at instant B.

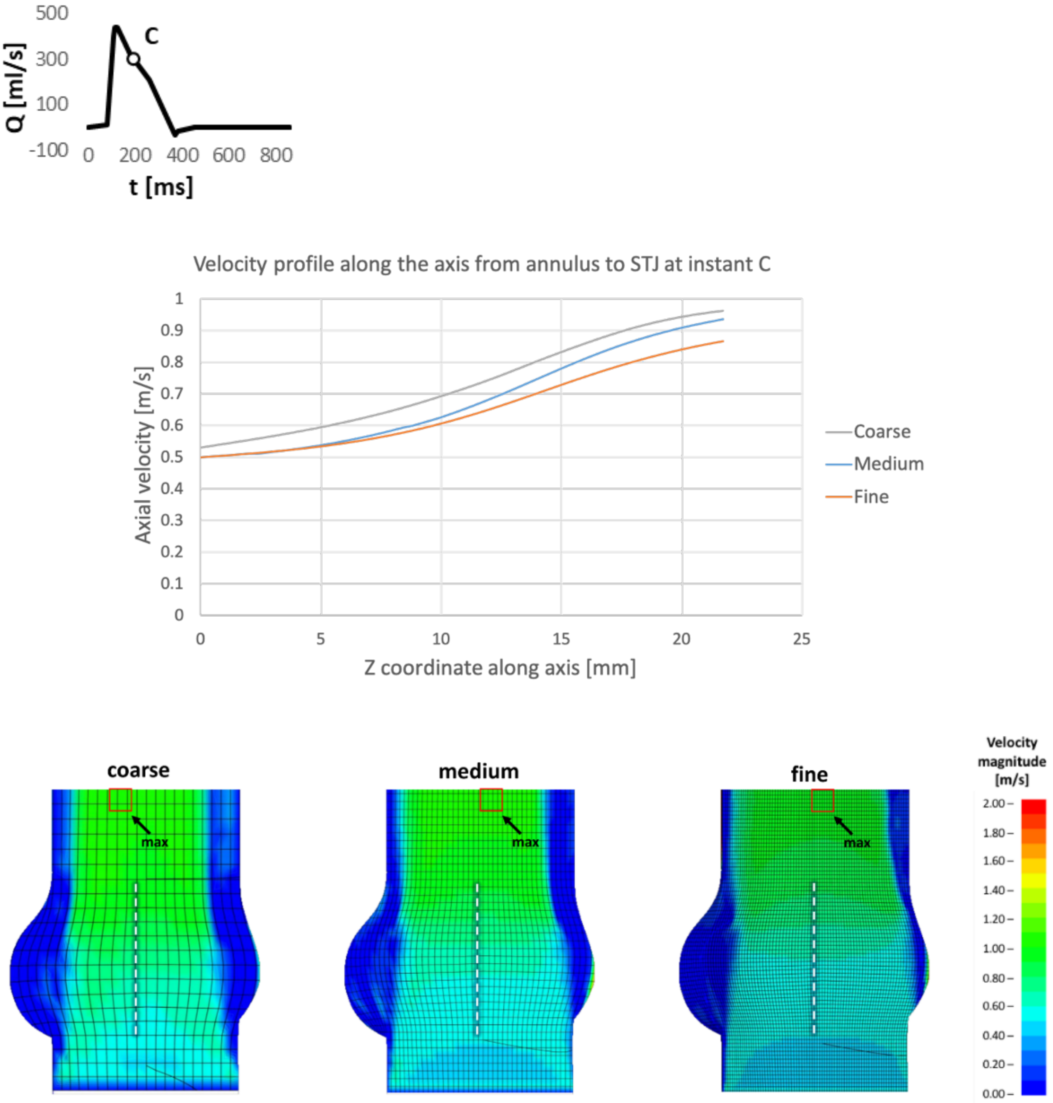

Figure 3.12. Velocity maps comparison at instant C.

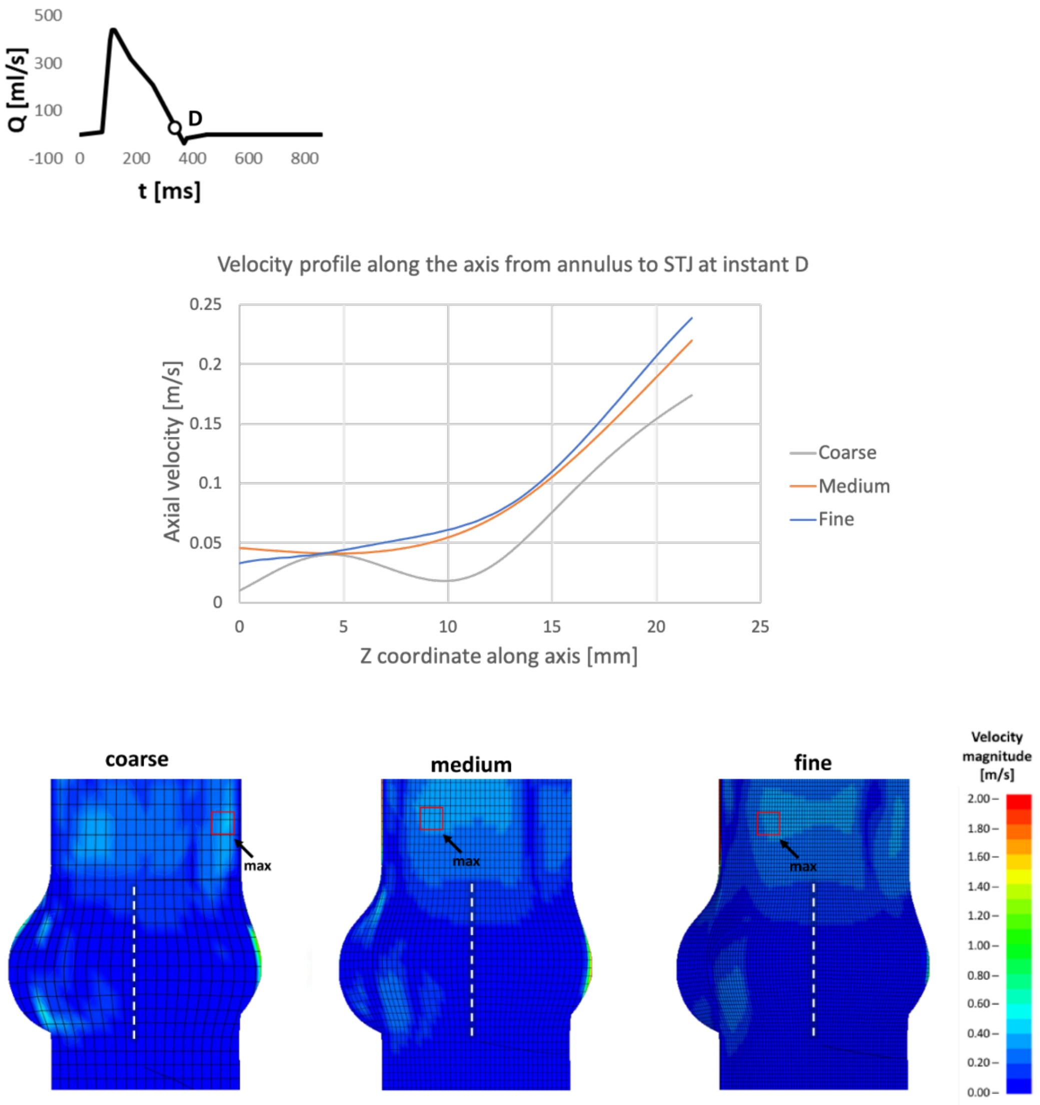

Figure 3.13. Velocity maps comparison at instant D.

From the comparison of the velocity profiles along the axis, the average discrepancy was found to vary from 0.03 m/s and 0.09 m/s between the medium and coarse mesh grid, and from 0.007 m/s to 0.08 m/s between the medium and fine mesh grid during the analysed instants of the cardiac cycle. In both cases, the average variations were less than two order of magnitudes lower than the peak systolic velocities. However, the valve in the coarse model was not able to close properly, leading to an unphysiological behavior during diastole.

The location where the maximum velocity was observed is consistent for the medium and fine meshes, confirming similar distributions, while regularly displaced for the coarse mesh.

The results were also compared in terms of maximum in plane stress experienced by the leaflets. As an example, Figure 3.14 shows distribution of the maximum in plane stress obtained at the peak of systole for the three meshes. Comparison of the stress levels for the entire cycle showed a variation in peak values between the medium and the fine mesh within 10% at the valve opening, and within 5% at the valve closure, resulting in acceptable level of grid convergence. Variation percentages of 34% and 11% were observed between the medium and coarse mesh grid at the valve opening and closure, respectively.

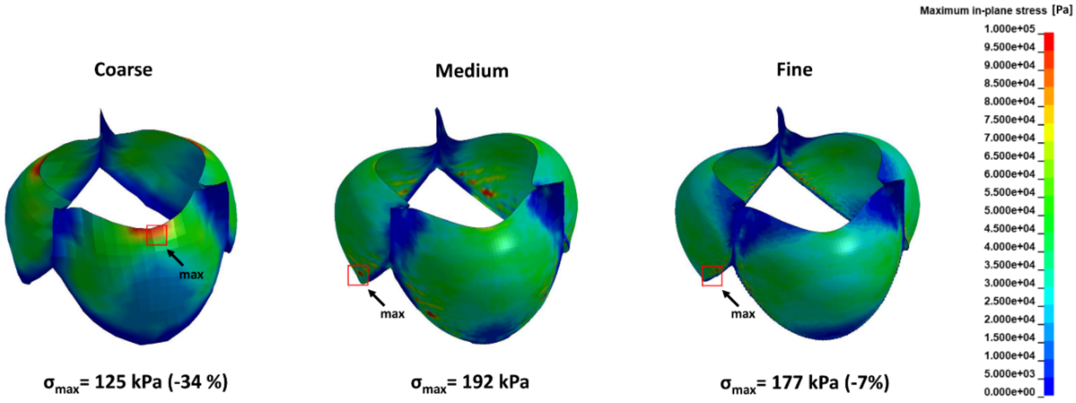

Figure 3.14. Comparison of the maximum in plane stress at the valve opening.

Hence, since the medium size mesh grid achieved an acceptable level of grid convergence, both in terms of fluid and structural parameters, this was selected to perform the study.

3.5.2 Meshing

Both the fluid and the structure were meshed using ICEM 17.0 (ANSYS, Inc., Canonsburg, PA, USA). The fluid was discretised into a structured mesh of 113,520 8-noded 1-point integration hexahedral Eulerian elements with a characteristic dimension of 1 mm which satisfied a convergence analysis (as described in section 3.5.1).

Two reservoirs were created at the level of the inlet and outlet (Figure 3.15.b), made of elements capable of supplying and absorbing fluid (Carmody et al., 2006). These were used to impose the fluids' boundary conditions, which were applied as a combination of physiological flow velocity and pressure differences, as described below. Finally, the control volume and reservoirs' mesh grids were discretised respecting the Valsalva sinuses symmetry, in order to guarantee a proper setting of the boundary conditions on the fluid domains, as recommended by Luraghi et al. (Luraghi, Migliavacca, & Rodriguez Matas, 2018).

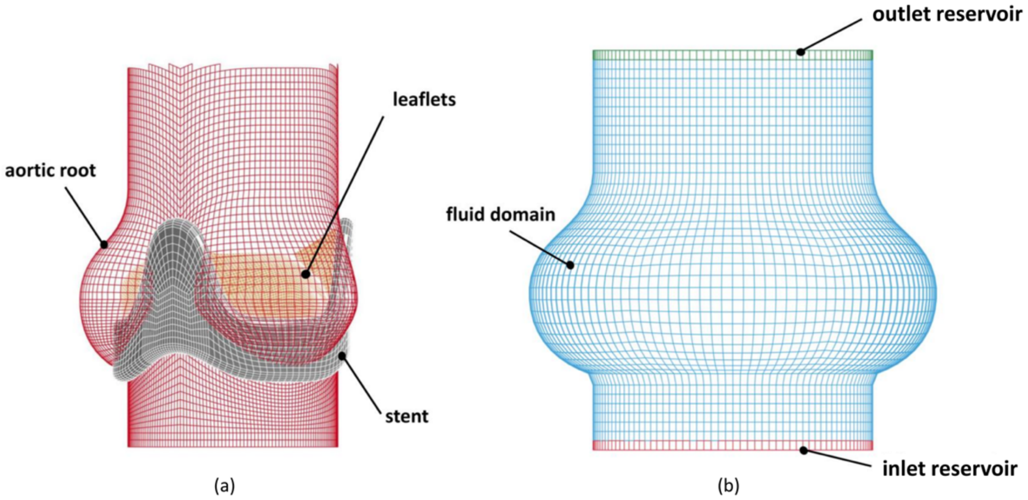

Figure 3.15. (a) Mesh of the structural components in the validation model, including the aortic root, the stent, and the leaflets; (b) mesh of the fluid domain, with the inlet and outlet reservoirs (Tango et al., 2018).

The choice of hexahedral elements was based on their superior performance in the FSI algorithm compared to tetrahedral elements, which typically lead to reduced accuracy and numerical instability during the remap phase (*LS-DYNA Aerospace Working Group Modeling Guidelines Document*, 2011).

The aortic root, the stent and the valve leaflets were discretized into 9960, 6852 and 6564 4-noded bi-linear nodal interpolation with one-point integration Belytschko-Tsay shell elements (Hallquist, 2006), respectively. Shell elements were preferred for the modelling of thin-walled structures, due to their computational efficiency compared to solid elements (Carmody et al., 2006). In fact, the ability to include several integration points through their thickness allows more accurate modelling of the bending of non-linear material models, with no significant increase in the computational time (Nobari et al., 2012).

The aortic leaflet and wall thicknesses were considered to be uniformly distributed with a value of 0.5 mm (Joda et al., 2016; Nobari et al., 2013; Sirois, Wang, & Sun, 2011) and 3 mm (Sturla et al., 2013), respectively. The attachment nodes of the leaflets were shared with the elements at the base of the Valsalva sinuses and commissural lines of the root.

The key features of each model are summarised in section 3.6.

3.5.3 Materials modelling: aortic tissues and blood properties

The leaflets mechanics is strictly influenced by its histological structure, which is composed of three layers whose main constituents are collagen and elastin fibers. Collagen fibres withstand mainly tensile loads, while the elastin plays a secondary role in resisting planar biaxial loads and is more important in returning the cusps to their unloaded shape (Billiar & Sacks, 2000). However, a material model including all these characteristics would be highly complex. Therefore, the cusps can be considered as a single layered tissue (Billiar & Sacks, 2000).

In order to validate the computational results against accurate *in vitro* studies (Toninato et al., 2016) on equivalent physical settings, the aortic root was initially modelled using a rigid material while the leaflets were modelled using a non-linear isotropic material model described by the Ogden function, with a density of 1100 $\frac{\mathrm{kg}}{\mathrm{m}^3}$.

Although due to the highly nonlinear, large deformation response of soft tissues, a standard form for the material constitutive model has been not agreed yet (Billiar & Sacks, 2000), soft tissues are usually modelled as nonlinear pseudo- or hyper-elastic materials (W. Zhang, Chen, & Kassab, 2007). Their behaviour is described by strain energy functions from which the stress-strain relationships can be derived, such as the Ogden equation. The Ogden model is an hyperelastic material model used to characterise the non-linear mechanical properties of complex materials such as rubbers, polymers, and biological tissue.

The Ogden model expresses the strain energy (W) by principal stretches (λ_α), α=1,2,3 (Guccione, J.M., Kassab, G., Ratcliffe, 2010):

$$\mathrm{W} = \sum_{p=1}^{N} \frac{\mu_p}{\alpha_p} \left(\lambda_1^{\alpha_p} + \lambda_2^{\alpha_p} + \lambda_3^{\alpha_p} - 3\right) \tag{14}$$

where μ, α and N are the materials constants.

The material constants used in the analysis were taken from a previous study (Bozkurt, Preston-Maher, Torii, & Burriesci, 2017) performed in our research group, where bovine pericardium specimens were tested and their mechanical properties were analysed and fitted using a four parameters Ogden equation with N=2; μ_1=$7.6 \cdot 10^{-6}$ MPa; $\mu_2 = 5.7 \cdot 10^{-4}$ MPa; α_1=α_2 = 26.26 (R^2= 0.981)(Figure 3.16).

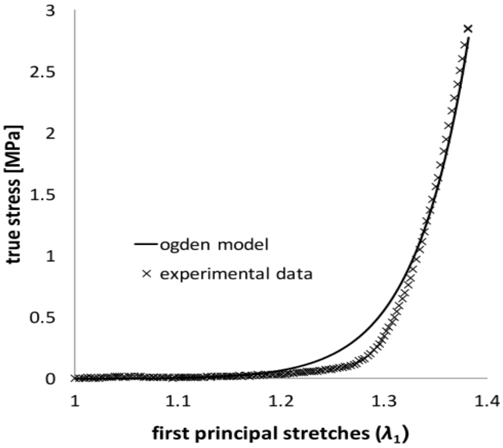

Figure 3.16. Ogden model used in the FSI analysis (Bozkurt et al., 2017).

As for the fluid modelling, the blood was assumed to be Newtonian, isothermal and incompressible with a dynamic viscosity of 0.004 Pa·s.

As stated by the ISO working group, these assumptions are legitimate since, despite blood is a non-Newtonian fluid due to its cellular content, it can be considered Newtonian in regions of high shear rates where the diameter of the vessel is quite large (Wei et al., 2018). In fact, the fluid employed in computational studies, is generally modelled as homogeneous, isothermal, incompressible, and Newtonian with blood-like properties of the density and dynamic viscosity (Wei et al., 2018).

Therefore, in large arteries such as the aorta, non-Newtonian effects are small and can generally be ignored (Li, 2004). In general, blood behaves as a homogeneous Newtonian fluid in vessels with a diameter larger than 1 mm and shear rates over 100 s^{-1} (Boulpaep, 2009; Truskey, George A., Fan Yuan, 2004).

As for the blood motion, it is still debated whether blood flow in the aorta can be considered laminar or turbulent. The pulsatile nature of the flow and the interplay between the fluid environment and the anatomical parts in the aortic vessel leads to very complex and highly unsteady, borderline turbulent flow, characterised by regions of flow reversal, three-dimensional separation and vortex formation and shedding (Yoganathan et al., 2005). The flow is defined as border-line turbulent flow because for most of the cardiac cycle it shows a very complex unsteady laminar behaviour with more than one temporal frequencies excited rather than a fully turbulent flow behaviour (Yoganathan et al., 2005). In fact, blood flow keeps laminar characteristics at all physiologically normal flow rates (Carmody et al., 2006).

3.5.4 Boundary conditions

An aortic pressure waveform was prescribed at the outlet cross section throughout the cardiac cycle, oscillating between 80 mmHg (diastolic) and 120 mmHg (systolic). For the inlet boundary conditions, the velocity flow waveform measured from the *in vitro* study used for validation (Toninato et al., 2016) was applied during systole. This enforced young healthy conditions at rest characterised by a cardiac output of 4 l/min, a heart rate of 70 bpm with 35% of systolic time, and a mean aortic pressure of 100 mmHg. Due to the proximity of the root to the ventricular chamber, which is substantially shorter than its entry length, the velocity was uniformly distributed over the inlet cross section. In order to best simulate the closing dynamics, which involves the closing leakage produced by the reversal of the transvalvular pressure difference, during diastole the velocity profile was replaced by the application of a ventricular pressure waveform, establishing the pressure drop measured during the same phase in the *in vitro* test (Toninato et al., 2016). This approach is reported to be appropriate to capture the physiological healthy valve opening-closure mechanics (Kalyana Sundaram, Balakrishnan, & Kumar, 2015). In fact, as stated by Sundaram et al. (Kalyana Sundaram et al., 2015) in a comparative study between different boundary conditions applied to a FSI analysis of the aortic valve, using a velocity controlled flow during systole, and a pressure controlled flow during diastole, on one hand, allows to capture a realistic valve closure since the valve orifice at the end of systole is obtained using a flow-driven boundary condition, and on the other, allows to overcome the limitations related to the use of pressure boundary conditions only throughout the cycle, where the valve opening is strongly dependent on the structural/inertial properties affecting the regurgitation volume measurement.

The boundary conditions applied to the fluid are summarised in Figure 3.17. Three consecutive cycles were run, discarding the results from the first cycle and using the other two to confirm that cyclic stability in the predicted flow parameters was achieved.

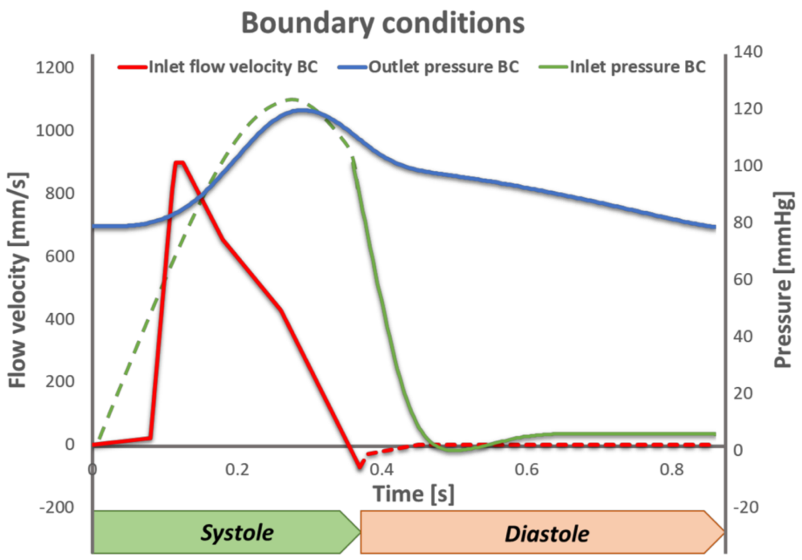

Figure 3.17. Velocity and pressure waveforms applied as boundary conditions (Tango et al., 2018).

3.6 Analysed configurations: young healthy, ageing and treated conditions

3.6.1 Pseudo physiological configuration used for validation

A preliminary computational model was created to replicate the *in vitro* configuration previously used to perform a fluid dynamic investigation of the aortic valve by means of PIV analysis (Toninato et al., 2016). This included a rigid silicone root which hosted a 29 mm Labcor (Labcor Laboratórios Ltda., Belo Horizonte, Brazil) stented porcine bioprosthesis. This surgical valve size was selected because its leaflets were of similar size to those of a native aortic valve with a 25 mm annulus (Toninato et al., 2016). In the experimental study, a groove was made in the silicone root to embed the stent and the sewing ring, thus reducing flow perturbations induced by the presence of these components. However, in order to maintain the correct position of the leaflets with respect to the aortic root, small portions of the frame remained exposed at the base of the Valsalva sinuses. In addition, the aortic chamber was rigid rather than compliant and, since it resulted unachievable to create a test fluid with the same viscosity and density as human blood whilst maintaining the required refractive index matching between the solution and the silicone root, higher fluid density than blood (1294 $\frac{\mathrm{kg}}{\mathrm{m}^3}$) had to be accepted for the blood substitute solution.

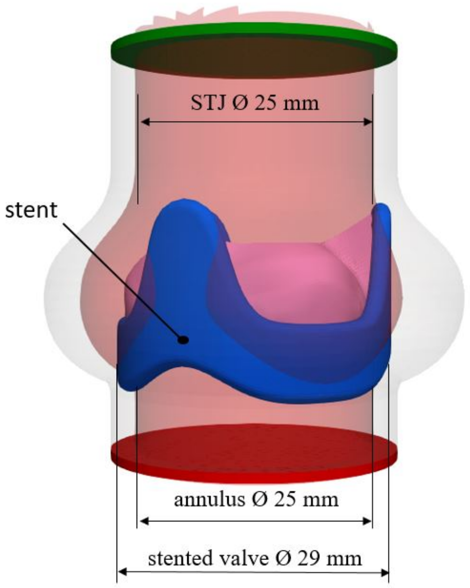

Figure 3.18. Pseudo physiological configuration computational model.

The preliminary numerical model replicated the inner surface of the idealised aortic root (without including the groove needed in the physical model to host the stent and sewing ring) and the external surfaces of the stent geometry, as measured from the physical model (Figure 3.18). Compenetration between the two components was allowed, mimicking the embedding of the stent into the groove of the mock root.

A summary of the dimensional and material properties used in the pseudo physiological configuration are shown in Table 3.1.

Table 3.1. Parameters used for the pseudo physiological configuration.

Parameters	Values
Annulus diameter [mm]	25
STJ diameter [mm]	25
Root Young modulus [MPa]	Rigid walls
Leaflets' thickness [mm]	0.5

3.6.2 Young healthy aortic valve configuration model

Once the preliminary model had been validated by comparison with the in vitro experimental data, modifications were made to provide a more accurate description of the young healthy condition. This was achieved by: a) removing the presence of the stent and sewing ring; b) including the compliance of the root walls, and c) adjusting the physical properties of the fluid, to match that of young healthy human blood. In particular, the aortic wall's material was modelled as linearly elastic, with a Young's modulus of 0.92 MPa and a Poisson's ration of 0.45. These were estimated to match the vessel compliance value of a hypercompliant young healthy aorta, as recommended in the international standard ISO 5840 (C = 0,32% / mmHg) (International Standard ISO 5840:2009) (see Table 3.2). No change was introduced in the constitutive model of the leaflets compared with the model implemented for validation. The fluid was maintained Newtonian, as this is considered acceptable by the ISO standards for the levels of shear rates and vessel diameters involved in the study (Wei et al., 2018). Its density was reduced to 1060 kg/m^3, corresponding to the standard value for young healthy human blood. The geometries and mesh of the root, leaflets and fluid domain were left unaltered (see Figure 3.19), as well as the boundary conditions prescribed to the fluid reservoirs.

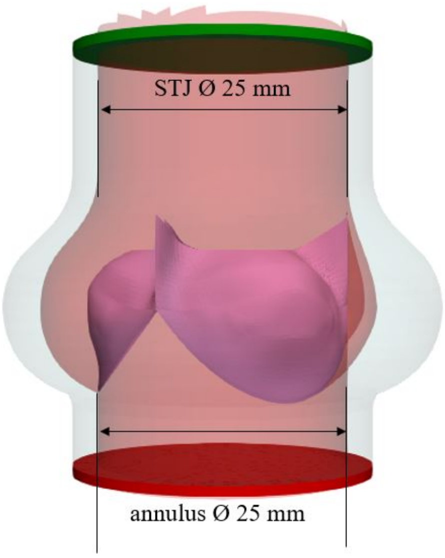

Figure 3.19. Young healthy native aortic valve configuration model.

In order to avoid a significant change in the shape of the pressurised aorta, a uniformly distributed pressure equal to 80 mmHg, directed inwards, was applied to all elements of the root wall above the leaflets attachment.

Table 3.2. Parameters used for the young healthy native configuration.

Parameters	Values
Annulus diameter [mm]	25
STJ diameter [mm]	25
Root Young modulus [MPa]	0.92 (hypercompliant aorta)*
Leaflets' thickness [mm]	0.5

*The Young modulus was estimated to match the vessel compliance value of a young healthy aorta, as recommended in the international standard ISO 5840 (C=0.32%/mmHg) (International Standard ISO 5840:2009).

3.6.3 Treated valve models: surgical and transcatheter valve implantation

3.6.3.1 Surgical model

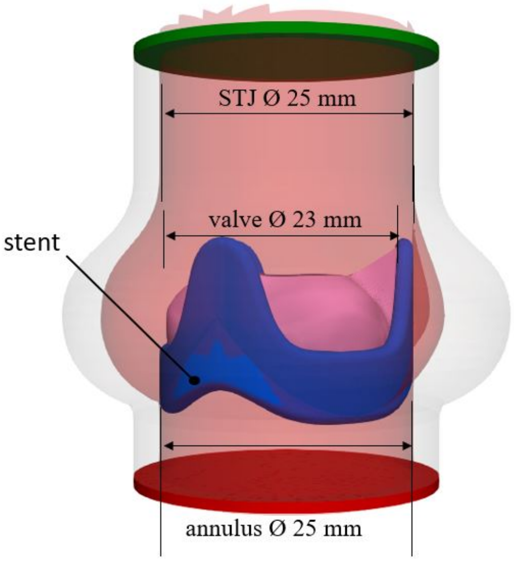

Figure 3.20. Surgical bioprosthesis configuration.

In order to investigate the impact that surgical valve replacements have on the blood flow, a 25 mm valve (including the stent, i.e. 23 mm leaflets) was placed in a supra-annular position in an aortic root with annulus and STJ diameters equal to 25 mm (Figure 3.20). Such procedure describes an optimum surgical valve implantation.

Flow parameters, boundary conditions, and mesh grids were maintained unchanged with respect to the young healthy model for both surgical and TAVI FSI analyses.

A summary of the main dimensional and material properties used in the surgical configuration are shown in Table 3.3.

Table 3.3. Parameters used for the surgical implantation configuration.

Parameters	Values
Annulus diameter [mm]	25
STJ diameter [mm]	25
Root Young modulus [MPa]	0.92 (hypercompliant aorta)*
Leaflets' thickness [mm]	0.5

*The Young modulus was estimated to match the vessel compliance value of a young healthy aorta, as recommended in the international standard ISO 5840 (C=0.32%/mmHg) (International Standard ISO 5840:2009).

3.6.3.2 TAVI model

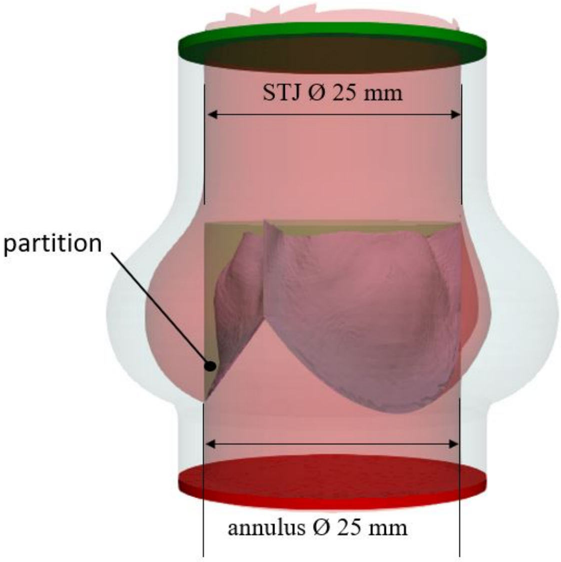

Figure 3.21. TAVI configuration.

The impact that TAVI may have on the physiological flow pattern was also investigated.

A barrier in between the operating aortic valve and the sinuses of Valsalva, representing a diseased native valve left in place after a TAVI procedure, was included into the FSI native young healthy model (Figure 3.21). This partition is an unavoidable condition introduced by current TAVI devices. This approximation is based on the configuration used by Ducci et al. in their previous studies (Ducci et al., 2016, 2013).

A summary of the main dimensional and material properties used in TAVI configuration are shown in Table 3.4.

Table 3.4. Parameters used in TAVI configuration.

Parameters	Values
Annulus diameter [mm]	25
STJ diameter [mm]	25
Root Young modulus [MPa]	3.25 (normal aorta) *
Leaflets' thickness [mm]	0.5

*The Young modulus was estimated to match the vessel compliance value of a normal healthy aorta, as recommended in the international standard ISO 5840 (C=0.09%/mmHg) (International Standard ISO 5840:2009).

3.6.4 Ageing configurations

The alterations that the ageing process may induce upon the flow dynamics were also studied. In particular, the presence of stiffened leaflets and dilation of the aortic root, were first investigated separately, in order to identify the implications related to each pathology, and then, combined together in another analysis. Such alterations are typically correlated, which is often the case in ageing patients (Crawford & Roldan, 2001; Wilton & Jahangiri, 2006).

3.6.4.1 Modelling of stiffened valve leaflets

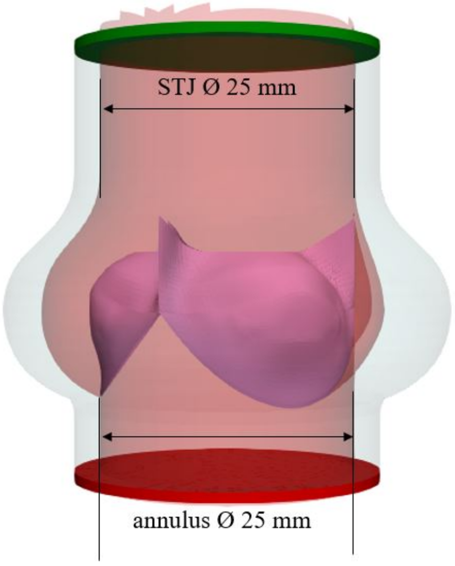

Figure 3.22. Stiffened valve leaflets configuration.

Ageing leads to degenerative changes upon the leaflets tissue which results from a complex interplay between the haemodynamics and biological processes (Bäck et al., 2013). As the disease evolves, due to the calcification process, the leaflets become stiffer and reduce their displacement, therefore resulting in a diminished EOA and in a faster forward jet (Otto, 2000). Thus, the effect induced by the presence of mildly stiffened leaflets on the global flow parameters and valve kinematics was studied.

Such condition was reproduced by doubling the thickness of the valve cusps from 0.5 mm to 1 mm (Seki & Fishbein, 2016). Flow parameters and boundary conditions were left unaltered with respect to the young healthy model (Table 3.5) for all ageing FSI analyses.

Table 3.5. Parameters used in the stiffened leaflets valve configuration.

Parameters	Values
Annulus diameter [mm]	25
STJ diameter [mm]	25
Root Young modulus [MPa]	3.25 (normal aorta) *
Leaflets' thickness [mm]	1 (Seki & Fishbein, 2016)

*The Young modulus was estimated to match the vessel compliance value of a normal healthy aorta, as recommended in the international standard ISO 5840 (C=0.09%/mmHg) (International Standard ISO 5840:2009).

3.6.4.2 Modelling of the aortic root dilation

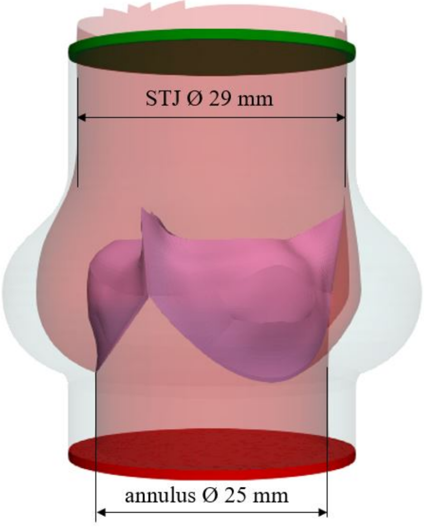

Figure 3.23. Dilated root configuration.

From previous studies it is clear how the flow conditions in the sinuses region and performance of the aortic valve change according to the aortic root geometrical shape and dimensions (Marom *et al.*, 2013; Barannyk and Oshkai, 2015; Toninato *et al.*, 2016). The progressive expansion of the aortic root and in particular of the STJ diameter, often due to ageing, strongly impairs the valve function (Maselli et al., 2007) therefore representing a potential cause of flow pattern alterations. Hence, an FSI model including an oversized aortic root was realized by linearly scaling the aortic root along each section from the annulus cross section, which was maintained at a diameter of 25 mm, up to the STJ level in order for the STJ to reach a diameter of 29 mm (see details in Table 3.6).

Table 3.6. Parameters used in the dilated root model.

Parameters	Values
Annulus diameter [mm]	25
STJ diameter [mm]	29
Root Young modulus [MPa]	3.25 (normal aorta) *
Leaflets' thickness [mm]	0.5

*The Young modulus was estimated to match the vessel compliance value of a normal healthy aorta, as recommended in the international standard ISO 5840 (C=0.09%/mmHg) (International Standard ISO 5840:2009).

3.6.4.3 Modelling of stiffened leaflets in a dilated root

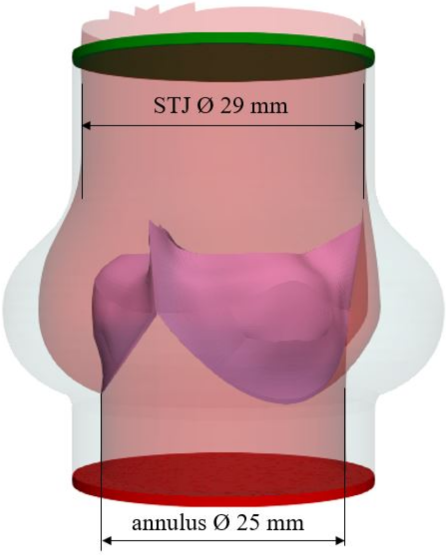

Figure 3.24. Dilated root and stiffened valve leaflets configuration.

As already pointed out, the presence of stiffened leaflets and enlarged aortic chamber, is often concomitant in the elderly. Therefore, a model combining these two features together also was implemented. The details are reported in Table 3.7.

Table 3.7. Parameters used in the dilated root and stiffened valve model.

Parameters	**Values**
Annulus diameter [mm]	25
STJ diameter [mm]	29
Root Young modulus [MPa]	3.25 (normal aorta) *
Leaflets’ thickness [mm]	1 (Seki & Fishbein, 2016)

*The Young modulus was estimated to match the vessel compliance value of a normal healthy aorta, as recommended in the international standard ISO 5840 (C=0.09%/mmHg) (International Standard ISO 5840:2009).

Chapter 4 FSI model validation

Introduction

The implantation of existing heart valve substitutes, following valvular pathologies and/or congenital abnormalities, has been shown to be correlated with alterations of the flow environment in proximity of the valve causing clinical complications (Lakshmi P. Dasi et al., 2009; Ducci et al., 2016; Falahatpisheh & Kheradvar, 2012).

Therefore, in the treatment of heart valve disease, knowledge of the flow conditions which need to be restored is crucial in order to develop an effective therapy. However, to date, understanding of the native aortic valve fluid dynamics is still relatively limited. Valvular pathologies are currently treated with the replacement of native heart valves with prosthetic devices, which are designed to mimic physiological valve operating function, even though the optimal flow conditions are not known yet.

Hence, in order to enhance the safety and efficacy of aortic valve treatments, having a clear understanding of the haemodynamics environment which regulates the heart valve well-functioning mechanism, is essential.

To augment the knowledge on this subject, a preliminary numerical model was designed to replicate a previous *in vitro* study performed by our group (Toninato et al., 2016) that, with all inherent limitations intrinsic in the experimental methodology, had attempted to model healthy physiological conditions.

For instance, the PIV system in their study did not allow the flow pattern in the entire aortic root to be captured since the presence of the stent shadowed some zones of investigation. In addition, the blood analogue did not fully match the blood properties since the fluid presented a lower dynamic viscosity and a slightly different density and the root compliance could not be taken into account. Also, being the optical system 2D and phase averaged, it could examine only a selected cross section of the aortic root, it could not identify out-of-plane structures and could not track all the cycles. However, this is, to our knowledge, the most accurate experiment focused on the aortic valve and root configuration, reported in the literature, which tries to closely match the physiological case.

The flow in that study was determined and analysed at specific instants of the systolic cycle. The experimental velocity fields obtained from this *in vitro* analysis are here used to achieve a quantitative and qualitative validation of the numerical model at the available instants, whilst a global verification of the acceptability of the computational simulation was confirmed via comparison of the effective orifice area (EOA), which is the primary parameter used in the ISO to quantify the systolic valve performance.

Hence, the experimental investigation was used as a reference to validate a 3D Fluid-structure interaction (FSI) analysis of the aortic root. The computational model provides information on the 3D flow field in the aortic valve overcoming experimental limitations and therefore achieving a more comprehensive understanding. In this scenario, a reliable numerical analysis such as FSI, can be used as a reference to identify what should be expected in terms of young healthy conditions.

The model was validated with equivalent physical settings, in a pulse duplicator replicating the physiological flow and pressure experienced in the left heart chambers. Numerical results were validated against experimental 2D velocity fields obtained by using PIV along with other valve hydrodynamic performance indicators.

Once validated, the numerical model could then be modified to eliminate the limitations and artefacts present in the experimental study, providing a more accurate description of the physiological aortic root haemodynamics (see Chapter 5).

The results presented in this chapter have been previously published in the Journal of Cardiovascular Engineering and Technology (Tango et al., 2018).

4.1 Results

An FSI analysis simulating the blood flow in the aortic root and aortic valve was performed. The model replicated the *in vitro* set up employed during the PIV investigation of an idealised physiological configuration of the aortic root and valve (Toninato et al., 2016), which included a 29 mm stented bioprosthetic valve with an annulus diameter of 25 mm and a rigid silicone root with a sino-tubular junction diameter of 25 mm and a groove to host the valve stent and suture ring.

Results were analysed using Ls-PrePost 4.3 and Paraview 5.4.1 post-processing software. The data from the last of the three simulated cycles of the numerical model were used to extract the velocity contour maps and corresponding velocity vectors.

The velocity fields of a sagittal section of the aortic root from the numerical study, matching the section analysed in the *in vitro* study, were compared against experimental measurements obtained at the four different instants of the cardiac cycle investigated with PIV in the *in vitro* experiment. As shown in Figure 4.1, the time instants considered corresponded to the following flowrate conditions: maximum increasing flowrate (instant ‘A’), peak flowrate (instant ‘B’), maximum decreasing flowrate (instant ‘C’) and end of systole zero flowrate (instant ‘D’).

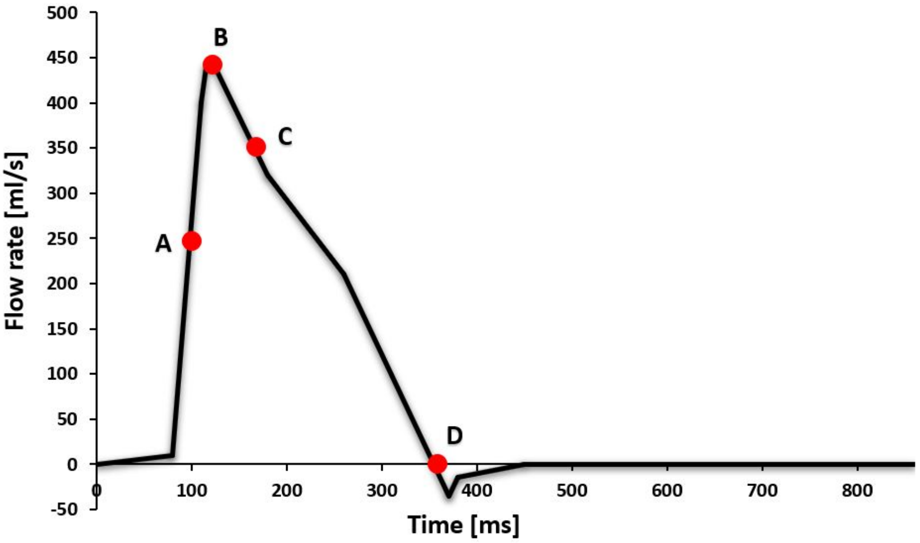

Figure 4.1. Diagram of the flowrate versus time during a heart cycle with the highlighted instants where the results were analysed.

The numerical velocity fields at each instant were qualitatively compared and validated against those obtained from the experiment, focusing on the flow distribution, direction and magnitude in the sinuses and central jet, as well as on the presence, development, size and (where applicable) direction of vortices and stagnant regions.

A quantitative validation was carried out by comparing the evolution, with respect to time within each cycle, of the velocity across the full field. The experimental data were plotted together with their standard deviation to take into account the cyclic variation of the velocity fields.

For further quantitative validation the downstream velocities across the root diameter aligned with one of the commissures, at the height of the STJ, were extracted from both studies and compared (for the *in vitro* analysis, the standard deviation was included).

The EOA was used as a quantitative parameter describing the global hydrodynamic performance across the whole simulated cycle for both the experimental and numerical analyses. Based on the international standard ISO 5840 recommendation (International Standard ISO 5840:2009), this is estimated as:

$$\mathrm{EOA} = \frac{q_{v_{RMS}}}{51.6\sqrt{\frac{\Delta p}{\rho}}}, \tag{15}$$

where $q_{v_{RMS}}$ is the root mean square forward flow during the positive differential pressure period, expressed in ml/s; Δp is the mean pressure difference measured during the positive differential pressure period, expressed in mmHg; and ρ is the density of the test fluid, expressed in g/cm^3 (Gorlin & Gorlin, 1951). Hence, this parameter takes into account both the flowrate and the transvalvular pressure difference during the entire systolic phase.

4.1.1 Qualitative comparison

The velocity fields of the sagittal aortic root cross section for the preliminary numerical model and the PIV analyses are presented in Figure 4.2. Due to optical obstruction from the pulse duplicator and shadow produced by the leaflets and stent, the experimental approach only allowed PIV analysis of a limited region of the sagittal cross section (Toninato et al., 2016). This area was identified in the numerical cross section, as indicated by the areas delimited by the white dashed border line in the top row of Figure 4.2.

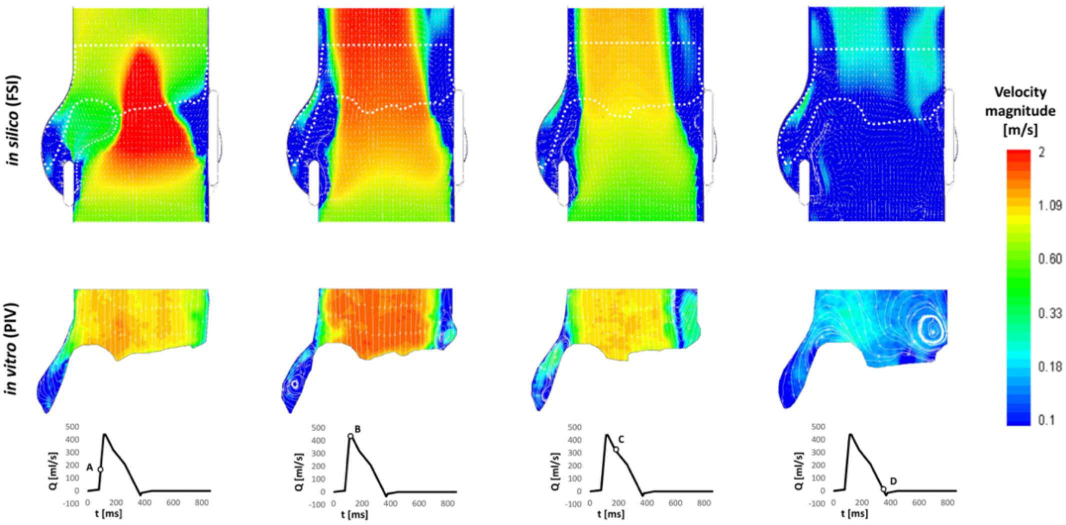

Figure 4.2. Comparison between in silico FSI and in vitro PIV of the flow velocity map and vectors fields at instants A, B, C and D of the cardiac cycle (Tango et al., 2018).

Three cardiac cycles driven by the physiological flowrate velocity at systole, and by the transvalvular pressure drop at diastole, were simulated. The data from the last cycle were used to extract the velocity contour maps and the corresponding velocity vectors.

Overall, a qualitative comparison of the PIV and FSI velocity maps magnitude and vector fields shows a good agreement between the results obtained with the two techniques. Small discrepancies may be due to the leaflets design idealisation which was based on a 120-degree geometrical symmetry in the numerical analysis, whilst the valvular prosthesis employed during the experiments presented some degree of asymmetry in the leaflets.

Furthermore, as already pointed out, computational techniques such as FSI, can expand the findings from experimental studies. In fact, the PIV experiments did not allow to investigate the flow both inside and outside the heart valve, while FSI data offered a 3D complete view of the haemodynamics within the aortic valve region.

4.1.2 Quantitative comparison

A quantitative comparison based on the peak component of the velocity across the analysed region at the same instants of the cardiac cycle across the two models is presented in Figure 4.3.

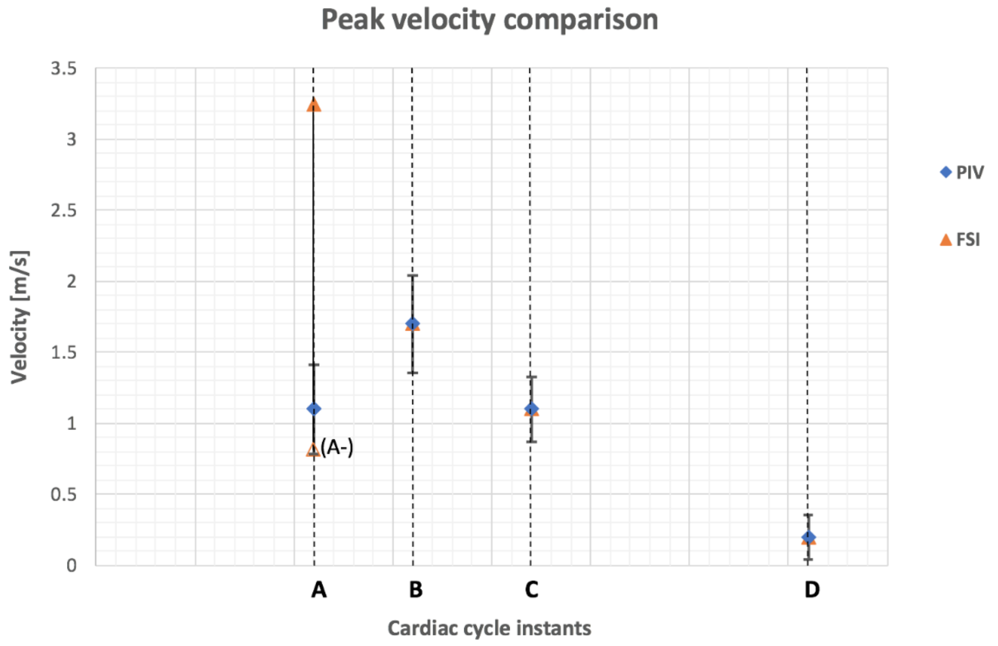

Figure 4.3. Comparison of the peak axial between the two models. The standard deviation of the PIV data is displayed as the error bar.

At instant ‘A’ in Figure 4.2, i.e. when the velocity reaches its maximum increase at the beginning of the valve opening, the main flow features of the FSI analysis are characterised by a diverging flow, supporting the opening of the leaflets, and a narrow, centralised fast jet flow with peak velocity of 3.2

m/s, compared with a broader jet and a peak velocity magnitude of 1.1 ± 0.31 m/s for the PIV study in the equivalent region (Figure 4.3).

Due to the discretisation of the numerical study, the exact time equivalent of instant 'A' from the *in vitro* study falls between two timesteps from the computational simulation. The peak velocity identified as 'A-' in Figure 4.3 indicates the peak velocity from the earlier instant, whilst the faster peak velocity marked as A in the chart represents the following instant.

At peak systole (instant 'B' in Figure 4.2), the valve cusps expand into the sinuses, the central jet deflects towards the sinus side of the aortic wall, and two slow flow recirculation zones develop at the proximal and distal outflow side of the leaflet, in both the numerical and in vitro models. A recirculation also forms above the commissure, maintaining this location throughout systole. A maximum ejection velocity of 1.7 m/s measured inside the vena contracta (the minimum diameter of the fast central jet) of the numerical model matches the value of 1.7 ± 0.34 m/s taken from the in vitro model (Figure 4.3). At a smaller scale, the distribution of fluid velocity in the sinus is also similar between the models, with a region of relatively high flow at the top of the sinus adjacent to the root wall. When the flow undergoes maximum deceleration (instant 'C' in Figure 4.2), the vortical structures formed in the sinuses are still present in both models, whilst the jet flow, with peak velocity of 1.1 m/s in the computational analysis correlating with 1.1 ± 0.23 m/s in the experimental study, and the jet flow still angles towards the sinus side root wall. A comparable width of slow and return flow is evident on the commissure side of the root, with a similar diameter central jet flow across both investigations. The sinus flow distribution is again similar in the overlapping velocity fields of the two analyses, with the faster sinus flow concentrated in the upper region alongside the root wall (Figure 4.2).

At the end of systole (instant 'D' in Figure 4.2, the two recirculations previously observed in the Valsalva sinus and above the commissure move towards the axis of the aorta in both the in vitro and in silico analyses. Again, the peak axial velocity of the numerical model, 0.2 m/s, matched the equivalent data from the in vitro investigation, 0.2 ± 0.16 m/s (Figure 4.3).

Further quantitative comparison was carried out by correlating the velocity profiles of the *in vitro* and *in silico* studies at the sinotubular junction, as shown in Figure 4.4.

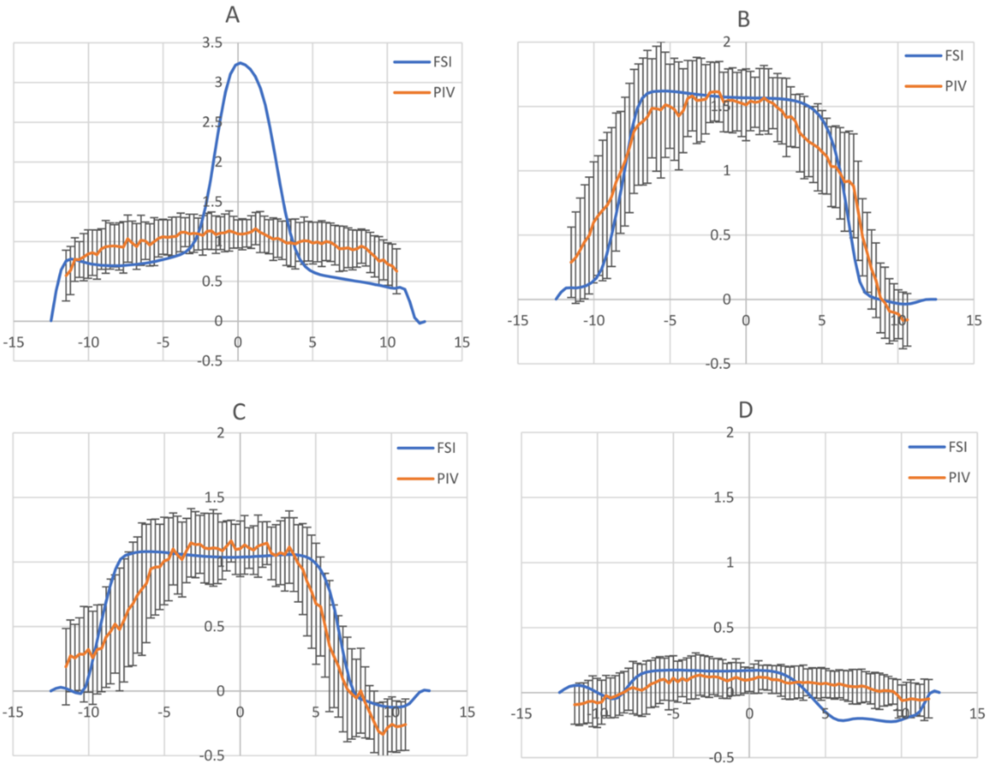

Figure 4.4. Comparison of the velocity profiles over the cross-section of the root at the Sino-Tubular junction and analysed at instants A, B, C and D of the cardiac cycle. The Particle Image Velocimetry (PIV) data includes an error bar representing the standard deviation of the measurements over 100 PIV image pairs (Tango et al., 2018).

Apart from the central jet portion of instant 'A', where the velocity ranges from 1.1 ± 0.15 m/s in the PIV analysis in contrast to a peak velocity of 3.2 m/s in the FSI analysis, the velocity profiles acquired from the numerical analysis were consistent with those from the in vitro data. For instants 'B'-'D', 90% of the velocity magnitudes across the STJ of the numerical model were within the standard deviation of the velocity measurement for the in vitro model, with 96% matching for 'B', 96% for 'C', and 77% for 'D'.

As shown in Figure 4.5, the EOA for the numerical simulation was calculated as 2.46 cm^2, in close agreement with the value estimated from the in vitro investigation of 2.43 ± 0.02 cm^2 (Toninato et al., 2016).

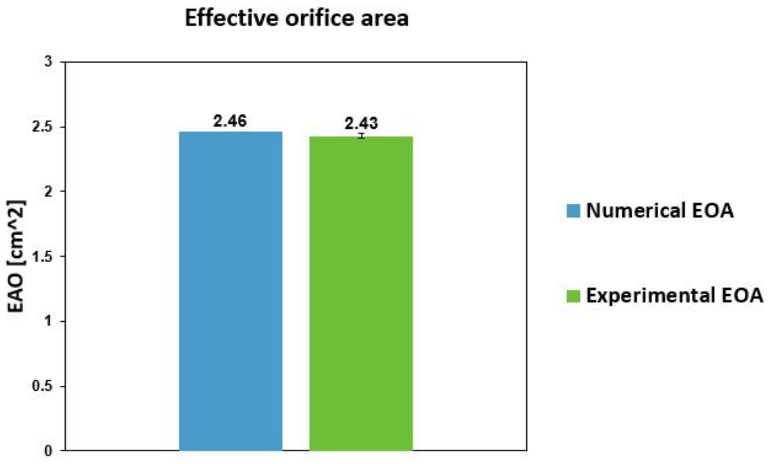

Figure 4.5. Effective orifice area graph.

Hence, the FSI analysis showed the ability to capture well the haemodynamics features already detected with the experimental investigation and the computational model is validated.

4.2 Discussion

FSI methods have been used to describe the behaviour of polymeric heart valves (Luraghi et al., 2017), transcatheter aortic valve implantation (TAVI) devices (W. Wu et al., 2016) and surgical bioprostheses (Hsu, Kamensky, Bazilevs, Sacks, & Hughes, 2014). However, despite the recent evolution of FSI methodologies, information in terms of haemodynamics and valve deformation within the aortic root is scarce (Chen & Luo, 2018).

Numerical studies can play a vital and illuminating role in the prediction of pathologies inducing flow alterations, offering a 3D view of the flow dynamics which is not available with experimental techniques, and therefore representing a powerful tool in therapeutic planning and the improvement of treatments for the cardiovascular system. This study demonstrates how the comparison of numerical models and experimental configurations can validate the former, leading to the production of accurate and reliable information about complex 3D flow occurring in physiological healthy conditions.

FSI is a very powerful tool which can provide information about the fluid dynamics environment in the aortic valve region, the valve leaflet opening-closing kinematics, as well as register the stresses the aortic cusps are subjected to during the valve functioning. However, their reliability and applicability are hampered by several assumptions such as simplifications in terms of geometry and materials modelling which are necessary given the complexity of the investigated problem. As such, validation of FSI model is an essential step before full integration into the clinical process (Kheradvar et al., 2015).

This study was undertaken to develop a reliable FSI model which provides a more accurate description of the haemodynamics expected in idealised young healthy, treated and ageing aortic roots.

The first part of the study attempted to achieve a validation of the numerical approach by comparing the relevant features with corresponding PIV experimental measurements. Although 2D PIV has previously been used for the validation of computational studies of mechanical (L. P. Dasi, Ge, Simon, Sotiropoulos, & Yoganathan, 2007; Guivier-Curien, Deplano, & Bertrand, 2009) and polymeric heart valves' behaviour (Sigüenza et al., 2018), the reliability of FSI models of biological valves has generally been established by comparison of the valve opening and closing time with *in vivo* measurements (Mao et al., 2016; Nobari et al., 2012; Ranga et al., 2006) or by comparing the resultant global flow features with previously published *in vivo, in vitro* and computational data (Cao, Bukač, & Sucosky, 2016). Where suitable *in vitro* experimental data have been available, the validity of the numerical analyses was supported by visual comparisons of the leaflets' position or angular displacement throughout the cardiac cycle (Carmody et al., 2006; I. K. Dumont, 2005; Kemp et al., 2013; Sodhani et al., 2017).

In this study a more comprehensive validation, based both on quantifiable haemodynamics parameters and PIV findings, was performed to ascertain the reliability of the numerical results obtained with the preliminary model. This was fulfilled by analysing the velocity maps obtained across a section of the aortic root, comparing the peak axial velocity and the velocity profiles at the STJ for 4 different instants in the systolic cycle, along with qualitative evaluation of the flow patterns at these instants. EOA was also acquired as a global hydrodynamic valve performance parameter for both techniques, enabling further quantitative comparison.

As also reported by (Sigüenza et al., 2018), achieving a satisfactory validation was not trivial, and involved the tuning of numerical parameters, such as the mesh grid resolution of the fluid and structure, the number of coupling points within the fluid-structure coupling definition, and the setting of appropriate algorithms able to contain the excessive distortion of the elements.

The qualitative and quantitative comparisons indicate a generally good agreement, confirming the consistency and periodicity of the results. The results were also closely matched in terms of EOA. The largest discrepancies were obtained for the velocity fields at instant 'A', corresponding to the opening of the valve, where a significant mismatch could be observed, though limited to the central region of the flow. This can be attributed to the fast dynamics that characterises this phase of the cycle, for which any slight difference in the instant analysed may result in significantly different configurations. As a consequence, the two investigations for instant 'A' do not necessarily analyse the same degree of valve opening in the two studies. The higher velocity central flow observed in the computational analysis is due to the development of an initial orifice at the centre of the valve, which can be observed for the first time at this timestep. On the contrary, the velocity distribution from the *in vitro* result suggests that this stage has not been reached yet. Analysing the timestep before that presented as instant 'A', indicated by the datum designated as 'A-' in Figure 4.3, resulted in a velocity distribution with no central jet, and lower magnitude than that of the experimental study, confirming that the numerical model was, in fact, reproducing similar flow dynamics to the *in vitro* model, but the timestep did not enable the display of the same exact instant from the experimental investigation. Differences may also result from the phase averaging over 100 cycles in the PIV study (Toninato et al., 2016), wherein variations between cycles (e.g. different extents of valve opening) could lead to a broader and less intense central jet than in the numerical study.

In summary, the preliminary FSI model showed the ability to reproduce and capture the haemodynamics features detected in the experimental investigation, especially once valve opening has been completed.

Chapter 5 Young healthy conditions

Introduction

The validated FSI model was then used to describe realistic young healthy, ageing (Chapter 6) and post-treatment situations (Chapter 7), supporting a better comprehension of the phenomena that participate in the correct valve functioning and serving as a benchmark to identify the changes produced by specific pathologies and treatments.

Therefore, the validated numerical framework was altered by removing the presence of the stent and adjusting the physical properties of the fluid and vessel wall, to better represent the young healthy native aortic valve. Details of the properties characterising the young healthy model are presented in section 3.6.2.

The valvular kinematics and the surrounding haemodynamics environment were first investigated to provide a characterisation of the mechanism behind the young healthy aortic valve function. Hence, data from the leaflets kinematics, flow dynamics, pressure and valve hydrodynamic performance were analysed and then compared with those extracted from the ageing (Chapter 6) and post treatment models (Chapter 7).

Part of the results presented in this chapter have been previously published in the Journal of Cardiovascular Engineering and Technology (Tango et al., 2018).

5.1 Results

5.1.1 Valve kinematics: valve opening, valve closure and ejection time (ET)

The valve kinematics was characterised by measuring the radial displacement of the upper middle node of one leaflet (given the 120° symmetry of the valve model this is representative of the entire valve), throughout the cardiac cycle.

Figure 5.1 shows the radial displacement of the valve leaflets replicating young healthy conditions. A top view of the valve is shown for all relevant instants capturing the valve motion.

Three main phases can be identified when characterising the leaflets motion: a valve opening phase (t_1-t_2 in Figure 5.1), followed by a slow reduction in the opening as systole progresses towards its end (t_2-t_3 in Figure 5.1), the valve closing phase (t_3-t_4 in Figure 5.1), and the closed phase (Wendt et al., 2015).

In agreement with the ISO standards 5840 (International Standard ISO 5840:2009), the valve opening and closing times characteristics were used to analyse the valve kinematics. Hence, the valve opening time (VOT) was calculated as the time between initiation of leaflets opening and full valve opening (t_1-t_2 in Figure 5.1) the valve closure time (VCT) as the time between initiation of valve closure and full valve closure (t_3-t_4 in Figure 5.1), and the ejection time (ET) as the total time between initiation of valve opening and complete valve closure (t_1-t_4 in Figure 5.1) (Ranga et al., 2006).

5.1.1.1 Young healthy conditions

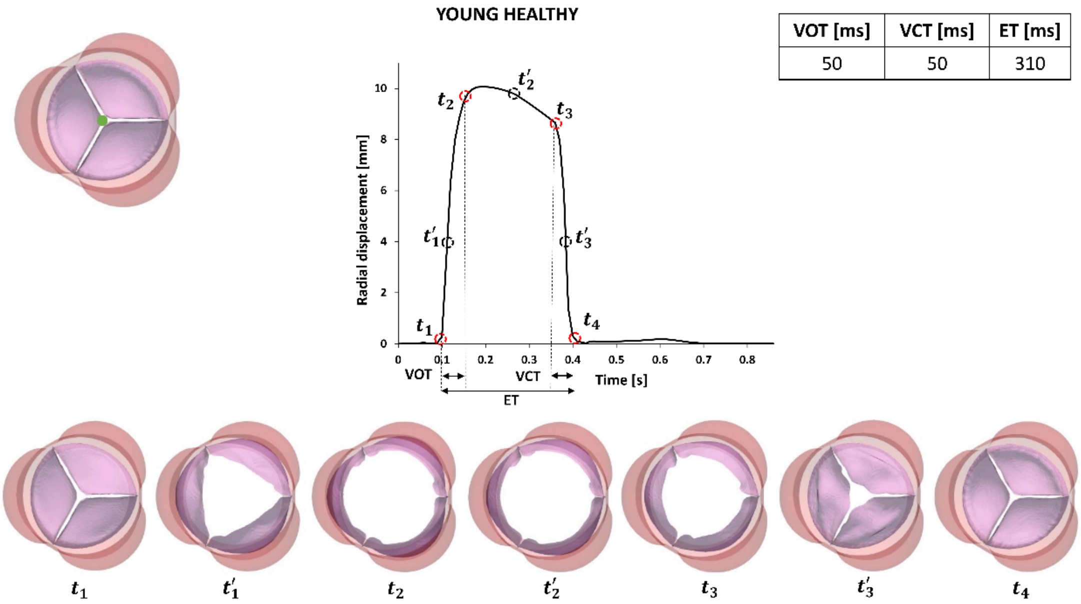

VOT [ms]	VCT [ms]	ET [ms]
50	50	310

Figure 5.1. Detailed view of leaflets kinematics throughout the cardiac cycle. The green point on the leaflet shows the location of the node where the displacement was tracked.

As indicated by (Leyh, Schmidtke, Sievers, & Yacoub, 1999), the VOT and VCTs can be obtained considering the time instants where the profile of radial displacement presents its maximum rate of increase and decrease, respectively.

In detail, the valve kinematics, represented in Figure 5.1 for the young healthy case, is characterised by four distinct phases: the opening phase, which extends from time t_1, corresponding to the instant when the leaflets separate from the closed configuration, to time t_2, corresponding to the instant when the leaflets have assumed the fully open configuration, the open phase, which extends from t_2 to t_3, corresponding to the initiation of valve closing, and the closed phase which extends from t_3 to t_4, corresponding to the time instant when the valve is fully closed.

In order to show a more detailed view of the leaflets kinematics phases, in addition to the above mentioned instants, other three instants t_1', lying in the middle of the t_1 - t_2 phase (opening), t_2', lying in the middle of the t_2 - t_3 phase (slow closure), and t_3', lying in the middle of the t_3 - t_4 phase (closure), were selected.

The calculated VOT, VCT and ET are shown in the top right corner of Figure 5.1. They were found to be consistent with *in vivo* (Leyh et al., 1999) and numerical studies (Nobari et al., 2012; Ranga et al., 2006).

Such procedure was applied also to treated and ageing configurations, in order to perform a comparison with respect to the ideal healthy case (see sections 6.1.1 and 7.1.1). Detailed graphs displaying the radial displacement and valve motion top view along with the related VOT, VCT and ET values for the other models are represented in Appendix .

5.1.2 Flow velocity

The analysis of the haemodynamics was performed by analysing the flow velocity maps and vectors in a slice bisecting one of the sinuses, and in a transverse plane at the level of the maximum diameter of Valsalva sinuses, obtained at the following instants of the cardiac cycle: systolic peak (A), end of systole (B), diastolic phase (C), end of diastole (D)(Figure 5.2).

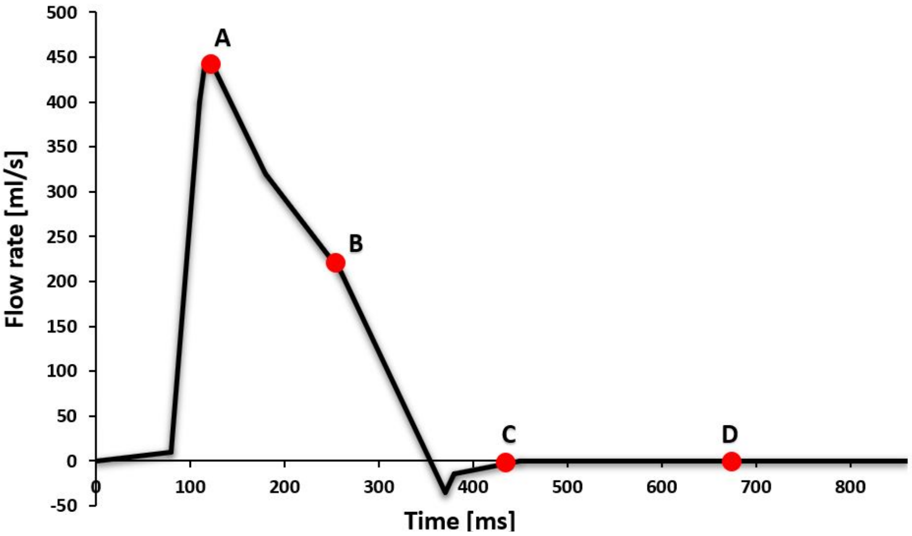

Figure 5.2. Time instants used for the analysis of the aortic valve haemodynamics.

Figure 5.3 shows the velocity contour maps and flow patterns visualised using velocity vectors across the sagittal cross section for the young healthy configuration.

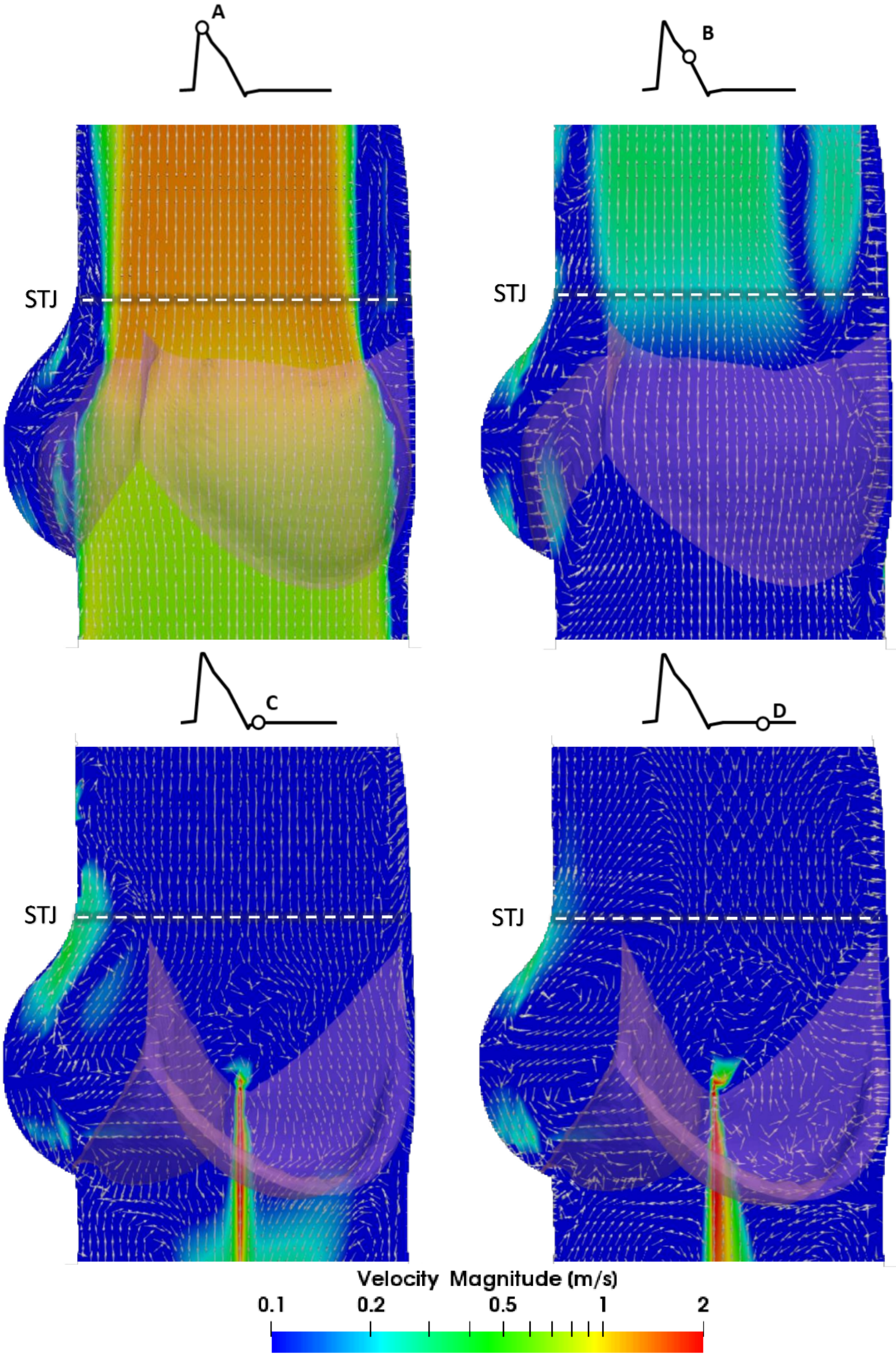

Figure 5.3. Velocity contour maps, vectors and profiles for the physiological young healthy aortic valve.

Opening is promoted by a radial component of the flow, which develops in the early systolic phase, occupying most of the Valsalva sinuses region (Figure 5.3 *instant A*).

At the systolic peak, the forward flow is pushing the valve to open, reaching a velocity peak magnitude of 1.28 m/s (Figure 5.3 *instant A*) which is consistent with other *in vivo* (Otto, 2000; Rossvoll et al., 1991), computational (Sturla *et al.*, 2013) and experimental works (R. Zhang & Zhang, 2018).

At the same time, a vortex establishes in the region adjacent to the ventricular side of the leaflets walls and persists up to the end of systole. During the ejection (Figure 5.3 *instant A*), the Valsalva sinuses provide a chamber to optimally host the reverted cusps shape by creating a suction pressure (as discussed in detail in section 5.1.3). The EOA is therefore extended into the entire aortic root cross section apart from a small region situated just above the cusps' commissures. It is important to mention how, in this case, which represents an accurate physiological healthy scenario, the function of vortical flow regions within the sinuses, is strongly debunked during the systolic phase.

At the end of systole (Figure 5.3 *Instants C, D*), the Valsalva sinuses play a primary role in promoting a centripetal flow which supports a prompt valve closing. Vortices become more evident during the diastolic phase, when two large counter-rotating recirculations, evolve, one on top of the other, and establish into the sinus, preventing blood stagnation and sealing the valve.

In order to achieve a more comprehensive insight into the flow dynamics within the aortic root, the velocity maps and vector fields were investigated also across a transversal cross section of the valve orifice extracted at the level of the aortic sinuses' maximum diameter.

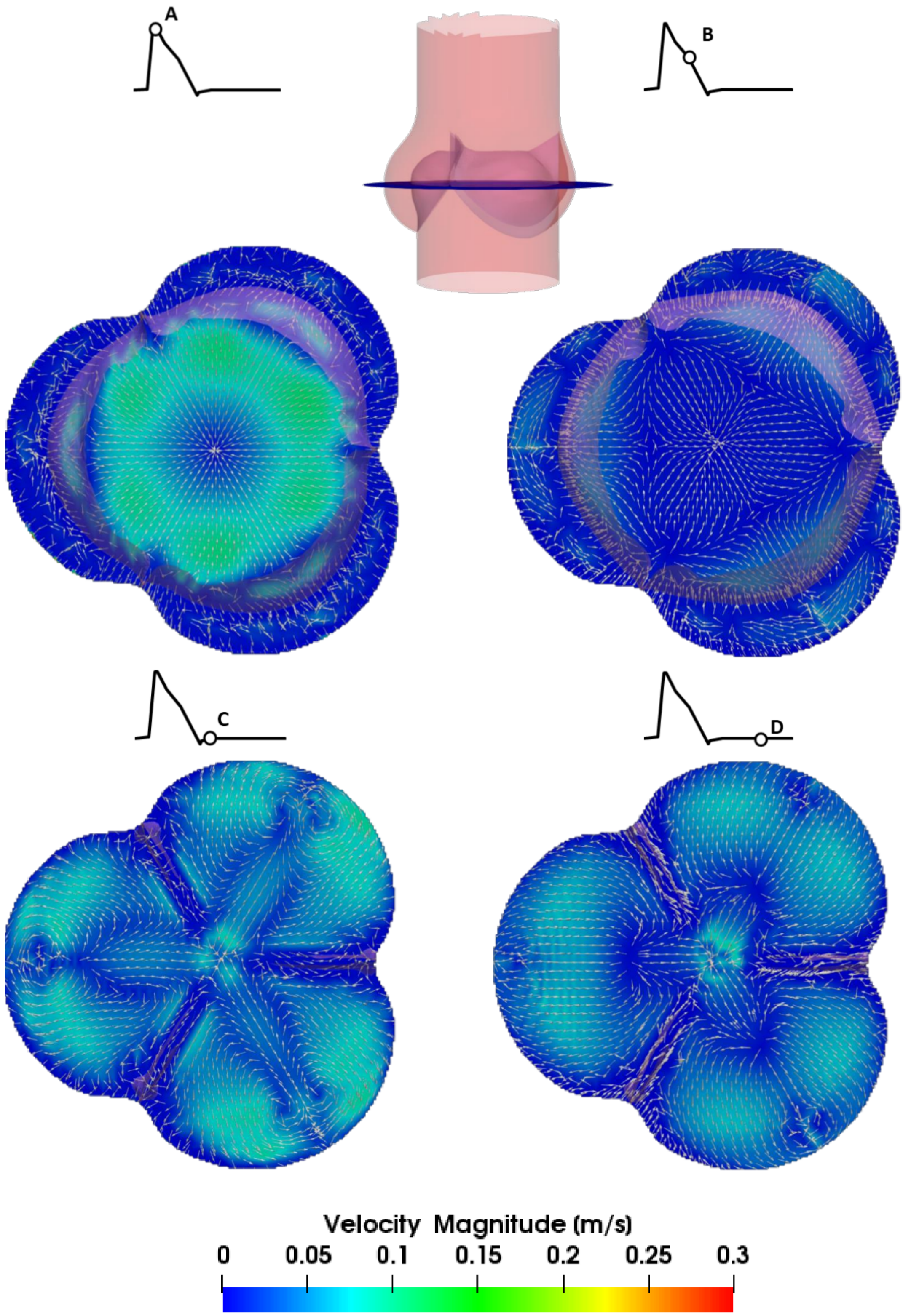

Figure 5.4. Flow contour maps and vectors across a transversal cross section of the young healthy aortic valve orifice.

During systole, no coherent rotational structures can be detected within the sinuses bulges. However, weak counter-rotating vortices can be identified close to the leaflets walls, next to the plane bisecting each sinus (Figure 5.4 *instant A*). These vortices then move towards the center of the valve leading to a triangular shape flow pattern (Figure 5.4 *instant B*). When the valve shuts (Figure 5.4 *instant C*), instead, two evident counter-rotating vortical structures establishes and expands in each sinus, persisting up to late diastole (Figure 5.4 *instant D*).

5.1.3 Pressure maps, effective orifice area (EOA) and transvalvular pressure gradient

Blood pressure distributions were examined across the same sagittal plane used to analyse the flow velocity at time frames A, B, C, and D.

Similarly to the analyses carried out in section 4.1, the Transvalvular pressure difference (ΔP) and effective orifice area (EOA) measurements were estimated for all configurations (see Eq. 13 section 4.1 for formulas). Such parameters are clinically used to assess the valve performance.

5.1.4 Young healthy conditions

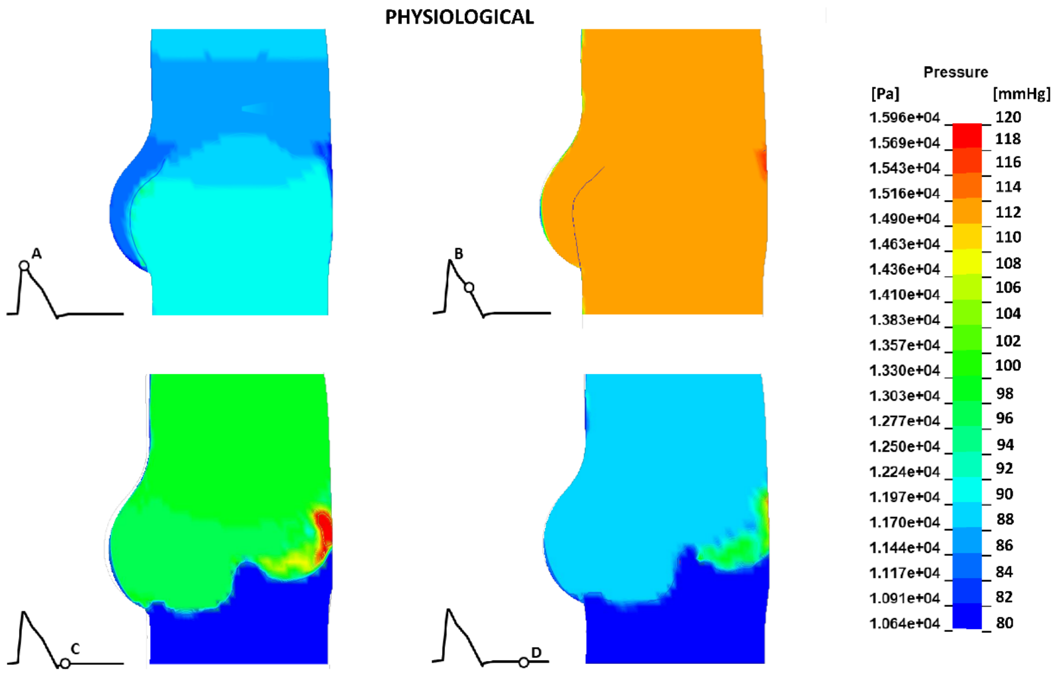

Figure 5.5. Pressure contour maps for the young healthy configuration.

The contour maps of the pressure for the physiological young healthy conditions are provided in Figure 5.5.

Consistently with the pressure waveforms prescribed as boundary conditions, at *instant A* shown in Figure 5.5, the ventricular pressure is higher than the aortic resulting in a progressively reducing pressure along the aortic root axis, whilst at late systole, when the valve is still fully open, the pressure value is almost constant in the entire aortic chamber (Figure 5.5 *instant B*). In diastole, uniform pressures can be detected downstream and upstream of the closed aortic cusps (Figure 5.5 *instants C and D*).

As shown in Figure 5.5 *instant A*, the healthy configuration promotes a mechanism which was not observed in the preliminary model (Chapter 4), nor in the literature: as the central jet increases in velocity, the flow contraction at the leaflets' tip generates a reduction in pressure which results in a suction effect in the gap between the leaflets and the sinus wall. This produces a pressure difference between the aortic outlet and the sinus area, measured of around 6 mmHg in this simulation, which contributes to further expand the leaflets towards the sinuses wall. This process, which has a stronger effect when the ejected flow becomes faster, leads to an EOA of 2.94 cm^2, therefore improving significantly the hydrodynamic valve performance. Hence, contrary to what reported in the literature, the valve efficiency seems to be dependent upon the presence of vortices but in the sense that, during systole, large recirculations within the sinus indicate a stiffened behavior of the valve cusps, and not an efficient functioning.

5.2 Discussion

Overall, the numerical simulation reproducing the native valve behaviour was able to mimic realistic physiological healthy flow conditions enabling capture of the main aortic valve fluid dynamics consistent with previous numerical studies (Carmody et al., 2006; De Hart et al., 2003; Sturla et al., 2013) and experimental studies (Ducci et al., 2016). It also identified a new feature of the blood flow: the development of a systolic vortex beside the inner leaflets' walls.

This is quite interesting since previous *in vivo* studies which reported the presence of vortices during systole, assumed that they establish between the sinus walls and aortic side of the leaflets surface, without showing the position of the cusps walls, though (Bissell, Dall'Armellina, & Choudhury, 2014; Escobar Kvitting et al., 2004; Oechtering et al., 2016). This may confirm the presence of vortices during the systolic phase of the cardiac cycle but suggest that they originate within the valve inner walls and not within the sinuses, as also observed in another study (Dimasi et al., 2012).

In particular, during systole, the young healthy leaflets protrude much deeper into the Valsalva sinuses, reducing their propensity to generate and host the recirculation areas observed in both the experimental (Toninato et al., 2016), preliminary (see Chapter 4) and surgically treated numerical models (see Chapter 7). A key function of the sinuses appears to be that of providing a chamber able to host the cusps during systole, reducing the cusps' impact on the flow through the valve. During ventricular ejection, the healthy aortic valve cusps expand very close to the vessel walls, enhancing the valve's geometric orifice area. This effect is amplified by a suction that establishes in the gap between the leaflets and the aortic wall, due to a Venturi effect induced by the fast jet flow, which is strongest at the maximum flowrate. Vortical zones, which appear to be negligible during the vast majority of the systolic cycle, become significant during diastole, contributing to prevent blood stagnation.

Further analysis of the results and discussion are provided in Chapter 6 and Chapter 7 as data from the young healthy configuration is used as benchmark to measure changes due to the ageing and post treatment conditions.

Chapter 6 Ageing effect

Introduction

Since the aim of this study is to achieve a full characterisation of the healthy well functioning aortic valve, and study the impact that ageing and prosthetic devices may have upon its efficiency, the validated FSI model was adapted to reproduce native young healthy conditions, which represent the gold standard, as well as aged and treated cases.

To analyse the effect of ageing, typical alterations associated with senility, such as stiffening of the tissues and progressive aortic root dilation (Crawford & Roldan, 2001; Wilton & Jahangiri, 2006), were studied. A detailed outline of the features characterising each configuration is presented in section 3.6.

Results obtained for the ageing configurations were analysed and compared with those of the young healthy root environment.

Therefore, consistently with what done for the young healthy configuration, leaflets kinematics, flow dynamics, pressure and valve hydrodynamic performance were investigated. Further, a brief analysis focused on blood damage factors was carried out.

The results presented in this chapter have been submitted to a peer reviewed journal.

6.1 Results

6.1.1 Valve kinematics: comparison young healthy vs ageing conditions

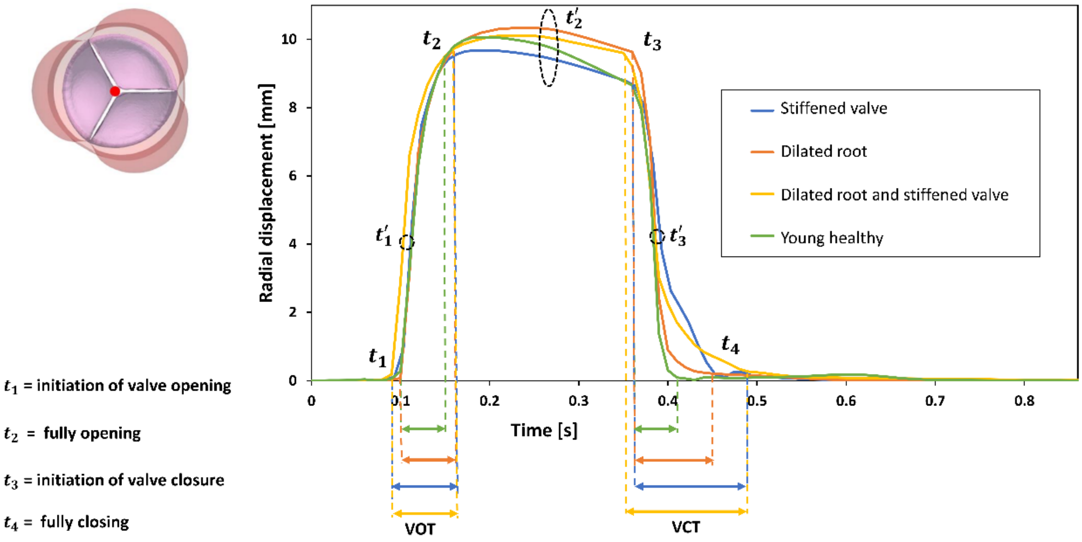

Figure 6.1. Graph used to compare the leaflets kinematics in young healthy (green), stiffened (blue), dilated root (orange) and dilated root with stiffened valve (yellow) configurations. The red point on the leaflet shows the location of the node where the displacement was tracked for all configurations.

As described in Figure 6.1 valve opening is initiated earlier for the models with stiffened leaflets whilst opening time for the dilated root configuration is synchronised with the young healthy case. However, they all present longer VOTs than the young healthy case with the valve reaching a fully open position at about 0.16 s of the cardiac cycle for all pathological conditions.

The configuration with stiffened leaflets and dilated aortic root, presents anticipated times both in early and late systole, and it is also the latest to achieve full opening and full closing, therefore resulting in the longest VOT and VCTs.

In terms of maximum radial displacement, the stiffened valve model, whose leaflets thickness is doubled with respect to healthy conditions, presents the smallest displacement (9.68 mm) with a difference in percentage of -3.79% with respect to the healthy analysis. In the other configurations, instead, a slightly wider leaflets displacement was observed. In particular, the difference in percentage compared to young healthy conditions is +2.75 % for the model with the dilated root, and +0.57% for the model with both stiff cusps and dilated aortic root. This might be explained by the presence of a larger chamber between the valve and the sinus wall due to the dilation of the aortic root, which allows for the leaflets to freely expand.

Table 6.1. Valve opening, closure and ejection times for healthy and virtually diseases configurations.

Configuration	VOT [ms]	VCT [ms]	ET [ms]
Healthy	50	50	310
Dilated root	60(+20%)	70(+40%)	330(+6%)
Stiffened valve	70(+40%)	116(+132%)	386(+24%)
Stiffened valve and dilated root	70(+40%)	130(+160%)	390(+25%)

As shown in Table 6.1, the values of VOT, VCT and ET gradually increase as the dilated aortic root model and the other configurations are considered. In particular, from the overall analysis of the pathological conditions models, it is worth highlighting how, whilst the biggest percentage difference in terms of VOT with respect to the young healthy valve case is +40 % (stiffened valve and stiffened valve in a dilated aortic root models), in terms of VCT such difference rises up drastically to a value of +160% (stiffened valve and dilated root model). Thus, the dilation of the aortic root is shown to not significantly affect the valve dynamics whilst, the presence of stiffened leaflets in the same model, results in relevant variations.

Assessment of the valve kinematics can be gained from Figure 6.2 where a visual comparison of the top view of valve displacement between healthy and ageing configurations during the most relevant time instants of the cardiac cycle, is shown. As expected, the models including a stiffened valve produce a slower valve opening, as clearly shown in instant $\mathtt{t}_1'$ (see Figure 6.2) and also present a narrower valve orifice when the valve is fully open (instant $\mathtt{t}_2$). In terms of closure, the combination of stiff leaflets and dilated root delays complete closure (see instant $\mathtt{t}_3'$ in Figure 6.2).

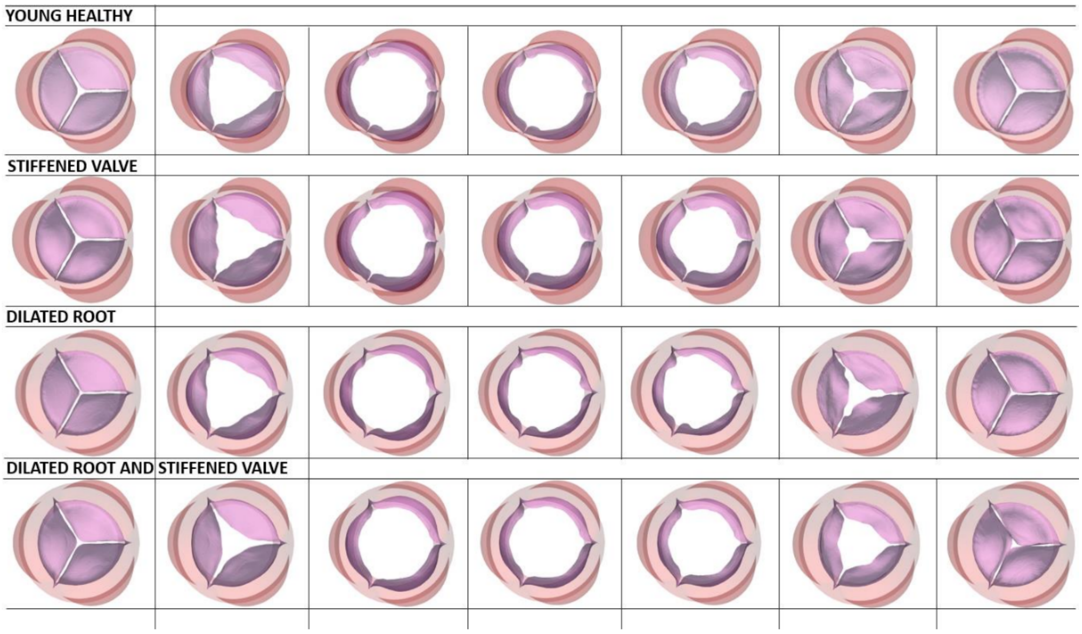

Figure 6.2. Valve top view for healthy and ageing configurations at the instants used for the calculation of the valvular kinematics parameters.

On the contrary, the model replicating a young healthy valve but anchored to dilated root walls, presents a wider opening with a shape of the cusps more similar to that of the healthy case.

These characteristics are directly associated with valve performance and therefore have an impact on the EOA and Transvalvular pressure gradients as discussed in section 5.1.3.

6.1.2 Flow velocity

6.1.2.1 Stiffened valve

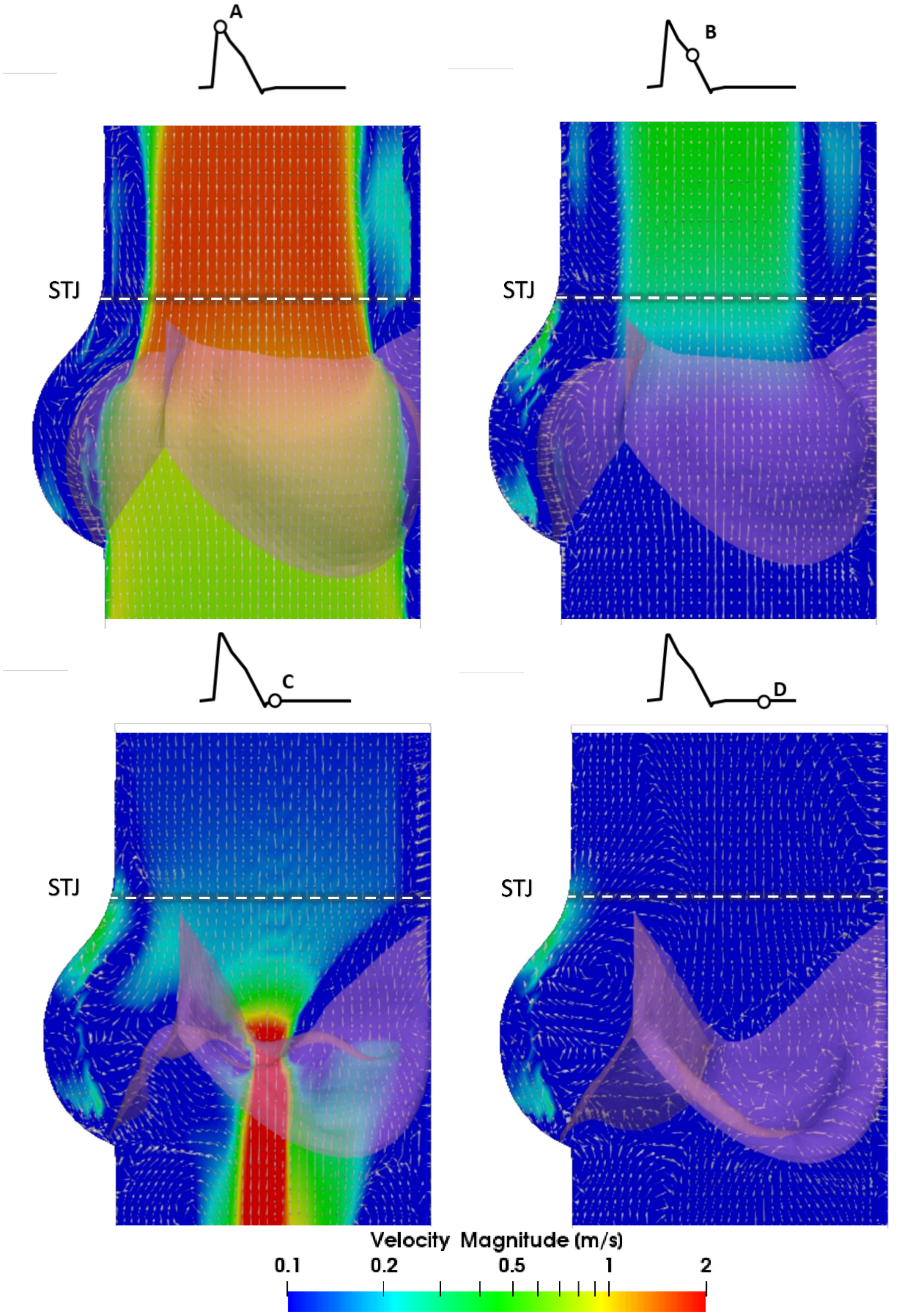

Figure 6.3.Velocity contour maps, vectors and profiles for the stiffened valve configuration.

The velocity maps and vectors extracted at the selected time instants analysed, revealed flow features mostly similar to those observed physiologically, despite the thickening of the leaflets, which was intended to replicate some mild stiffening of the valve. During the systolic peak, the valve succeeds in reaching a completely open configuration. However, as expected in case of stenotic valve (Bäck et al., 2013), the velocity magnitude of the jet (1.53 m/s) is higher than in the healthy case by a percentage of 19.5%. This suggests that in presence of mild stiffening, the valve opening is not considerably affected but the increased valve resistance due to leaflets stiffening causes an increase of the peak velocity.

In terms of flow pattern, as observed in the analysis of the young healthy valve, no recirculations can be observed within the sinuses bulges however, vortices can be detected at the leaflet tip and next to the ventricular side of the leaflet walls (Figure 6.3 *instant A*). They persist up to the end of systole, when large vortical structures establish within the sinuses supporting leaflets closure and eventually pushing the valve to shut at the end of diastole (Figure 6.3 *instant B*). Hence, as already pointed out, the haemodynamics seems to be consistent with the ideal conditions, however the stiffening of the cusps results in significantly longer opening and closing phases.

Velocity magnitude is slightly higher with respect to physiological healthy conditions also across the transversal cross section of the aortic sinuses (Figure 6.4). Herein the flow patterns are coherent with the young healthy case, even though the size of the vortices present in diastole is strongly reduced.

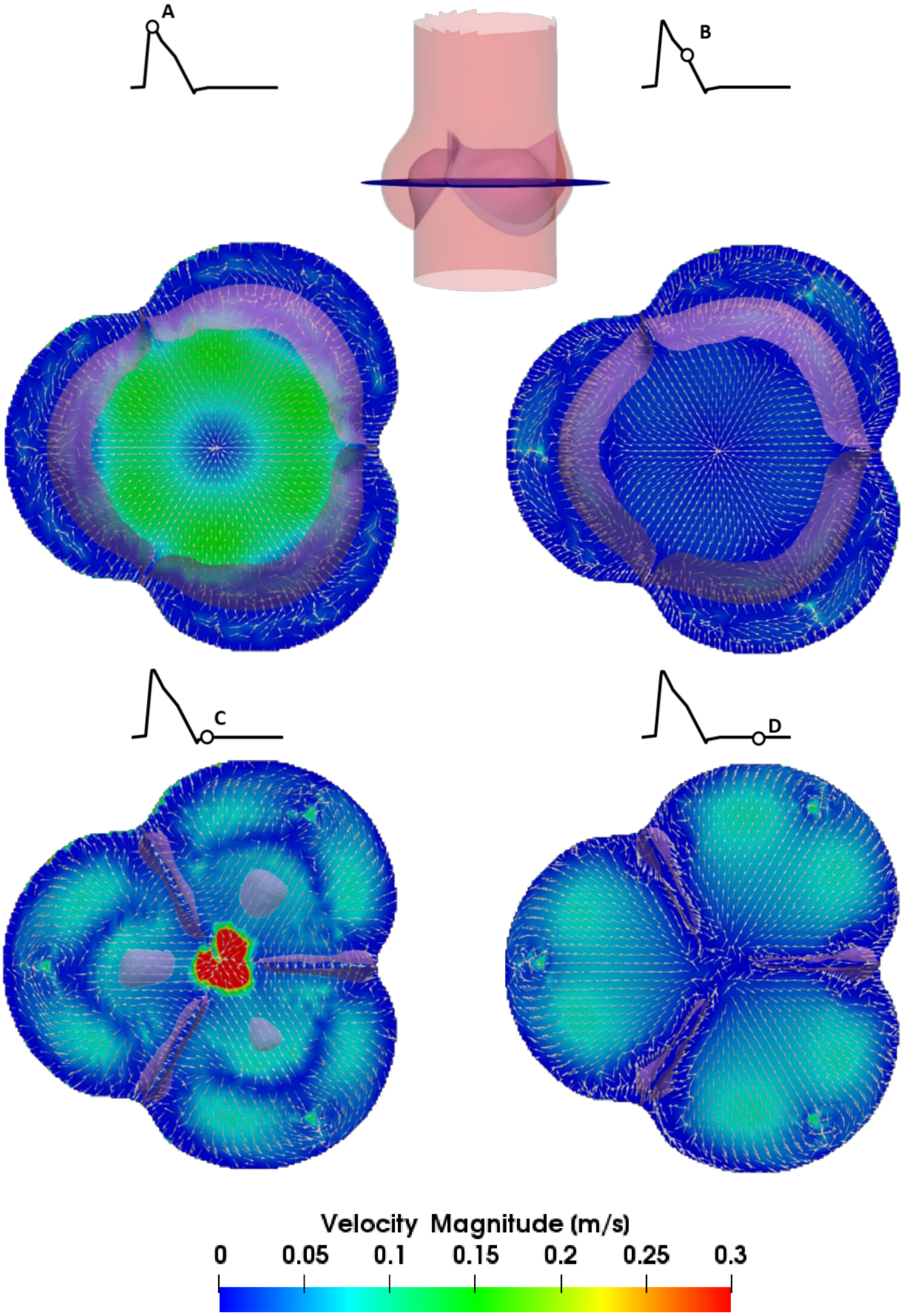

Figure 6.4. Flow velocity maps and vectors across a transversal plane of the stiffened valve orifice.

6.1.2.2 Dilated root

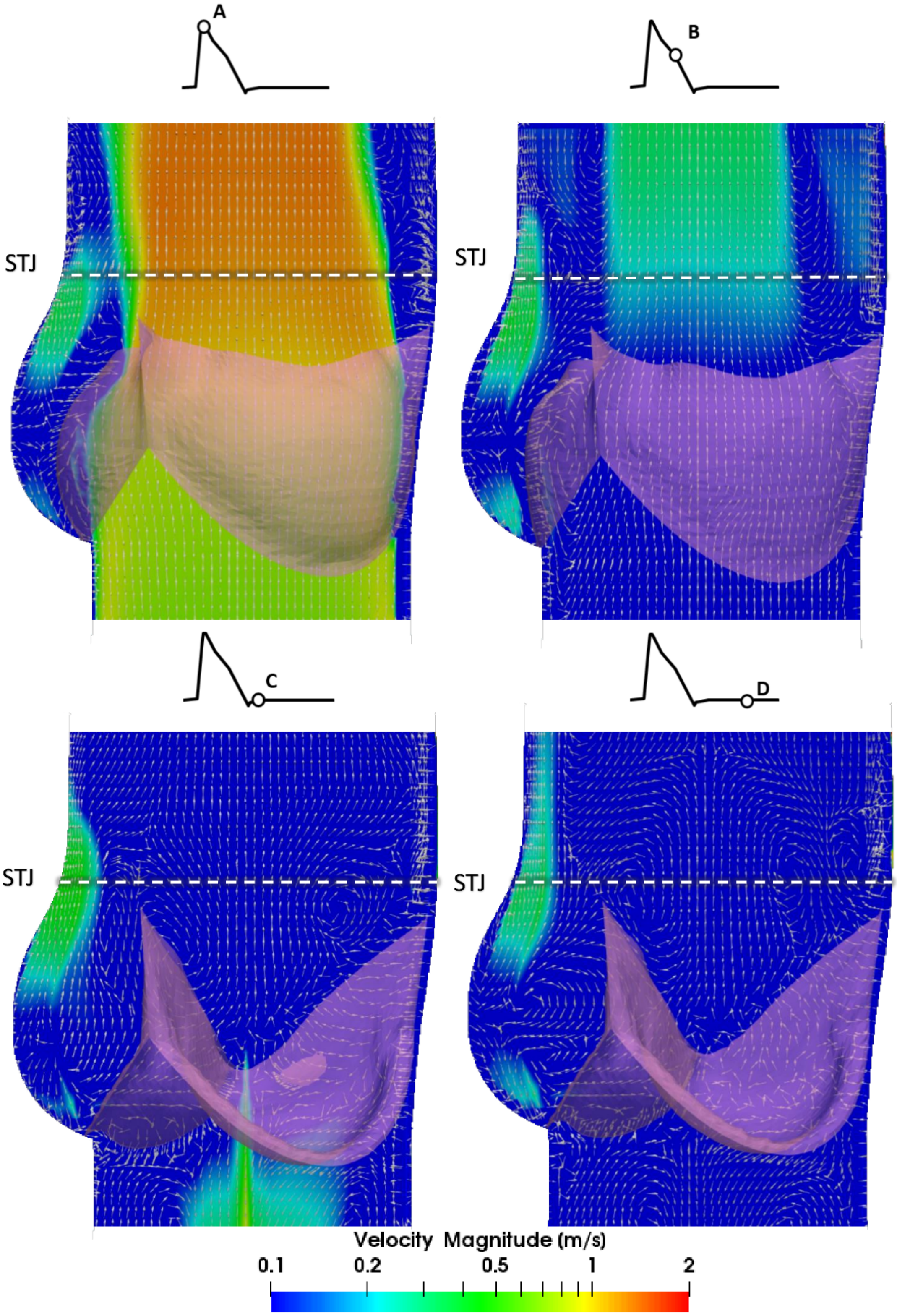

Figure 6.5. Velocity contour maps, vectors and profiles for the dilated root configuration.

In the model representing a dilated aortic root, the leaflets undergo a much wider opening, this is likely to be due to the presence of longer leaflets' edges and larger chamber between the valve and the sinus wall.

The systolic recirculations observed for the young healthy case within the leaflets internal walls are also present herein; the maximum velocity of the slightly angulated forward flow at the systolic peak is 1.24 m/s, lower by 3.1% with respect to young healthy conditions. Larger and more structured vortices than in the young healthy configuration can be identified, in particular in the top regions of the sinuses. Recirculations at the walls are so large that, although the root is much wider, the jet is significantly narrowed, with consequent reduction of the EOA (*instant B* of Figure 6.5).

In diastole, two vortical structures can be observed in *instant C* of Figure 6.5 which then split into multiple smaller vortices in *instant D* of Figure 6.5. These structures allow blood washout within the aortic root.

It is worth to notice how, despite the expansion experienced by the root, the model maintains the main features of a physiologically functioning valve.

The analysis of the flow in a transversal plane at the level of the sinuses (Figure 6.6), shows that the vector field matches closely young healthy physiological data, with recirculations arising in each half of each sinus (Figure 6.6 *instants A,B*); the velocity magnitude is slightly lower, consistently with what already observed in the sagittal plane. Furthermore, similarly to the healthy case, features such as the presence of counter rotating vortices next to the plane bisecting each sinus, were also identified in this configuration (Figure 6.6 *instants C,D*).

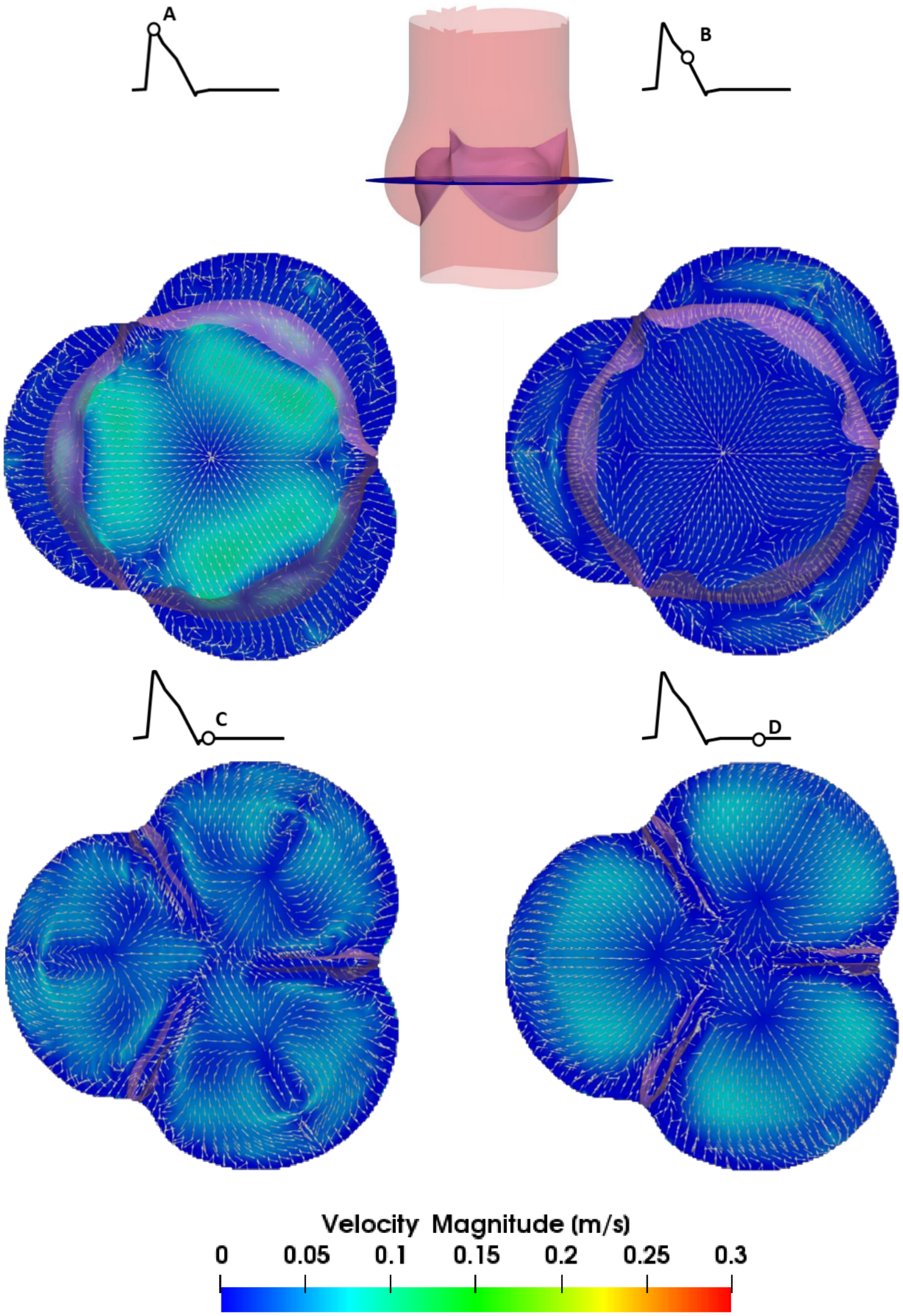

Figure 6.6. Flow contour maps and vectors across a transversal plane of the dilated aortic root valve model.

6.1.2.3 Dilated root and stiffened valve

The combined effect of leaflets stiffening and dilated root chamber on the flow downstream of the valve was investigated and is shown in Figure 6.7 .

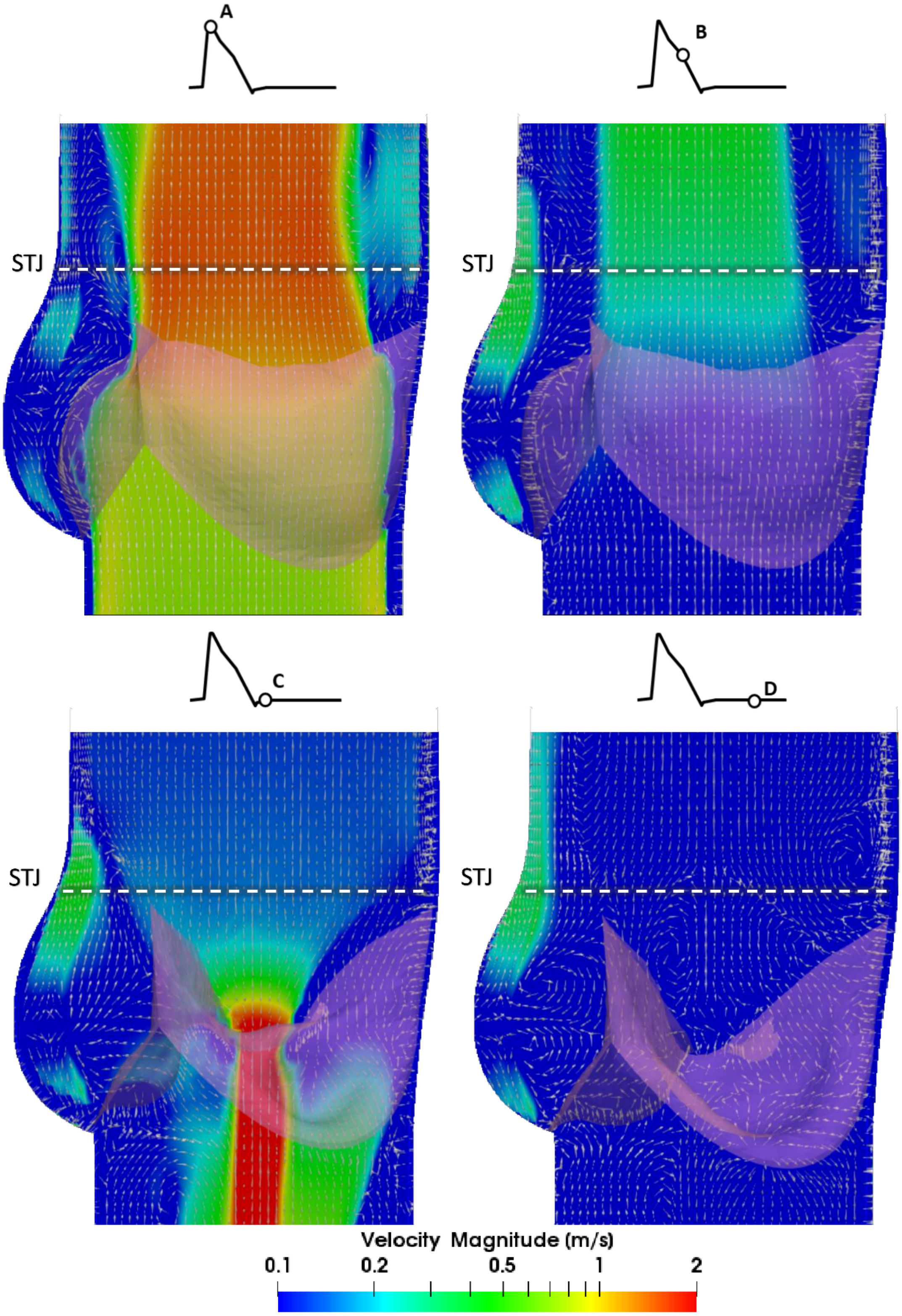

Figure 6.7. Velocity contour maps, vectors and profiles for the stiffened valve in a dilated aortic root model.

The results showed some features typical of the stiffened valve model, such as the delay in the leaflets' closure, and others typical of the dilated root model, such as a wider valve opening characterised by the presence of vortices within the leaflets inner walls up to the end of systole. However, at *instant C*, given the sinus expanded geometry and stiffened behaviour of the cusps, significant regurgitation can be observed through the valve orifice with absence of recirculations areas above the valve which would have allowed a smoother closure. Only in late diastole multiple small vortical structures can be seen within the sinus and close to the leaflets sealing edges, preventing blood stasis.

The jet flow reaches a peak of 1.39 m/s at systole which is slightly higher with respect to young healthy conditions by 8.6%.

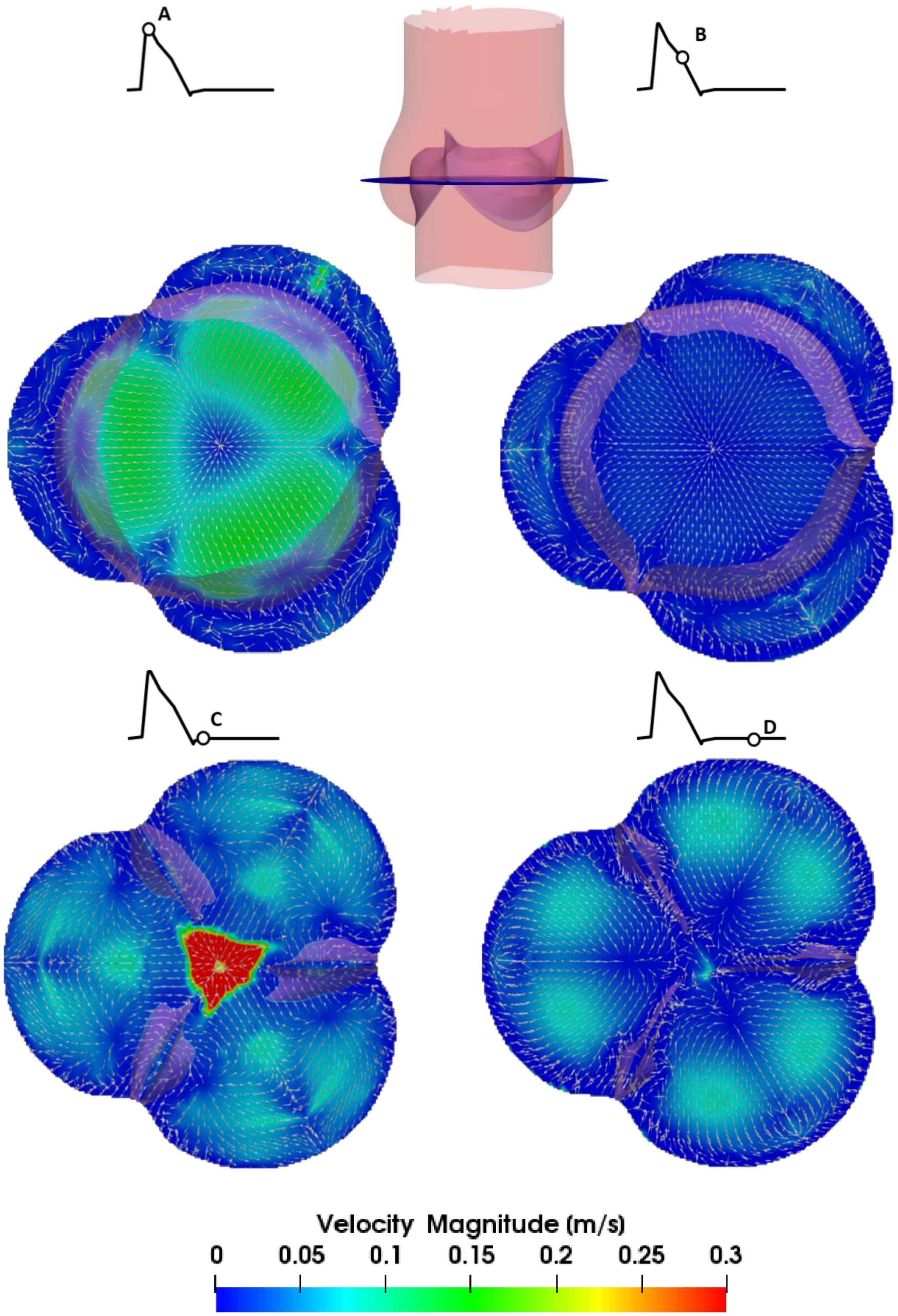

Figure 6.8. Flow contour maps and vectors across a transversal plane of the stiffened aortic valve in a dilated root model.

The instantaneous flow velocities of the transversal cross section of the Valsalva sinuses, do not present coherent vortical structures as observed in the previous analyses, and tiny recirculations can be identified at late diastole only.

6.1.3 Comparison young healthy vs ageing conditions

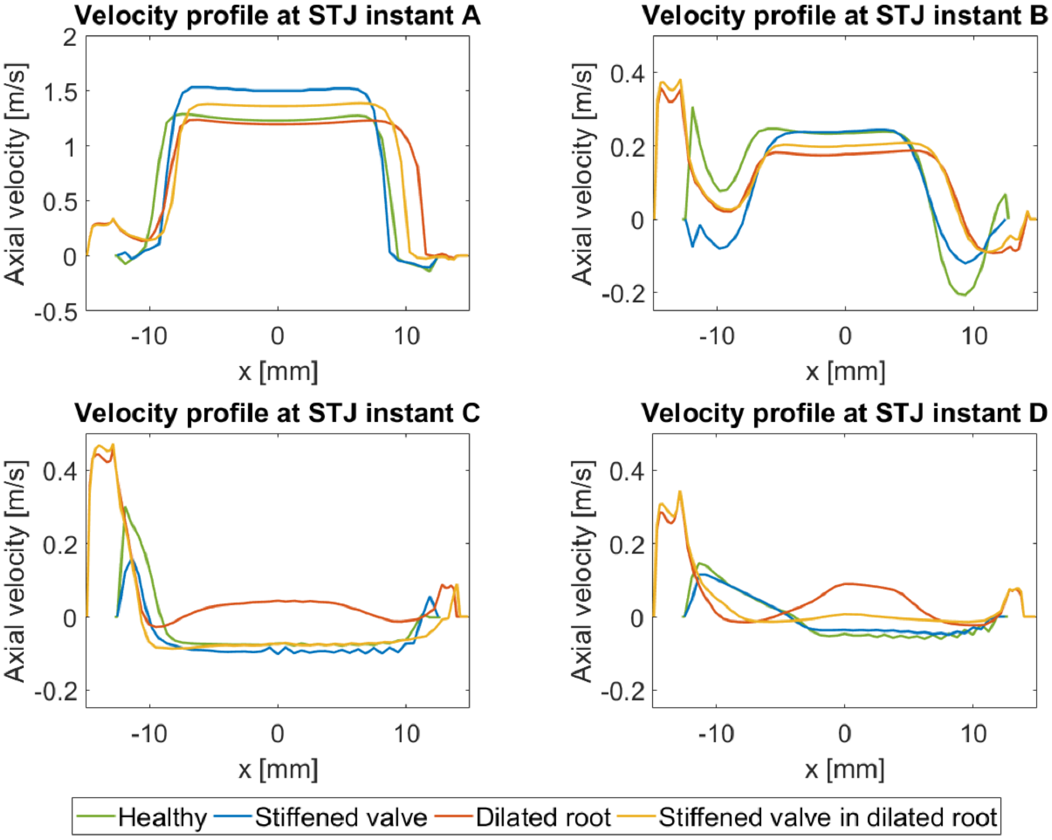

Figure 6.9. Comparison of the velocity profiles extracted at the STJ level for the healthy (green), stiffened valve (blue), dilated root (orange), stiffened valve in a dilated root (yellow) models.

A summary of the configurations investigated can be gained from Figure 6.9 where a direct comparison of the STJ axial velocity profile is provided at each relevant instant of the cardiac cycle.

From the velocity profiles extracted at the STJ for the young healthy and ageing conditions, it can be seen how major departures from the young healthy model can be observed at the systolic peak (Figure 6.9 *instant A*) where the average difference (calculated over the entire velocity profile) is 0.2 m/s for the stiffened valve model, 0.25 m/s for the model incorporating a dilated root, and 0.27 m/s for the analysis including mildly stiffened leaflets and dilation of the root. The smallest average differences are instead identified at *instant D* which corresponds to the late diastolic phase.

In terms of velocity profiles, throughout the cardiac cycle, the model replicating a mildly stiffened valve behavior is the one more closely matching young healthy conditions, with average discrepancies of 0.2 m/s at *instant A*, 0.063 m/s at *instant B*, 0.032 m/s at *instant C*, and 0.011 m/s at *instant D*.

On the other hand, the dilated root model, is the one showing larger discrepancies when compared to ideal native conditions (0.25 m/s at *instant A*, 0.13 m/s at both *instants B* and *C*, and 0.1 at *instant D*). This is mainly due to the introduction of geometry variations which allowed the jet to expand further at instant A.

In young healthy conditions the width of the fast jet flow at instant A is 16.16 mm therefore occupying 0.64% of the STJ cross section.

In the dilated root configuration, the maximum velocity of the slightly angulated forward flow at the systolic peak is 1.24 m/s, lower than the young model by 3.1%. The central flow width at the STJ is slightly wider than in the young healthy configuration (+5.19%). However, despite the presence of a wider aortic chamber at the STJ level for the jet to expand, the flow occupies just 0.58 % of the available space. Therefore, the root enlargement does not result in an accordingly enhanced central flow.

Narrower central jets are observed when stiffened cusps are present (-11.7%) and when the effect of stiffening is combined with the presence of a dilated root (-5.63%) along with peak velocities of 1.53 m/s and 1.39 m/s, respectively 19.5% and 8.6% higher with respect to young healthy conditions.

From the velocity profiles of Figure 6.9 and streamlines of Figure 6.10 it is also interesting to notice how the jet at the systolic peak, which is well aligned with the axis of the aortic root for the models with no dilatation, takes an angle when the diameter at the STJ becomes significantly larger than the one at the annulus, due to the presence of larger vortices above the sinuses than above the commissures. These narrow the systolic jet, which changes little compared to the young healthy case, even for the case where the tissues are not stiffened.

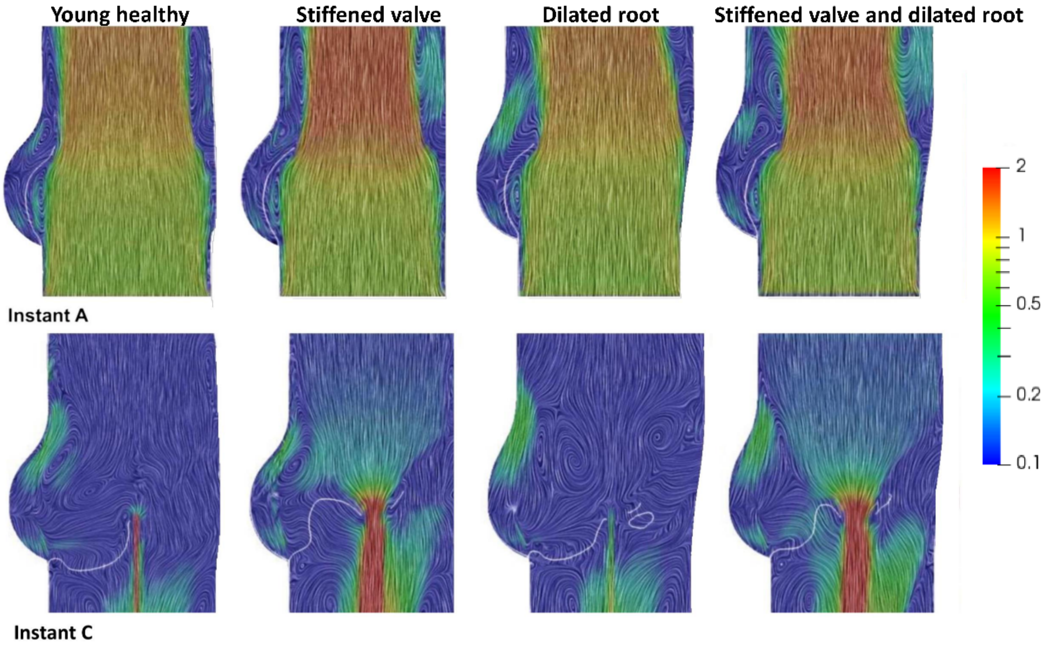

Figure 6.10. Velocity maps including leaflets opening (systolic peak) and closure profile (early diastole) obtained for the young healthy and pathological models. The velocity streamlines are visualised using line integral convolution (LIC).

From Figure 6.10 it can be better appreciated how all the models including the stiffening of the valve leaflets present a delayed closure and therefore a significant regurgitation through the valve orifice at early diastole.

The small reverse flow jet observed in all models at late diastole is a common artefact of the FSI methodology which requires the inclusion of a small gap (0.1 mm) between the leaflets of the closed valve configuration in order for the valve to open.

Thus, the analysis of the regurgitation levels is more significative for the closing regurgitant volume occurring during the valve closure, than for the leakage occurring after closure, which is due to the methodology employed and depends on the length of the free edges (this is larger for the enlarged roots).

6.1.4 Pressure maps, effective orifice area (EOA) and transvalvular pressure gradient

6.1.4.1 Stiffened valve

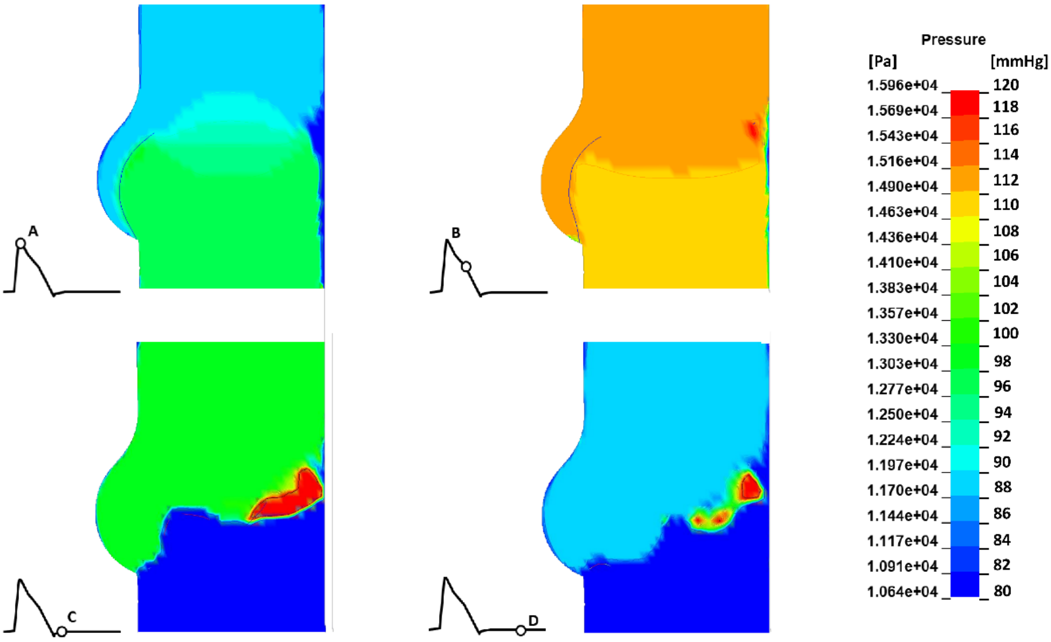

Figure 6.11. Pressure contour maps for the stiffened valve model.

Pressure contour maps for the stiffened valve model at the selected time instants are provided in Figure 6.11.

In this model, which was designed to resemble mild stiffening disease affecting the aortic valve, the ventricular pressure at the systolic peak is higher than in healthy conditions as a consequence of the leaflets thickening, due, in turn, to ageing. Contrary to what observed in the young healthy case, suction is absent at *instant A* in Figure 6.11 and pressure keeps changing along the root also at *instant B* in Figure 6.11. Diastolic phases are consistent with young healthy conditions, though.

6.1.4.2 Dilated root

As already acknowledged by investigating the leaflets valvular kinematics, velocity maps and by visual comparison of the leaflets opening profiles, this pathological condition, which mimics the expansion of the root chamber is the closest to reproduce young healthy conditions (Figure 6.12). However, slightly higher pressure values are detected at the systolic peak (*Instant A* Figure 6.12), maintaining a physiological transvalvular pressure difference throughout systole. No significant suction effect can be identified (*Instant A* Figure 6.12). The other phases are mostly conforming to the young healthy configuration.

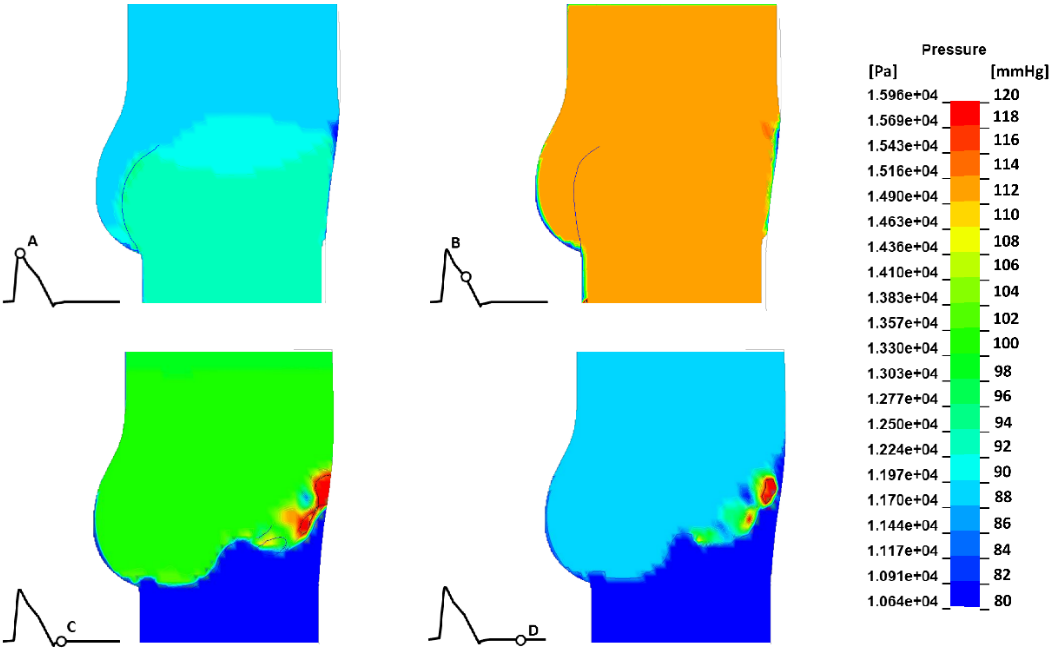

Figure 6.12. Pressure contour maps for the dilated root model.

6.1.4.3 Dilated root and stiffened valve

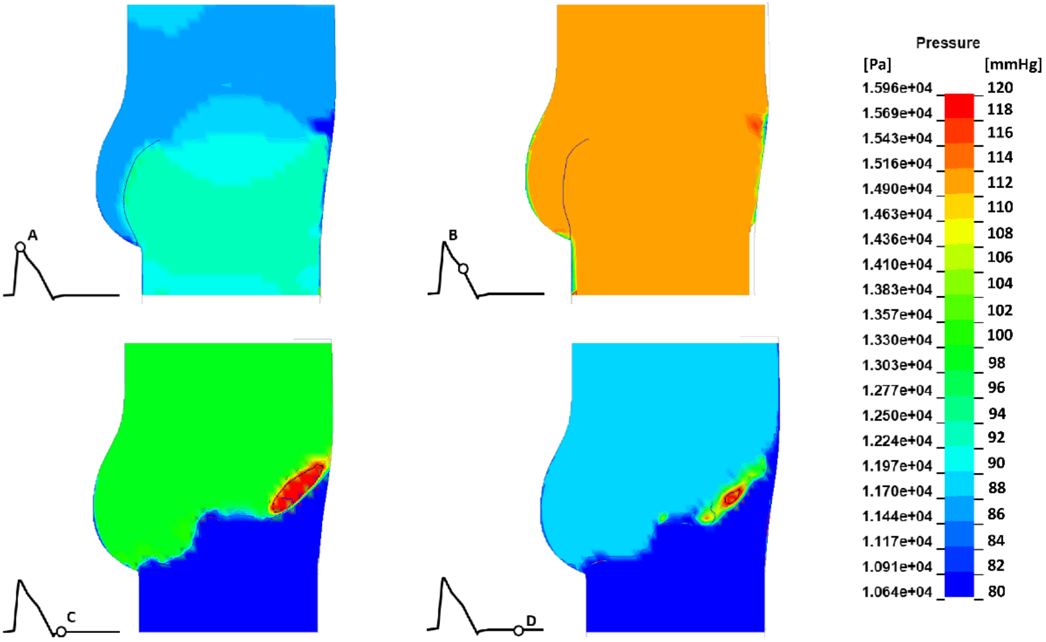

Figure 6.13. Pressure maps for the stiffened valve and dilated root model.

As already identified in the other pathological models, pressures are mostly consistent with healthy maps, apart from *instant A* (Figure 6.13) where ventricular pressure measurements are slightly higher due to the increased resistance offered by the aortic valve to the forward flow and suction is lower.

6.1.5 Comparison young healthy vs ageing conditions

The introduction of ageing-related alterations in the FSI models has been shown to directly affect the valve performance.

As expected, the pressure overload caused by the leaflets stiffening, is totally reflected on the transvalvular pressure measurement which reaches 7.68 mmHg, therefore significantly impairing the valve performance.

The dilated root model, on the other hand, presents the best hydrodynamic performance with an EOA which is even greater with respect to the young healthy case by 7.4% (3.16 cm^2).

It is worth to notice how, in the model used for the investigation of the two above mentioned pathologies combined together, the changes in the root geometry lead to a systolic gradient pressure of 6.38 mmHg which is by 17% lower than the ΔP experienced by the stiffened valve model with a normal aorta, although both include stiffened leaflets (see Table 6.2).

Transvalvular pressure drop and EOA are two strictly correlated measurements, therefore a higher ΔP can severely impinge on the efficiency of the valve functioning.

In detail, the EOA, is reduced by 23.1% and by 15.6% with respect to young healthy conditions for the stiffened valve and calcific cusps in a dilated root models, respectively.

The analysis of the results shows how variations in the dimensions and shape of the ascending aorta have a strong impact on the valve performance and therefore well-functioning.

Table 6.2. Transvalvular pressure drop and EOA values for healthy and ageing configurations.

Configuration	**ΔP[mmHg]**	**EOA $[cm^2]$**
Healthy	4.56	2.94
Stiffened valve	7.68 (+68.4%)	2.26 (-23.1%)
Dilated root	3.95 (-13.3%)	3.16 (+7.4%)
Stiffened valve and dilated root	6.38 (+40%)	2.48 (-15.6%)

6.1.6 Pressure within the sinus

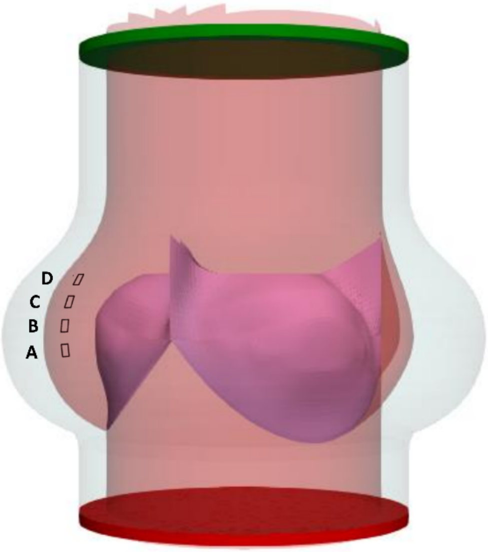

Figure 6.14. Fluid elements within the aortic sinus where pressure was registered.

The pressure waveforms of four fluid elements located within the sinus was monitored throughout the cardiac cycle. This was accomplished in order to identify in which time frame the maximum suction effect, calculated as the pressure difference between the aortic pressure at the outlet and the selected sinus element, is occurring, and how such parameter may vary at different sinus heights. The elements under investigation were located from the level of the maximum sinus diameter up to the level of the open leaflet edge. (Figure 6.14).

6.1.6.1 Young healthy vs ageing conditions

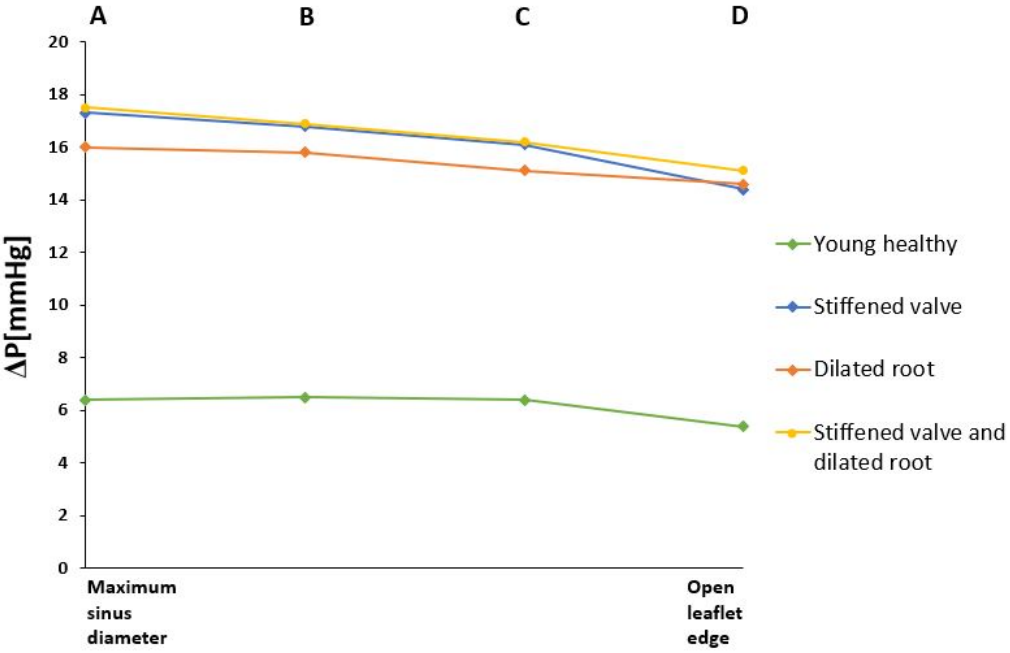

Figure 6.15. Graph showing the maximum suction effect values for the healthy and ageing configurations at sinus elements A, B, C and D at the valve opening instant.

The pressure difference between the investigated elements within the sinus and the aortic outlet is shown in Figure 6.15. The ageing models graphs are comparable to the healthy curve trend where pressure variation maintains almost constant for elements A, B and C and then drops at element D, which is the one close to the open leaflet edge (Figure 6.15).

For all ageing models, fluid element *'A',* which is the closest to the sinus, experiences the maximum difference in pressure between the aortic outlet and the sinus area. Pressure maps do not show observable differences between elements located at mid-sinus and at elements closer to the STJ with maximum variations within -16.7% for the stiffened valve, -8.75% for the dilated root and -13.7% for the stiffened valve in a dilated root models, respectively.

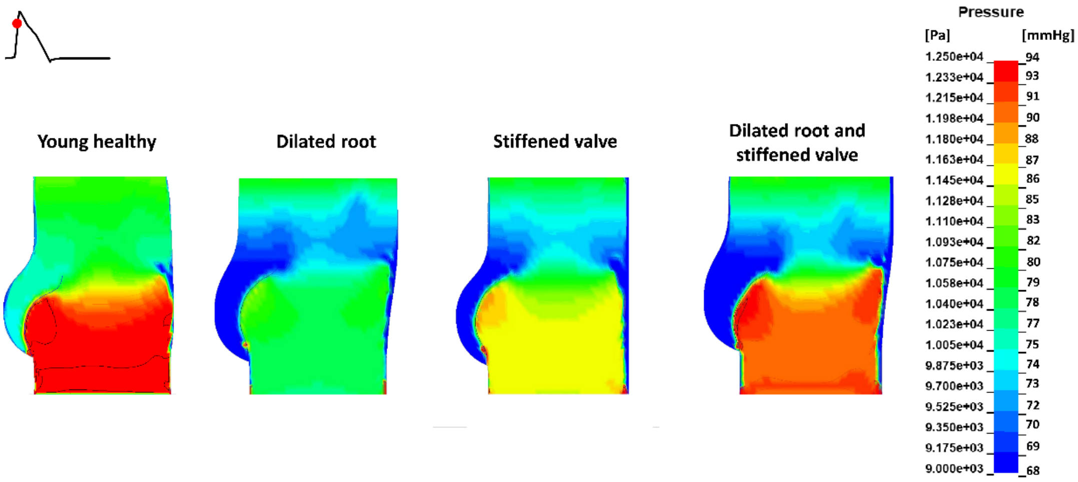

Figure 6.16. Pressure maps showing the maximum suction effect for young healthy and 'ageing' models at the instant preceding the systolic peak.

As shown in Figure 6.16,which displays the pressure distributions at the instant preceding the systolic peak, the maximum difference occurs at the same instant in both healthy and ageing models with higher values detected in ageing conditions (the average pressure variation between the different ageing models is 16 mmHg). This may be due to the presence of a larger chamber for the models including a dilated aorta, and to the leaflets thickening for the models reproducing mild leaflets stiffening. The latter induces a lower pressure within the sinus area which results in a bigger pressure difference.

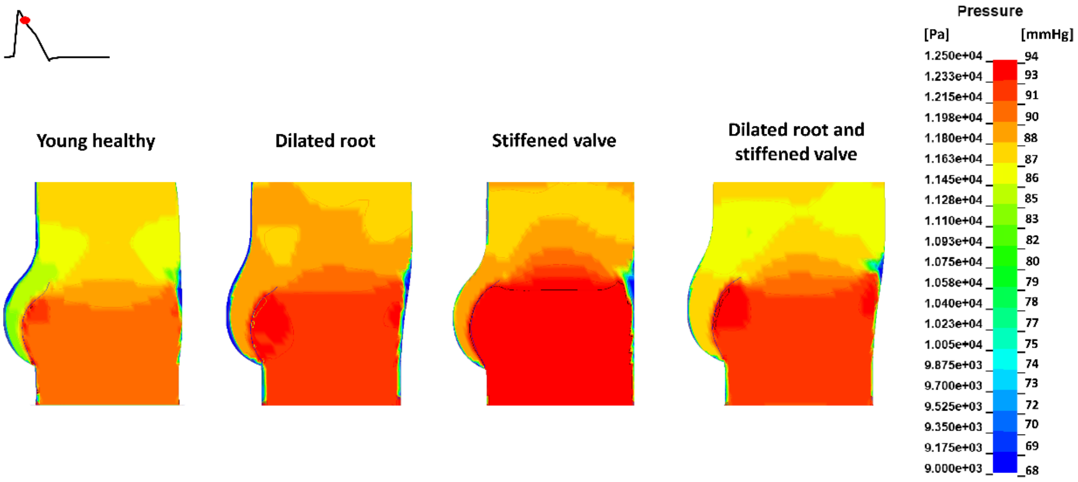

Figure 6.17. Pressure maps showing the maximum suction effect for young healthy and 'ageing' models at the instant following the systolic peak.

However, it is meaningful to notice that, even though the peak in pressure difference is smaller in the young healthy case, the suction effect in this case is continuous whilst it fades very rapidly in ageing conditions likely due to the presence of a stronger central jet. As shown in Figure 6.17, which displays the pressure contour maps when the valve is fully open, suction is completely absent in the ageing models whilst it persists in healthy conditions.

6.1.7 Energy loss

Energy loss allows to assess the valve performance in terms not only of forward flow but also of closing regurgitation. These parameters represent a meaningful and powerful tool to identify clinically asymptomatic patients which unconsciously, are at high risk (Akins, Travis, & Yoganathan, 2008).

Energy loss was calculated by integrating the flow rate times the transvalvular pressure over a relevant flow interval (Azadani et al., 2009) using the following equation:

$$\text{Energy loss} = 0.1333 * \int_{t_1}^{t_2} \Delta P * Q * dt \tag{16}$$

where 0.1333 is a conversion factor applied to convert the energy from millimetres of mercury*millilitres (mmHg*ml) to millijoules (mJ), t_1 and t_2 are the time instants used for integration, dt is the analysed time interval and ΔP and Q are respectively the transvalvular pressure (in mmHg) and flow rate (in $\frac{ml}{s}$) over that time interval.

For the forward energy, the integral was computed between the beginning and the end of the systolic phase; for the closing energy the integration was performed in the interval between the end of systole and the valve closure instant.

6.1.7.1 Young healthy vs ageing conditions

Forward and closing energy values for the young healthy configuration were found to be 67.7 mJ and 36.9 mJ, respectively (see Table 6.3). Comparing these data against those obtained for ageing conditions it can be better appreciated that among the models replicating ageing, the one based on the dilation of the aortic root but with normal size leaflets, presents the lowest forward and closing energy values. However, the energy associated with closing is 72.16 mJ compared to only 36.9 mJ for the young healthy case (see Table 6.3). This is due to the valvular kinematics behaviour where the cusps remain open for a longer time.

Table 6.3. Energy loss values for healthy and ageing configurations.

Configuration	Forward energy loss [mJ]	Closing energy loss [mJ]	Total energy loss [mJ]
Young healthy	67.7	36.9	104.6
Stiffened valve	107.78 (+59.2%)	108.92 (+195.17%)	216.7 (+107.17%)
Dilated root	51.77 (-23.53%)	72.16 (+95.5%)	123.93 (+18.4%)
Stiffened valve and dilated root	85.87 (+26.83%)	103.99 (+181.81%)	189.86 (+81.51%)

Globally, the energy losses variations with respect to the young healthy case were found to be +107.17% for the stiffened valve configuration, +18.4% for the model with the dilated aorta, and +81.51% for the analysis with stiff leaflets and dilated root. The presence of a larger root chamber seems to improve energy efficiency however, they pay back during closing.

6.1.8 Blood damage

Other fluid dynamic parameters acting at a more local scale need to be taken into account, in order to evaluate the safety and efficacy of heart valves. As mentioned previously in section 1.6, alteration of the physiological healthy flow may lead to increased aortic wall and leaflet stresses, and an elevated risk of haemolysis. Also, during the cardiac cycle the levels of shear stress experienced by the blood vary greatly, with undesirable phenomena resulting in non-physiologically high shear stress (Corbett, Ajdari, Coskun, & N-Hashemi, 2010), and red blood cell damage (Lakshmi P. Dasi et al., 2009). High blood shear stresses result into haemolysis, especially when exacerbated by prolonged exposure, with the rupture of red blood cells membrane releasing their contents, and increasing platelet activation levels and thrombogenicity of the blood (Corbett, Ajdari, Coskun, & N-Hashemi, 2010; Leverett, Hellums, Alfrey, & Lynch, 1972). Activated platelets are complementary to the aggregation of red blood cells, and have been identified as the primary cells involved in cardioembolism, via haemostasis and thrombosis (Heemskerk, Bevers, & Lindhout, 2002; Morbiducci et al., 2009). As both the magnitude and alignment of particle velocities have a significant role in platelet activation, any deviation from the healthy, physiological behaviour is of clinical concern (Morbiducci et al., 2009). The specific magnitude at which haemolysis begins to occur is not agreed upon in the literature, ranging from 20 to 500 Pa, but the higher the shear stress and longer the exposure, the greater the haemolysis potential (Caro, Pedley, Schroter, & Seed, 2012; Leverett et al., 1972; Yen, Chen, Chern, & Lu, 2014).

Regions characterised by strong vortical areas provide biomechanical and biochemical conditions that promote platelet activation and therefore may trigger thrombosis (Biasetti, Spazzini, Swedenborg, & Christian Gasser, 2012; D. Bluestein, Chandran, & Manning, 2010; Hope et al., 2013). Such vortical structures and dynamics constitutes the source of high wall shear stress (WSS) (Bäck et al., 2013). Also, stagnation areas, characterised by long residence times, are susceptible to thrombus formation (Menichini & Xu, 2016).

Hence, viscous shear stress and WSS magnitude maps were computed and analysed at the selected instants of the cardiac cycle, in order to investigate the thrombogenic potential correlated with high levels of shear stress.

However, the intrinsic limitations of the numerical approach adopted, must be taken into account. In detail, WSS results cannot be considered fully accurate since the ALE solver is not a full Navier-Stokes solver and, therefore, does not account for fluid boundary layer effects (Hallquist, 2006; *LS-DYNA Aerospace Working Group Modeling Guidelines Document*, 2011). Also, in order to accurately resolve the boundary layer, the fluid mesh grid should be refined in proximity of the boundary layer. However, this could not be accomplished since the ALE method in LS-DYNA requires the mesh grid of the fluid and structure domains to have similar resolutions, and maintain them during the entire cycle, in order to avoid any sort of leakage.

6.1.8.1 Fluid shear stress in healthy and ageing conditions

Fluid shear stresses (τ) were calculated using the symmetric component of the Velocity Gradient matrix which is called Strain-rate tensor (Batchelor & Batchelor, 2000). The latter is the strain or shear rate which is the velocity gradient perpendicular to the direction of shearing (Y. S. Wu, 2015).

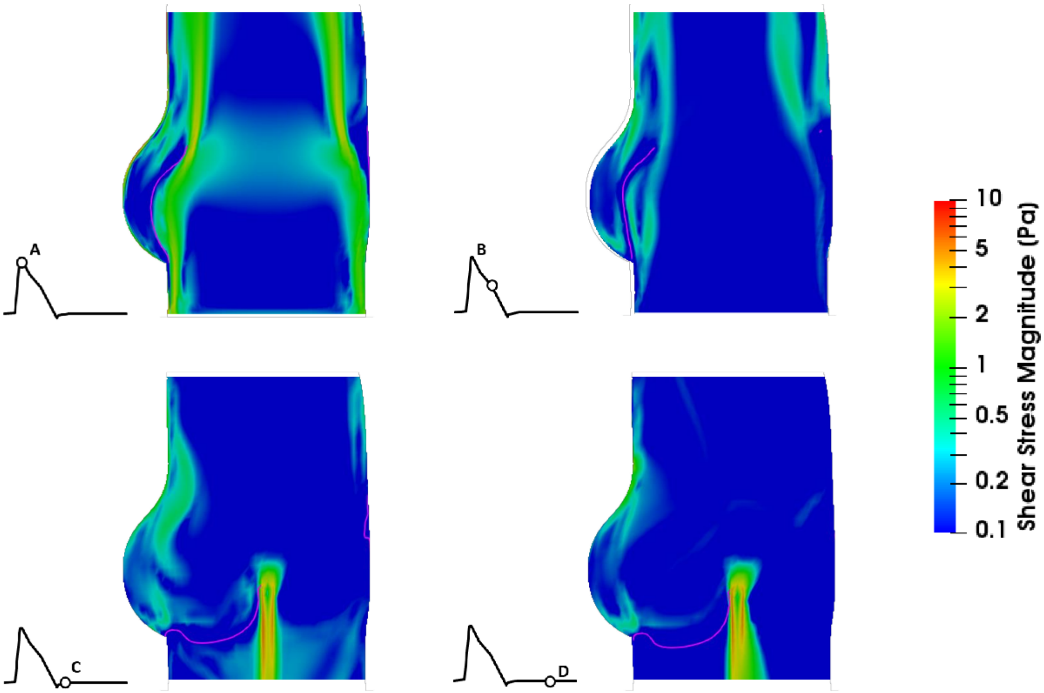

Figure 6.18. Fluid shear stress magnitude contour maps for the young healthy model.

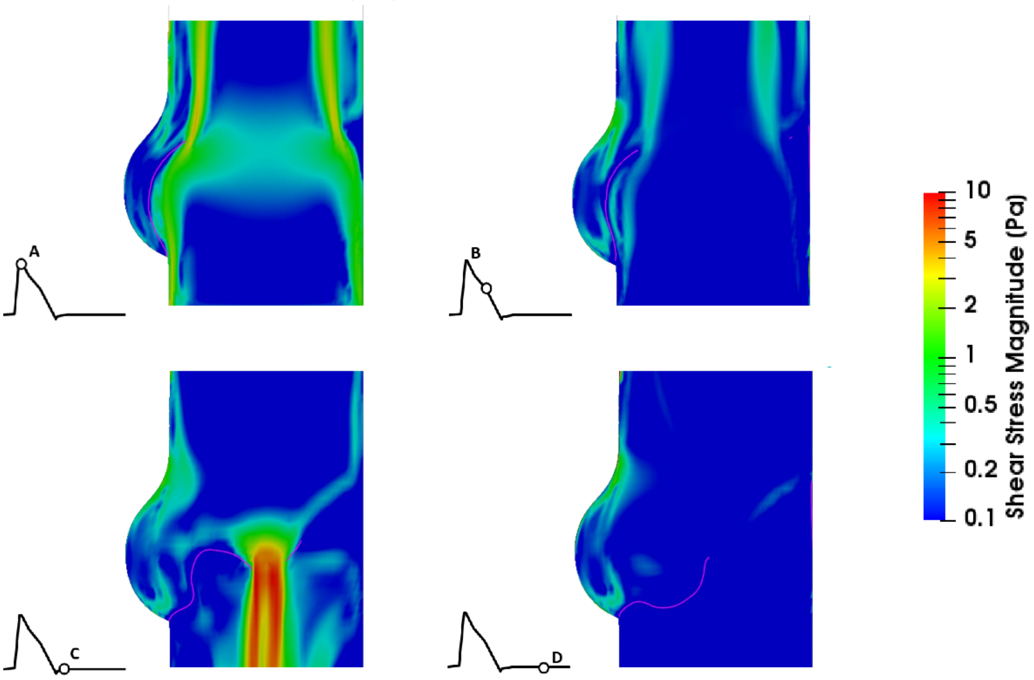

Figure 6.19. Fluid shear stress magnitude contour maps for the stiffened valve model.

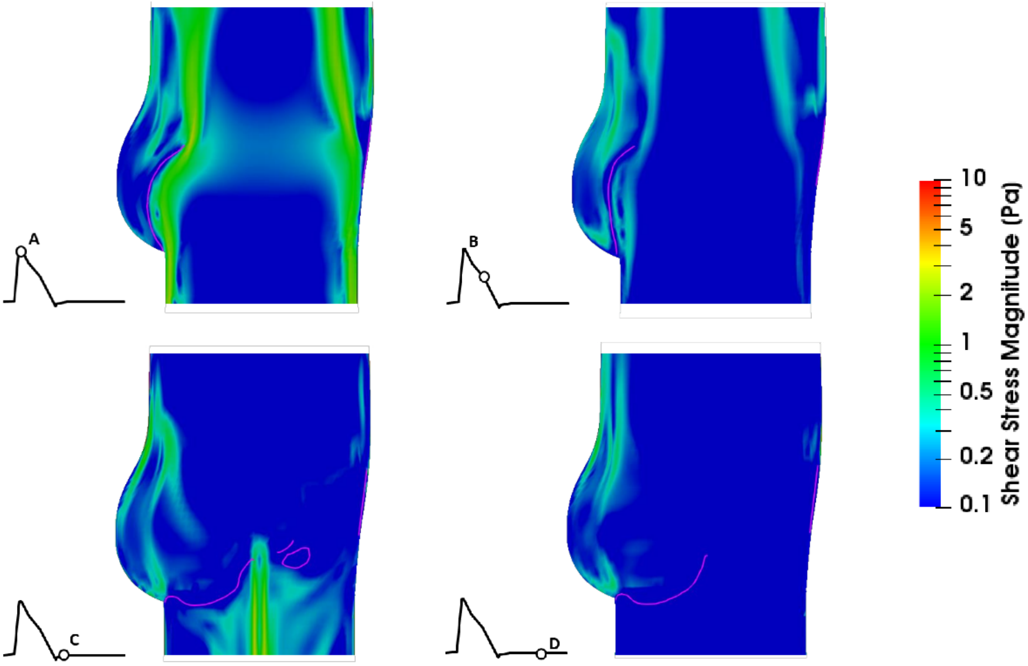

Figure 6.20. Fluid shear stress magnitude contour maps for the dilated root model.

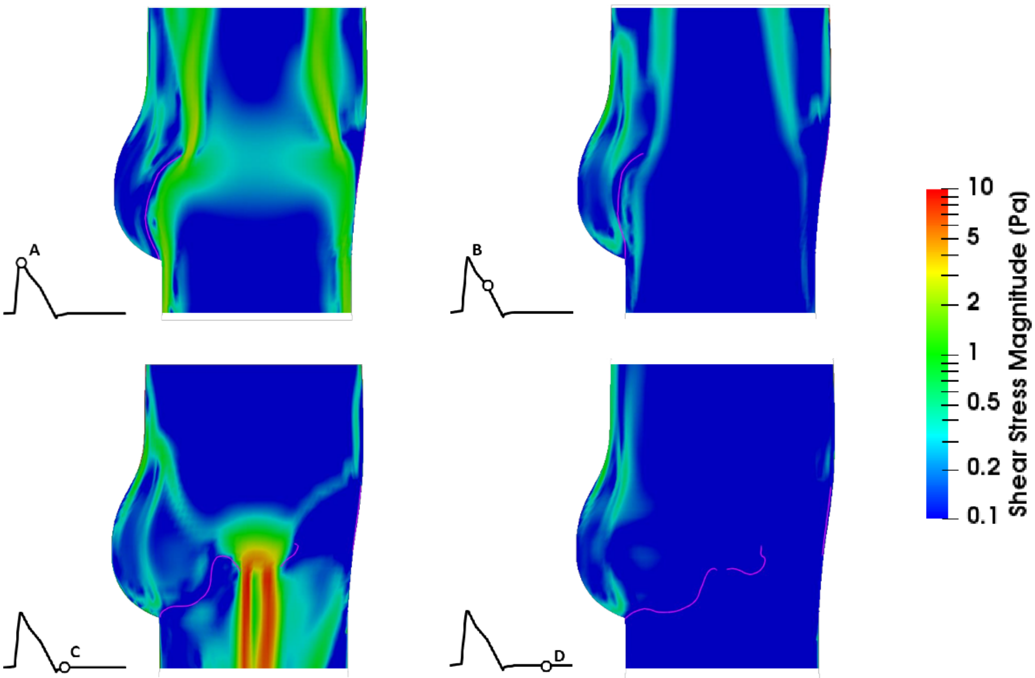

Figure 6.21. Fluid shear stress magnitude contour maps for the stiffened valve and dilated root model.

Figure 6.18, Figure 6.19, Figure 6.20 and Figure 6.21 show the shear stress magnitude distributions tracked at the analysed time frames of the cardiac cycle for the young healthy and ageing aortic root configurations .

Table 6.4.Maximum shear stress values for healthy and ageing models.

Configuration	Maximum shear stress [Pa]
Healthy	9.2
Stiffened valve	10.4 (+13.04%)
Dilated root	9.9 (+7.6%)
Dilated root and stiffened valve	12.02 (+30.6%)

Peaks were identified at valve closure for all models. The corresponding values are reported in Table 6.4. However, as mentioned above, such results need to be carefully interpreted given the limitation introduced by the numerical method during valve coaptation (see section 6.1.3).

No significant variations can be observed between the different configurations. The analyses replicating a stiffened valve behavior present the higher fluid shear stresses, though.

6.1.8.2 Wall shear stress in healthy and ageing conditions

The WSS (τ_w) can be defined as the gradient of velocity normal to the wall, in this specific case normal to the leaflets surface, and calculated following this formula:

$$\tau_w = \mu \frac{\partial u_t}{\partial n}\bigg|_{wall} \tag{17}$$

where u_t denotes the wall tangential velocity and n is the normal unit vector at the wall (Perktold & Peter, 1990).

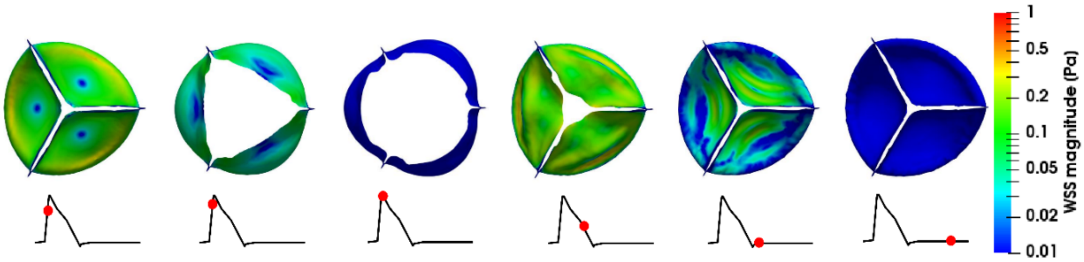

Figure 6.22. WSS acting on the leaflets for the young healthy configuration.

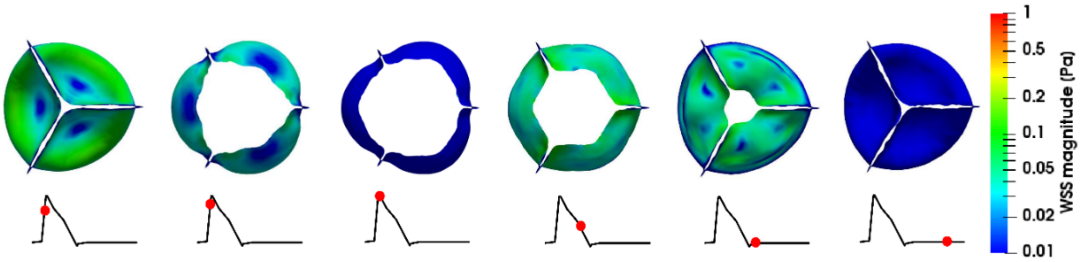

Figure 6.23. WSS acting on the leaflets for the stiffened valve configuration.

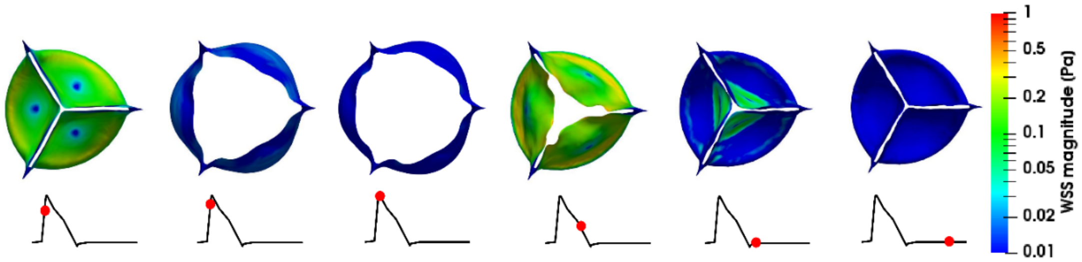

Figure 6.24. WSS acting on the leaflets for the dilated root configuration.

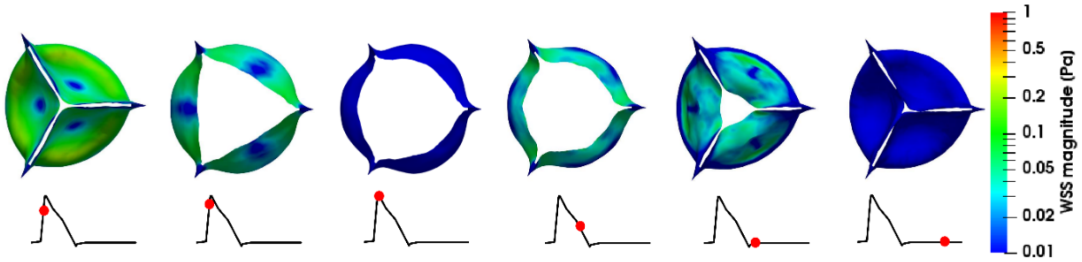

Figure 6.25. WSS acting on the leaflets for the stiffened valve in a dilated root configuration.

Contour plots of the WSS magnitude acting on the leaflets of the young healthy, stiffened valve, dilated root and stiffened valve in a dilated root model at different instants of the cardiac cycle are described in Figure 6.22, Figure 6.23, Figure 6.24, and Figure 6.25, respectively.

WSS peaks are detected during the valve closing phase for all models.

Among prosthetic devices, TAVI presents the highest levels of WSS magnitude which can be detected at the cusps' commissures and belly while the valve is closing, consistently with the physiological healthy pattern.

Although no specific range of values indicating the healthy shear stress experienced by the valve cusps has been agreed and defined yet in the literature, the analysed shear stress maps are found to be consistent with shear stress levels indicating a healthy behaviour according to a study from Yoganathan *et al.* (Weston, LaBorde, & Yoganathan, 1999).

Therefore, considering the results obtained both in terms of shear stress and WSS, it can be concluded that potential cases of blood damage for the investigated ageing and treated conditions, cannot be associated with high shear stress.

6.2 Discussion

Apart from works based on 2D geometry (Amindari et al., 2017) and multiscale approach (Weinberg, Schoen, & Mofrad, 2009) with a focus on the calcification process, this is the first computational study to provide a thourough overview of the haemodynamic changes due to the ageing process.

The results were processed following the same procedure used for the ideal young healthy case to draw a comparison and analyse how common ageing diseases may impinge upon the operating system of the native aortic valve.

Different parameters were considered in the comparison between young healthy and ageing conditions, including the leaflets kinematics, flow velocity, pressure distributions and valve hydrodynamic performance indicators (EOA, Transvalvular pressure drop and energy loss).

To be able to evaluate how stiffening and reshaping contribute individually to the alteration of the haemodynamics within the aortic root, three different models were realised: one modelling a mild stiffening of the tissues that typically results in an increase of the thickness on the entire surface of the leaflets (Sahasakul, Edwards, Naessens, & Tajik, 1988), another replicating the mean dilation of the aortic chamber observed at an age of 40 (Vriz et al., 2014), and the last reproducing the combination of these two effects together.

Longer VOT and VCT were observed in all ageing configurations. In particular, the model with a stiffened valve anchored in a dilated root, presents significantly extended opening and closure times since, in addition to a delayed closure, the leaflets displacement opening and closing initiation phases occur earlier than in the other ageing models. The most significant variations in terms of valvular kinematics are detected during closure (longer VCT) for all configurations.

The configurations with stiffened cusps were the first to initiate opening immediately followed by the model resembling the progressive dilation of the root chamber, which, instead, was synchronised with the young healthy valve.

This is justified by the fact that the leaflets were modelled in a semiopen configuration, as described in (Tango et al., 2018).This is consistent with observations on the explanted calcified human valves, which typically show an intermediate configuration (Cheng, Chang, Huang, Wang, & Lin, 2017; Schoen, 2008). Hence, they move to the initial unstressed configuration as soon as the diastolic pressure becomes insufficient to force them in the fully closed positions. However, once the unstressed configuration has been reached, they find more difficult moving to the fully open state, so that the full opening is achieved later than for soft tissues. Similarly, in the closing stages higher pressures are required to force the leaflets to move from the semi-open design configuration to the complete coaption. This is consistent with the change of slope observed for the two stiffened models in the diagrams of the radial displacement (Figure 6.1) during the closing phase.

In terms of leaflets radial displacement, apart from the model resembling the stiffening of the valve, whose cusps' maximum extension is smaller by 4% than that detected in native conditions (9.68 mm), both configurations including a dilated chamber produce a slightly wider displacement, respectively by 2.6 % for the model with a dilated root only (10.33 mm), and by 0.5% for the model including cusps stiffening and root dilation (10.11 mm). This might be explained by the presence of longer leaflets free edges and larger sinuses.

Nevertheless, whilst for the model with young healthy leaflets in a dilated aortic chamber this translates into an enhanced EOA, which is by 7.4 % higher than that of the native conditions, for the stiffened valve anchored in a dilated chamber, this leads to an EOA measurement of 2.48 cm^2 which is by 15.6% narrower than that observed physiologically (see Table 6.2). However, it is important to take into consideration that, despite the cusps of the enlarged root model open more, and the aortic valve is 13.5% bigger than the young healthy valve along the cross section, the EOA estimation does not reflect such change in dimensions, but instead, it is smaller by 6.5% when compared to the expected value.

Also, the closing energy level is almost double compared to the healthy configuration (+95.5%) so, larger roots pay back during closing. This also applies to the presence of stiffened leaflets, where the delay in closing is strongly affecting energy loss levels with a global value which is 107.17% higher than in the native young aortic valve.

Therefore, it seems that the presence of stiff leaflets alone, even if only mildly stiffened, affects extensively the haemodynamics and valve performance within the ascending aorta and definitely to a greater extent than the expansion of the aortic root.

In terms of flow velocities, apart from the dilated root model, they all present higher peak velocities at the maximum flow rate with respect to the young healthy conditions. This is a direct consequence of the leaflets stiffening. In particular, the model with mild stiffened leaflets shows the highest velocity peak among all virtual pathological cases (1.53 m/s). However, the same valve with the same stiffened behavior but positioned in an oversized root chamber attenuates this value by 9.1 % (1.39 m/s).

Nevertheless, as stated previously, it is important to take into consideration that the dilated root model was built by linearly scaling the healthy model geometry along the cross section and therefore its leaflets dimensions are 13.5% bigger than those of the young healthy models at their free edge. Hence, this might have had an impact on the overall valve performance.

In terms of flow pattern, all the main flow features detected physiologically are still preserved in the ageing models. Despite this, the combination of stiffened leaflets and dilated aortic root, which is often the case in ageing patients (Crawford & Roldan, 2001; Wilton & Jahangiri, 2006), leads to the overall worst performance, being the least coherent with what observed in optimal conditions in both sagittal and transversal planes.

With regard to the velocity profiles, despite the STJ dilated model is the closest to physiological young healthy conditions, the average discrepancies for the velocity profiles extracted at the STJ at the different instants of the cardiac cycle is higher than those of the other two ageing configurations. This is due to the root dimensions which allow for the development of a much larger central jet. The stiffened models instead, present delayed closure and significant regurgitation (Figure 6.7) at early diastole. Also, due to the anatomical variations, the opening profile results in slightly angulated jets at the systolic peak for the models including a dilated root whilst mostly symmetrical for the model with stiffened leaflets only.

It is also worth mentioning that progressive root dilation condition is usually correlated with other valvular diseases such as the presence of stiffened leaflets, which together severely impinge upon the valve performance and function, leading to a high transvalvular pressure drop and a very reduced EOA (Seki & Fishbein, 2016).

The young healthy model confirms that the primary function of the Valsalva sinuses is hosting the open leaflets, reducing their interference with the central jet(Tango et al., 2018). In fact, the vortical zones into the sinuses are evident only at the distal region, and do not appear to play a role during the systolic phase. This mechanism was observed also in all analysed ageing models.

The main central jet generated during systole generates some pressure difference between the aortic outlet and chamber between the open leaflets and the sinus walls, producing a suction effect which promotes the expansion of the leaflets into the sinuses. This suction effect, in the young health model persists throughout most of the systolic phase. On the contrary, for the ageing models it is evident only at the systolic peak, when suction is stronger than for the young case, and then rapidly disappears.

In fact, contrary to what observed in treated conditions (Chapter 7), where the leaflets radial displacement is significantly reduced due to the presence of the supporting stent, in the ageing models, despite the simulation of leaflets thickening and the introduction of root anatomical variations, the shape of the cusps protruding into the sinuses was consistent with the physiological young healthy behaviour.

With regard to the occurrence of thrombotic events, no correlation could be found with such events and high levels of vorticity and/or WSSs for all ageing configurations.

Chapter 7 Post treatment conditions

Introduction

The validated FSI model was then adapted to describe post treatment conditions. In particular, both surgical and transcatheter replacement procedures were investigated. A detailed outline of the features characterising each configuration is presented in section 3.6.

As done for the study of ageing effects, the data obtained for the treated cases were analysed and compared against those of the young healthy root environment. For the details on the methodology applied for the analysis of each variable of interest please refer to Chapter 6 as the post processing of the results followed the same procedure used for the models reproducing ageing.

7.1 Results

7.1.1 Valve kinematics: comparison young healthy vs post treatment

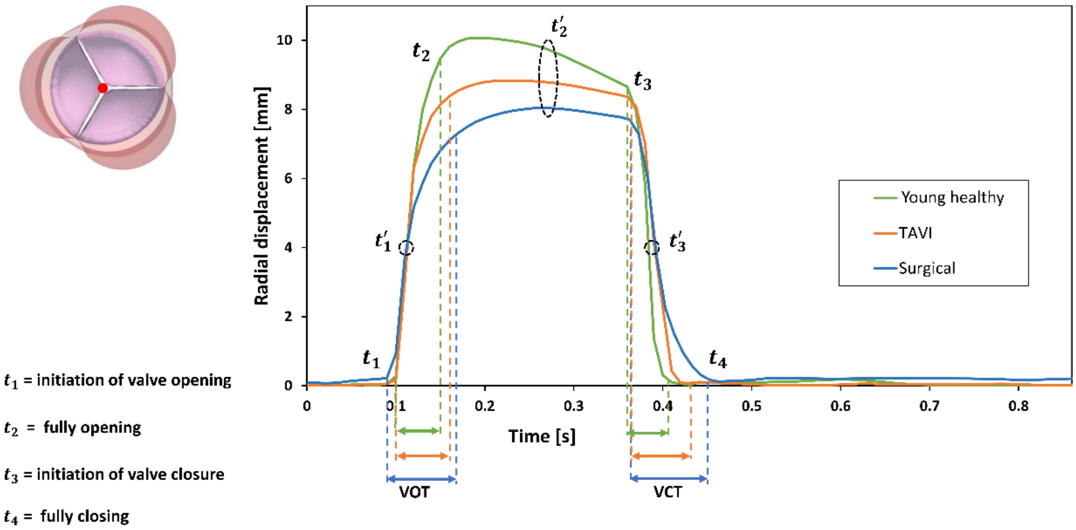

Figure 7.1. Graph used to compare the leaflets kinematics in young healthy (green), surgical (blue) and TAVI (orange) configurations. The red point on the leaflet shows the location of the node where the displacement was tracked for all configurations.

Figure 7.1 shows the leaflets' radial displacement for the healthy and treated conditions during the cardiac cycle.

It is worth to notice that the surgical valve opens slightly earlier than TAVI and healthy configurations and is the latest to achieve the full closure. TAVI instead, presents VOT and VCTs closer to the healthy valve, with values of 60 and 70 ms, respectively.

During late systole, the healthy model is the first to initiate the closing phase, immediately followed by the TAVI and surgical models which instead, are synchronised.

As shown in Table 7.1, moving from the healthy case to TAVI and surgical configurations, the valvular kinematics parameters VOT, VCT and ET values increase, presenting the highest difference in percentage with respect to the young healthy case during valve closure (VCT) as 40% and 80% for TAVI and surgical, respectively.

Table 7.1. Valve opening, closure and ejection times for healthy and treated configurations.

Valve configuration	**VOT [ms]**	**VCT [ms]**	**ET [ms]**
Healthy	50	50	310
Surgical	80(+60%)	90(+80%)	362(+16%)
TAVI	60(+20%)	70(+40%)	330(+6%)

In terms of magnitude, the healthy valve exhibits the greatest radial displacement, with the leaflets reaching a maximum extension of 10.06 mm at the systolic peak. The equivalent configurations for the surgical prosthesis and TAVI devices, show a maximum displacement of 8.04 mm and 8.83 mm, with a reduction of 20% and 12 % compared to the young healthy case, respectively. It is also worth mentioning that the valve fully open position does not correspond to the time when the leaflets maximum radial displacement is achieved. This is due to the behaviour of the cusps which first open, and then radially expand.

Figure 7.2 displays the top view of the valve at the selected instants of the cardiac cycle.

Despite the leaflets geometry was left unaltered for all models, the prosthetic devices show a different kinematics in opening and closing indicating a reduction in the ability of the leaflets to expand, this has an effect on the valve performance indicators such as EOA and Transvalvular pressure drop, as discussed in section 5.1.3.

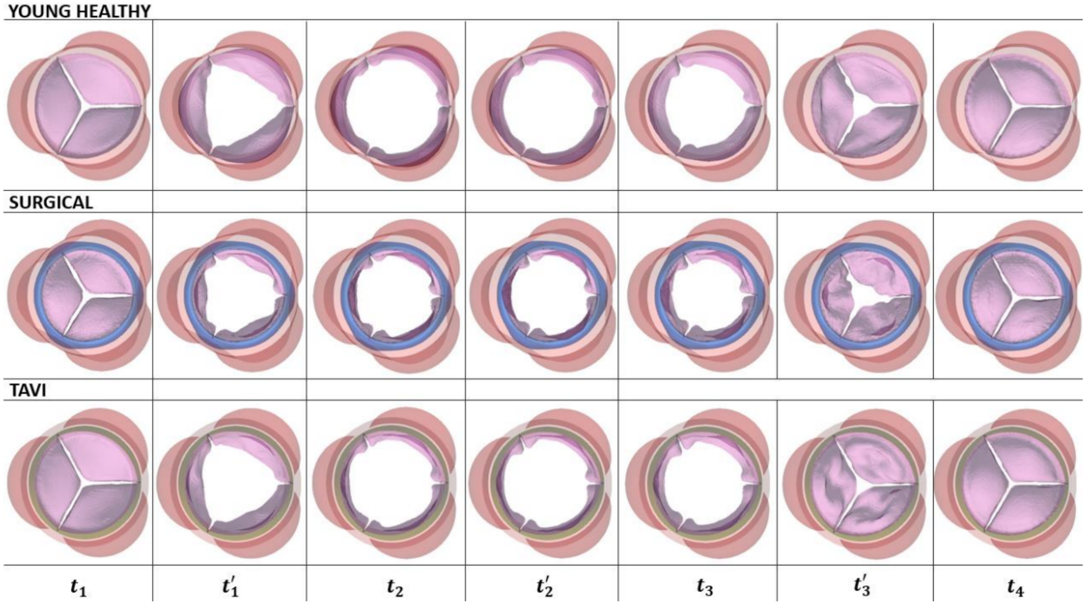

Figure 7.2. Valve top view for healthy and virtually treated configurations at the instants used for the calculation of the valvular kinematics parameters.

In detail, the valve diameter in the surgical configuration is smaller due to the presence of the stent and therefore presents the narrowest valve orifice.

In terms of closure, surgical configuration appears to be the stiffest as shown by its increased VCT.

The TAVI model, although characterised by leaflets of identical dimensions to the young healthy model, still does not match the same valve extension.

7.1.2 Flow velocity

7.1.2.1 Surgical

The resultant instantaneous flow dynamics and global flow parameters following the virtual insertion of a surgical bioprosthesis, were investigated so that the vortical behaviour and haemodynamics were compared to those of the native young healthy root environment. Figure 7.3 shows the corresponding velocity contour maps and vectors obtained at the selected time instants.

Opening starts with a radial flow in the sinus, located above the stent which forms a little vortex (*instant A* in Figure 5.3). A recirculation similar to that detected within the leaflets walls in physiological healthy conditions at systole (*instant A,B* in Figure 5.3) is still present in the surgically treated case, but its entity is strongly reduced.

Compared to the young healthy configuration (Figure 5.3), the model including a stented bioprosthesis exhibits a much narrower valve orifice (Figure 7.3). since the leaflets are smaller due to the presence of the stent. This results in a faster jet with the velocity at the STJ level reaching a peak magnitude of 2.13 m/s at the systolic ejection compared to only 1.28 m/s of the young healthy case.

A series of vortices and counter vortices can be identified in the sinus side, at the wall, whilst a single large recirculation can be observed just above the commissure (*instant B* in Figure 5.3).

Contrary to the young healthy case, herein, vortices into the Valsalva sinuses can be detected also when the valve is open.

During early diastole (Figure 7.3 *instant C*) the presence of the stent forces an axial flow at the leaflets belly, whose curvature reversal is slower than in the young healthy model. This leads to the development of a single washing vortex located further away from the leaflets, which then expands and moves towards the leaflets at the last stages of diastole (Figure 7.3 *instant D*).

Recirculations at diastole are supposed to aid valve closure; hence this configuration results in a delayed valve closure compared to the healthy case.

Overall, the haemodynamics in this model are altered as a result of the introduction of a surgical bioprosthesis.

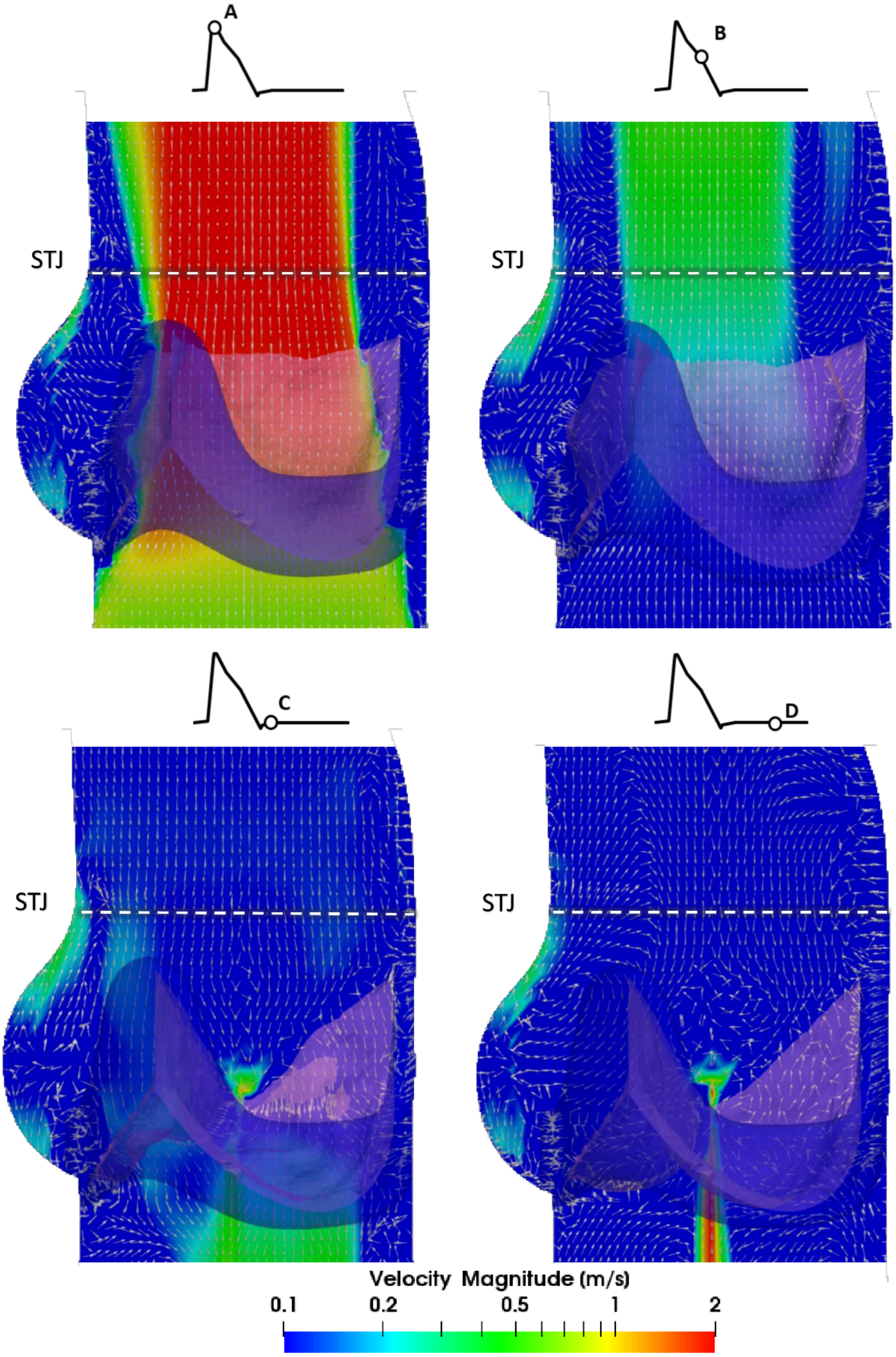

Figure 7.3. Velocity contour maps, vectors and profiles for the surgical configuration.

When a cross section orthogonal to the main flow and bisecting the aortic bulges is considered (Figure 7.4), bigger recirculation areas were observed in the Valsalva sinuses during systole, given the reduced valve opening, however they fade during the diastolic phase probably due to the stent, which acts as a barrier for the full development of such vortices (Figure 7.4), as opposed to what observed in young healthy conditions (Figure 5.4).

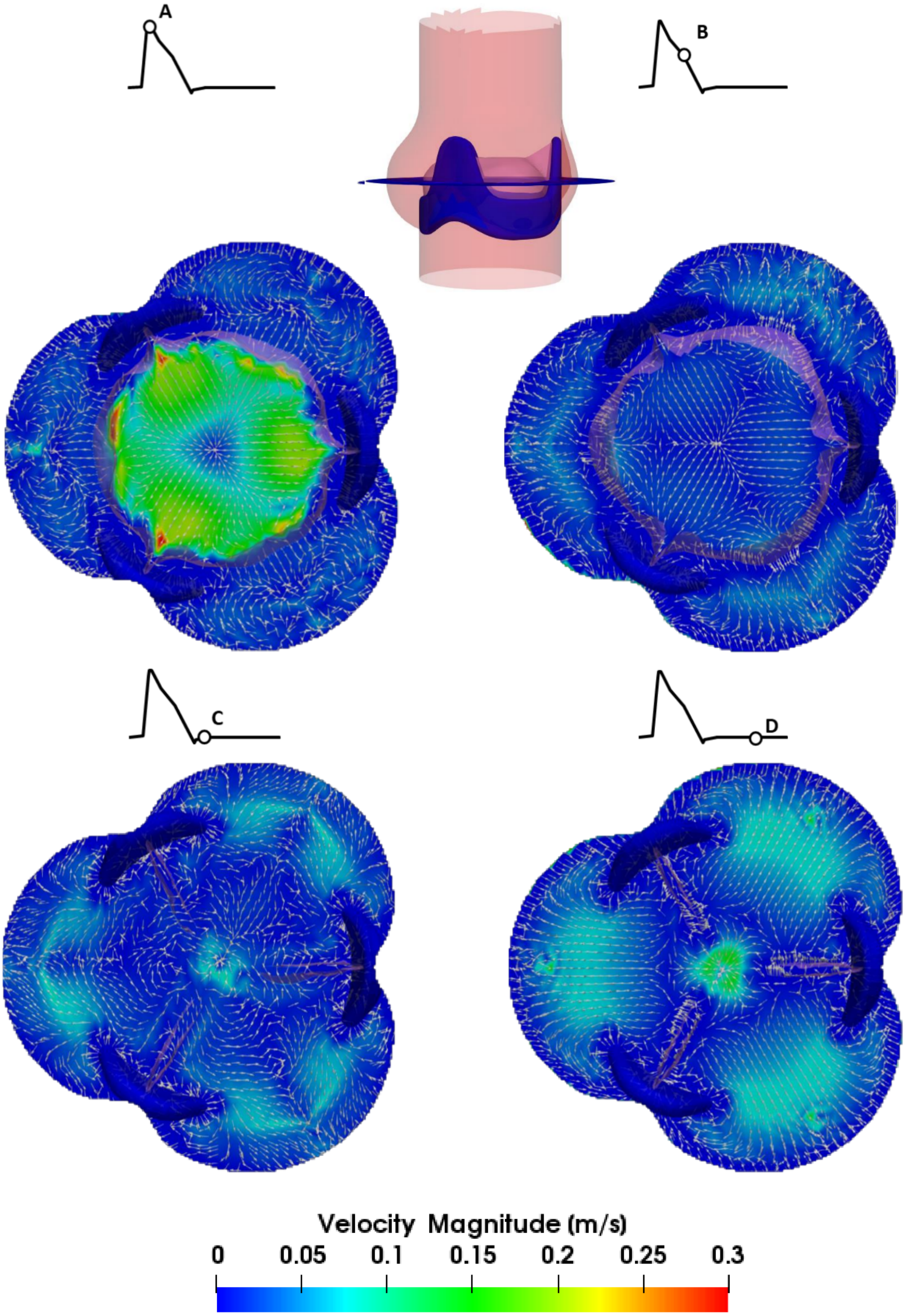

Figure 7.4. Flow contour maps and vectors across a transversal cross plane of the surgical bioprosthetic valve orifice.

7.1.2.2 TAVI

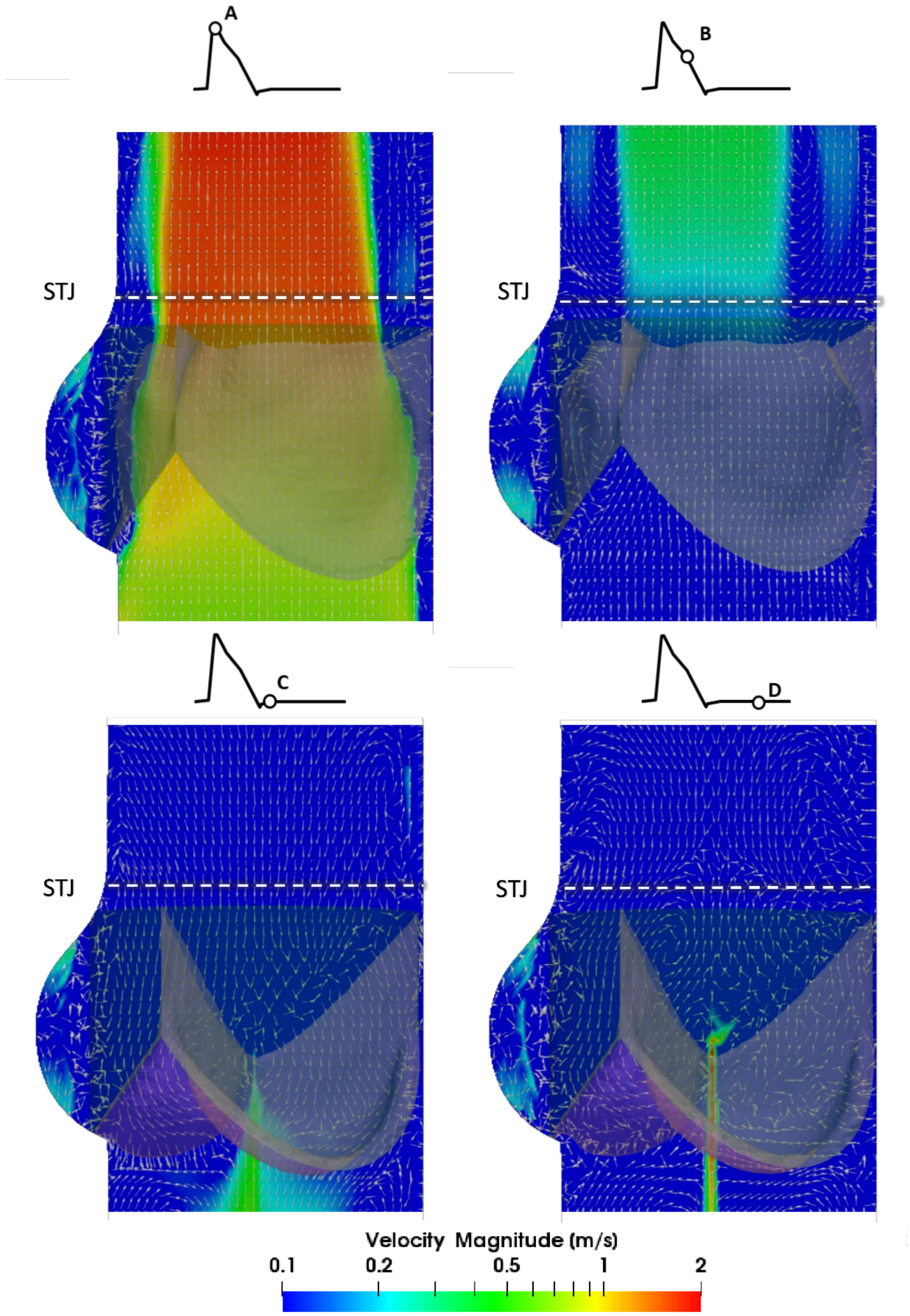

Figure 7.5. Velocity contour maps, vectors and profiles for TAVI configuration.

The flow dynamics occurring downstream of a TAVI at the four reference instants is provided in Figure 7.5.

A mostly symmetrical jet with a peak velocity of 1.6 m/s can be observed at instant A (Figure 7.5). No defined vortical structures can be detected within the Valsalva sinuses throughout the cardiac cycle. This is due to the insertion of the partition designed to replicate TAVI conditions, which reduces the available space in the cavity between the partition and the sinus wall. Vortices within the leaflets walls and at the jet edges become evident at late systole (Figure 7.5 *instant B*).

Large recirculations in proximity to the leaflets are detected in the early stage of diastole (Figure 7.5 *instant C*) and then split into multiple smaller vortices at the end of the diastolic phase (Figure 7.5 *instant D*).

Despite the presence of TAVI partition, which provides a simplified model of the native leaflets and stent, the haemodynamics of the TAVI model resembles physiological healthy results more closely than the surgical device configuration.

However, vortical activity within the sinus is very different from the young healthy configuration. Also, due to the presence of the partition, the shape of the open leaflets is very similar to that of the surgical model.

Hence, TAVI presents a prompt closure compared to the surgical bioprosthesis and the valve dynamics features at systole are more conforming to healthy values. However, it is important to point out that the presence of the partition totally obstructs the blood flow in washing out the sinus, resulting in blood stasis.

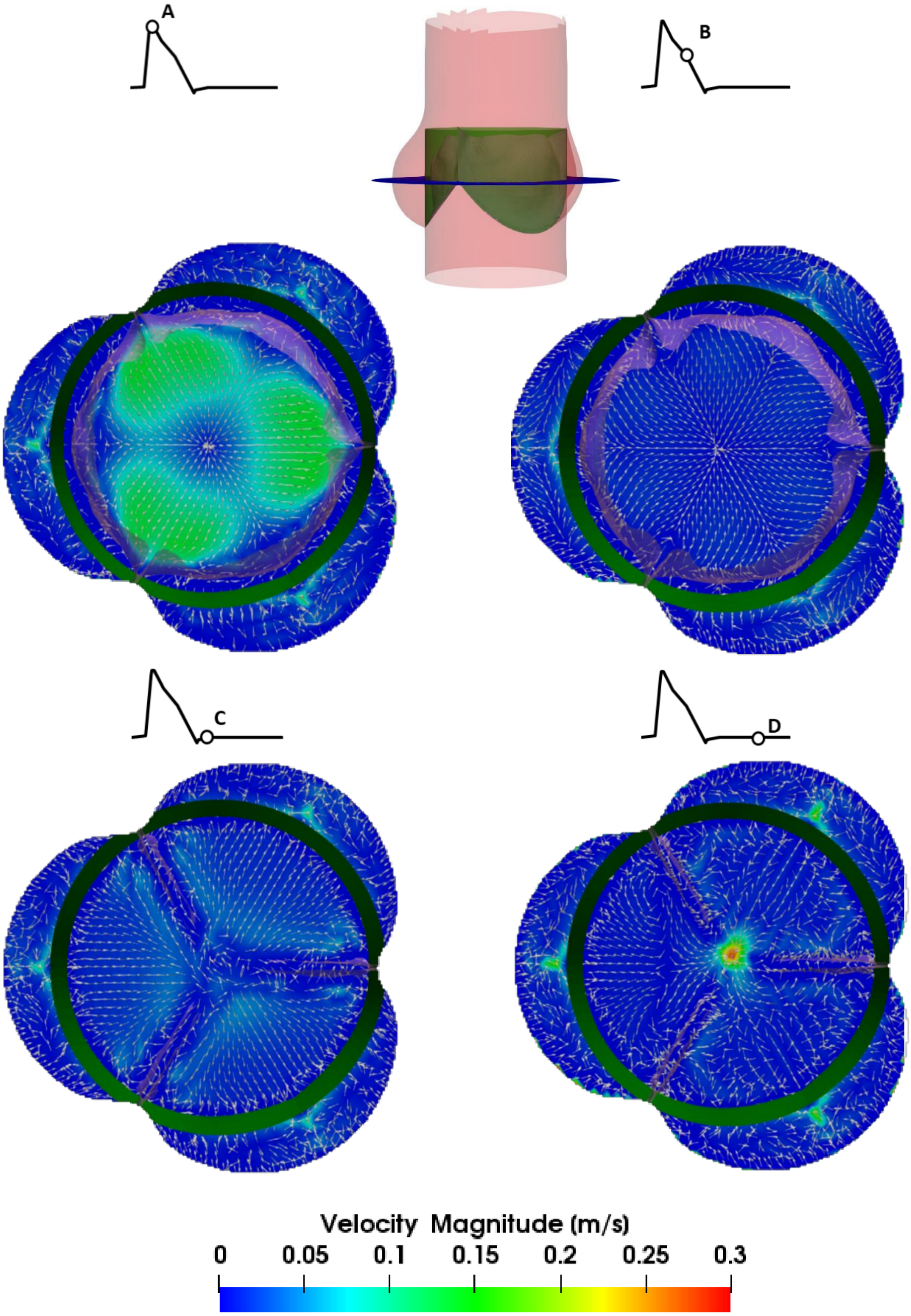

Figure 7.6. Flow contour maps and vectors across a transversal cross section of the TAV orifice.

Flow dynamics across the plane orthogonal to the valve axis and bisecting the Valsalva sinuses, is characterised by radial flow during systole (Figure 7.6 *instants A,B*), whilst in diastole, contrary to the young healthy situation, no vortical areas can be detected (Figure 7.6 *instants C,D*).

7.1.3 Comparison young healthy vs post treatment

A comparison of the axial velocity profiles at the sino-tubular junction for the young healthy (green), surgical (blue) and TAVI (orange) configurations, is provided in Figure 7.7.

Major departures from the healthy conditions can be detected in the surgical model, where, at the maximum flowrate, the calculated peak velocity difference expressed in percentage reaches +66.4 % compared with only +25 % for TAVI model.

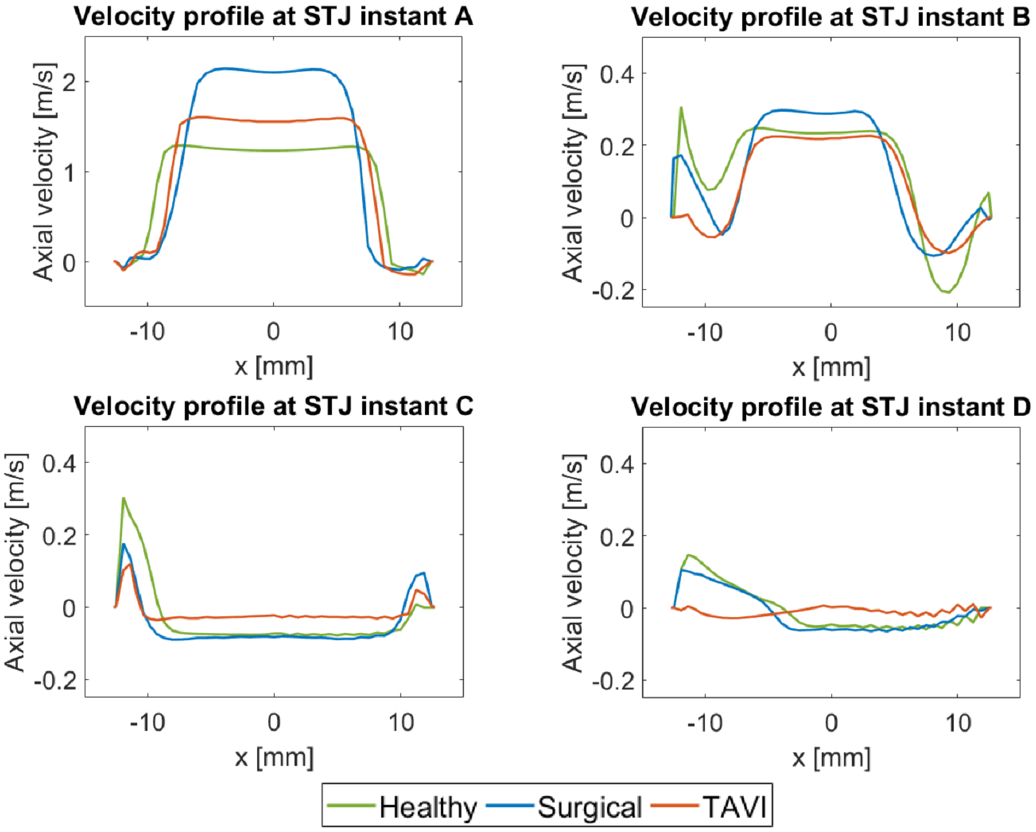

Figure 7.8. Comparison of the velocity profiles extracted at the STJ level for young healthy (green), surgical (blue) and TAVI (orange) models.

Overall, the comparison of the velocity profiles at the STJ shows how the major differences between the three models arise during the systolic peak (Figure 7.8 *instant A*) with an average departure (calculated over the entire profile) from the young healthy velocity profile values of 0.54 m/s for the surgical model and of 0.25 m/s for the TAVI model. Hence, TAVI velocity profiles are more consistent with healthy values also during the other instants of the cardiac cycle, apart from diastole where the average deviation from healthy conditions reaches 0.054 m/s and 0.053 m/s compared to an average difference of 0.033 m/s and 0.014 m/s between healthy and surgical, respectively at early and late diastole.

The comparison of the different configurations shows how the introduction of geometrical constraints has a major impact upon the valve functioning.

Although the valve leaflets are identical in terms of geometry, boundary constraints and material properties, in the absence of the stent (young healthy condition) they undergo a much wider opening, taking a bulging shape which closely matches the profile of the sinuses. As a result, the gap that forms between the leaflet and the aortic wall is reduced and does not allow the formation of large flow recirculations. This happens also for the TAVI case, since the partition acts as a barrier which obstructs the flow in circulating freely within the Valsalva sinuses.

A better view of the flow for the young healthy and treated configurations can be gained from Figure 7.9 where the streamlines at the leaflets' maximum opening and early closure are displayed using line integral convolution (LIC).

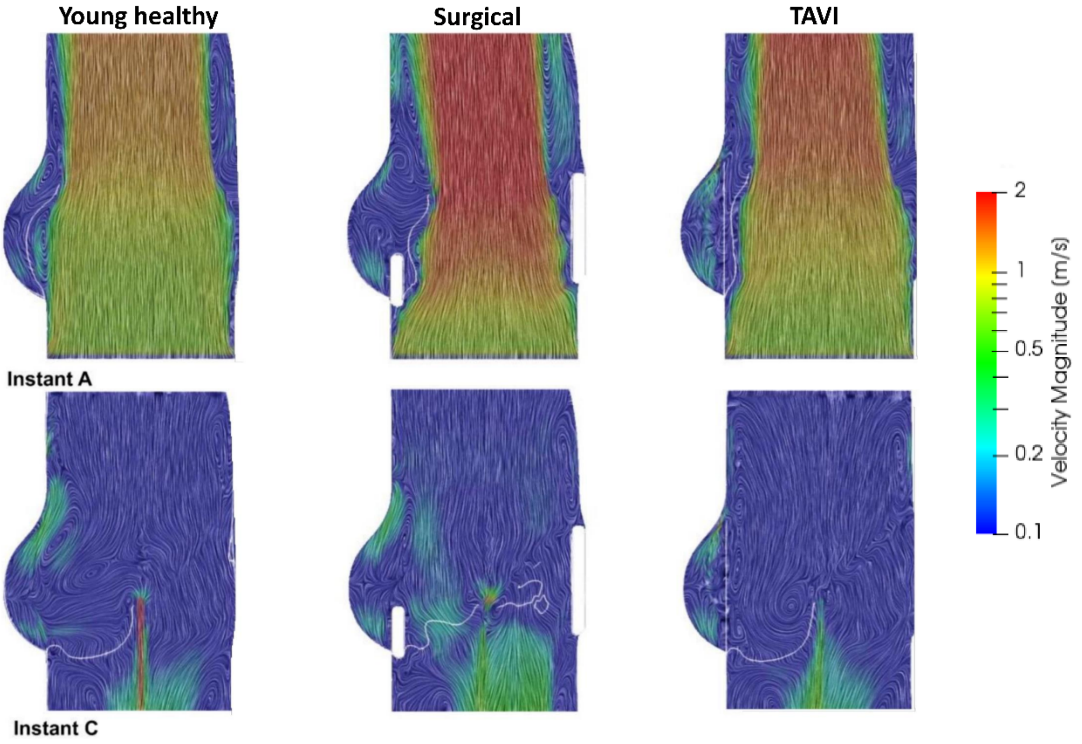

Figure 7.9. Velocity maps including leaflets opening (systolic peak, instant A) and closure profile (early diastole, instant C) obtained for the young healthy and virtually treated models. The velocity streamlines are visualised using line integral convolution (LIC).

It clearly shows how the presence of a stented prosthesis in the model representing a surgical valve procedure, determines a marked reduction in the ability of the leaflets to expand, leaving a much larger chamber between the valve and the sinus wall, thus enabling the formation of vortices within this volume.

However, the leaflets for the surgical prosthesis are smaller than those of the young healthy configuration therefore, even if they could expand, they would not possibly fill the sinus.

It is also worth mentioning that, during systole, the flow behaviour consists in a mostly symmetrical central jet for the healthy and TAVI case, and in an angulated and asymmetrical central forward flow for the surgical case.

7.1.4 Pressure maps, effective orifice area (EOA) and transvalvular pressure gradient

7.1.4.1 Surgical

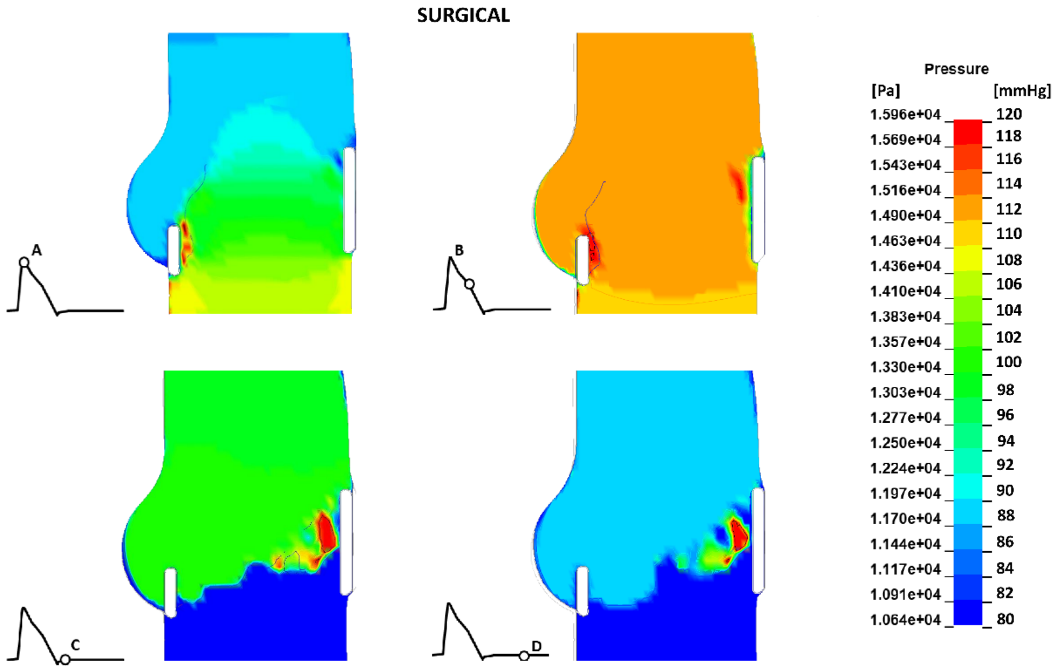

Figure 7.10. Pressure contour maps for the surgical bioprosthesis model.

An analysis of the pressure contour maps for the surgical treatment is shown in Figure 7.10.

The surgical configuration, as a result of its delayed opening at the systolic peak, presents a higher ventricular pressure with respect to the healthy case therefore leading to an increased ΔP (*Instant A* of Figure 5.5 and Figure 7.10). Pressure distributions in the other time frames are mostly coherent with young healthy pressure maps, though (*Instants B,C,D* of Figure 5.5 and Figure 7.10).

7.1.4.2 TAVI

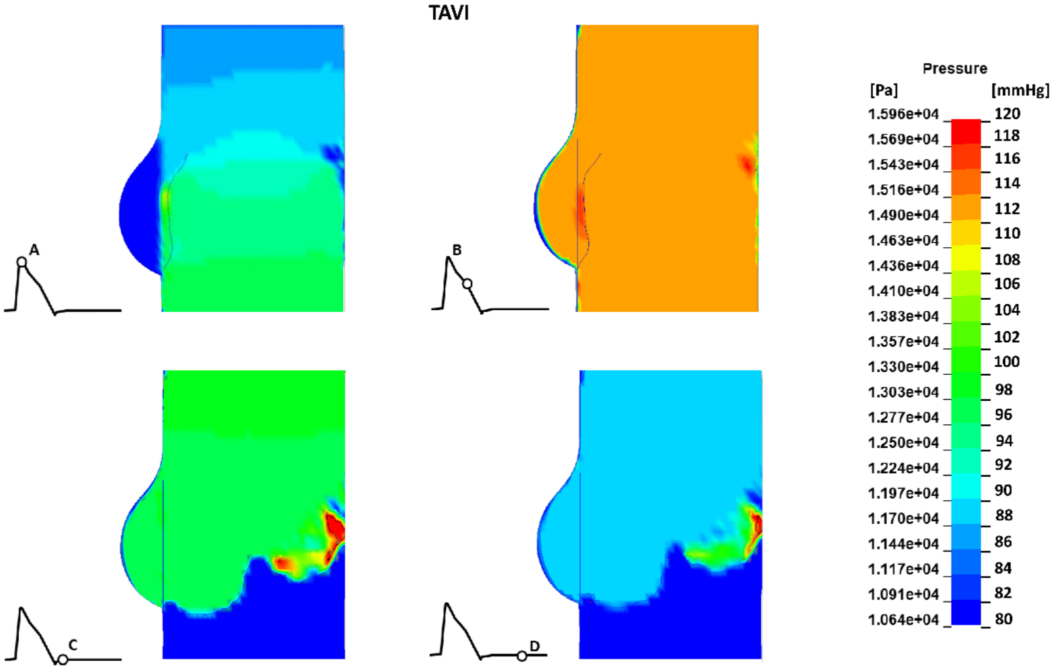

Figure 7.11.Pressure contour maps for TAVI configuration.

TAVI pressure distributions are more closely resembling those of the young healthy configuration and, at the maximum flowrate, the suction at the sinuses walls is even higher than that of the young healthy model (*Instant A* of Figure 5.5 and Figure 7.11). This is likely occurring due to the presence of the partition which splits the Valsalva sinuses into two different regions. However, this does not act on the prosthetic leaflets, which are also constrained by the presence of the barrier but are located between the native leaflets and the wall. Interestingly, it might have some effect on the coronary flow.

7.1.5 Comparison young healthy vs post treatment

The global analysis of pressure distributions within the young healthy aortic root, suggests that the function of the Valsalva sinuses during the ejection is to provide a chamber to optimally host the reverted cusps shape by creating a suction pressure (Figure 5.5 *instant A*). This mechanism strongly reduces the pressure drop and enhances the EOA, resulting in better hydrodynamic valve performance than those reported for surgical and TAVI configurations with a mean Transvalvular systolic pressure drop of 4.56 mmHg and an EOA equal to 2.94 cm^2.

In the surgical model instead, the higher ventricular pressure loads experienced by the bioprosthetic leaflets during systole results in a Transvalvular pressure drop value of 13.11 mmHg and therefore an EOA of only 1.73 cm^2. As shown in Table 7.2, which reports the valve performance indicators computed for the native and treated cases, TAVI clinical parameters are definitely improved when compared to the biological prosthesis, showing a percentage difference with respect to young healthy conditions of -20.7% for the EOA.

Table 7.2. Transvalvular pressure drop (ΔP) and EOA values for healthy and treated configurations.

Valve configuration	**ΔP[mmHg]**	**EOA $[cm^2]$**
Healthy	4.56	2.94
Surgical	13.11 (+187.5%)	1.73 (-41.1%)
TAVI	7.25 (+59%)	2.33 (-20.7%)

7.1.6 Pressure within the sinus

7.1.6.1 Young healthy vs post treatment conditions

For the young healthy case, the maximum pressure difference between the aortic outlet and the sinus is occurring at the instant preceding the systolic peak for all the elements, regardless their position with an average value of 6.2 mmHg (see Figure 7.12).

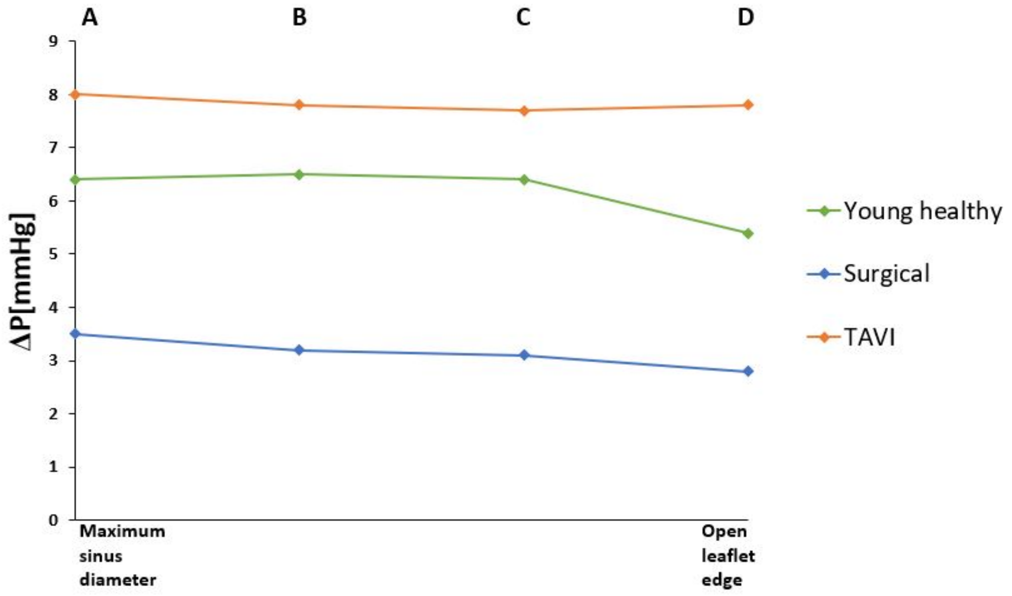

Figure 7.12. Graph showing the maximum suction effect values for the young healthy and treated configurations at sinus elements A, B, C and D at the valve opening instant.

Pressure values in healthy conditions are very similar for elements A, B and C whilst a drop can be observed at element D where pressure difference decreases to 5.4 mmHg.

The same trend can be observed also in the surgical configuration model (Figure 7.12), where such difference remains nearly constant among the different selected elements but its magnitude is strongly reduced (average 3.2 mmHg).

With regard to TAVI, such difference is slightly higher (average 7.8 mmHg) in terms of magnitude than the young healthy case. This is likely due to the presence of the partition walls (average 7.8 mmHg) which create a suction chamber but, at the same time, prevent such effect from having an impact on the cusps functioning.

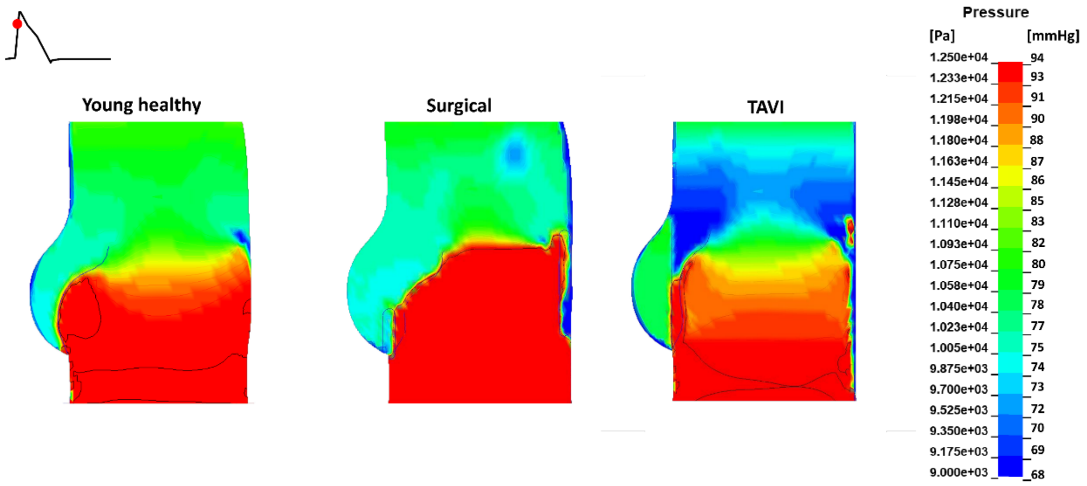

Figure 7.13. Pressure maps showing the maximum suction effect for physiological and 'treated' models at the instant preceding the systolic peak.

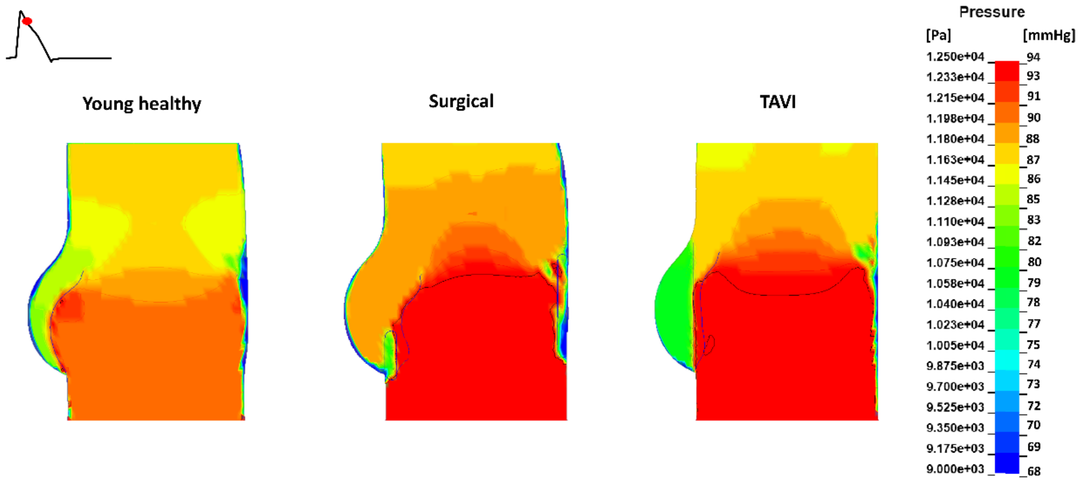

Figure 7.14. Pressure maps showing the maximum suction effect for physiological and 'treated' models at the instant following the systolic peak.

Contrary to what is observed for the young healthy and surgical cases, where the maximum variation occurs at the valve opening instant (see Figure 7.13), such variation in TAVI can only be detected after the systolic peak (Figure 7.14).

Also in the 'treated' models, the maximum pressure difference occurs simultaneously for all elements. Discrepancies between elements A, B, C and

D are found to be within -15.6 % for the young healthy, -3.75% for TAVI and -20% for surgical models, respectively.

7.1.7 Energy loss

7.1.7.1 Young healthy vs post treatment

As expected, forward and closing energy values for the healthy young model are lower compared to those of the treated configurations (see Table 7.3).

Table 7.3. Energy loss values for healthy and virtually treated configurations.

Valve configuration	Forward energy loss [mJ]	Closing energy loss [mJ]	Total energy loss [mJ]
Healthy	67.7	36.9	104.6
Surgical	191.14 (+182.33%)	83.29 (+125.71%)	274.43 (+162.36%)
TAVI	101.61 (+50.08%)	82.89 (+124.63%)	7.5 (+76.38%)

The deviation from the healthy condition in terms of global energy loss (calculated as the sum of the forward and closing energy values), was found to be 162.36% for the surgical bioprosthesis and +76.38% for the TAVI device. The surgical prosthesis presents the highest forward energy whilst in terms of closing energy loss they present very similar values.

7.5.1 Blood damage

7.5.1.1 Fluid shear stress in healthy and treated conditions

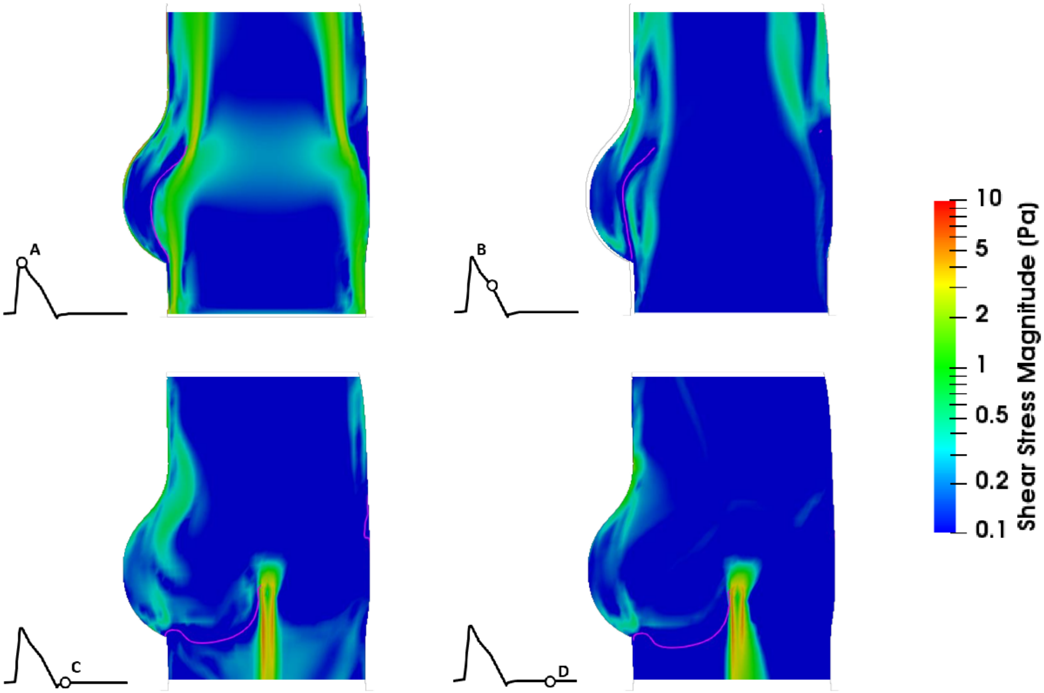

Figure 7.15. Fluid shear stress magnitude contour maps for the young healthy model.

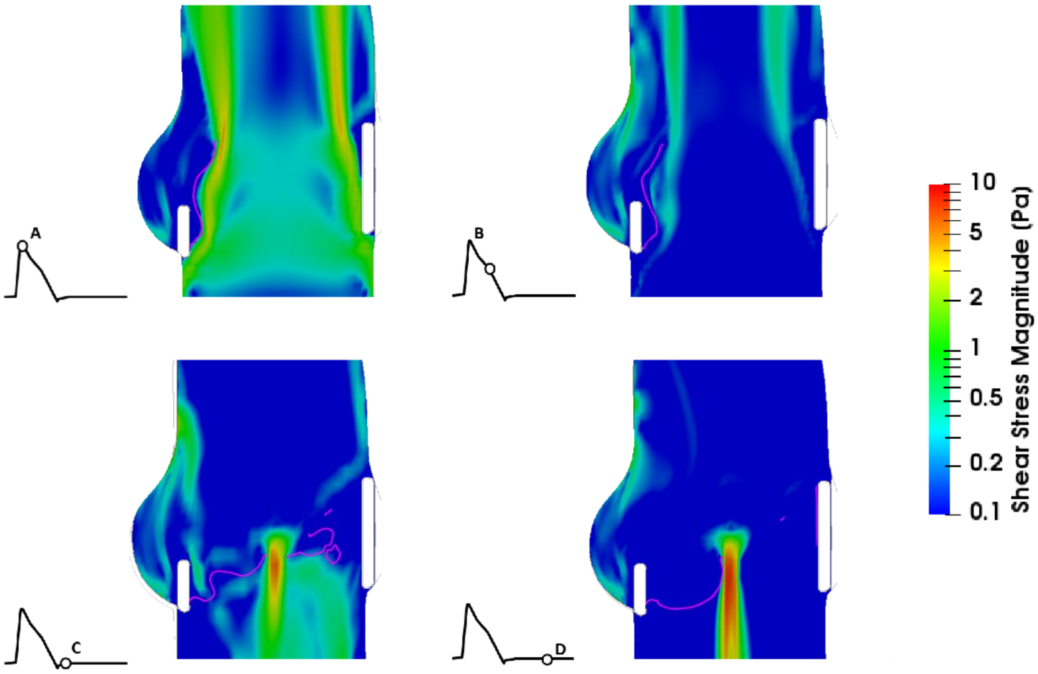

Figure 7.16. Fluid shear stress magnitude contour maps for the surgical model.

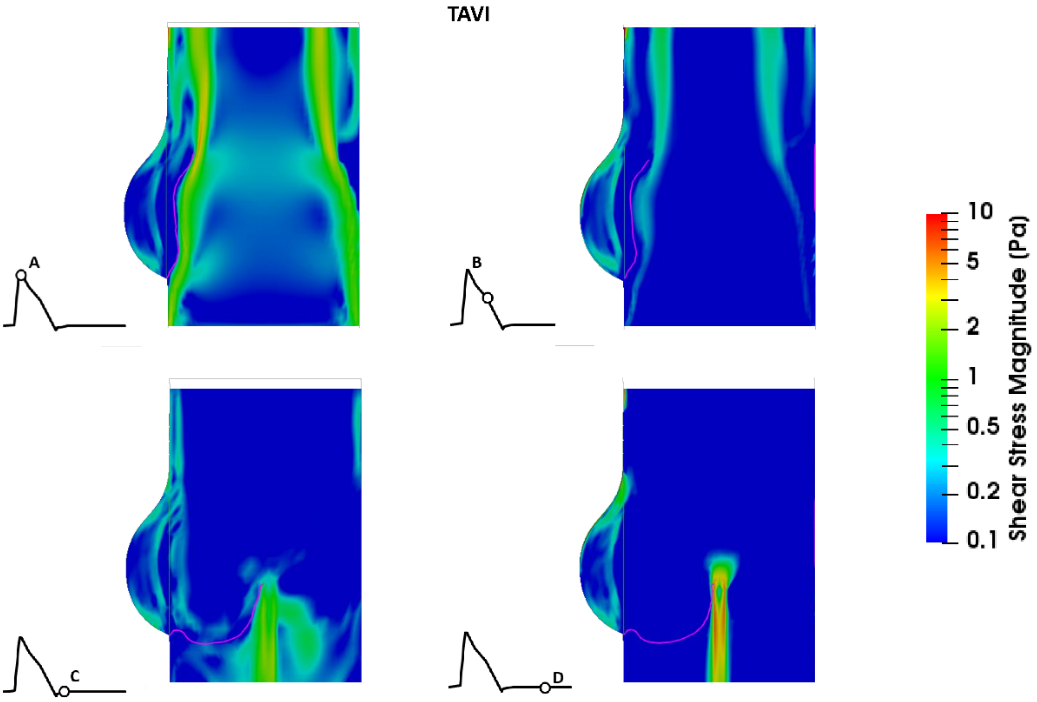

Figure 7.17. Fluid shear stress magnitude contour maps for TAVI model.

As in Chapter 6 for ageing conditions, fluid shear stress maps were also analysed in models replicating post treatment conditions.

In all configurations, higher values of shear stress were detected at valve closure. Table 7.4 shows the maximum shear stress levels calculated over the entire cardiac cycle.

Table 7.4. Maximum shear stress values for healthy and post treatment models.

Configuration	**Maximum shear stress [Pa]**
Healthy	9.2
Surgical	9.5 (+3.2%)
TAVI	9.4 (+2.1%)

However, as already mentioned in section 6.1.8.1, the limitations due to FSI methodological artefacts need to be taken into account (see section 6.1.3).

Also in post treatment configurations, the shear stress magnitude falls well below the hemolytic threshold indicated by Leverett *et al.* (Leverett et al., 1972).

7.5.1.2 Wall shear stress in healthy and treated conditions

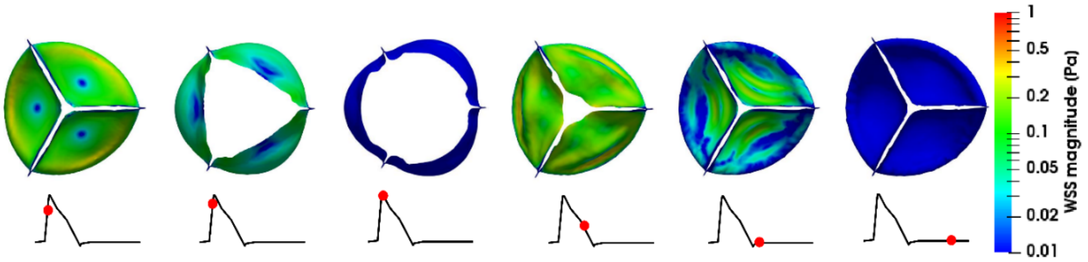

Figure 7.18. WSS acting on the leaflets for the young healthy configuration.

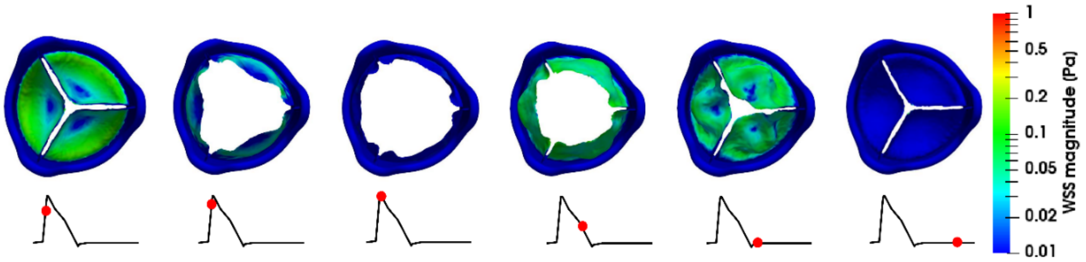

Figure 7.19. WSS acting on the leaflets for the surgical configuration.

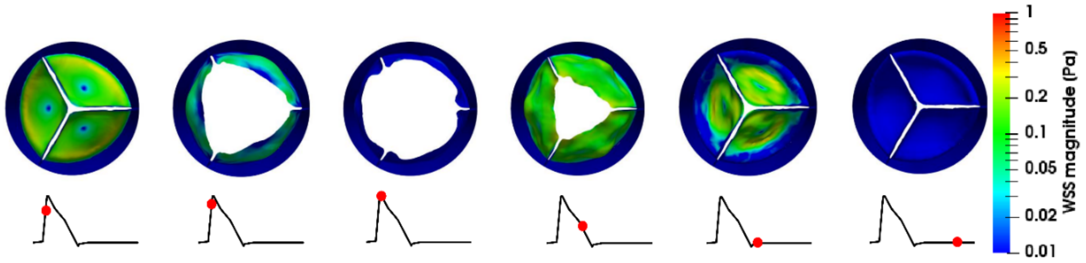

Figure 7.20. WSS acting on the leaflets for TAVI configuration.

Figure 7.18, Figure 7.19 and Figure 7.20 show contour plots of the WSS magnitude acting on the leaflets of the young healthy and post treatment configurations at different instants of the cardiac cycle.

Higher values of WSS are shown during the valve closing phase for all configurations.

Among prosthetic devices, TAVI presents the highest levels of WSS magnitude which can be detected at the cusps' commissures and belly while the valve is closing, consistently with the physiological healthy pattern.

Also in this case, as reported previously in section 6.1.8.2 for ageing models, given the low levels of fluid shear stress and WSS acting on the leaflets blood damage, if present, cannot be correlated with high shear stress values.

7.6 Discussion

The healthy model was also adapted to reproduce post treatment conditions.

As in the numerical study replicating ageing conditions (Chapter 6), valvular kinematics, velocity fields, pressure distributions and valve performance indicators were analysed and compared with ideal native healthy conditions. This allowed the way in which existing treatments may positively affect the aortic valve well-function to be investigated.

The valve kinematics were studied via tracking the leaflets' radial displacement, and the valve opening and closing times were examined.

In addition to shorter valve opening and closing times compared to the treated configurations, the native healthy leaflets present also a maximum radial displacement which is 20% and 12% higher than that measured for surgical and TAVI cases, respectively.

Whilst TAVI and young healthy configurations open simultaneously, the surgical bioprosthesis opens slightly earlier and is the last to complete a competent closure. This results in an ejection time of 362 ms (42% of the cardiac cycle) compared to only 310 ms (36% of the cardiac cycle) and 330 ms (38% of the cardiac cycle) for young healthy and TAVI conditions.

Then, an analysis of the velocity maps and vectors provided an insight into the global flow features and blood flow patterns within the Valsalva sinuses.

Contrary to most FSI works which, given the complexity of simulating leaflets coaptation, address the systolic phase of the cardiac cycle only (Kheradvar et al., 2015), in this study, the time frames selected for the investigation of the velocity and pressure distributions, included both systolic and diastolic phases.

A systolic peak velocity of 1.28 m/s was measured in the young healthy model. This value significantly increases in the treated configurations with peak velocities of 2.13 m/s and 1.6 m/s for surgical and TAVI devices, respectively. Hence, due to its acceleration, the jet at the maximum flowrate is slightly inclined for the surgical valve, whilst mostly symmetrical for native and TAVI conditions.

The analysis of the velocity profiles extracted at the STJ shows how the implantation of a surgical bioprosthesis produces higher velocities and therefore presents major discrepancies with respect to the young healthy native valve (Figure 7.8 *instants A and B*). However, diastolic velocity profiles are matching healthy values more closely than TAVI (Figure 7.8 *instants C and D*).

The bigger variations occur at *instant A* due to the highly dynamic behaviour characterising the valve opening. In terms of flow pattern across the sagittal plane, surgical and TAVI treatments still preserve some physiological healthy features such as systolic recirculations in the region adjacent to the leaflets inner walls and diastolic large recirculations supporting closure, although the full vortex development for the surgical heart valve only occurs at late diastole, therefore translating into a much stiffer and delayed closure mechanism.

In the transversal plane, vortical activity is strongly reduced when compared to the young healthy case scenario where instead, two counter rotating vortices are observed next to the plane bisecting each sinus throughout the diastolic phase, likely promoting a fully sealing of the valve's cusps (Figure 5.4, Figure 7.4, Figure 7.6).

With regard to the valve hydrodynamic indicators, the detected valve kinematics and flow velocity features described above have been shown to directly impair the valve global performance.

In fact, the EOA value for the young healthy case was measured to be 2.94 cm^2 , whilst it was found to be strongly (1.77 cm^2) and slightly (2.33 cm^2) reduced for surgical and TAVI treatments respectively, in accordance with data reported by other works focused on surgical bioprostheses (Cleveland et al., 2017; Eichinger et al., 2004; Jamieson et al., 2005) and TAVI devices (Külling et al., 2018; Maleki et al., 2015). It is worth mentioning that, because of the presence of the stent, the leaflets diameter at the base of the surgical prosthesis was 23 mm and not 25 mm as in the other models, though.

Energy losses results also denoted a reduced efficiency for the 'virtually treated' models. Global energy loss discrepancies of 162.36% and 76.38% were reported for surgical and TAVI configurations with respect to the young healthy valve. The altered flow dynamics observed in TAVI mostly during the diastolic phase resulted in a closing energy of 82.89 mJ, which is 124.63% higher than the healthy value.

Overall, major changes could be detected in the valve opening and functional mechanisms between the young healthy and virtually treated models.

For instance, whilst in the surgical case vortices within the sinus were detected at systole, in healthy conditions such features are absent given the wide radial displacement of the leaflets which does not allow for the formation of recirculations within the sinus area.

This study suggests that the presence of systolic vortices in the sinuses, subject of much of the literature to date (Bellhouse & Talbot, 1969; Salica et al., 2016; Toninato et al., 2016), is not associated with healthy operating conditions, but rather with stiffened dynamics due to calcifications, geometric mismatch or other non-physiological causes, such as the constricting presence of a supporting stent, as in the presented *post treatment* cases. It also highlights that experimental settings based on the inclusion of a bioprosthesis to mimic the native aortic valve, cannot be representative of realistic healthy native conditions.

Similarly, although based on the same design, the leaflets kinematics profiles result in a completely distinct opening behaviour (Figure 7.9). This may be due to the presence of the stent for the surgical configuration and, of the partition for TAVI, which obstruct the leaflets in expanding further within the sinuses. It is worth to notice that TAVI devices, despite the barrier created with the partition, provide systolic features more similar to those observed for the physiological healthy behaviour.

Nevertheless, as already mentioned in section 2.3.2, they may present thrombogenic potential. In particular, as described in the literature, an higher incidence of silent ischemic lesions and dementia was observed after TAVI rather than surgical valve replacement (Kahlert et al., 2010; Rodés-Cabau et al., 2010). These complications are likely to be associated with haemodynamics irregularities downstream the valve which eventually escalate into thrombus formation (Ducci et al., 2013). This may be due to the presence of calcific native leaflets and stent design, which completely obstructs the blood flow in circulating within the sinus therefore creating permanent stagnation, as observed in *instants A,B,C and D* of Figure 7.5.

However, recently, such complications were also identified in patients with surgical biological prostheses (Makkar et al., 2015), to a lesser extent, though. In order to shed some light on this matter, shear stresses were also investigated but no major alterations that could be associated to blood damage, were detected.

Hence, this study confirms that the presence of prosthetic devices whether transcatheter or surgical implanted heart valves, has a significant impact on the valve well-functioning, possibly leading to post procedural complications in the long term, given also the possible insurgence of comorbidities.

Chapter 8 Conclusions and Future works

8.1 Conclusions

In this study, the use of numerical FSI models, validated with *in vitro* findings, has led to a more complete understanding of the physiological healthy mechanisms that determine the aortic valve function.

The study has revealed an alternative phenomenon to what is currently described in the literature, where the function of vortical flow regions within Valsalva sinuses during the systolic phase appears strongly disproved. This leads to a more efficient functioning, that has not been reported before.

The model presented can serve as a benchmark for the flow conditions associated with a young healthy functioning mechanism of the aortic valve, providing optimum valve performance indicators. This represents an important basis for improving investigation of the haemodynamics change produced both in ageing and in existing treated conditions.

The investigation performed upon the implantation of prosthetic devices enlightened how the latter produces major alterations in terms of haemodynamics which compromise the valve function and lead to diminished performance.

Whilst in the young healthy case the sinuses promote a radial flow which supports a prompt opening, in the surgically treated model the presence of the stent obstructs the leaflets in expanding fully, resulting in a faster jet.

Globally, surgical valves presented the worst performance however, it is important to take into account that, due to the presence of the stent, their leaflets are smaller. TAVI, on the other hand, showed good systolic features but a high closing energy value. Also, the presence of the partition in TAVI completely isolates the haemodynamics established within the sinus from the central jet, so that no suction effect could act on the leaflets, it might have some impact on the flow in the coronary arteries, though.

Stented devices were therefore found to consistently affect the global flow dynamics, particularly in terms of valve opening behaviour. In fact, currently modelled prosthetic devices are still far from accurate in terms of replicating native conditions. Their design does not allow for the biological leaflets to achieve a full opening since their shape is based on a cylindrical opening profile.

Hence, neither surgical bioprostheses nor TAVI devices are able to fully restore physiological healthy conditions.

On the other hand, the occurrence of aging diseases such as stiffening and progressive aortic root dilation, has shown to markedly alter the haemodynamics and mechanical efficiency of the aortic valve. The results suggest that even low degrees of tissue stiffening strongly affect the valve functioning, whilst aortic root dilation can mitigate the impairment due to the altered mechanical properties by enlarging the available flow areas.

In terms of valvular dynamics, all ageing simulations showed significant deviations from healthy conditions particularly in terms of closing times.

Although it might seem that the performance of the aortic valve within the dilated aortic root is improved when compared to the healthy configuration, this is misleading if we consider that the aortic valve is bigger in that case and for instance parameters such as the EOA are not accordingly enhanced. This is also confirmed by the suction effect which is observed to be higher at valve opening in the ageing cases, but not to last as seen in the young healthy model.

However, in both young healthy and ageing models the emerging function of the sinuses appears to be that of hosting the reverted cusps by supporting the leaflets' radial displacement within the sinuses bulges, rather than promoting the formation of systolic vortices. In fact, contrary to the post treatment configuration, ageing cases are consistent with the healthy model in terms of leaflets opening shape.

This study confirms the role that numerical approaches can play in the prediction of pathologies induced by flow alterations, providing a full view of the flow dynamics within the aortic root that are limited using experimental techniques.

In conclusion, the proposed model is suitable to predict the haemodynamics in young healthy, ageing and post treatment conditions, supplying a powerful tool for therapeutic planning and for the design of novel/improved devices.

8.2 Limitations

Although the validated FSI model was shown to realistically and accurately simulate the fluid dynamics established in the aortic root, some assumptions still need to be considered. The shape and dimensions of the aortic valve and root are based on an idealised model assuming that the 3 Valsalva sinuses and their corresponding leaflets are identical, thereby introducing a 120-degree geometrical symmetry. In reality, the native aortic valve and root are characterised by individually specific shapes and dimensions presenting relevant degrees of asymmetry. The physiology of the native aorta is longer and more complex than that presented in this study, which could induce alterations to the fluid dynamics. Moreover, the presence of coronary arteries was not taken into account and requires future studies, as does the effect of different degrees of wall compliance upon the haemodynamics of the region. Finally, the outlet of the fluid domain is relatively close to the aortic root so that the associated boundary layer effect cannot be fully eliminated.

As for the numerical method employed, the FSI solver employed is only applicable to laminar flow and it is not appropriate to model boundary layer flow effects. It introduces some limitations in terms of time duration since it is based on an explicit time integrated solution wherein the time step is limited based on element size and material sound speed. LS-DYNA ALE method is more time consuming than the Lagrangian method since adds additional computational time due to advection and interface reconstruction and coupling process.

8.3 Future works

8.3.1 Modelling of patient specific geometries

The shape and dimensions of the aortic valve and root used to describe young healthy, ageing and post treatment conditions are based on idealised models assuming that three Valsalva sinuses and their corresponding leaflets are identical, therefore introducing a 120-degree geometrical symmetry. However, native aortic valve and vessel geometrical shape and dimensions are strongly dependent upon the dimensions and size within each individual, presenting a certain degree of asymmetry.

Using imaging methods such as magnetic resonance imaging (MRI) and three-dimensional echocardiography, patient specific properties such as the leaflets, aortic root geometries and thicknesses could be used to build the numerical model. Also, validation could be more easily performed by direct comparison of the results from the simulation with *in vivo* data.

8.3.1 Population specific models

Conducting population-specific studies selecting patients belonging to specific clinical categories could be very valuable in the identification of common characteristic associated with a specific population. Data from groups of patients would not only allow to achieve a greater accuracy, but also help in the classification of patients according to a different metrics.

8.3.2 Modelling of coronary arteries

The presence of coronary arteries has been shown to have an impact upon the local fluid dynamics within the sinuses (Moore & Dasi, 2015). In the future, this can be accomplished by first establishing the position of the coronary ostia in the sinuses of Valsalva as reported in the literature. Then, to match the physiology of a normal human heart, a left coronary artery (LCA) sinus, a right coronary artery (RCA) sinus, and a non- coronary artery (NCA) sinus can be inserted into the FSI model. All reported effects upon sinus haemodynamics (whether in presence or absence of coronary arteries) can be compared, alongside any evidence of pulsatile flow within the coronaries during the cardiac cycle.

The results could be examined to develop a characterization of the flow pattern within a sinus of Valsalva in the presence and absence of coronaries.

8.3.3 Modelling of thrombus formation

The computational models could be adapted to investigate the formation of thrombi after aortic valve replacement by means of particle tracking techniques. This would further shed some light on post treatment complications detected after TAVI and surgical valve implantation (Makkar et al., 2015).

8.3.4 Modelling of calcification

Integrating leaflets' calcification pattern models within the numerical analyses would also be really interesting since it would allow to investigate how different levels of calcification and patient-specific patterns affect the valve function and likely identify factors that may have on impact on the formation of calcification.

Appendix A

Valve kinematics: valve opening, valve closure and ejection time

Ageing conditions

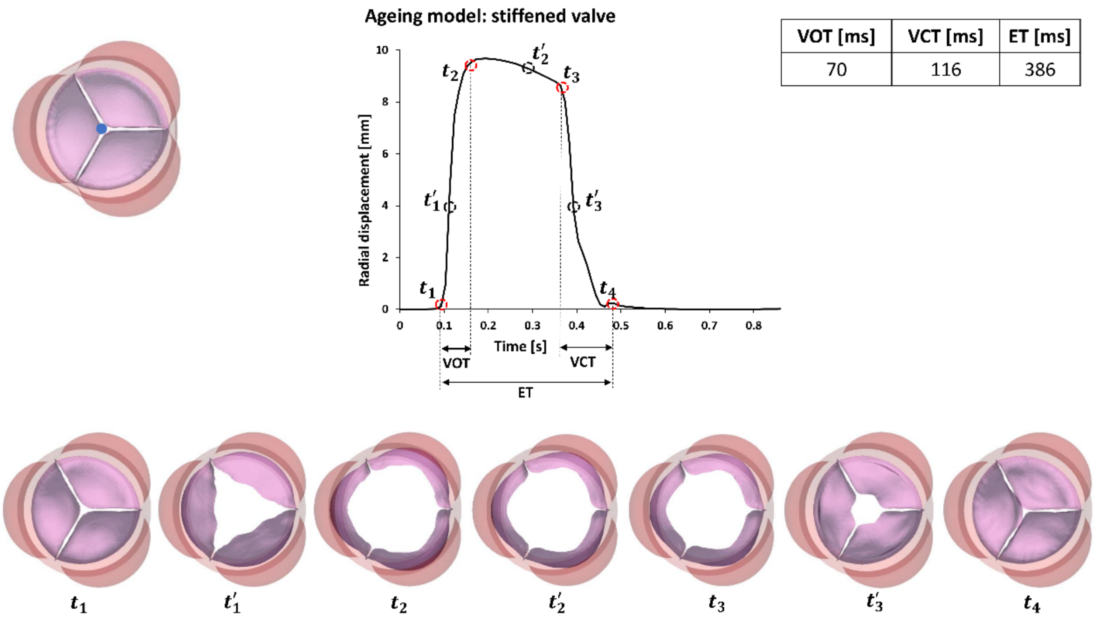

VOT [ms]	VCT [ms]	ET [ms]
70	116	386

Figure A1. Detailed view of leaflets kinematics throughout the cardiac cycle for the stiffened valve model. The blue point on the leaflet shows the location of the node where the displacement was tracked.

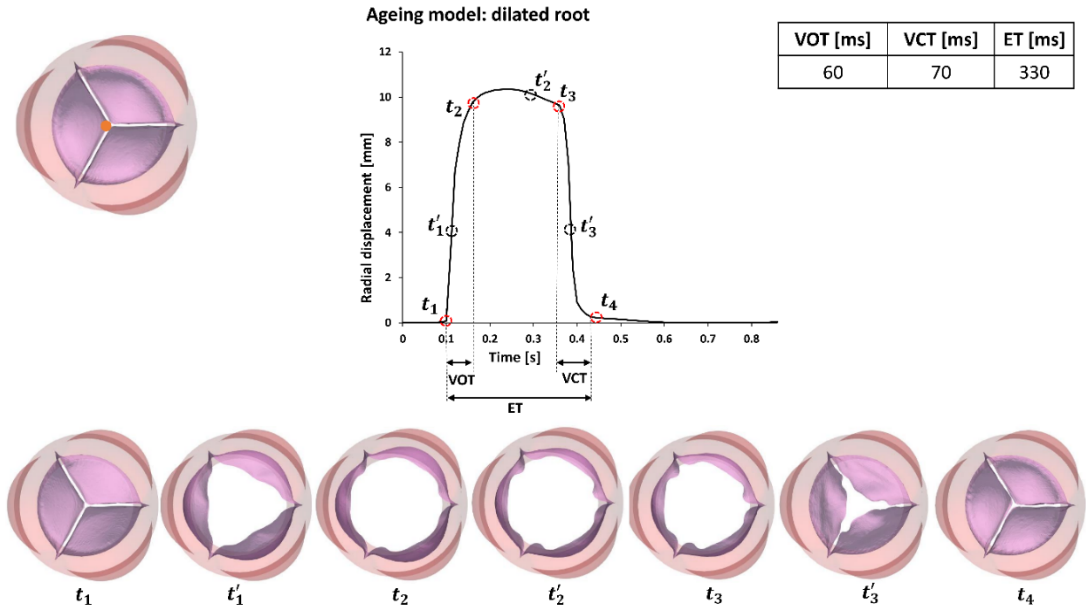

VOT [ms]	VCT [ms]	ET [ms]
60	70	330

Figure A2. Detailed view of leaflets kinematics throughout the cardiac cycle for the dilated root model. The orange point on the leaflet shows the location of the node where the displacement was tracked.

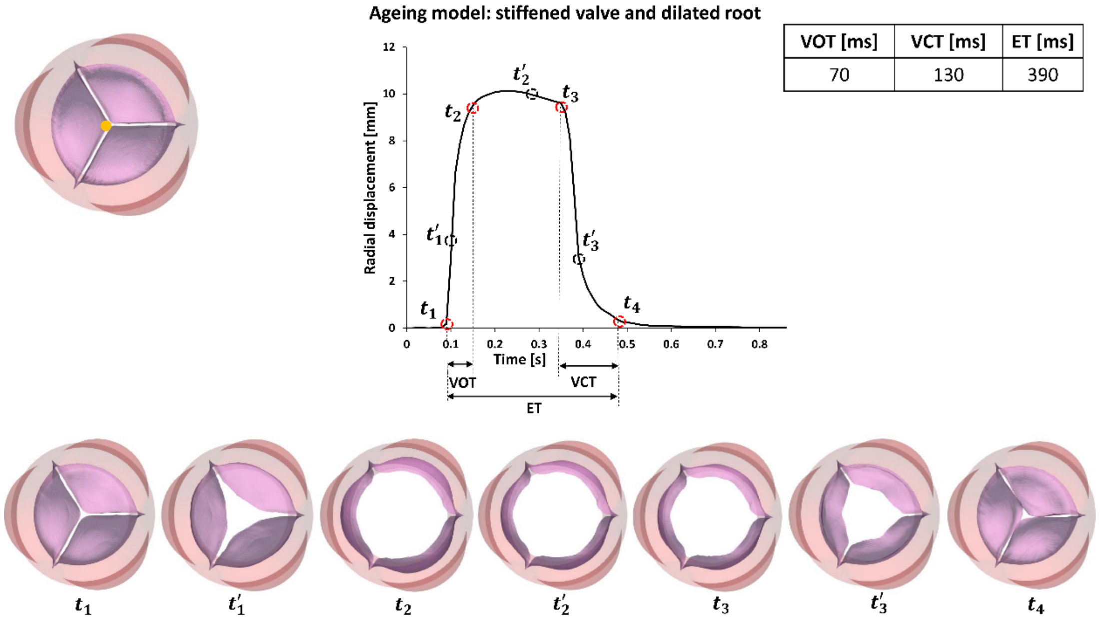

VOT [ms]	VCT [ms]	ET [ms]
70	130	390

Figure A3. Detailed view of leaflets kinematics throughout the cardiac cycle for the stiffened valve and dilated root model. The blue point on the leaflet shows the location of the node where the displacement was tracked.

Post treatment conditions

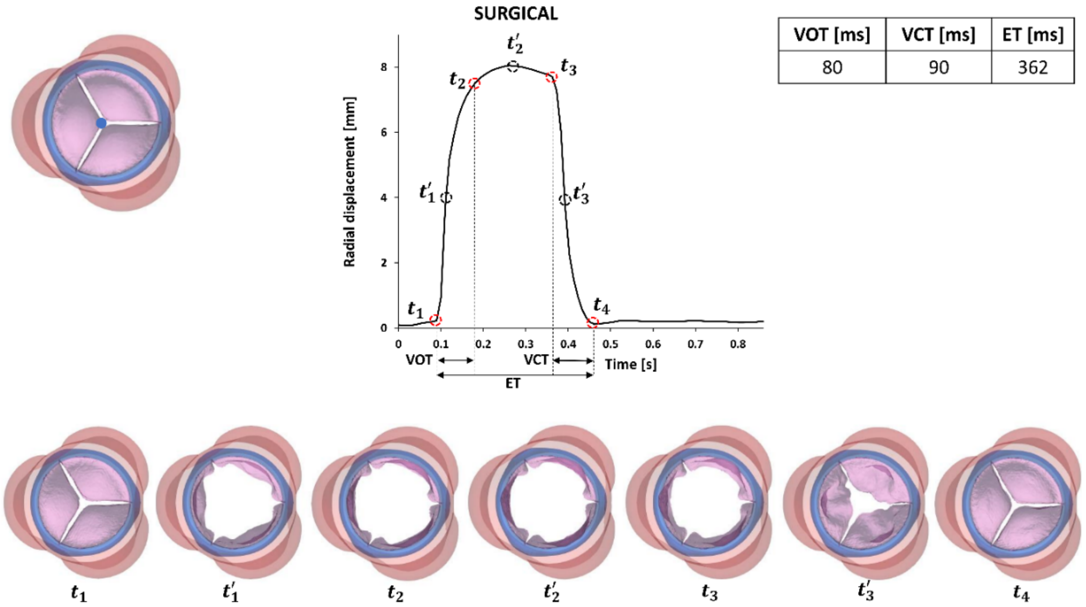

VOT [ms]	VCT [ms]	ET [ms]
80	90	362

Figure A4. Detailed view of leaflets kinematics throughout the cardiac cycle for the surgical model. The blue point on the leaflet shows the location of the node where the displacement was tracked.

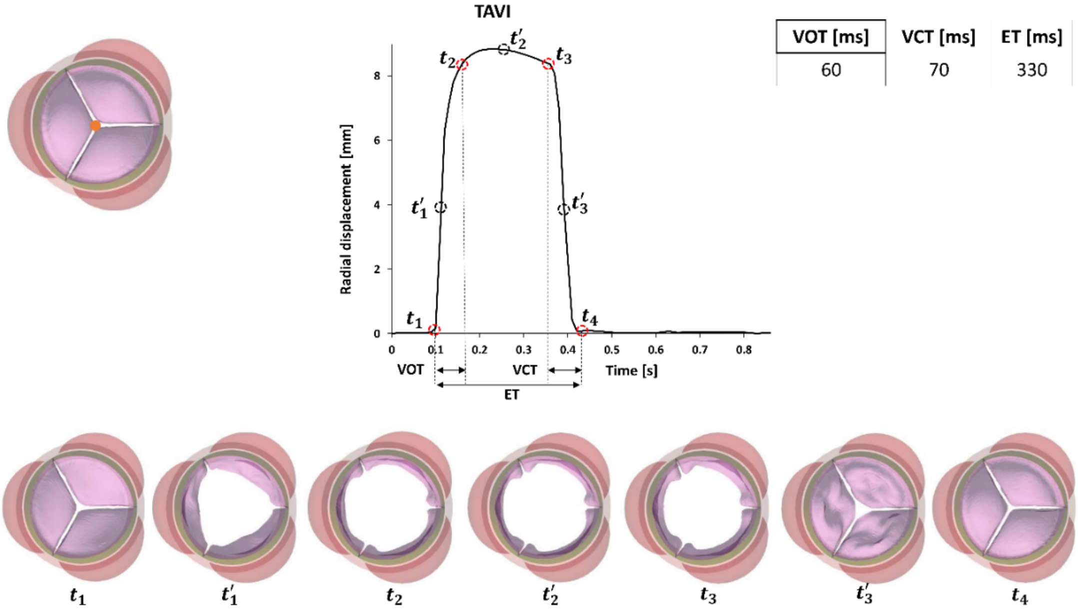

VOT [ms]	VCT [ms]	ET [ms]
60	70	330

Figure A5. Detailed view of leaflets kinematics throughout the cardiac cycle for TAVI model. The orange point on the leaflet shows the location of the node where the displacement was tracked.

Publications and presentations

Tango, A. M., Ducci, A., & Burriesci, G. (2017). *Fluid-structure-interaction model of Transcatheter Aortic Valve Implantation configuration: comparison with an in-vitro study.*

Presented at: 7th International Conference on Computational Bioengineering, Compiègne, France.

Tango, A. M., Salmon, J.A., Ducci, A., & Burriesci, G. (2018). *Experimental validation of Fluid Structure Interaction Models of the Aortic Valve by Means of Particle Image Velocimetry.*

Presented at: 8th World Congress of Biomechanics, Dublin, Ireland.

Tango, A.M., Salmon, J.A., Ducci, A., Burriesci, G. (2018) *Fluid-structure-interaction model of a Prosthetic Aortic Valve Implantation configuration: comparison with an in-vitro study.*

Presented at: Frontiers of Simulation and Experimentation for Personalised Cardiovascular Management and Treatment, London, UK.

Tango, A.M., Salmon, J.A., Ducci, A., Burriesci, G. (2018) *Young healthy Aortic Valve Dynamics - Extension after PIV Validation of a Fluid Structure Interaction.*

Presented at: 9th International Congress on Industrial and Applied Mathematics, Valencia, Spain.

J. Salmonsmith, A. M. Tango, A. Ducci, and G. Burriesci, "Haemodynamics issues with transcatheter aortic valve implantation," in *Transcatheter Aortic Valve Implantation: Clinical, Interventional, and Surgical Perspectives.*, A. Giordano, G. Biondi-Zoccai, and G. Frati, Eds. Springer International (2019).

Tango, A. M., Salmonsmith, J., Ducci, A., & Burriesci, G. (2018). Validation and Extension of a Fluid–Structure Interaction Model of the Young healthy Aortic Valve. *Cardiovascular Engineering and Technology*, *9*(4), 739–751.

Bibliography

Abbas, A. E., Franey, L. M., Goldstein, J., & Lester, S. (2013). Aortic valve stenosis: To the gradient and beyond - The mismatch between area and gradient severity. *Journal of Interventional Cardiology*, *26*(2), 183–194.

Akins, C. W., Travis, B., & Yoganathan, A. P. (2008). Energy loss for evaluating heart valve performance. *The Journal of Thoracic and Cardiovascular Surgery*, *136*(4), 820–833.

Amindari, A., Saltik, L., Kirkkopru, K., Yacoub, M., & Yalcin, H. C. (2017). Assessment of calcified aortic valve leaflet deformations and blood flow dynamics using fluid structure interaction modeling. *Informatics in Medicine Unlocked*, *9*(July), 191–199.

Andersen, H. R., Knudsen, L. L., & Hasenkam, J. M. (1992). Transluminal implantation of artificial heart valves. Description of a new expandable aortic valve and initial results with implantation by catheter technique in closed chest pigs. *European Heart Journal*, *13*(5), 704–708.

Anderson, R. H. (2000). Clinical anatomy of the aortic root. *Heart (British Cardiac Society)*, *84*(6), 670–673.

Aquelet, N., Seddon, C., Souli, M., & Moatamedi, M. (2005). Initialisation of volume fraction in fluid/structure interaction problem. *International Journal of Crashworthiness*, *10*(3), 237–247.

Aquelet, Nicolas. (2012). ALE Adaptive Mesh Refinement in LS-DYNA ff. *12th International LS-DYNAff Users Conference*, (2), 1–20.

Azadani, A. N., Jaussaud, N., Matthews, P. B., Ge, L., Guy, T. S., Chuter, T. A. M., & Tseng, E. E. (2009). Energy Loss Due to Paravalvular Leak With Transcatheter Aortic Valve Implantation. *The Annals of Thoracic Surgery*, *88*(6), 1857–1863.

B.Hilton, Robert E.Yutzey, K. (2011). Heart valve structure and function in development and disease. *Annual Review of Physiology*, 29–46.

Bäck, M., Gasser, T. C., Michel, J.-B., & Caligiuri, G. (2013). Biomechanical factors in the biology of aortic wall and aortic valve diseases. *Cardiovascular Research*, *99*(2), 232–241.

Bagot, C. N., & Arya, R. (2008). Virchow and his triad: A question of attribution. *British Journal of Haematology*, *143*(2), 180–190.

Bakhtiary, F., Dzemali, O., Steinseiffer, U., Schmitz, C., Glasmacher, B., Moritz, A., & Kleine, P. (2007). Opening and closing kinematics of fresh and calcified aortic valve prostheses: An in vitro study. *Journal of Thoracic and Cardiovascular Surgery*, *134*(3), 657–662.

Balachandran, K., Sucosky, P., & Yoganathan, A. P. (2011). Hemodynamics and Mechanobiology of Aortic Valve Inflammation and Calcification. *International Journal of Inflammation*, *2011*, 1–15.

Barannyk, O., & Oshkai, P. (2015). The Influence of the Aortic Root Geometry on Flow Characteristics of a Prosthetic Heart Valve. *Journal of Biomechanical Engineering*, *137*(5), 051005.

Baskurt, O. K., & Meiselman, H. J. (2003). Blood Rheology and Hemodynamics. *Seminars in Thrombosis and Hemostasis*, *29*(5), 435–450.

Batchelor, C. K., & Batchelor, G. K. (2000). *Introduction to Fluid Dynamics*. Cambridge University Press.

Baumgartner, H., Hung, J., Bermejo, J., Chambers, J. B., Evangelista, A., Griffin, B. P., … Quiñones, M. (2009). Echocardiographic Assessment of Valve Stenosis: EAE/ASE Recommendations for Clinical Practice. *Journal of the American Society of Echocardiography*, *22*(1), 1–23.

Bavo, A. M., Rocatello, G., Iannaccone, F., Degroote, J., Vierendeels, J., & Segers, P. (2016). Fluid-Structure Interaction Simulation of Prosthetic Aortic Valves: Comparison between Immersed Boundary and Arbitrary Lagrangian-Eulerian Techniques for the Mesh Representation. *Plos One*, *11*(4), e0154517.

Bellhouse, B. J., & Bellhouse, F. H. (1968). Mechanism of closure of the aortic valve. *Nature*, *217*(5123), 86–87.

Bellhouse, B. J., Bellhouse, F. H., & Reid, K. G. (1968). Fluid mechanics of the aortic root with application to coronary flow. *Nature*, *219*(5158), 1059–1061.

Bellhouse, B. J., & Talbot, L. (1969). Fluid mechanics of the aortic valve. *British Heart Journal*, *31*(3), 391.

Ben-Dor, I., Malik, R., Minha, S., Goldstein, S. a., Wang, Z., Magalhaes, M. a., … Waksman, R. (2014). Coronary Blood Flow in Patients With Severe Aortic Stenosis Before and After Transcatheter Aortic Valve Implantation. *The American Journal of Cardiology*, *114*(8), 1264–1268.

Berntson, G., Quigley, K., Norman, G., & Lozano, D. (2016). Cardiovascular psychophysiology. In *Handbook of Psychophysiology* (Vol. 32, pp. 183–216). Cambridge: Cambridge University Press.

Biasetti, J., Spazzini, P. G., Swedenborg, J., & Christian Gasser, T. (2012). An integrated fluid-chemical model toward modeling the formation of intra-luminal thrombus in abdominal aortic aneurysms. *Frontiers in Physiology*, *3 JUL*(July), 1–16.

Billiar, K. L., & Sacks, M. S. (2000). Biaxial mechanical properties of the natural and glutaraldehyde treated aortic valve cusp--Part II: A structural constitutive model. *Journal of Biomechanical Engineering*, *122*(1), 23–30.

Bissell, M. M., Dall'Armellina, E., & Choudhury, R. P. (2014). Flow vortices in the aortic root: in vivo 4D-MRI confirms predictions of Leonardo da Vinci. *European Heart Journal*, *35*(20), 1344–1344.

Black, M. M., Howard, I. C., Huang, X., & Patterson, E. A. (1991). A three-dimensional analysis of a bioprosthetic heart valve. *Journal of Biomechanics*, *24*(9).

Bloomfield, G. S., Gillam, L. D., Hahn, R. T., Kapadia, S., Leipsic, J., Lerakis, S., … Douglas, P. S. (2012). A practical guide to multimodality imaging of transcatheter aortic valve replacement. *JACC: Cardiovascular Imaging*, *5*(4), 441–455.

Bloomfield, P. (2002). *Choice of heart valve prosthesis*.

Bluestein, D., Chandran, K. B., & Manning, K. . B. (2010). Towards Non-thrombogenic Performance of Blood Recirculation Devices. *Ann Biomed Eng.*, *38*(3), 1236–1256.

Bluestein, Danny, Rambod, E., & Gharib, M. (1999). Vortex Shedding as a Mechanism for Free Emboli Formation in Mechanical Heart Valves. *Journal of Biomechanical Engineering*, *122*(2), 125–134.

Boon, A., Cheriex, E., Lodder, J., & Kessels, F. (1997). Cardiac valve calcification: Characteristics of patients with calcification of the mitral annulus or aortic valve. *Heart*, *78*(5), 472–474.

Borazjani, I. (2013). Fluid-structure interaction, immersed boundary-finite element method simulations of bio-prosthetic heart valves. *Computer Methods in Applied Mechanics and Engineering*, *257*, 103–116.

Boulpaep, W. F. B. E. L. (2009). *Medical physiology : a cellular and molecular* *approach*. Philadelphia, PA: Saunders/Elsevier.

Bozkurt, S., Preston-Maher, G. L., Torii, R., & Burriesci, G. (2017). Design, Analysis and Testing of a Novel Mitral Valve for Transcatheter Implantation. *Annals of Biomedical Engineering*, *45*(8), 1852–1864.

Breddin, H. K. (1989). Thrombosis and Virchow's triad: What is established? *Seminars in Thrombosis and Hemostasis*, *15*(3), 237–239.

Bui, T. (2010). Explicit and Implicit Methods In Solving Differential Equations. *Honors Scholar Program*, 1–45.

Burriesci, G., Marincola, F. C., & Zervides, C. (2010). Design of a novel polymeric heart valve. *Journal of Medical Engineering & Technology*, *34*(1), 7–22.

Cannegieter, S. C., Rosendaal, F. R., & Briet, E. (1994). Thromboembolic and bleeding complications in patients with mechanical heart valve prostheses. *Circulation*, *89*(2), 635–641.

Cao, K., Bukač, M., & Sucosky, P. (2016). Three-dimensional macro-scale assessment of regional and temporal wall shear stress characteristics on aortic valve leaflets. *Computer Methods in Biomechanics and Biomedical Engineering*, *19*(6), 603–613.

Capelli, C., Corsini, C., Biscarini, D., Ruffini, F., Migliavacca, F., Kocher, A., … Rath, C. (2017). Pledget-Armed Sutures Affect the Haemodynamic Performance of Biologic Aortic Valve Substitutes: A Preliminary Experimental and Computational Study. *Cardiovascular Engineering and Technology*, *8*(1), 17–29.

Carabello, B. a. (2007). *Aortic Valve Disease*. 381–392.

Carmody, C. J., Burriesci, G., Howard, I. C., & Patterson, E. A. (2006). An approach to the simulation of fluid-structure interaction in the aortic valve. *Journal of Biomechanics*, *39*(1), 158–169.

Caro, C., Pedley, T., Schroter, R., Seed, W., & Parker, K. (2012). *The Mechanics of the Circulation*. Cambridge: Cambridge University Press.

Caro, C. G., Pedley, T. J., Schroter, R. C., & Seed, W. A. (2012). *The Mechanics of Circulation* (2nd ed.). Cambridge.

Carpentier, A. (2007). The surprising rise of nonthrombogenic valvular surgery. *Nature Medicine*, *13*(10), 1165–1168.

Chandran, K. (2010). Role of Computational Simulations in Heart Valve Dynamics and Design of Valvular Prostheses. *Cardiovasc. Eng. Technol.*, *1*(1), 18–38.

Chandran, K. B., Rittgers, S. E., & Yoganathan, A. P. (2012). *Biofluid Mechanics - The Human Circulation* (Second). CRC Press, Inc.

Charitos, E. I., & Sievers, H.-H. (2013). Anatomy of the aortic root: implications for valve-sparing surgery. *Annals of Cardiothoracic Surgery*, *2*(1), 53–56.

Chen, Y., & Luo, H. (2018). A computational study of the three-dimensional fluid–structure interaction of aortic valve. *Journal of Fluids and Structures*, *80*, 332–349.

Cheng, C. L., Chang, H. H., Huang, P. J., Wang, W. C., & Lin, S. Y. (2017). Ex vivo assessment of valve thickness/calcification of patients with calcific aortic stenosis in relation to in vivo clinical outcomes. *Journal of the Mechanical Behavior of Biomedical Materials*, *74*(March), 324–332.

Cleveland, J. D., Bowdish, M. E., Eberhardt, C. E., Mack, W. J., Crabtree, J. A., Vassiliades, T. A., … Cohen, R. G. (2017). Evaluation of Hemodynamic Performance of Aortic Valve Bioprostheses in a Model of Oversizing. *Annals of Thoracic Surgery*, *103*(6), 1866–1876.

Cohen, Michael V., Gorlin, R. (1972). Modified calculation orifice equation valve for the of mitral area Cardioversion of atrial after valve replacement * fibrillation. *The American Heart Journal*, *84*(6), 839–840.

Corbett, S. C., Ajdari, A., Coskun, A. U., & N-Hashemi, H. (2010). In vitro and computational thrombosis on artificial surfaces with shear stress. *Artificial Organs*, *34*(7), 561–569.

Corbett, S. C., Ajdari, A., Coskun, A. U., & Nayeb-Hashemi, H. (2010). Effect of pulsatile blood flow on thrombosis potential with a step wall transition. *ASAIO Journal*, *56*(4), 290–295.

Cozijnsen, L., Braam, R. L., Waalewijn, R. A., Schepens, M. A. A. M., Loeys, B. L., Van Oosterhout, M. F. M., … Mulder, B. J. M. (2011). What is new in dilatation of the ascending aorta?: Review of current literature and practical advice for the cardiologist. *Circulation*, *123*(8), 924–928.

Crawford, M. H., & Roldan, C. A. (2001). Prevalence of aortic root dilatation and small aortic roots in valvular aortic stenosis. *American Journal of*

Cardiology, *87*(11), 1311–1313.

Cribier, a. (2002). Percutaneous Transcatheter Implantation of an Aortic Valve Prosthesis for Calcific Aortic Stenosis: First Human Case Description. *Circulation*, *106*(24), 3006–3008.

Croft, L. R., Mofrad, M.R.K., M. R. K. (2010). Computational Modeling in Biomechanics. In S. De, F. Guilak, & M. Mofrad R. K. (Eds.), *Computational Cardiovascular mechanics*. Dordrecht: Springer Netherlands.

Dare, A. J., Veinot, J. P., Edwards, W. D., Tazelaar, H. D., & Schaff, H. V. (1993). New observations on the etiology of aortic valve disease: A surgical pathologic study of 236 cases from 1990. *Human Pathology*, *24*(12), 1330–1338.

Dasi, L. P., Ge, L., Simon, A. H., Sotiropoulos, F., & Yoganathan, P. A. (2007). Vorticity dynamics of a bileaflet mechanical heart valve in an axisymmetric aorta. *Physics of Fluids*, *19*(6).

Dasi, Lakshmi P., Simon, H. A., Sucosky, P., & Yoganathan, A. P. (2009). Fluid mechanics of artificial heart valves. *Clinical and Experimental Pharmacology and Physiology*, *36*(2), 225–237.

De Hart, J., Peters, G. W. M., Schreurs, P. J. G., & Baaijens, F. P. T. (2003). A three-dimensional computational analysis of fluid-structure interaction in the aortic valve. *Journal of Biomechanics*, *36*(1), 103–112.

De Tullio, M. D., Cristallo, A., Balaras, E., & Verzicco, R. (2009). Direct numerical simulation of the pulsatile flow through an aortic bileaflet mechanical heart valve. *Journal of Fluid Mechanics*, *622*, 259.

Dimasi, A., Cattarinuzzi, E., Stevanella, M., Conti, C. A., Votta, E., Maffessanti, F., … Redaelli, A. (2012). Influence of Mitral Valve Anterior Leaflet in vivo Shape on Left Ventricular Ejection. *Cardiovascular Engineering and Technology*, *3*(4), 388–401.

Ducci, A., Pirisi, F., Tzamtzis, S., & Burriesci, G. (2016). Transcatheter aortic valves produce unphysiological flows which may contribute to thromboembolic events: An in-vitro study. *Journal of Biomechanics*, *49*(16), 4080–4089.

Ducci, A., Tzamtzis, S., Mullen, M. J., & Burriesci, G. (2012). Phase-resolved velocity measurements in the Valsalva sinus downstream of a Transcatheter Aortic Valve. *16th Int Symp on Applications of Laser*

Techniques to Fluid Mechanics, 9-12 July.

Ducci, A., Tzamtzis, S., Mullen, M. J., & Burriesci, G. (2013). Hemodynamics in the Valsalva sinuses after transcatheter aortic valve implantation (TAVI). *The Journal of Heart Valve Disease*, *22*(5), 688–696.

Dumesnil, J. G., & Yoganathan, A. P. (1991). Theoretical and practical differences between the Gorlin formula and the continuity equation for calculating aortic and mitral valve areas. *The American Journal of Cardiology*, *67*(15), 1268–1272.

Dumont, I. K. (2005). *Experimental and numerical modeling of heart valve dynamics*. 1–272.

Dumont, K., Stijnen, J. M. A., Vierendeels, J., van de Vosse, F. N., & Verdonck, P. R. (2004). Validation of a Fluid–Structure Interaction Model of a Heart Valve using the Dynamic Mesh Method in Fluent. *Computer Methods in Biomechanics and Biomedical Engineering*, *7*(3), 139–146.

Eichinger, W., Botzenhardt, F., Guenzinger, R., Bleiziffer, S., Keithahn, A., Bauernschmitt, R., & Lange, R. (2004). The effective orifice area/patient aortic annulus area ratio: a better way to compare different bioprostheses? A prospective randomized comparison of the Mosaic and Perimount bioprostheses in the aortic position. *The Journal of Heart Valve Disease*, *13*, 382–388; discussion 388.

Einstein, D. R., Reinhall, P., Nicosia, M., Cochran, R. P., & Kunzelman, K. (2003). Dynamic Finite Element Implementation of Nonlinear, Anisotropic Hyperelastic Biological Membranes. *Computer Methods in Biomechanics and Biomedical Engineering*, *6*(1), 33–44.

Ellis, T. J., Yoganathan, A. P. (1996). *Velocity measurements and flow patterns within the hinge region of a Medtronic Parallel bileaflet mechanical valve with clear housing*. *5*.

Escobar Kvitting, J. P., Ebbers, T., Wigström, L., Engvall, J., Olin, C. L., & Bolger, A. F. (2004). Flow patterns in the aortic root and the aorta studied with time-resolved, 3-dimensional, phase-contrast magnetic resonance imaging: Implications for aortic valve-sparing surgery. *Journal of Thoracic and Cardiovascular Surgery*, *127*(6), 1602–1607.

Falahatpisheh, A., & Kheradvar, A. (2012). High-speed particle image velocimetry to assess cardiac fluid dynamics in vitro: From performance to validation. *European Journal of Mechanics B/Fluids*, *35*, 2–8.

Farley, A., McLafferty, E., & Hendry, C. (2012). The cardiovascular system. *Nursing Standard*, *27*(9), 35–39.

Filová, E., Straka, F., Ejovský, T. M. I. Ř., Mašín, J., & Œková, L. B. A. Č. (2009). *Tissue-Engineered Heart Valves*. *58*.

Furie, B., & Furie, B. C. (2008). Mechanisms of Thrombus Formation. *New England Journal of Medicine*, *359*(9), 938–949.

Fuster, V., Topol, E.J. , Nabel, E. G. (2005). *Atherothrombosis and Coronary Artery Disease*. Philadelphia, PA, PA: Lippincott Williams & Wilkins.

Gao, G., Wu, Y., Grunkemeier, G. L., Furnary, A. P., & Starr, A. (2004). Durability of Pericardial Versus Porcine Aortic Valves. *Journal of the American College of Cardiology*, *44*(2), 384–388.

Garcia, D., & Kadem, L. (2006). What Do You Mean by Aortic Valve Area: Geometric Orifice Area, Effective Orifice Area, or Gorlin Area? *J Heart Valve Dis*, *15*(5), 601–608.

Gassler, N., & Schnabel, P. A. (2010). Pathology of Aortic Stenosis. In *Cardiovascular Interventions in Clinical Practice* (pp. 71–85). Oxford, UK: Wiley-Blackwell.

Ge, L., Jones, S. C., Sotiropoulos, F., Healy, T. M., & Yoganathan, A. P. (2003). Numerical Simulation of Flow in Mechanical Heart Valves: Grid Resolution and the Assumption of Flow Symmetry. *Journal of Biomechanical Engineering*, *125*(5), 709.

Gorlin, R., & Gorlin, S. G. (1951). Hydraulic formula for calculation of the area of the stenotic mitral valve, other cardiac valves, and central circulatory shunts. *American Heart Journal*, *41*(5), 1–29.

Grande, K. J., Cochran, R. P., Reinhall, P. G., & Kunzelman, K. S. (2000). Mechanisms of aortic valve incompetence: finite element modeling of aortic root dilatation. *The Annals of Thoracic Surgery*, *69*(6), 1851–1857.

Griffith, B. E. (2012). Immersed boundary model of aortic heart valve dynamics with physiological driving and loading conditions. *International Journal for Numerical Methods in Biomedical Engineering*, *28*(3), 317–345.

Groves, E. M., Falahatpisheh, A., Su, J. L., & Kheradvar, A. (2014). The Effects of Positioning of Transcatheter Aortic Valve on Fluid Dynamics of the Aortic Root. *ASAIO Journal (American Society for Artificial*

Internal Organs : 1992), *60*(5), 545–552.

Guala, A., Camporeale, C., & Ridolfi, L. (2015). Compensatory effect between aortic stiffening and remodelling during ageing. *PLoS ONE*, *10*(10), 1–14.

Guccione, J.M., Kassab, G., Ratcliffe, M. B. (2010). *Computational cardiovascular mechanics*. Springer Science & Business Media.

Guivier-Curien, C., Deplano, V., & Bertrand, E. (2009). Validation of a numerical 3-D fluid-structure interaction model for a prosthetic valve based on experimental PIV measurements. *Medical Engineering and Physics*, *31*(8), 986–993.

Gunning, P. S., Saikrishnan, N., McNamara, L. M., & Yoganathan, A. P. (2014). An In Vitro Evaluation of the Impact of Eccentric Deployment on Transcatheter Aortic Valve Hemodynamics. *Annals of Biomedical Engineering*, *42*(6), 1195–1206.

Gunning, P. S., Vaughan, T. J., & McNamara, L. M. (2014). Simulation of self expanding transcatheter aortic valve in a realistic aortic root: Implications of deployment geometry on leaflet deformation. *Annals of Biomedical Engineering*, *42*(9), 1989–2001.

Hall, J. E., & Guyton, A. C. (2011). *Guyton and Hall textbook of medical physiology*. Philadelphia: Saunders Elsevier.

Hallquist, J. O. (2006). *LS-DYNA Theory Manual*.

Hammermeister, K., Sethi, G. K., Henderson, W. G., Grover, F. L., Oprian, C., & Rahimtoola, S. H. (2000). Outcomes 15 years after valve replacement with a mechanical versus a bioprosthetic valve: Final report of the Veterans Affairs randomized trial. *Journal of the American College of Cardiology*, *36*(4), 1152–1158.

Harken, D. E., Taylor, W. J., Lefemine, A. a, Lunzer, S., Low, H. B. C., Cohen, M. L., & Jacobey, J. a. (1962). Aortic valve replacement with a gaged ball valve. *The American Journal of Cardiology*, *9*(2), 292–299.

Hatoum, H., Moore, B. L., Maureira, P., Dollery, J., Crestanello, J. A., & Dasi, L. P. (2017). Aortic sinus flow stasis likely in valve-in-valve transcatheter aortic valve implantation. *Journal of Thoracic and Cardiovascular Surgery*, *154*(1), 32-43.e1.

Heemskerk, J. W. M., Bevers, E. M., & Lindhout, T. (2002). Platelet activation and blood coagulation. *Thrombosis and Haemostasis*, *88*(2), 186–193.

Honda, S., Kitai, T., Okada, Y., Tani, T., Kim, K., Kaji, S., … Furukawa, Y. (2012). Impact of aortic regurgitation on the prognosis of severe aortic stenosis. *Heart*, *98*(21), 1591–1594.

Hope, M. D., Sedlic, T., & Dyverfeldt, P. (2013). Cardiothoracic Magnetic Resonance Flow Imaging. *Journal of Thoracic Imaging*, *28*(4), 217–230.

Howard, I. C., Patterson, E. A., & Yoxall, A. (2003). On the opening mechanism of the aortic valve: Some observations from simulations. *Journal of Medical Engineering and Technology*, *27*(6), 259–266.

Hsu, M.-C., Kamensky, D., Bazilevs, Y., Sacks, M. S., & Hughes, T. J. R. (2014). Fluid–structure interaction analysis of bioprosthetic heart valves: significance of arterial wall deformation. *Computational Mechanics*, *54*(4), 1055–1071.

Hutson, H. N., Marohl, T., Anderson, M., Eliceiri, K., Campagnola, P., & Masters, K. S. (2016). Calcific aortic valve disease is associated with layer-specific alterations in collagen architecture. *PLoS ONE*, *11*(9), 1–18.

International Standard ISO 5840:2009. (n.d.). *Cardiovascular implants - Cardiac valve prostheses (ISO 5840:2015).*

Iung, B., Gabriel, B., Eric G., B., François, D., Christa, G.-B., Olaf W., L., … Alec, V. (2003). A prospective survey of patients with valvular heart disease in Europe: The Euro Heart Survey on Valvular Heart Disease. *European Heart Journal*, *24*(13), 1231–1243.

Iung, B., & Vahanian, A. (2011). Epidemiology of valvular heart disease in the adult. *Nature Reviews Cardiology*, *8*(3), 162–172.

J.R. Levick. (2009). *An Introduction to Cardiovascular Physiology 5E.* Taylor & Francis.

Jahandardoost, M., Fradet, G., & Mohammadi, H. (2015). A novel computational model for the hemodynamics of bileaflet mechanical valves in the opening phase. *Proceedings of the Institution of Mechanical Engineers, Part H: Journal of Engineering in Medicine*, *229*(3), 232–244.

Jamieson, W. R. E., Burr, L. H., Miyagishima, R. T., Germann, E., MacNab, J. S., Stanford, E., … Ling, H. (2005). Carpentier-Edwards supra-annular aortic porcine bioprosthesis: Clinical performance over 20 years. *Journal of Thoracic and Cardiovascular Surgery*, *130*(4), 994–1000.

Joda, A., Jin, Z., Haverich, A., Summers, J., & Korossis, S. (2016). Multiphysics simulation of the effect of leaflet thickness inhomogeneity and material anisotropy on the stress–strain distribution on the aortic valve. *Journal of Biomechanics*, *49*(12), 2502–2512.

Kahlert, P., Knipp, S. C., Schlamann, M., Thielmann, M., Al-Rashid, F., Weber, M., … Eggebrecht, H. (2010). Silent and apparent cerebral ischemia after percutaneous transfemoral aortic valve implantation: A diffusion-weighted magnetic resonance imaging study. *Circulation*, *121*(7), 870–878.

Kalyana Sundaram, G. B., Balakrishnan, K. R., & Kumar, R. K. (2015). Aortic valve dynamics using a fluid structure interaction model - The physiology of opening and closing. *Journal of Biomechanics*, *48*(10), 1737–1744.

Katritsis, D., Kaiktsis, L., Chaniotis, A., Pantos, J., Efstathopoulos, E. P., & Marmarelis, V. (2007). Wall Shear Stress: Theoretical Considerations and Methods of Measurement. *Progress in Cardiovascular Diseases*, *49*(5), 307–329.

Kemp, I., Dellimore, K., Rodriguez, R., Scheffer, C., Blaine, D., Weich, H., & Doubell, A. (2013). Experimental validation of the fluid-structure interaction simulation of a bioprosthetic aortic heart valve. *Australasian Physical and Engineering Sciences in Medicine*, *36*(3), 363–373.

Kheradvar, A., Groves, E. M., Falahatpisheh, A., Mofrad, M. K., Hamed Alavi, S., Tranquillo, R., … Griffith, B. (2015). Emerging Trends in Heart Valve Engineering: Part IV. Computational Modeling and Experimental Studies. *Annals of Biomedical Engineering*, *43*(10), 2314–2333.

Kidane, A. G., Burriesci, G., Cornejo, P., Dooley, A., Sarkar, S., Bonhoeffer, P., … Seifalian, A. M. (2009). Current developments and future prospects for heart valve replacement therapy. *Journal of Biomedical Materials Research - Part B Applied Biomaterials*, *88*(1), 290–303.

King, M. J., Corden, J., David, T., & Fisher, J. (1996). A three-dimensional, time-dependent analysis of flow through a bileaflet mechanical heart valve: Comparison of experimental and numerical results. *Journal of Biomechanics*, *29*(5), 609–618.

Kirali, K., & Günay, D. (2017). Isolated Aortic Root Aneurysms. In *Aortic Aneurysm*: *Vol. i* (p. 13). InTech.

Klabunde, R. E. (2011). Cardiovascular Physiology Concepts. In *Lippincott Williams & Wilkins*. Lippincott Williams & Wilkins.

Kodali, S. K., Williams, M. R., Smith, C. R., Svensson, L. G., Webb, J. G., Makkar, R. R., … Leon, M. B. (2012). Two-Year Outcomes after Transcatheter or Surgical Aortic-Valve Replacement. *New England Journal of Medicine*, *366*(18), 1686–1695.

Ku, D. N., Casa, L. D. C., & Hastings, S. M. (2017). Choice of a hemodynamic model for occlusive thrombosis in arteries. *Journal of Biomechanics*, *50*, 110–113.

Külling, M., Külling, J., Wyss, C., Hürlimann, D., Reho, I., Salzberg, S., … Biaggi, P. (2018). Effective orifice area and hemodynamic performance of the transcatheter Edwards Sapien 3 prosthesis: Short-term and 1-year follow-up. *European Heart Journal Cardiovascular Imaging*, *19*(1), 23–30.

Kumar, D. R., Hanlin, E. R., Glurich, I., Mazza, J. J., & Yale, S. H. (2010). Virchow's contribution to the understanding of thrombosis and cellular biology. *Clinical Medicine and Research*, *8*(3–4), 168–172.

Kumar, G., Raghav, V., Lerakis, S., & Yoganathan, A. P. (2015). High Transcatheter Valve Replacement May Reduce Washout in the Aortic Sinuses: an In-Vitro Study. *The Journal of Heart Valve Disease*, *24*(1), 22–29.

Kyrle, P. A., & Eichinger, S. (2013). Is Virchow ' s triad complete ? *Blood Journal*, *114*(6), 1138–1139.

Laadhari, A., & Székely, G. (2017). Eulerian finite element method for the numerical modeling of fluid dynamics of natural and pathological aortic valves. *Journal of Computational and Applied Mathematics*, *319*, 236–261.

Laas, J., Kleine, P., Hasenkam, M. J., & Nygaard, H. (1999). Orientation of tilting disc and bileaflet aortic valve substitutes for optimal hemodynamics. *Annals of Thoracic Surgery*, *68*(3), 1096–1099.

Leverett, L. B., Hellums, J. D., Alfrey, C. P., & Lynch, E. C. (1972). Red Blood Cell Damage by Shear Stress. *Biophysical Journal*, *12*(3), 257–273.

Leyh, R. G., Schmidtke, C., Sievers, H.-H., & Yacoub, M. H. (1999). Opening and closing characteristics of the aortic valve after different types of valve-preserving surgery. *Circulation*, *100*(21), 2153–2160.

Li, J. K.-J. (2004). *Dynamics of the vascular system*.

Lowe, G. D. O. (2004). Virchow ' s Triad Revisited : Abnormal Flow. *Pathophysiology of Haemostasis and Thrombosis*, *33*, 455–457.

LS-DYNA Aerospace Working Group Modeling Guidelines Document. (2011).

Lu, M. T., Thadani, S. R., & Hope, M. D. (2013). Quantitative Assessment of Asymmetric Aortic Dilation with Valve-related Aortic Disease. *Academic Radiology*, *20*(1), 10–15.

Luraghi, G., Migliavacca, F., & Rodriguez Matas, J. F. (2018). Study on the Accuracy of Structural and FSI Heart Valves Simulations. *Cardiovascular Engineering and Technology*, 1–16.

Luraghi, G., Wu, W., De Gaetano, F., Rodriguez Matas, J. F., Moggridge, G. D., Serrani, M., … Migliavacca, F. (2017). Evaluation of an aortic valve prosthesis: Fluid-structure interaction or structural simulation? *Journal of Biomechanics*, *58*, 45–51.

Lutter, G., Ardehali, R., & Cremer, J. (2004). *Percutaneous Valve Replacement : Current State and future prospects*.

M. Souli, A. Ouahsine, L. L. (2017). ALE formulation for fluid-structure interactions. *Computer Methods in Applied Mechanics and Engineering*, *118*, 203–254.

Mackman, N. (2008). Triggers, targets and treatments for thrombosis. *Nature*, *451*(7181), 914–918.

Makkar, R. R., Fontana, G., Jilaihawi, H., Chakravarty, T., Kofoed, K. F., De Backer, O., … Søndergaard, L. (2015). Possible Subclinical Leaflet Thrombosis in Bioprosthetic Aortic Valves. *New England Journal of Medicine*, *373*(21), 2015–2024.

Maleki, H., Shahriari, S., Labrosse, M., Rodés-Cabau, J., Pibarot, P., & Kadem, L. (2015). Effect of Aortic Annulus Size and Prosthesis Oversizing on the Hemodynamics and Leaflet Bending Stress of Transcatheter Valves: An InVitro Study. *Canadian Journal of Cardiology*, *31*(8), 1041–1046.

Mao, W., Li, K., & Sun, W. (2016). Fluid–Structure Interaction Study of Transcatheter Aortic Valve Dynamics Using Smoothed Particle

Hydrodynamics. *Cardiovascular Engineering and Technology*, *7*(4), 374–388.

Marom, G. (2015). Numerical Methods for Fluid–Structure Interaction Models of Aortic Valves. *Archives of Computational Methods in Engineering*, *22*(4), 595–620.

Marom, G., Halevi, R., Haj-Ali, R., Rosenfeld, M., Schäfers, H. J., & Raanani, E. (2013). Numerical model of the aortic root and valve: Optimization of graft size and sinotubular junction to annulus ratio. *Journal of Thoracic and Cardiovascular Surgery*, *146*(5), 1227–1231.

Maselli, D., De Paulis, R., Scaffa, R., Weltert, L., Bellisario, A., Salica, A., & Ricci, A. (2007). Sinotubular Junction Size Affects Aortic Root Geometry and Aortic Valve Function in the Aortic Valve Reimplantation Procedure: An In Vitro Study Using the Valsalva Graft. *Annals of Thoracic Surgery*, *84*(4), 1214–1218.

Mendelson, K., & Schoen, F. J. (2006). Heart valve tissue engineering: Concepts, approaches, progress, and challenges. *Annals of Biomedical Engineering*, *34*(12), 1799–1819.

Menichini, C., & Xu, X. Y. (2016). Mathematical modeling of thrombus formation in idealized models of aortic dissection: initial findings and potential applications. *Journal of Mathematical Biology*, *73*(5), 1205–1226.

Midha, P. A., Raghav, V., Sharma, R., Condado, J. F., Okafor, I. U., Rami, T., … Yoganathan, A. P. (2017). The Fluid Mechanics of Transcatheter Heart Valve Leaflet Thrombosis in the Neo-Sinus. *Circulation*, 1598–1609.

Miller, G. E. (2006). Artificial Organs. In *Synthesis Lectures on Biomedical Engineering* (Vol. 1).

Mohammadi, H., Cartier, R., & Mongrain, R. (2016). Review of numerical methods for simulation of the aortic root: Present and future directions. *International Journal for Computational Methods in Engineering Science and Mechanics*, *17*(3), 182–195.

Mohler, E. R., Gannon, F., Reynolds, C., Zimmerman, R., Keane, M. G., & Kaplan, F. S. (2001). Bone formation and inflammation in cardiac valves. *Circulation*, *103*(11), 1522–1528.

Moore, B. L., & Dasi, L. P. (2015). Coronary Flow Impacts Aortic Leaflet

Mechanics and Aortic Sinus Hemodynamics. *Annals of Biomedical Engineering*, *43*(9), 2231–2241.

Morbiducci, U., Ponzini, R., Nobili, M., Massai, D., Montevecchi, F. M., Bluestein, D., & Redaelli, A. (2009). Blood damage safety of prosthetic heart valves. Shear-induced platelet activation and local flow dynamics: A fluid-structure interaction approach. *Journal of Biomechanics*, *42*(12), 1952–1960.

Muraru, D., Badano, L. P., Vannan, M., & Iliceto, S. (2012). Assessment of aortic valve complex by three-dimensional echocardiography: A framework for its effective application in clinical practice. *European Heart Journal Cardiovascular Imaging*, *13*(7), 541–555.

Nataf, P. (2006). Dilation of the thoracic aorta: medical and surgical management. *Heart*, *92*(9), 1345–1352.

Nicosia MA, Cochran RP, Einstein DR, Rutland CJ, K. K. (2003). A coupled fluid-structure finite element model of the aortic valve and root. *J. Heart Valve Disease*, *12*, 781–789.

Nishimura, R. A. (2002). Aortic valve disease. *Circulation*, *106*(7), 770–772.

Nobari, S., Mongrain, R., Gaillard, E., Leask, R., & Cartier, R. (2012). Therapeutic vascular compliance change may cause significant variation in coronary perfusion: A numerical study. *Computational and Mathematical Methods in Medicine*, *2012*.

Nobari, S., Mongrain, R., Leask, R., & Cartier, R. (2013). The effect of aortic wall and aortic leaflet stiffening on coronary hemodynamic: A fluid-structure interaction study. *Medical and Biological Engineering and Computing*, *51*(8), 923–936.

Nobili, M., Morbiducci, U., Ponzini, R., Del Gaudio, C., Balducci, A., Grigioni, M., … Redaelli, A. (2008). Numerical simulation of the dynamics of a bileaflet prosthetic heart valve using a fluid-structure interaction approach. *Journal of Biomechanics*, *41*(11), 2539–2550.

Oechtering, T. H., Hons, C. F., Sieren, M., Hunold, P., Hennemuth, A., Huellebrand, M., … Frydrychowicz, A. (2016). Time-resolved 3-dimensional magnetic resonance phase contrast imaging (4D Flow MRI) analysis of hemodynamics in valve-sparing aortic root repair with an anatomically shaped sinus prosthesis. *The Journal of Thoracic and Cardiovascular Surgery*, *152*(2), 418-427.e1.

Olson, L. J., Subramanian, R., & Edwards, W. D. (1984). Surgical pathology of pure aortic insufficiency: a study of 225 cases. *Mayo Clinic Proceedings*, *59*(12), 835–841.

Otto, C.M., Bonow, R. O. (2014). *Valvular Heart Disease: A Companion to Braunwald's Heart Disease* (4th ed.). Elsevier Health Sciences.

Otto, C. M. (2000). Aortic Stenosis — Listen to the Patient, Look at the Valve. *New England Journal of Medicine*, *343*(9), 652–654.

Otto, C. M. (2006). Valvular Aortic Stenosis. Disease Severity and Timing of Intervention. *Journal of the American College of Cardiology*, *47*(11), 2141–2151.

Otto, C. M., Burwash, I. G., Legget, M. E., Munt, B. I., Fujioka, M., Healy, N. L., … Schwaegler, R. G. (1997). Prospective Study of Asymptomatic Valvular Aortic Stenosis. *Circulation*, *95*(9), 2262–2270.

Padala, M., Sarin, E. L., Willis, P., Babaliaros, V., Block, P., Guyton, R. A., & Thourani, V. H. (2010). An Engineering Review of Transcatheter Aortic Valve Technologies. *Cardiovascular Engineering and Technology*, *1*(1), 77–87.

Pappano, Achilles J., Withrow Gil Wier, and M. N. L. (2012). *Cardiovascular physiology* (10th ed.). Elsevier Health Sciences.

Perktold, K., & Peter, R. (1990). Numerical 3D-simulation of pulsatile wall shear stress in an arterial T-bifurcation model. *Journal of Biomedical Engineering*, *12*(1), 2–12.

Peskin, C. S. (1972). Flow patterns around heart valves: A numerical method. *Journal of Computational Physics*, *10*(2), 252–271.

Peter F Davies. (2008). Hemodynamic shear stress and the endothelium incardiovascular pathophysiology. *Nature Clinical Practice Cardiovascular Medicine*, *6*(1), 16–26.

Pibarot, P., & Dumesnil, J. G. (2009). Prosthetic Heart Valves. *Circulation*, *119*(7), 1034–1048.

Pietrabissa, R. (1996). *Biomateriali per protesi e organi artificiali*. Pàtron.

Querzoli, G., Fortini, S., Espa, S., Costantini, M., & Sorgini, F. (2014). Fluid dynamics of aortic root dilation in Marfan syndrome. *Journal of Biomechanics*, *47*(12), 3120–3128.

Ragavendra R. Baliga, Kim A. Eagle, William F Armstrong, David S Bach, E. R. B. (Ed.). (2008). *Practical cardiology*. Lippincott Williams & Wilkins.

Rajamannan, N. M., Evans, F. J., Aikawa, E., Grande-Allen, K. J., Demer, L. L., Heistad, D. D., … Otto, C. M. (2011). Calcific aortic valve disease: Not simply a degenerative process: A review and agenda for research from the national heart and lung and blood institute aortic stenosis working group. *Circulation*, *124*(16), 1783–1791.

Rajamannan, N. M., Subramaniam, M., Rickard, D., Stock, S. R., Donovan, J., Springett, M., … Spelsberg, T. (2003). Human Aortic Valve Calcification Is Associated With an Osteoblast Phenotype. *Circulation*, *107*(17), 2181–2184.

Ranga, A., Bouchot, O., Mongrain, R., Ugolini, P., & Cartier, R. (2006). Computational simulations of the aortic valve validated by imaging data: evaluation of valve-sparing techniques. *Interactive CardioVascular and Thoracic Surgery*, *5*(4), 373–378.

Rao, S. S. (2005). *The Finite Element Method in Engineering*. Elsevier.

Reul, H., Vahlbruch, A., Giersiepen, M., Schmitz-Rode, T., Hirtz, V., & Effert, S. (1990). The geometry of the aortic root in health, at valve disease and after valve replacement. *Journal of Biomechanics*, *23*(2), 181–191.

Robert O. Bonow, Douglas L. Mann, Douglas P. Zipes, P. L. (2011). *Braunwald's Heart Disease: A Textbook of Cardiovascular Medicine* (9th ed.). Elsevier Health Sciences.

Rodés-Cabau, J., Dumont, E., Boone, R. H., Larose, E., Bagur, R., Gurvitch, R., … Webb, J. G. (2010). Cerebral embolism following transcatheter aortic valve implantation: Comparison of transfemoral and transapical approaches. *Journal of the American College of Cardiology*, *57*(1), 18–28.

Ross, D. N. (1961). Homograft Replacement of the Aortic Valve. *Lancet*, *2*(7254), 487.

Rossvoll, O., Samstad, S., Torp, H. G., Linker, D. T., Skjærpe, T., Angelsen, B. A. J., & Hatle, L. (1991). The Velocity Distribution in the Aortic Anulus in Normal Subjects: A Quantitative Analysis of Two-dimensional Doppler Flow Maps. *Journal of the American Society of Echocardiography*, *4*(4), 367–378.

Roudaut, R., Serri, K., & Lafitte, S. (2007). Thrombosis of prosthetic heart valves: Diagnosis and therapeutic considerations. *Heart*, *93*(1), 137–142.

Rozeik, M., Wheatley, D., & Gourlay, T. (2014). The aortic valve: structure, complications and implications for transcatheter aortic valve replacement. *Perfusion*, *29*(4), 285–300.

Sacks, M. S, & Yoganathan, A. P. (2007). Heart valve function: a biomechanical perspective. *Philosophical Transactions of the Royal Society B: Biological Sciences*, *362*(1484), 1369–1391.

Sacks, Michael S. (2000). Biaxial mechanical evaluation of planar biological materials. *Journal of Elasticity*, *61*(1–3), 199–246.

Sacks, Michael S., David Merryman, W., & Schmidt, D. E. (2009). On the biomechanics of heart valve function. *Journal of Biomechanics*, *42*(12), 1804–1824.

Sacks, Michael S., Merrryman, W. D., & Schmidt, D. E. (2010). On the Biomechanics of Heart Valve. *Journal of Biomechanics*, *42*(12), 1804–1824.

Sadeghpour, F., Fatouraee, N., & Navidbakhsh, M. (2017). Haemodynamic of blood flow through stenotic aortic valve. *Journal of Medical Engineering & Technology*, *41*(2), 108–114.

Sahasakul, Y., Edwards, W. D., Naessens, J. M., & Tajik, A. J. (1988). Age-related changes in aortic and mitral valve thickness: Implications for two-dimensional echocardiography based on an autopsy study of 200 normal human hearts. *The American Journal of Cardiology*, *62*(7), 424–430.

Saibal, Kar, Prediman, K. S. (2006). Impact of new percutaneous techniques of aortic valve replacement on cardiology/cardiac surgical practice. In T. F. Ziyad M. Hijazi, Carlos E. Ruiz, Philipp Bonhoeffer (Ed.), *Transcatheter valve repair* (p. 384). CRC Press.

Saikrishnan, N., Gupta, S., & Yoganathan, A. P. (2013). Hemodynamics of the Boston Scientific Lotus™ Valve: An In Vitro Study. *Cardiovascular Engineering and Technology*, *4*(4), 427–439.

Saikrishnan, N., & Yoganathan, A. (2013). Transcatheter valve implantation can alter the fluid flow fields in the aortic sinuses and ascending aorta: an in vitro study. *Journal of the American College of Cardiology*, *61*(10), E1957.

Salica, A., Pisani, G., Morbiducci, U., Scaffa, R., Massai, D., Audenino, A., …

De Paulis, R. (2016). The combined role of sinuses of Valsalva and flow pulsatility improves energy loss of the aortic valve. *European Journal of Cardio-Thoracic Surgery*, *49*(4), 1222–1227.

Schnabel, P. A., Lichtenberg, A., Herpel, E., Warth, A., & Gassler, N. (2010). Pathology of Aortic Insufficiency. In *Cardiovascular Interventions in Clinical Practice* (pp. 126–133). Oxford,UK: Wiley-Blackwell.

Schoen, F. J. (2008). Evolving concepts of cardiac valve dynamics: The continuum of development, functional structure, pathobiology, and tissue engineering. *Circulation*, *118*(18), 1864–1880.

Schoen, F. J., & Levy, R. J. (1999). Tissue Heart Valves : Current Challenges and Future Research Perspectives. *Journal of Biomedical Materials Research. Part B, Applied Biomaterials*, *47(4)*, 439–465.

Schoen, F. J., & Levy, R. J. (2005). Calcification of tissue heart valve substitutes: Progress toward understanding and prevention. *Annals of Thoracic Surgery*, *79*(3), 1072–1080.

Seki, A., & Fishbein, M. C. (2016). Age-related Cardiovascular Changes and Diseases. In *Cardiovascular Pathology* (pp. 57–83). Elsevier.

Shadden, S. C., Astorino, M., & Gerbeau, J. F. (2010). Computational analysis of an aortic valve jet with Lagrangian coherent structures. *Chaos*, *20*(1).

Sherman, M. (1992). A power-law formulation of laminar flow in short pipes. *Journal of Fluids Engineering*, *114*(4), 601–605.

Sigüenza, J., Pott, D., Mendez, S., Sonntag, S. J., Kaufmann, T. A. S., Steinseifer, U., & Nicoud, F. (2018). Fluid-structure interaction of a pulsatile flow with an aortic valve model: A combined experimental and numerical study. *International Journal for Numerical Methods in Biomedical Engineering*, *34*(4), e2945.

Silverthorn, D. U. (2013). *Human Physiology: An Integrated Approach*. Pearson Education M.U.A.

Sirois, E., Wang, Q., & Sun, W. (2011). Fluid Simulation of a Transcatheter Aortic Valve Deployment into a Patient-Specific Aortic Root. *Cardiovascular Engineering and Technology*, *2*(3), 186–195.

Smith, C., & Stojko, S. (2004). The Application of Fluid Structure Interaction Techniques within Finite Element Analyses of Water-Filled Transport Flasks. *14th International Symposium on the Packaging and*

Transportation of Radioactive Materials (PATRAM 2004), Berlin, Germany, September 20-24, 2004, (Patram).

Sodhani, D., Reese, S., Moreira, R., Jockenhoevel, S., Mela, P., & Stapleton, S. E. (2017). Multi-scale modelling of textile reinforced artificial tubular aortic heart valves. *Meccanica*, *52*(3), 677–693.

Souli, M., & Benson, D. J. (2013). Arbitrary Lagrangian-Eulerian and Fluid-Structure Interaction. In *Arbitrary Lagrangian-Eulerian and Fluid-Structure Interaction*.

Stella, J. A., & Sacks, M. S. (2007). On the Biaxial Mechanical Properties of the Layers of the Aortic Valve Leaflet. *Journal of Biomechanical Engineering*, *129*(5), 757–766.

Stewart, B. F., Siscovick, D., Lind, B. K., Gardin, J. M., Gottdiener, J. S., Smith, V. E., … Otto, C. M. (1997). Clinical factors associated with calcific aortic valve disease. *Journal of the American College of Cardiology*, *29*(3), 630–634.

Sturla, F., Votta, E., Stevanella, M., Conti, C. A., & Redaelli, A. (2013). Impact of modeling fluid-structure interaction in the computational analysis of aortic root biomechanics. *Medical Engineering and Physics*, *35*(12), 1721–1730.

Sun, L., Chandra, S., & Sucosky, P. (2012). Ex Vivo Evidence for the Contribution of Hemodynamic Shear Stress Abnormalities to the Early Pathogenesis of Calcific Bicuspid Aortic Valve Disease. *PLoS ONE*, *7*(10), e48843.

Sutton, J. P. et al. (1995). The Forgotten Interleaflet Triangles : A Review of the Surgical Anatomy of the Aortic Valve. *The Annals of Thoracic Surgery*, *59*(2), 412–427.

Swanson, W. M., & Clark, R. E. (1974). Dimensions and Geometric Relationships of the Human Aortic Value as a Function of Pressure. *Circulation Research*, *35*(6), 871–882.

Tamburino,C.,Ussia, G. P. (2012). *Percutaneous Treatment of Left Side Cardiac Valves: A Practical Guide for the Interventional Cardiologist*. Springer Science & Business Media,.

Tango, A. M., Salmonsmith, J., Ducci, A., & Burriesci, G. (2018). Validation and Extension of a Fluid–Structure Interaction Model of the Healthy Aortic Valve. *Cardiovascular Engineering and Technology*, *9*(4), 739–751.

Ted Belytschko, Wing Kam Liu, Brian Moran, K. E. (2013). *Nonlinear Finite Elements for Continua and Structures* (John Wiley & Sons, Ed.).

Thubrikar M. (1990). *The Aortic Valve*.

Thubrikar, M. J., Labrosse, M. R., Zehr, K. J., Robicsek, F., Gong, G. G., & Fowler, B. L. (2005). Aortic root dilatation may alter the dimensions of the valve leaflets. *European Journal of Cardio-Thoracic Surgery*, *28*(6), 850–855.

Toggweiler, S., Gurvitch, R., Leipsic, J., Wood, D. A., Willson, A. B., Binder, R. K., … Webb, J. G. (2012). Percutaneous aortic valve replacement: Vascular outcomes with a fully percutaneous procedure. *Journal of the American College of Cardiology*, *59*(2), 113–118.

Toninato, R., Salmon, J., Susin, F. M., Ducci, A., & Burriesci, G. (2016). Physiological vortices in the sinuses of Valsalva: An in vitro approach for bio-prosthetic valves. *Journal of Biomechanics*, *49*(13), 2635–2643.

Truskey, George A., Fan Yuan, D. F. K. (2004). *Transport Phenomena in Biological Systems*. Pearson/Prentice Hall.

Tu, J., Inthavong, K., & Wong, K. K. L. (2015). *Computational Hemodynamics – Theory, Modelling and Applications*.

Underwood, M. J., Khoury, G. El, Deronck, D., Glineur, D., & Dion, R. (2000). *The aortic root : structure , function , and surgical reconstruction*. (c), 376–380.

Vahanian, A., Alfieri, O., Al-Attar, N., Antunes, M., Bax, J., Cormier, B., … Walther, T. (2008). Transcatheter valve implantation for patients with aortic stenosis: a position statement from the European Association of Cardio-Thoracic Surgery (EACTS) and the European Society of Cardiology (ESC), in collaboration with the European Association of Percu. *European Heart Journal*, *29*(11), 1463–1470.

Vahidkhah, K., Barakat, M., Abbasi, M., Javani, S., Azadani, P. N., Tandar, A., … Azadani, A. N. (2017). Valve thrombosis following transcatheter aortic valve replacement: significance of blood stasis on the leaflets. *European Journal of Cardio-Thoracic Surgery*, *51*, ezw407.

Vahidkhah, K., Cordasco, D., Abbasi, M., Ge, L., Tseng, E., Bagchi, P., & Azadani, A. N. (2016). Flow-Induced Damage to Blood Cells in Aortic Valve Stenosis. *Annals of Biomedical Engineering*, *44*(9), 2724–2736.

Vahidkhah, K., Javani, S., Abbasi, M., Azadani, P. N., Tandar, A., Dvir, D., & Azadani, A. N. (2017). Blood Stasis on Transcatheter Valve Leaflets and Implications for Valve-in-Valve Leaflet Thrombosis. *Annals of Thoracic Surgery*, *104*(3), 751–759.

van Loon, R., Anderson, P. D., & van de Vosse, F. N. (2006). A fluid-structure interaction method with solid-rigid contact for heart valve dynamics. *Journal of Computational Physics*, *217*(2), 806–823.

Van Steenhoven, A. A. ., & Van Dongen, M. E. H. (1979). Model studies of the closing behaviour of the aortic valve. *J. Fluid. Mech.*, *90*, 21–32.

Vesely, I. (2003). The evolution of bioprosthetic heart valve design and its impact on durability. *Cardiovascular Pathology*, *12*(5), 277–286.

Vesely, Ivan. (1997). The role of elastin in aortic valve mechanics. *Journal of Biomechanics*, *31*(2), 115–123.

Vesely, Ivan, & Noseworthy, R. (1992). Micromechanics of the fibrosa and the ventricularis in aortic valve leaflets. *Journal of Biomechanics*, *25*(1), 101–113.

Vlahakes, G. J. (2007). Mechanical heart valves: The test of time... *Circulation*, *116*(16), 1759–1760.

Vogel, S., & Thein, S. L. (2018). Platelets at the crossroads of thrombosis, inflammation and haemolysis. *British Journal of Haematology*, *180*(5), 761–767.

Vriz, O., Aboyans, V., D'Andrea, A., Ferrara, F., Acri, E., Limongelli, G., … Bossone, E. (2014). Normal values of aortic root dimensions in healthy adults. *American Journal of Cardiology*, *114*(6), 921–927.

W.Vongpatanasin, L. D. Hillis, R. A. L. (1996). Prosthetic Heart Valves. *The New England Journal of Medicine*, 407–416.

Wald, S., Liberzon, A., & Avrahami, I. (2017). A numerical study of the hemodynamic effect of the aortic valve on coronary flow. *Biomechanics and Modeling in Mechanobiology*.

Ward, R. P. and L. (2006). *Aortic stenosis: Pathophysiologic, clinical, and echocardiographic manifestations*.

Webb, J. G., & Wood, D. A. (2012). Current status of transcatheter aortic valve replacement. *Journal of the American College of Cardiology*, *60*(6), 483–492.

Wei, Z. A., Sonntag, S. J., Toma, M., Singh-Gryzbon, S., & Sun, W. (2018). Computational Fluid Dynamics Assessment Associated with Transcatheter Heart Valve Prostheses: A Position Paper of the ISO Working Group. *Cardiovascular Engineering and Technology*.

Weinberg, E. J., & Kaazempur Mofrad, M. R. (2007). Transient, Three-dimensional, Multiscale Simulations of the Human Aortic Valve. *Cardiovascular Engineering*, *7*(4), 140–155.

Weinberg, E. J., Schoen, F. J., & Mofrad, M. R. K. (2009). A computational model of aging and calcification in the aortic heart valve. *PLoS ONE*, *4*(6), 1–10.

Wendt, D., Stühle, S., Marx, P., Benedik, J., Wendt, H., Stühle, T., … Kowalczyk, W. (2015). The investigation of systolic and diastolic leaflet kinematics of bioprostheses with a new in-vitro test method. *Minimally Invasive Therapy and Allied Technologies*, *24*(5), 274–281.

Weston, M. W., LaBorde, D. V., & Yoganathan, A. P. (1999). Estimation of the Shear Stress on the Surface of an Aortic Valve Leaflet. *Annals of Biomedical Engineering*, *27*(4), 572–579.

Wheatley, D. J., Fisher, J., Reece, I. J., Spyt, T., & Breeze, P. (1987). Primary tissue failure in pericardial heart valves. *The Journal of Thoracic and Cardiovascular Surgery*, *94*(3), 367–374.

White, F. M. (2002). Fluid Mechanics. In *McGraw-Hill,New York*.

Wilton, E., & Jahangiri, M. (2006). Post-stenotic aortic dilatation. *Journal of Cardiothoracic Surgery*, *1*(1), 1–11.

Wootton, D. M., & Ku, D. N. (1999). Fluid Mechanics of Vascular Systems, Diseases, and Thrombosis. *Annual Review of Biomedical Engineering*, *1*(1), 299–329.

Wu, W., Pott, D., Mazza, B., Sironi, T., Dordoni, E., Chiastra, C., … Migliavacca, F. (2016). Fluid–Structure Interaction Model of a Percutaneous Aortic Valve: Comparison with an In Vitro Test and Feasibility Study in a Patient-Specific Case. *Annals of Biomedical Engineering*, *44*(2), 590–603.

Wu, Y. S. (2015). Multiphase Fluid Flow in Porous and Fractured Reservoirs. In *Multiphase Fluid Flow in Porous and Fractured Reservoirs*.

Yacoub, M. H., Kilner, P. J., Birks, E. J., & Misfeld, M. (1999). The aortic outflow and root: a tale of dynamism and crosstalk. *The Annals of Thoracic Surgery*, *68*(99), S37–S43.

Yankah, C. A., Weng, Y., & Hetzer, R. (2010). Aortic Root Surgery. In C. A. Yankah, Y. Weng, & R. Hetzer (Eds.), *Aortic Root Surgery: The Biological Solution*. Heidelberg: Steinkopff.

Yap, C. H., Saikrishnan, N., & Yoganathan, A. P. (2012). Experimental measurement of dynamic fluid shear stress on the ventricular surface of the aortic valve leaflet. *Biomechanics and Modeling in Mechanobiology*, *11*(1–2), 231–244.

Yen, J. H., Chen, S. F., Chern, M. K., & Lu, P. C. (2014). The effect of turbulent viscous shear stress on red blood cell hemolysis. *Journal of Artificial Organs*, *17*(2), 178–185.

Yoganathan, A. P. (1988). Fluid mechanics of aortic stenosis. *European Heart Journal*, *9*(suppl E), 13–17.

Yoganathan, A. P., Chandran, K. B., & Sotiropoulos, F. (2005). Flow in prosthetic heart valves: State-of-the-art and future directions. *Annals of Biomedical Engineering*, *33*(12 SPEC. ISS.), 1689–1694.

Yoganathan, A. P., He, Z., & Casey Jones, S. (2004). Fluid Mechanics of Heart Valves. *Annual Review of Biomedical Engineering*, *6*(1), 331–362.

Zhang, R., & Zhang, Y. (2018). An Experimental Study of Pulsatile Flow in a Compliant Aortic Root Model under Varied Cardiac Outputs. *Fluids*, *3*(4), 71.

Zhang, W., Chen, H. Y., & Kassab, G. S. (2007). A rate-insensitive linear viscoelastic model for soft tissues. *Biomaterials*, *28*(24), 3579–3586.

Zilla, P., Brink, J., Human, P., & Bezuidenhout, D. (2008). Prosthetic heart valves: Catering for the few. *Biomaterials*, *29*(4), 385–406.